

# **Modelling the optical, kinetic, and thermodynamic properties of soot precursor molecules**

Angiras Menon

Churchill College

A dissertation submitted for the  
degree of Doctor of Philosophy



**UNIVERSITY OF  
CAMBRIDGE**

September 2020



---

## Declaration

This thesis is the result of my own work and includes nothing which is the outcome of work done in collaboration except as declared in the Preface and specified in the text. It is not substantially the same as any that I have submitted, or, is being concurrently submitted for a degree or diploma or other qualification at the University of Cambridge or any other University or similar institution except as declared in the Preface and specified in the text. I further state that no substantial part of my thesis has already been submitted, or, is being concurrently submitted for any such degree, diploma or other qualification at the University of Cambridge or any other University or similar institution except as declared in the Preface and specified in the text. This thesis contains fewer than 65,000 words including appendices, bibliography, footnotes, tables and equations and has fewer than 150 figures. Some of the work in this dissertation has been published:

1. **A. Menon**, J.A.H Dreyer, J.W.Martin, J. Akroyd, J.Robertson, and M. Kraft. Optical band gap of cross-linked, curved, and radical polyaromatic hydrocarbons. *Phys. Chem. Chem. Phys.*, 21(29):16240–16251, 2019. doi:[10.1039/C9CP02363A](https://doi.org/10.1039/C9CP02363A)
2. J.W.Martin, **A. Menon**, C.T. Lao, J. Akroyd, and M. Kraft. Dynamic polarity of curved aromatic soot precursors. *Combust. Flame.*, 206:150–157, 2019. doi:[10.1016/j.combustflame.2019.04.046](https://doi.org/10.1016/j.combustflame.2019.04.046)
3. **A. Menon**, G. Leon , J. Akroyd, and M. Kraft. A density functional theory study on the kinetics of seven-member ring formation in polyaromatic hydrocarbons. *Combust. Flame.*, 217:152-174, 2020. doi:[10.1016/j.combustflame.2020.03.032](https://doi.org/10.1016/j.combustflame.2020.03.032)
4. **A. Menon**, J.W. Martin, G. Leon , D. Hou, L. Pascazio, X. You., and M. Kraft. Reactive localized  $\pi$ -radicals on rim-based pentagonal rings: properties and concentration in flames. *Proc. Combust. Inst.*, In Press, 2020.
5. **A. Menon**, J.W. Martin, J. Akroyd , and M. Kraft. Reactivity of Polycyclic Aromatic Hydrocarbon Soot Precursors: Kinetics and Equilibria. *J. Phys. Chem. A*, In Press, 2020.

The work presented in this dissertation has also contributed, to a lesser degree, to the following publications:

- 
1. J.W.Martin, K.L. Bowal, **A. Menon**, R.I Slavchov, J. Akroyd, S. Mosbach, and M. Kraft. Polar curved polycyclic aromatic hydrocarbons in soot formation. *Proc. Combust. Inst.*, 37(1):1117–1123, 2019. doi:[10.1016/j.proci.2018.05.046](https://doi.org/10.1016/j.proci.2018.05.046)
  2. J.W. Martin, D. Hou, **A. Menon**, L Pascazio, J. Akroyd, X. You, and M. Kraft. Reactivity of Polycyclic Aromatic Hydrocarbon Soot Precursors: Implications of Localized  $\pi$ -Radicals on Rim-Based Pentagonal Rings. *J. Phys. Chem. C*, 123(43):26673–26682, 2019. doi:[10.1021/acs.jpcc.9b07558](https://doi.org/10.1021/acs.jpcc.9b07558)
  3. G. Leon, **A. Menon**, L. Pascazio, E.J. Bringley, J. Akroyd, and M. Kraft. Kinetic Monte Carlo statistics of curvature integration by HACA growth and bay closure reactions for PAH growth in a counterflow diffusion flame. *Proc. Combust. Inst.*, Accepted for presentation at 38th International Combustion Symposium, 2020.
  4. L. Pascazio, J.W. Martin, **A. Menon**, D. Hou, J. X. You, and M. Kraft. Aromatic penta-linked hydrocarbons in soot nanoparticle formation. *Proc. Combust. Inst.*, Accepted, 2020.

Other works not presented in this thesis include:

1. N.B. Krdzavac, S. Mosbach, D. Nurkowski, P. Buerger, J.Akroyd, J.W. Martin, **A. Menon**, and M. Kraft, An ontology and semantic web service for quantum chemistry calculations. *J. Chem. Inf. Model.*, 59(7):3154–3165, 2019. doi:[10.1021/acs.jcim.9b00227](https://doi.org/10.1021/acs.jcim.9b00227)
2. **A. Menon**, N.B. Krdzavac, and M. Kraft, From data base to knowledge graph - using data in chemistry. *Curr. Opin. Chem. Eng.*, 26:33–37, 2019. doi:[10.1016/j.coche.2019.08.004](https://doi.org/10.1016/j.coche.2019.08.004)
3. F. Farazi, N.B. Krdzavac, J. Akroyd, S. Mosbach, **A. Menon**, D. Nurkowski, and M. Kraft, Linking reaction mechanisms and quantum chemistry: An ontological approach. *Comput. Chem. Eng.*, 137:106813, 2020. doi:[10.1016/j.compchemeng.2020.106813](https://doi.org/10.1016/j.compchemeng.2020.106813)

Angiras Menon  
September 2020



# Modelling the optical, kinetic, and thermodynamic properties of soot precursor molecules

Angiras Menon

This thesis investigates the optical, kinetic, and thermodynamic properties of soot precursor molecules, namely polyaromatic hydrocarbons (PAHs), by applying *ab initio* quantum chemical methods. In particular, density functional theory (DFT) is applied to study the properties of several different types of PAHs, including curved PAHs, localized  $\pi$ -radical PAHs, and cross-linked PAHs. These studies help model the gas phase chemistry that leads to the formation of these different types of PAHs, and also help assess their relevance to the formation of soot.

The optical band gaps (OBGs) of curved, cross-linked, and radical PAHs are computed using a DFT method corroborated with UV/Visible spectroscopy measurements. Curved PAHs are shown to increase the OBG due to hybridisation changes. In contrast,  $\pi$ -radical character was found to decrease the band gap. Crosslinks are observed to minimally impact the OBG of the monomers. The effect of  $\sigma$ -radicals on the OBG was also shown to be negligible. The results suggest that curved and  $\pi$ -radical PAHs of moderate size can also explain the optical properties of flames.

The persistence of the polarity of curved aromatics in flame conditions is investigated by using DFT to calculate their barriers and rates of inversion. Curved PAHs above 11–15 ( $\approx 0.8$  nm) rings in size were seen to be unable to invert at flame temperatures. This is seen to be a function of the number of pentagons, and hence curvature. *Ab initio* quantum molecular dynamics of a 1 nm curved PAH and  $C_3H_3^+$  chemi-ion suggest molecular dipole fluctuations of 10–20%, with the chemi-ion and PAH being bound for the entire simulation. This suggests curved PAHs are persistently polar at 1500 K and can bind substantially to ions in flames.

The kinetics of seven-member ring formation in PAHs containing a five-member ring is investigated. Seven-member ring formation by the hydrogen-abstraction-acetylene-addition (HACA) mechanism is studied for two different PAHs, one closed shell and one resonance-stabilised-radical (RSR) PAH. The seven-member ring forms more quickly for the RSR PAH. Seven-member

ring formation by four different bay closure processes is also studied. The rate constants determined for the pathways are then used in kinetic simulations in 0D homogeneous reactors. The hydrogen abstraction based pathway is seen to dominate until higher temperatures, where the carbene pathway takes over. The results suggest that seven-member ring formation in PAHs containing a five-member ring is possible at flame temperatures.

The impact of localized  $\pi$ -radicals on soot formation is explored by developing a simple mechanism for their formation and computing their relative concentrations under flame conditions using 0D homogeneous reactor simulations. It is seen that flame temperatures at the onset of nucleation (1400–1500 K) promote the formation of localized  $\pi$ -radicals on rim-based pentagonal rings, whilst lower temperatures favor fully saturated rings, and higher temperatures favor the  $\sigma$ -radical. A kinetic Monte Carlo study indicates that multiple localized  $\pi$ -radicals can form on a single PAH suggesting localized  $\pi$ -radicals on rim-based pentagonal rings could be important to understanding the mechanism of soot formation.

The rate and equilibrium constants of cross-linking reactions between PAHs of various reactive edge types is computed. The forward rate constants confirms that reactions involving aryl  $\sigma$ -radicals are generally fast, but the reactions between aryl  $\sigma$ -radicals and localized  $\pi$ -radicals were notably faster than others. Computed equilibrium constants showed that reactions involving  $\sigma$  and  $\pi$ -radical PAHs are the most favorable at flame temperatures. Calculations for larger PAHs showed that the formation of bonded-and-stacked structures results in substantially enhanced equilibrium constants for the reaction of two large localized  $\pi$ -radicals. This suggests that combined physical and chemical interactions between larger  $\pi$ -radical PAHs could be important in flame environments.

---

## Acknowledgements

First of all, I would like to express my sincere thanks to my supervisor Prof. Markus Kraft for his guidance and advice throughout the project. I also would like to thank Dr. Sebastian Mosbach, for his involvement and help in many aspects of the work described in this thesis, and Dr. Jethro Akroyd, for his advice, patience and supervision during both my undergraduate and postgraduate years.

I want to thank all members of the Computational Modelling Group who have been great company. I want to thank my fellow PhD students, from Kimberly Bowal, Eric J. Bringley, and Gustavo León Cázares, who started the PhD with me and have been constant providers of support, Astrid Boje, Casper Lindberg, Noel Manuputty, Louise Martin, Vishvak Kannan, Shaohua Wu, and Xiaochi Zhou who made my Singapore experience, Luca Banetta and Chung Lao who provided great tea time conversations, Janusz Sikorski who provided great historical conversations, to Jacob Martin, whose constant enthusiasm for all things carbon science is infectious. I also want to thank Drs. Jochen Dreyer, Daniel Nurkowski, Laura Pascazio, and Radomir Slavchov, for their support and postdoc wisdom.

I would like to thank all my friends who made the Department of Chemical Engineering such a great place, namely Sai Darshan Adloor, Eugenia Biral, Zach Bond, Apoorv Jain, Walter Kähm, Ana Morgado, Luís Rocha, Dushanth Seevaratnam, Oliver Vanderpooten, Joseph Wong, and Maria Zacharopoulou. I could not list all of you here, but know you all contributed to a welcoming department.

I am very grateful for the financial support provided by Johnson Matthey and the National Research Foundation Singapore through the Cambridge CARES program.

Last, but most importantly, I would like to thank my parents, Meenakshi Nath and Raghunandan Menon, and brother, Advait Menon, for everything. This thesis would not exist without the constant love and support you have given me my whole life and you will always have my gratitude.

*Angiras Menon, September 2020, Cambridge*



# Contents

|   |           |
|---|-----------|
| List of figures . . . . .                                       | xiv       |
| List of tables . . . . .  | xxiii     |
| <b>1 Introduction</b>   | <b>1</b>  |
| 1.1 Motivation . . . . .  | 2         |
| 1.1.1 Soot as an environmental pollutant . . . . .              | 2         |
| 1.1.2 Carbon nanomaterials . . . . .                            | 4         |
| 1.2 Aim . . . . .   | 5         |
| 1.3 Novel elements of the thesis . . . . .                      | 6         |
| 1.4 Structure of the thesis . . . . .                           | 8         |
| <b>2 Background</b>   | <b>11</b> |
| 2.1 Formation of soot nanoparticles in flames . . . . .         | 12        |
| 2.2 Experimental Techniques . . . . .                           | 14        |
| 2.2.1 Gas Phase measurements of PAHs . . . . .                  | 14        |
| 2.2.2 Particle Phase measurements of soot and PAHs . . . . .    | 17        |
| 2.3 Formation and Growth of PAHs . . . . .                      | 25        |
| 2.3.1 Formation of the first aromatic ring . . . . .            | 25        |
| 2.3.2 Growth beyond benzene - PAHs . . . . .                    | 27        |
| 2.4 Inception of soot from PAHs . . . . .                       | 31        |
| 2.4.1 Inception by physical interactions between PAHs . . . . . | 33        |
| 2.4.2 Inception by chemical bonding between PAHs . . . . .      | 34        |

## CONTENTS

---

|          |  |           |
|----------|--|-----------|
| 2.4.3    | Combined physical and chemical interactions between PAHs . . . . .                     | 36        |
| 2.5      | Summary . . . . .  | 38        |
| <b>3</b> | <b>Theory and computational methods</b>  | <b>39</b> |
| 3.1      | Quantum chemistry . . . . .  | 40        |
| 3.1.1    | The Schrödinger Equation . . . . .   | 40        |
| 3.1.2    | Approximation methods for solving the Schrödinger Equation . . . . .                   | 43        |
| 3.1.3    | Computational methods for solving the Schrödinger Equation . . . . .                   | 45        |
| 3.2      | Statistical Thermodynamics . . . . .   | 61        |
| 3.2.1    | Partition Functions . . . . .  | 62        |
| 3.2.2    | Deriving thermodynamic properties from the partition functions . . . . .               | 70        |
| 3.3      | Transition State Theory . . . . .  | 72        |
| 3.3.1    | Canonical Transition State Theory . . . . .  | 73        |
| 3.3.2    | Microcanonical Transition State Theory . . . . .                                       | 74        |
| 3.3.3    | Reactions with Barriers . . . . .  | 75        |
| 3.3.4    | Barrierless Reactions . . . . .  | 77        |
| 3.3.5    | Tunneling Corrections . . . . .  | 80        |
| 3.3.6    | Pressure Dependence . . . . .  | 82        |
| 3.4      | Kinetic Simulations and Sensitivity Analysis . . . . .                                 | 84        |
| 3.4.1    | Kinetic Simulations . . . . .  | 84        |
| 3.4.2    | Sensitivity Analysis . . . . .   | 86        |
| <b>4</b> | <b>Optical band gap of cross-linked, curved, and radical polyaromatic hydrocarbons</b> | <b>87</b> |
| 4.1      | Introduction . . . . .   | 88        |
| 4.2      | Materials and Methods . . . . .  | 90        |
| 4.2.1    | Ultraviolet-visible spectroscopy . . . . .   | 90        |
| 4.2.2    | Density Functional Theory . . . . .  | 91        |

## CONTENTS

---

|          |   |            |
|----------|---|------------|
| 4.3      | Results and discussion . . . . .  | 93         |
| 4.3.1    | Choice of functional . . . . .  | 93         |
| 4.3.2    | Comparison with higher level methods . . . . .  | 95         |
| 4.3.3    | Trends for Flat PAHs of varying symmetry . . . . .  | 97         |
| 4.3.4    | Trends for cross-linked PAHs . . . . .  | 98         |
| 4.3.5    | Trends for curved PAHs . . . . .  | 104        |
| 4.3.6    | Trends for open-shell PAHs . . . . .  | 109        |
| 4.4      | Conclusions . . . . .   | 113        |
| <b>5</b> | <b>Investigating the polarity of curved PAHs at flame conditions</b>                        | <b>115</b> |
| 5.1      | Introduction . . . . .  | 116        |
| 5.2      | Methodology . . . . .   | 118        |
| 5.3      | Results and discussion . . . . .  | 121        |
| 5.3.1    | Inversion of curved PAH at flame temperatures and timescales . . . . .                      | 121        |
| 5.3.2    | Fluctuations of the dipole moment . . . . .   | 127        |
| 5.4      | Conclusions . . . . .   | 130        |
| <b>6</b> | <b>Kinetics of seven-member ring bay closures in PAHs</b>                                   | <b>131</b> |
| 6.1      | Introduction . . . . .  | 132        |
| 6.2      | Methodology . . . . .   | 134        |
| 6.2.1    | Density Functional Theory calculations . . . . .  | 136        |
| 6.2.2    | Computation of rate constants . . . . .   | 137        |
| 6.2.3    | Kinetic simulations . . . . .   | 140        |
| 6.3      | Results and Discussion . . . . .  | 140        |
| 6.3.1    | Potential Energy Surfaces . . . . .   | 140        |
| 6.3.2    | Rate Constants . . . . .  | 163        |
| 6.3.3    | Kinetic simulations in a 0D homogeneous reactor . . . . .                                   | 171        |
| 6.4      | Conclusions . . . . .   | 178        |
| <b>7</b> | <b>Modelling the properties and concentration of localised <math>\pi</math>-radicals in</b> |            |

## CONTENTS

---

|  |            |
|--|------------|
| <b>flames</b>  | <b>181</b> |
| 7.1 Introduction . . . . .   | 182        |
| 7.2 Methodology . . . . .  | 183        |
| 7.2.1 Computational Chemistry Methods . . . . .  | 183        |
| 7.2.2 Rate Constant Calculations . . . . .   | 183        |
| 7.2.3 Spin-density calculations and Clar analysis . . . . .  | 188        |
| 7.2.4 Kinetic Simulations . . . . .  | 189        |
| 7.2.5 Kinetic Monte Carlo Simulations . . . . .  | 189        |
| 7.3 Results and discussion . . . . .   | 190        |
| 7.3.1 Localisation of $\pi$ -radicals . . . . .  | 190        |
| 7.3.2 Reaction mechanism for localised $\pi$ -radicals on<br>rim-based pentagonal rings . . . . .        | 192        |
| 7.3.3 Concentration profiles in flames . . . . .   | 198        |
| 7.4 Conclusions . . . . .  | 206        |
| <b>8 Kinetics and equilibria of cross-linking reactions between different<br/>reactive edges on PAHs</b> | <b>207</b> |
| 8.1 Introduction . . . . .   | 209        |
| 8.2 Methodology . . . . .  | 211        |
| 8.3 Results and Discussion . . . . .   | 217        |
| 8.3.1 Bond energies and classification of cross-links . . . . .  | 217        |
| 8.3.2 Barrier Heights . . . . .  | 219        |
| 8.3.3 Rate Constants . . . . .   | 222        |
| 8.3.4 Equilibrium Constants . . . . .  | 229        |
| 8.3.5 Enhancement due to Bonding and Stacking . . . . .  | 231        |
| 8.4 Conclusions . . . . .  | 234        |
| <b>9 Conclusions</b>   | <b>237</b> |
| 9.1 Conclusions of the thesis . . . . .  | 237        |
| 9.2 Suggestions for further work . . . . .   | 240        |
| 9.2.1 Cross-link reaction pathways for PAHs . . . . .  | 240        |



## CONTENTS

---

|          |  |            |
|----------|--|------------|
| 9.2.2    | Molecular dynamics studies on combined physical and chemical clustering between PAHs . . . . . | 241        |
| 9.2.3    | Implementation of process rates into kinetic Monte Carlo simulations . . . . .                 | 242        |
|          | <b>Nomenclature</b>  | <b>244</b> |
|          | <b>Bibliography</b>  | <b>257</b> |
| <b>A</b> | <b>Additional data for Chapter 4</b>   | <b>291</b> |

## LIST OF FIGURES

---

### List of figures

|     |   |    |
|-----|---|----|
| 1.1 | Molecular structure of naphthalene, the smallest PAH. . . . .   | 2  |
| 1.2 | Haze observed over the city of Mumbai, India. Credit - Wikipedia CC BY 4.0. . . . .   | 3  |
| 1.3 | Contribution of black carbon emissions to various climate effects world wide. Figure reproduced from Bond et al. (2013) with permission from John Wiley and Sons ©. . . . .   | 4  |
| 1.4 | Oil Furnace Method for the production of carbon blacks - Wikipedia CC BY 4.0. . . . .   | 5  |
| 2.1 | Schematic of the main processes occurring during soot formation in flames. Fuel pyrolysis and single ring species are taken from Hansen et al. (2009); Johansson et al. (2018).The structures and AFM images of larger PAHs are taken from Commodo et al. (2019). Nanoparticles and primary particles imaged with helium ion microscopy (HIM) are taken from Schenk et al. (2013). HRTEM of primary particles and SEM for a lamp black aggregate particles are taken from Martin et al. (2018). This figure is provided courtesy of Jacob Martin © and is used with permission. | 13 |
| 2.2 | Experimental schematic of line of sight laser extinction measurements. This figure is reproduced from Botero et al. (2016b) with permission from Elsevier © . . . . .   | 18 |
| 2.3 | Sample HRTEM image of soot extracted from a flame. This figure is adapted from Botero et al. (2018) with permission from Elsevier ©   | 22 |
| 2.4 | Sample STM (left) and HR-AFM (right) imaging of young soot particles extracted from a flame. This figure is adapted from Schulz et al. (2019) with permission from Elsevier © (2019) . . . .  | 24 |
| 2.5 | Potential energy surface for HACA growth from benzene to naphthalene. This figure is adapted from Mebel et al. (2017) with permission from the American Chemical Society © (2017) . . . .   | 28 |
| 2.6 | Formation of indene from benzyl by acetylene addition. This figure is adapted from Mebel et al. (2017) with permission from the American Chemical Society © . . . . .   | 29 |

## LIST OF FIGURES

---

|     |  |     |
|-----|--|-----|
| 2.7 | Various proposed mechanisms for the inception of soot nanoparticles from PAHs. This figure is courtesy of Jacob Martin © and is used with permission. . . . .  | 32  |
| 3.1 | Sample 1-D potential energy surface for an aromatic decomposition reaction with a barrier. . . . .   | 76  |
| 3.2 | Sample potential energy surface for a barrierless aromatic decomposition reaction. . . . .   | 77  |
| 4.1 | Comparison of the percentage errors between the OBGs obtained from experimental UV-Vis absorption experiments and DFT simulations using different hybrid functionals. Also shown are the structures of the three PAHs we tested. . . . .   | 94  |
| 4.2 | Comparison between the optical band gaps obtained from DFT simulations and UV-Vis absorption measurements of 19 different PAHs. Also shown are the molecular structures for some representative PAHs. . . . .  | 95  |
| 4.3 | Plot of the optical band gap of PAHs against number of rings, $M$ . Previous literature results from similar fittings done by Adkins and Miller Adkins and Miller (2017) and Robertson Robertson and O'Reilly (1987) are also shown. . . . .   | 98  |
| 4.4 | a) Plot of optical band gap against number of linked monomers for homogeneous aromers. An exponential decay curve has been fitted to guide the eye, with the dashed lines representing the expected asymptotic gap value. The blue shaded region represents flame optical band gap measurements from Botero et al. (2016a) b) LUMO orbitals of p-ternaphthyl (top) and p-terpyrenyl (bottom) . . . . . | 100 |
| 4.5 | Optical band gap of cross-linked structures of naphthalene, pyrene, coronene, and ovalene. $M_{\max}$ is defined as the number of rings in the largest PAH monomer fragment in the cross-linked PAH (blue for pyrene, green for coronene, red for ovalene). The horizontal lines on the bar plot show the optical band gap of the 4 different monomer PAHs for reference. . . . .                      | 102 |

## LIST OF FIGURES

---

|      |   |     |
|------|---|-----|
| 4.6  | Optical band gap and change in energy of biphenyl rotational conformers as a function of the dihedral angle, $\theta$ . Examples of some of the rotational conformers in the scan are illustrated in the plot, with the atoms comprising the dihedral angle $\theta$ highlighted in blue. The beige and blue shaded regions represent the rotational conformers accessible at 298K and their corresponding OBG values.  | 103 |
| 4.7  | Optical band gap of curved PAHs with a varying number of rings. The blue shaded region corresponds to measurements from Botero et al. (2016a). The PAHs are numbered according to the number of pentagons they contain. The lines shown are power-law fittings, comparing the fit to all the peri-condensed flat PAHs calculated in section 3.2. The full list of curved PAHs studied is taken from Martin et al. (2017b).                                    | 106 |
| 4.8  | Plot of the OBG of corannulenes subjected to different amounts of strain.   | 108 |
| 4.9  | Comparison between the OBG of open-shell flat PAHs containing one radical site and their closed-shell counterparts. The gray numbers represent the number of unique radical sites the PAH in question possess. Examples are given for naphthalene (2), pyrene (4), and pentacene (5) with each unique potential radical site demarcated with a Greek letter. The straight line plotted represents the open and closed-shell counterparts having the same OBG. | 110 |
| 4.10 | Optical band gap of different resonance-stabilised-radical (RSR) PAHs as compared to closed-shell peri-condensed PAHs and acene series PAHs. The RSR PAHs include peri-condensed, indenyl-like, triangulene, and cyclopentamethylene RSR PAHs. The lines shown are power-law fittings, comparing the fits to all the peri-condensed flat PAHs calculated in section 3.2.  | 112 |
| 5.1  | Curved PAH molecules chosen in this study with <b>3-5</b> chosen from a previous study by Martin (2019).  | 118 |
| 5.2  | Energies and geometries of the inversion transition states.   | 121 |
| 5.3  | Geometries of molecule <b>2</b> at equilibrium and at the transition state <b>TS2</b> .   | 122 |
| 5.4  | Molecular geometries with blue arrows indicating the relative amplitude and direction of the imaginary vibrations associated with the transition states of molecules <b>2</b> and <b>3</b> .  | 122 |

---

## LIST OF FIGURES

---

|     |   |     |
|-----|---|-----|
| 5.5 | Inversion barriers and molecular geometries for molecules <b>3</b> , <b>4</b> and <b>5</b> as well as their $\pi$ -radicals <b>3'</b> , <b>4'</b> and <b>5'</b> dashed line. . . . .  | 123 |
| 5.6 | Characteristic time for inversion for the species shown in Figure 5.1 with $\pi$ -radicals shown in dashed line. . . . .  | 124 |
| 5.7 | Inversion barrier as a function of the number of rings for structures in this work and from previously studied cPAH (Biedermann et al., 1999; Chen et al., 2014b). The dashed line highlights the inversion barrier 66.3 kcal/mol which provides a characteristic time of 1 ms at 1500 K from our calculations. . . . .   | 126 |
| 5.8 | Barrier for inversion for molecule <b>4</b> in the presence of an ion. . . . .  | 127 |
| 5.9 | Dynamics of molecule <b>4</b> and the chemi-ion. a) dynamics of the complex over the first picosecond shown with a line at each atom with the geometry at 1 ps shown with a ball and stick model. b) Fluctuation of the bowl during a low frequency bending model vibration. The dipole moment was calculated for the bowl fragment. c) dynamics of the complex over the second picosecond with the geometry shown with the ball and stick model for the final structure at 2 ps. . . . . | 128 |
| 6.1 | The starting PAH reactants which can integrate seven-member rings studied in this work. PAHs A and B can form a seven-member ring by the HACA mechanism. PAHs C and D can form a seven-member ring by bay closure reactions. . . . .  | 135 |
| 6.2 | Jump process illustrating formation of seven-member ring by HACA acting on PAH A and B. . . . .   | 135 |
| 6.3 | Jump process illustrating formation of seven-member ring by various bay closures in PAH C and D above. . . . .  | 136 |
| 6.4 | Falloff curves for the pressure-dependent rate constants of the unimolecular reactions in the HACA pathway for PAH A as computed by RRKM theory with tight transition states. . . . .   | 139 |
| 6.5 | Potential energy surface for the formation of a seven-member ring by HACA on PAH A at 0 K. The relative energy of the different species are computed at both the M06-2X/cc-pVTZ and B3LYP/6-311+G(d,p) level of theory. . . . .   | 143 |

## LIST OF FIGURES

---

|      |  |     |
|------|--|-----|
| 6.6  | Potential energy surface for the formation of a seven-member ring by HACA followed by hydrogen migration to the acetylene group on PAH A at 0 K. The relative energy of the different species are computed at both the M06-2X/cc-pVTZ and B3LYP/6-311+G(d,p) level of theory. . . . .                    | 144 |
| 6.7  | Potential energy surface for the formation of ethynyl-substituted products by HACA on PAH A at 0 K. The relative energy of the different species are computed at both the M06-2X/cc-pVTZ and B3LYP/6-311+G(d,p) level of theory. . . . .   | 145 |
| 6.8  | Potential energy surface for the formation of a seven-member ring by HACA on PAH B at 0 K. The relative energy of the different species are computed at both the M06-2X/cc-pVTZ and B3LYP/6-311+G(d,p) level of theory. . . . .  | 147 |
| 6.9  | Potential energy surface for the formation of a seven-member ring by HACA followed by hydrogen migration to the acetylene group on PAH B at 0 K. The relative energy of the different species are computed at both the M06-2X/cc-pVTZ and B3LYP/6-311+G(d,p) level of theory. . . . .                    | 148 |
| 6.10 | Potential energy surface for the formation of byproducts of HACA on PAH B at 0 K. The relative energy of the different species are computed at both the M06-2X/cc-pVTZ and B3LYP/6-311+G(d,p) level of theory. . . . .   | 149 |
| 6.11 | Potential energy surface for the formation of byproducts of HACA on PAH B at 0 K. The relative energy of the different species are computed at both the M06-2X/cc-pVTZ and B3LYP/6-311+G(d,p) level of theory. . . . .   | 150 |
| 6.12 | Potential energy surface for the formation of a seven-member ring by hydrogen abstraction (pathways a and b) followed by cyclisation and bay closure in PAH C at 0 K. The relative energy of the different species are computed at both the M06-2X/cc-pVTZ and B3LYP/6-311+G(d,p) level of theory. . . . | 151 |
| 6.13 | Potential energy surface for the formation of a seven-member ring by hydrogen addition (pathways c and d) followed by cyclisation and bay closure in PAH C at 0 K. The relative energy of the different species are computed at both the M06-2X/cc-pVTZ and B3LYP/6-311+G(d,p) level of theory. . . . .  | 153 |

## LIST OF FIGURES

---

- 6.14 Potential energy surface for the formation of a seven-member ring by carbene formation (pathways e and f) followed by cyclisation and bay closure in PAH C at 0 K. The relative energy of the different species are computed at both the M06-2X/cc-pVTZ and B3LYP/6-311+G(d,p) level of theory. . . . . 155
- 6.15 Potential energy surface for the formation of a seven-member ring by direct cyclisation (pathway g) and bay closure in PAH C at 0 K. The relative energy of the different species are computed at both the M06-2X/cc-pVTZ and B3LYP/6-311+G(d,p) level of theory. . 156
- 6.16 Potential energy surface for the formation of a seven-member ring by hydrogen abstraction (pathways a and b) followed by cyclisation and bay closure in PAH D at 0 K. The relative energy of the different species are computed at both the M06-2X/cc-pVTZ and B3LYP/6-311+G(d,p) level of theory. . . . 157
- 6.17 Potential energy surface for the formation of a seven-member ring by hydrogen addition (pathways c and d) followed by cyclisation and bay closure in PAH D at 0 K. The relative energy of the different species are computed at both the M06-2X/cc-pVTZ and B3LYP/6-311+G(d,p) level of theory. . . . . 158
- 6.18 Potential energy surface for the formation of a seven-member ring by carbene formation (pathways e and f) followed by cyclisation and bay closure in PAH D at 0 K. The relative energy of the different species are computed at both the M06-2X/cc-pVTZ and B3LYP/6-311+G(d,p) level of theory. . . . . 160
- 6.19 Potential energy surface for the formation of a seven-member ring by direct cyclisation (pathways g and h) and bay closure in PAH D at 0 K. The relative energy of the different species are computed at both the M06-2X/cc-pVTZ and B3LYP/6-311+G(d,p) level of theory. . . . . 161
- 6.20 Potential energy surfaces at 0 K for the conversions of radicals between pathways a and b in HACA and hydrogen abstraction pathways. The relative energy of the different species are computed at both the M06-2X/cc-pVTZ and B3LYP/6-311+G(d,p) level of theory. . . . . 162

## LIST OF FIGURES

---

|      |   |     |
|------|---|-----|
| 6.21 | Kinetic simulation for the HACA seven-member ring formation on PAH A at different temperatures. The figure shows the results for the rate constants at the M06-2X/cc-pVTZ level of theory in a continuous line and the B3LYP/6-311G+(d,p) in a dashed line. The sum of the two ethynyl side products is plotted. The contribution of both HACA pathways studied are included together in this figure. . . . . | 173 |
| 6.22 | Kinetic simulation of the HACA seven-member ring formation on PAH B at different temperatures. Continuous lines show both pathways consuming the starting PAH simultaneously. Dashed lines show high energy pathway only. Dotted lines show low energy pathway only. . . . .  | 174 |
| 6.23 | Forward and reverse rate constants of hydrogen abstraction (left) and acetylene addition (right) for pathway a (dashed lines) and pathway b (dotted lines) on PAH B. Units are $\text{cm}^3\text{mol}^{-1}\text{s}^{-1}$ for bimolecular reactions and $\text{s}^{-1}$ for unimolecular reactions. . . . .  | 175 |
| 6.24 | Kinetic simulations for the seven-member bay closure of PAH C at different temperatures. Each simulation is shown in different line pattern. Solid lines show hydrogen abstraction initiated bay closure, dashed lines show hydrogen addition assisted bay closure, dotted lines show the carbene cyclisation and dash-dotted lines show the direct cyclisation. . . . .                                      | 176 |
| 6.25 | Kinetic simulations of the seven-member bay closure for PAH D at different temperatures. Each simulation is shown in different line pattern. Solid lines show hydrogen abstraction initiated bay closure, dashed lines show hydrogen addition assisted bay closure, dotted lines show the carbene cyclisation and dash-dotted lines show the direct cyclisation. . . . .                                      | 178 |
| 7.1  | Temperature dependent rate constant for acenaphthelene A2R5 and coronene A7R5 for some critical reactions in the reaction mechanism. . . . .  | 185 |
| 7.2  | Fitted Morse potentials for barrierless reactions. The interaction potential energy surfaces were fitted to the B3LYP/6-311G(d,p) level of theory. . . . .  | 187 |
| 7.3  | Temperature dependent rate constant for the three barrierless reactions computed using the Gorin model and variational TST (VTST). . . . .  | 188 |



## LIST OF FIGURES

---

|      |   |     |
|------|---|-----|
| 7.4  | Spin density isosurface=0.025 shown on the molecular geometry with the Clar analysis. The spin density of the most spin rich carbon site is also shown indicating the degree of localisation. . . . .   | 192 |
| 7.5  | Potential energy surfaces for the reactions on five-member rings in acenaphthylene leading to the formation of localised $\pi$ -radicals on rim-based pentagonal rings at 0 K. Energies are computed at the CBS-QB3//B3LYP/6-311G(d,p) level of theory. . . . . | 193 |
| 7.6  | Comparison between rate constant computed for the A2R5- + H radical recombination reaction using B3LYP and CASSCF(2e,2o). . . . .   | 198 |
| 7.7  | 0-dimensional homogeneous gas-phase reactor simulations of reactions involving acecoronene (A7R5) at atmospheric pressure and typical flame compositions. The degree of saturation of the five-membered ring is shown in the figure. . . . .                    | 199 |
| 7.8  | Normalised sensitivity coefficients for the main PAHs to the rate constants in the kinetic mechanism. Data is shown for three temperatures, 1400,1500,and 1800 K. Only non-zero sensitivity coefficients are displayed. . . . .                                 | 202 |
| 7.9  | Kinetic simulations of a 0D homogeneous reactor with varying initial mole fractions of atomic hydrogen at temperatures of 1400 K and 1500 K. . . . .  | 204 |
| 7.10 | Kinetic Monte Carlo simulation for the time evolution of rim-based pentagonal rings for two (top) and three (bottom) site species at atmospheric pressure and typical flame compositions at 1000 K. These results are the average of five runs. . . . .         | 206 |
| 8.1  | PAH monomers studied in this work classified by the reactive edge type they contain. . . . .  | 211 |
| 8.2  | Potential energy surfaces for barrierless cross-linking reactions studied in this work. The energies are computed at the BS-UM06-2X/cc-PVTZ level of theory, and are fitted to a Morse potential. . . . .   | 214 |
| 8.2  | (Continued.) Potential energy surfaces for barrierless cross-linking reactions studied in this work. The energies are computed at the BS-UM06-2X/cc-PVTZ level of theory, and are fitted to a Morse potential. . . . .  | 215 |

## LIST OF FIGURES

---

|     |   |     |
|-----|---|-----|
| 8.3 | Comparison of the rate constant of phenyl radical recombination estimated using BS-UM06-2X/cc-pVTZ and VTST to those estimated by Tranter et al. (2010) and Jin et al. (2020). . . . .  | 217 |
| 8.4 | Bond energies of cross-linking between PAHs of different edge types computed at the M06-2X-D3/cc-pVTZ level of theory. . . . .  | 218 |
| 8.5 | Full BEP plot of the barrier heights against bond enthalpy for the various cross-linking reactions. . . . .   | 221 |
| 8.6 | Arrhenius plots for the forward rate constants of forming a cross-linking between PAHs with different reactive edge types. . . . .  | 223 |
| 8.7 | Equilibrium constants for forming a cross-link between PAHs with different reactive edge types. . . . .   | 230 |
| 8.8 | Equilibrium constants for cross-linking reactions between larger PAH reactions that can result in bonded and stacked structures. The dashed lines represent the equilibrium constant for smaller PAHs with the same reactive edge types, and the arrows represent the enhancement effect. . . . . | 232 |
| A.1 | Species . . . . .   | 292 |
| A.2 | Example plot of absorbance against wavelength spectra for naphthalene zoomed in on the low energy absorption band. The method for determining the wavelength at the absorption edge is illustrated, along with the method of extrapolation. . . . .   | 295 |

---

## List of tables

|     |  |     |
|-----|--|-----|
| 5.1 | Inversion barriers $E_{inv}$ (kcal/mol), values from the Arrhenius fitting of the form $k = A \exp(-E_a/k_bT)$ ( $s^{-1}$ and kcal/mol), the rate of inversion at 1500 K ( $cm^3 mol^{-1} s^{-1}$ ) and the characteristic time, $\tau = 1/k$ , at 1500 K (s). . . . . | 125 |
| 6.1 | Arrhenius fittings for the rate constants for all pathways studied. Rates are computed at the M06-2X/cc-pVTZ//B3LYP/6-311G(d,p) level of theory. The units are cm, kcal, mol, K, and s. . . . .  | 163 |
| 7.1 | Modified Arrhenius rate parameters for the localised $\pi$ -radical mechanism. The units are kcal/mol, K, $cm^3 mol^{-1} s^{-1}$ and $s^{-1}$ . . . . .  | 195 |
| 7.2 | Comparison of barrier heights predicted by CBS-QB3, G4MP2, and M06-2X methods. The units are kcal/mol. . . . .   | 196 |
| 8.1 | Predicted barrier heights for formation of cross-links between PAHs at the M06-2X-D3/cc-pVTZ level of theory. . . . .  | 220 |
| 8.2 | Arrhenius fittings for the rate constants for the cross-linking between PAHs possessing different reactive edge types. Rates are computed at the M06-2X/cc-pVTZ//B3LYP/6-311G(d,p) level of theory. The units are cm, kcal, mol, K, and s. . . . .                     | 226 |
| A.1 | List of PAHs studied experimentally in this work and their properties. . . . .   | 293 |
| A.2 | Experimental and DFT Band Gaps, HOMO energies, and LUMO energies in electron volts. . . . .  | 294 |
| A.3 | HOMO-LUMO gaps of naphthalene, biphenyl, and Fluorene as computed by various different hybrid functionals, given in electron volts. . . . .  | 294 |



# Chapter 1

## Introduction

*The ordinary novel would trace the history of the diamond - but I say, 'Diamond, what! This is carbon.' And my diamond may be coal or soot, and my theme is carbon.*

*- D.H. Lawrence*

## 1 INTRODUCTION

---

### 1.1 Motivation

Polycyclic aromatic hydrocarbons, also called polyaromatic hydrocarbons or polynuclear aromatic hydrocarbons, (PAHs) are organic species consisting of multiple aromatic rings, the simplest of which is naphthalene, seen in Figure 1.1.

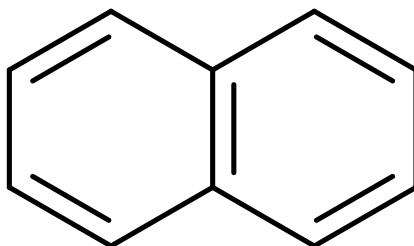


**Figure 1.1:** *Molecular structure of naphthalene, the smallest PAH.*

PAHs are found in a variety of carbon sources, such as coal and tar and through thermal decomposition of organic matter such as biomass. PAHs have also been seen to be a significant component interstellar dust arising from the formation of new stars and exoplanets, and are thus hypothesised to comprise a significant proportion of all of the carbon in the universe (Tielens, 2008).

The majority of studies into the properties of PAHs are motivated by their role as precursors to the formation of carbonaceous nanoparticles in flame and combustion environments. There are two key motivations for understanding carbon particulate formation in flames and the role and properties of PAHs that lead to the formation of said carbonaceous nanoparticles. Firstly, soot pollution is known to be a key contributor to significant hazards related to public human health as well as a major contributor to global warming and radiative climate forcing (Fiore et al., 2015). Secondly, carbonaceous nanoparticles and carbon nanomaterials comprise a variety of industrially useful materials that are synthesized through combustion processes.

#### 1.1.1 Soot as an environmental pollutant

The harmful effects of soot on the human body are well known. Several studies have shown that soot, black carbon, and polyaromatic hydrocarbons all display a variety of toxicological effects, including carcinogenic behaviour, respiratory issues, and cardiovascular disease effects (Niranjan and Thakur, 2017). The earliest studies of these harmful effects of soot are attributed to

## 1.1 Motivation

---

Sir Percival Pott and Sir James Paget ([Denkler, 2004](#)), who demonstrated the carcinogenic effect of soot on the skin. Subsequent studies have also detailed and summarised the contribution of soot to cardiovascular disease ([Novakov and Rosen, 2013](#); [Niranjan and Thakur, 2017](#)). Perhaps the most well-known and directly observable effects of soot as a public health concern are from respiratory concerns. This is most readily seen in the haze observed in most highly populated-high activity cities in India and China, as seen in [Figure 1.2](#).

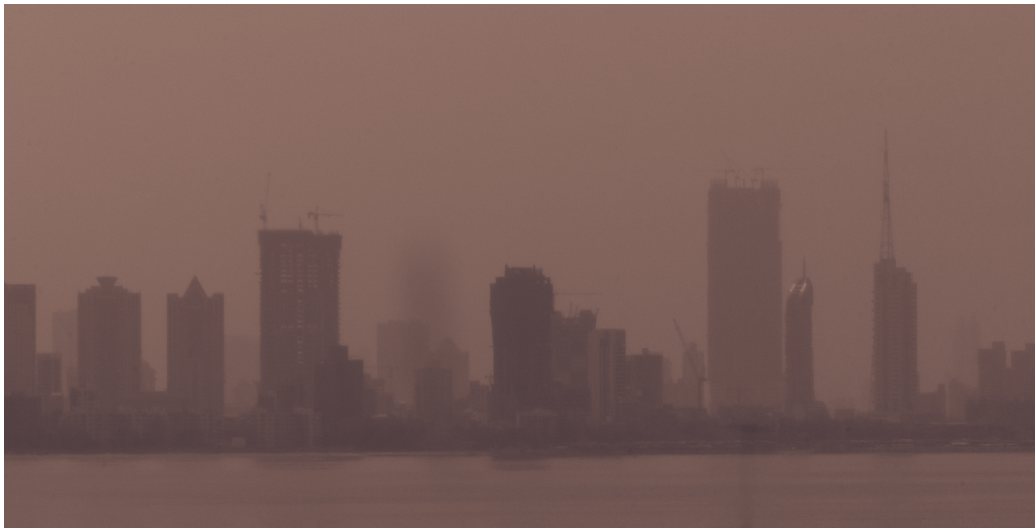


**Figure 1.2:** *Haze observed over the city of Mumbai, India. Credit - Wikipedia CC BY 4.0.*

Soot emissions are also implicated as contributors to global climate change effects. The main contribution of soot, frequently referred to as black carbon in the context of climate change emissions, is through radiative forcing effects, where recent estimates place soot emitted from fossil fuel combustion as the second largest contributor after those of greenhouse gases CO<sub>2</sub> and CH<sub>4</sub> ([Fiore et al., 2015](#)).

Soot is also thought to contribute to the melting of snow and polar ice caps due to the alteration of local albedo by soot deposits on said ice-caps, as well as to precipitation and circulation effects by absorbing aerosols ([Bond et al., 2013](#)):

## 1 INTRODUCTION

---

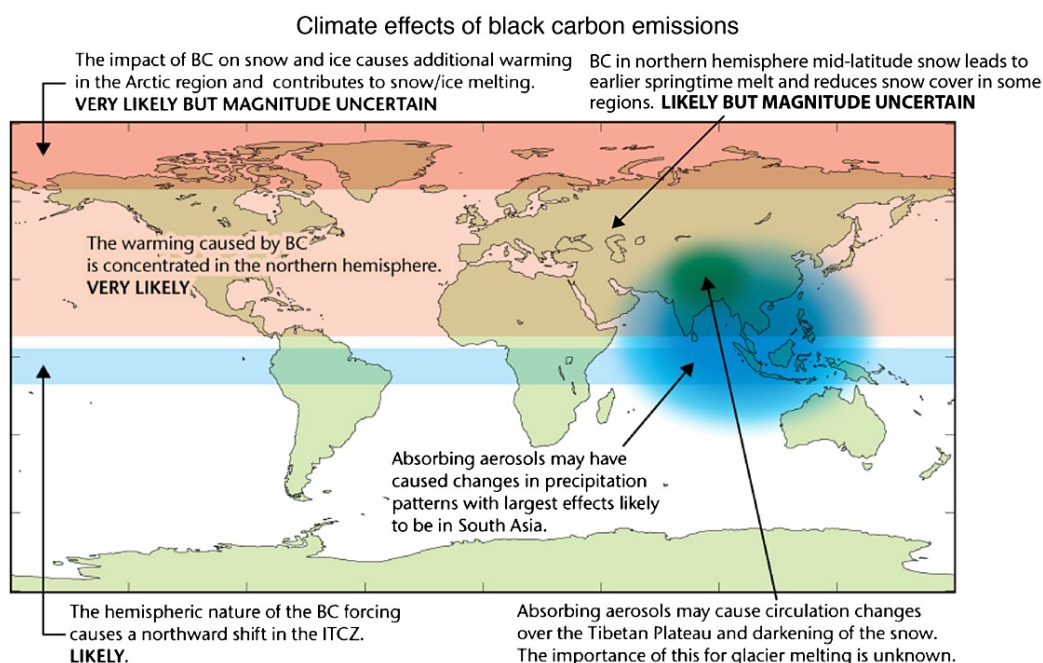


**Figure 1.3:** Contribution of black carbon emissions to various climate effects world wide. Figure reproduced from [Bond et al. \(2013\)](#) with permission from John Wiley and Sons ©.

As a consequence, there is a real desire to reduce soot emissions in order to mitigate their environmental effects. Doing so requires understanding of how soot forms and by relation understanding the properties of PAHs, the widely accepted soot precursors ([Frenklach, 2002a](#)).

### 1.1.2 Carbon nanomaterials

Carbonaceous nanoparticles and nanomaterials are not just harmful, but are also widely used. In particular, carbon black (not to be confused with black carbon), is a highly structured carbon particle that is the most produced nanoparticle product by volume worldwide ([Zdetsis and Economou, 2016](#)). Carbon blacks are typically produced in reactors with high temperatures and long residence times, resulting in significantly more mature and carbonised particles in comparison to soot or black carbon methods. One very common production method for industrial carbon blacks are the furnace methods, such as the oil furnace method, seen in [Figure 1.4](#).

Carbon blacks find applications in a variety of industries. The most common of these see carbon blacks used as fillers for tires, as well as in dyes and inks for



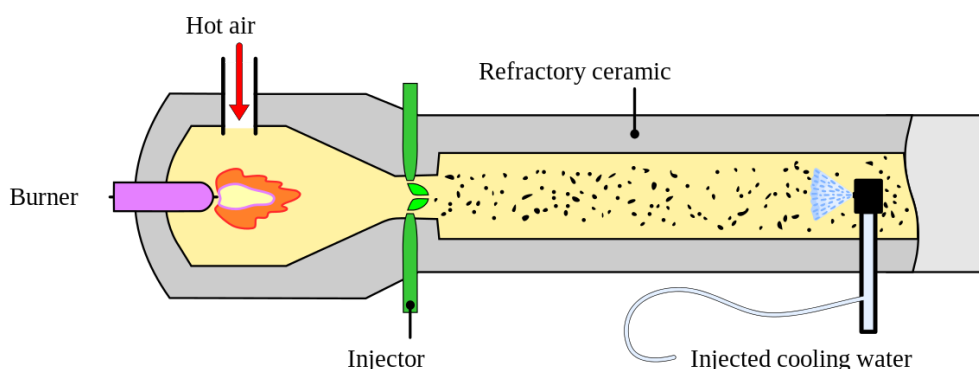


**Figure 1.4:** *Oil Furnace Method for the production of carbon blacks - Wikipedia CC BY 4.0.*

paints and printers. Indeed, the contents of this thesis could be considered an application of carbon blacks by extension. Carbon black nanoparticles are more recently attracting interest for applications in the lithium-ion battery industry, as well as as quantum dot applications for organic solar cells. As a result, there is a desire to be able to fine tune the properties of these carbon black nanoparticles for the application of interest, and doing so requires understanding of how these carbon blacks form during the combustion processes, and how their nanostructure evolves ([Zabula et al., 2011](#)).

Carbon blacks are a subset of non-graphitizing carbon nanomaterials. Other such materials include glassy carbons, porous nano-carbons, and activated carbons. These have a variety of applications, including gas storage, water purification and filtration systems, catalyst supports, electrode materials, and high stress ceramics. These carbon nanomaterials have had their topology explored recently, and can be thought of as extended 3D-graphene networks containing various five-member and seven-member ring defects ([Martin et al., 2019a](#)). The growth and formation of such carbon nanomaterials is also related to the modelling of the PAH subunits that can be thought to make up these carbon nanomaterials.

## 1.2 Aim

**The purpose of this work** is to model the optical, thermodynamic, and kinetic properties of a variety of unique PAHs by the application of first principle quantum chemical methods. This is to better understand how such PAHs form and how their

## 1 INTRODUCTION

---

properties may impact the formation of carbonaceous nanoparticles in a flame environment.

### 1.3 Novel elements of the thesis

This thesis presents the following **novel developments**:

- The HOMO-LUMO gap of a variety of PAHs is computed using a density functional theory method with accuracy benchmarked against UV/Visible Spectroscopy measurements for numerous smaller PAHs. In particular, the HOMO-LUMO gap is computed for a set of curved, cross-linked, and radical PAHs for the first time. Curved and  $\pi$ -radical PAHs were seen to have higher and lower HOMO-LUMO gaps respectively than flat pericondensed PAHs of the same size, whilst  $\sigma$ -radical character and homogeneous cross-linking were seen to have minimal impact on the optical properties.
- The persistence of the polarity of curved PAHs under flame conditions is explored computationally. By applying transition state theory, the rates of inversion of curved PAHs of different sizes and degrees of curvature are computed. The results show that only small, low-curvature curved PAHs invert at flame temperatures. Additionally, this stability to inversion is not impacted by the presence of ions formed by chemical reactions in flames (chemi-ions), with the chemi-ion-curved PAH complex seen to bind stably at flame conditions.
- The potential energy surfaces for the formation of PAHs containing a five/seven-member ring pair are computed using hybrid density functional theory. Such PAHs have recently been seen to be key to the nanostructure of 3D graphenes, and PAHs with this site type have also been imaged in nascent soot particles. Transition state theory is then applied to compute the rates of formation of these novel curved PAHs through different pathways, including hydrogen abstraction, hydrogen addition, carbene, and direct cyclization pathways.

- The properties and concentrations of a new type of localised  $\pi$ -radical PAHs are studied. The spin properties of these localised  $\pi$ -radical PAHs are computed to show substantial localization and, by extension, reactivity. A simple mechanism for the formation of these localised  $\pi$ -radical PAHs is developed and applied in 0D homogeneous reactor simulations and kinetic Monte Carlo simulations, showing that these localised  $\pi$ -radical PAHs are expected to be present in substantial concentrations in flame temperatures, with multiple radical sites also being a possibility.
- The rate and equilibrium constants of cross-linking between PAHs containing different reactive edge types are computed by applying density functional theory along with canonical and variational transition state theory. These PAHs include those with rim five-member rings, curved PAHs,  $\sigma$ -radical and  $\pi$ -radical PAHs. The localised  $\pi$ -radical PAHs are seen to be notably reactive, both in combination with themselves and with  $\sigma$ -radical PAHs. It was also found that the ability of larger localised  $\pi$ -radical PAHs to form bonded-and-stacked structures enhances the equilibrium constant well beyond what is expected for simple increases in physical van der Waals interactions.

### 1.4 Structure of the thesis

The remainder of this thesis is structured as follows. **Chapter 2** provides relevant background information on the formation of soot nanoparticles in a flame environment, with a focus on PAH chemistry and soot inception.

**Chapter 3** contains a description of the computational procedures used in this thesis. In particular, a brief explanation of quantum chemistry, statistical mechanics, transition state theories, and kinetic simulations can be found in this chapter.

**Chapter 4** presents the computed HOMO-LUMO gaps of different categories of PAHs, including curved, radical, and cross-linked PAHs. The HSE06 DFT functional is employed, having been cross-checked with UV/Visible spectroscopy measurements. Computed PAH HOMO-LUMO gaps are compared to experimentally measured optical band gaps in flames identifying curved,  $\pi$ -radical and heterogeneous cross-linked PAHs as those of interest. The properties and formation of these PAHs are then studied in subsequent chapters.

**Chapter 5** answers the question of whether curved PAHs are persistently polar at flame temperatures, or whether they are able to invert readily, hence mitigating the effect of their permanent dipole moments. The rates of inversion of these curved PAHs are determined, and the impact and binding of curved PAHs with chemi-ions is also explored.

**Chapter 6** explores the formation of seven-member ring formation in PAHs. Recent experimentally imaged PAHs are used as a basis for potential PAHs with appropriate reactive sites to form seven-member rings. Rate constants for different pathways leading to the formation of five-member-seven-member ring pairs are computed, and used in 0D homogenous reactor simulations to determine how likely these pathways are to occur at flame temperatures.

**Chapter 7** studies the concentration and properties of localised  $\pi$ -radical PAHs. Spin density analyses are used to determine the degree of localization of localised  $\pi$ -radical PAHs containing rim five-member rings. Pathways for the formation of such PAHs are studied by constructing a mechanism based on hydrogen

abstraction and addition reactions on a rim five-member ring. The concentrations of localised  $\pi$ -radical PAHs containing rim five-member rings is also studied.

**Chapter 8** determines the rate and equilibrium constants for cross-linking reactions between PAHs containing different reactive edge types, including  $\sigma$ - and  $\pi$ -radical PAHs, rim five-member rings, and curved PAHs. The likelihood of reactions between these different reactive edge types is compared. The formation of larger bonded-and-stacked PAH dimers and the impact this has on the equilibrium is also studied.

Finally, conclusions and avenues for further research regarding PAH chemistry and are presented in **Chapter 9**. A nomenclature and bibliography can be found at the end of the thesis.



# Chapter 2

## Background

*In this chapter, a brief background on the formation of carbonaceous nanoparticles in flames is provided. Some experimental techniques for studying soot formation are detailed. Next, the formation of the first few-ring PAHs, widely accepted to be the precursors to soot, is described briefly. This is followed by a discussion of key processes that allow for the growth of PAHs, namely the HACA mechanism, as well as other potential routes involving  $\pi$ -radical species and carbon migration routes. Finally, the various hypothesized mechanisms behind soot inception are discussed in turn. This provides the background required for this thesis, that a variety of PAHs, whether curved, cross-linked, or radical, are considered to be relevant to gas-phase PAH chemistry and soot formation.*

### 2.1 Formation of soot nanoparticles in flames

Soot formation in combustion consists of several complex interacting physical and chemical processes occurring on a very rapid timescales. The main processes are illustrated in Figure 2.1:

Broadly, one can see five key steps that lead to the formation of soot. The first consists of fuel pyrolysis reactions, during which the fuel breaks down and results in the formation of small hydrocarbons and, crucially, hydrocarbon radicals (Hansen et al., 2009). The next step consists of the gas-phase chemistry that results in the formation of the first aromatic species (Johansson et al., 2018), and the growth to larger polyaromatic hydrocarbon structures (Commodo et al., 2019). The third step is nanoparticle inception, by which gas-phase precursors self assemble to form the first nascent soot nanoparticles. The fourth step concerns the formation of soot primary particles, mainly through interactions with gas-phase PAHs via surface growth reactions as well as condensation of PAHs onto the soot particles. The fifth step consists of particle dynamics, such as nanoparticle aggregation and sintering, by which primary soot nanoparticles form mature soot aggregates that are commonly observed as emissions from combustion (Schenk et al., 2013; Martin et al., 2018).

Of these processes, the least well understood process is the inception process, by which gas phase molecular precursors like PAHs self-assemble to form a condensed phase at high temperatures (Bockhorn, 1994; Wang, 2011). This poses a challenge when modelling soot nanoparticle formation, as particle models are often very sensitive to how inception is treated (Wang, 2011; Yapp and Kraft, 2013). As a consequence of this, accurate treatment of the preceding gas phase precursor chemistry also becomes important, as modelling inception requires as its input accurate gas-phase concentrations of the relevant PAHs that are thought to lead to soot formation. Identifying potential PAHs as soot precursors, capturing the relevant gas-phase reaction mechanisms that result in the formation these PAHs in the necessary timescale, and understanding how these PAHs can then interact to form soot are major challenges of the field, and are what motivates the work presented in this thesis.



## 2.1 Formation of soot nanoparticles in flames

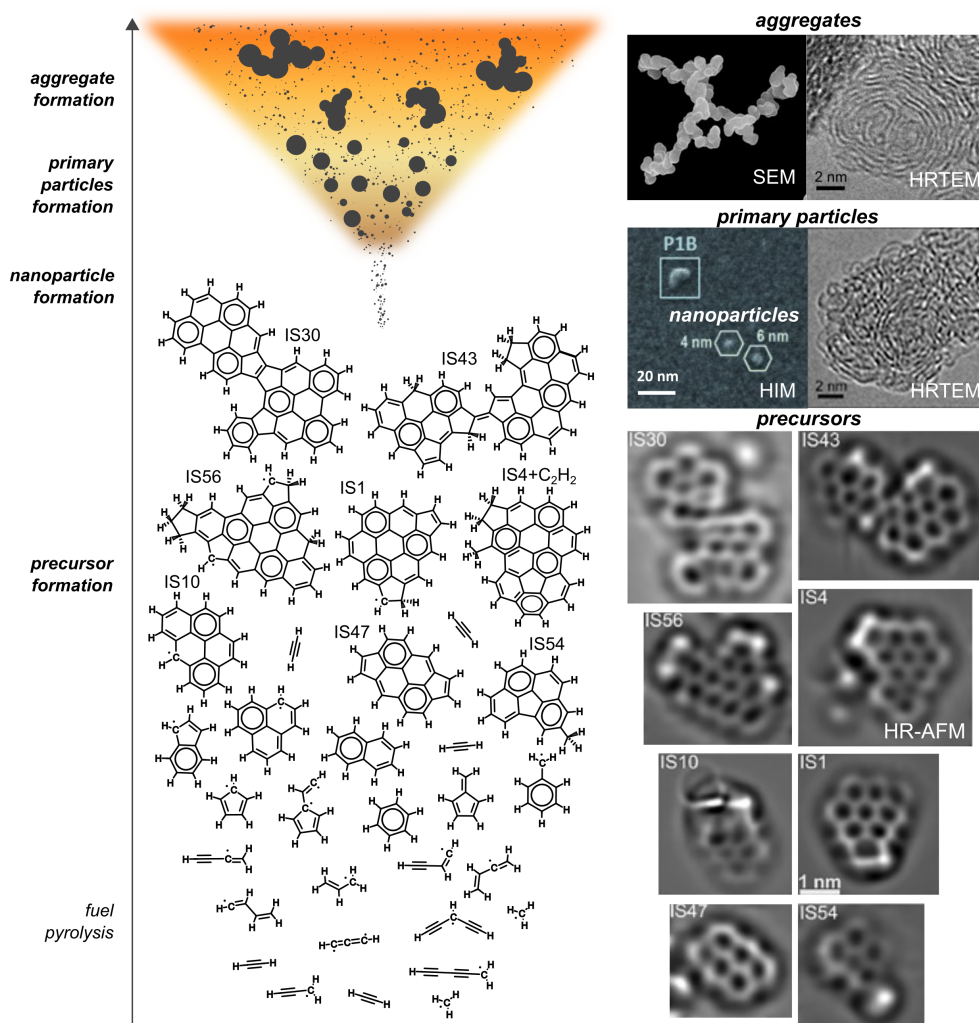


**Figure 2.1:** Schematic of the main processes occurring during soot formation in flames. Fuel pyrolysis and single ring species are taken from [Hansen et al. \(2009\)](#); [Johansson et al. \(2018\)](#). The structures and AFM images of larger PAHs are taken from [Commodo et al. \(2019\)](#). Nanoparticles and primary particles imaged with helium ion microscopy (HIM) are taken from [Schenk et al. \(2013\)](#). HRTEM of primary particles and SEM for a lamp black aggregate particles are taken from [Martin et al. \(2018\)](#). This figure is provided courtesy of Jacob Martin © and is used with permission.

## 2.2 Experimental Techniques

Soot nanoparticles vary greatly in size, with nascent nanoparticles being only a few nanometers in diameter, compared to several hundred nanometers for mature soot aggregates. Additionally, these nanoparticles vary substantially as their chemical composition and physical properties continuously evolve during their residence time in the flame. As a consequence, a variety of experimental techniques are required to probe the properties of both the soot nanoparticles as well as the gas phase combustion chemistry that leads to their formation.

Gas-phase measurements usually center on key observables, which include temperature, pressure and the concentration of key chemical species, including radicals, small hydrocarbons, and even PAH concentrations. A variety of different particle measurement techniques exist, some of which are *in situ*, which take measurements within the flame itself and aim to minimize flame disturbance. On the other hand, other techniques are *ex-situ* techniques, which make use of sampling techniques to extract particles from the flame before making the relevant measurements. Generally, the key particle properties are those that help describe soot particles, which generally are present in a bimodal size distribution (Wang, 2011). Such properties include particle number concentration, average particle size, particle size distributions, density, and chemical composition, to name a few.

### 2.2.1 Gas Phase measurements of PAHs

Several experimental studies have sought to determine concentrations of key gas phase species during combustion, namely the concentration and the sizes of PAH molecules present in the gas phase. Typically, these employ mass spectrometry to measure a distribution of masses, and can cover mass ranges up to 2000 amu, which covers small and moderately sized PAHs that are attributed to soot formation (Happold et al., 2007a). However, it is worth noting that detecting larger PAHs frequently poses a challenge due to their lower concentrations and difficulty in ionizing (Desgroux et al., 2013). Additionally, mass spectrometry does not directly provide any structural information about the PAHs measured, and so assignment of peaks is a key issue in interpreting said spectra.

## 2.2 Experimental Techniques

---

Several studies have looked at measurements of small PAHs using mass spectrometry. [Yang et al. \(2007\)](#) conducted a study of a premixed benzene–oxygen–argon flames at low pressure using synchrotron photo-ionisation and molecular-beam sampling mass spectrometry. Whilst their study identified a number of different PAHs present in the gas-phase during combustion, the largest of these was pyrene, at a mole fraction of  $10^{-5}$ . The authors suggest that the benzene flame studied was not rich enough for species larger than pyrene to be detected. Similarly, [Li et al. \(2009\)](#) detected pyrene with a similar mole fraction in a toluene flame, as well as larger species up to a molecular mass of 240 amu. [Faccinnetto et al. \(2011\)](#) investigated the PAH contents of soot in a low-pressure methane-air premixed flat flame, again finding primarily lower molecular weight PAHs to be in high concentrations, with the peaks of the spectra appearing to follow the grid of stabilomers of [Stein and Fahr \(1985\)](#). These species primarily consist of peri-condensed PAHs, and are frequently attributed to the various mass spectra peaks.

An order of magnitude decrease in concentration with each additional aromatic ring has been reported in several studies ([Homann, 1985](#); [Keller et al., 2000](#); [Wang, 2011](#)), with peak concentrations mainly around the smaller PAH (20 carbon) region ([Öktem et al., 2005](#)). These studies are often used to assert that soot formation from PAHs is driven primarily by smaller aromatics. However, it is worth noting that both [Faccinnetto et al. \(2011\)](#) and [Keller et al. \(2000\)](#) noted secondary maximum peaks in the 40 to 50 carbon atom region, suggesting that larger PAHs might be present in larger concentrations than initially expected. More recent studies have also affirmed the presence of larger PAHs, up to even 838 Daltons in mass ([Jacobson et al., 2020](#)).

Several early studies on the measurements of PAHs in the gas phase are known. [Siegmann et al. \(1995\)](#) performed time-of-flight mass spectrometry (TOF-MS) in conjunction with two-photon laser ionization to measure the concentration of various PAHs as a function of height-above-burner (HAB), finding that the size of PAH increases with increasing height-above-burner and hence increasing residence time. This was taken as evidence of step-wise addition growth mechanisms for PAHs, *i.e.* HACA. However, smaller PAHs in the range of 5-7

## Background

---

rings were also observed earlier in the flame than would be expected through a mass addition process such as HACA. This was taken as evidence for a reactive dimerization process between smaller PAHs that leads to the formation of larger PAHs.

Similar suggestions of reactive dimerization have been suggested by Homann (Homann, 1998), who used resonance-enhanced multiphoton ionisation mass spectrometry (REMPI-MS) to detect PAH molecules in the region of several thousand atomic mass units, and also noted secondary modes in the mass-spectra that corresponds to cross-linking between smaller pericondensed aromatic molecules. Such studies also noted the potential presence of curved aromatic species due to detection of negative ions, and pathways leading to the growth of not just soot, but fullerenic species as well (Homann, 1998; Bachmann et al., 1996). Studies by Grotheer have made use of online laser ionization molecular beam mass spectroscopy to also study larger PAHs (Happold et al., 2007a,b). By utilizing different wavelengths, they found two main types of soot precursors, which were attributed primarily to stacks of large peri-condensed PAHs with a periodicity of 500 Da.

Several other types of PAHs have also been detected in flames. This includes those containing aliphatic functional groups, which Öktem et al. (2005) and Zhao et al. (2007) suggested were in substantial concentrations. Öktem et al. (2005) used photo-ionisation aerosol mass spectrometry to study the chemical composition of a combustion aerosol. This technique uses gentler photo-fragmentation of particle samples and can analyse particles in near real time, allowing the simultaneous study of aliphatic and aromatic compounds. Noticeably, for a premixed ethylene–oxygen–argon flame, the number of aliphatic hydrocarbons increased substantially with increasing temperature and height above burner, suggesting aliphatics contribute substantially in later stages of precursor chemistry and soot formation. Similar studies making use of photoionization mass spectra and high resolution mass spectrometry with nanospray desorption electron spray ionization have also detected substantial aliphatic and oxygenated species (Skeen et al., 2013; Cain et al., 2014). Both of these studies suggested that PAH growth pathways beyond HACA could be important to consider, as could aliphatic and

oxygenated PAHs. However, it was still seen that the early PAHs and initial points of soot formation contained primarily peaks that could be attributed to the standard peri-condensed PAHs, and more recent studies have challenged the importance of aliphatics (Zhang et al., 2020).

The importance of radical PAHs has also been suggested by several works (McKinnon and Howard, 1990; Howard, 1991). This proposes that alternative growth and formation pathways relying on reactions involving resonance-stabilized-radical (RSR) PAHs, which are essentially PAHs with an odd number of electrons in the  $\pi$ -electron network. Typically, this manifests in species that have an odd number of carbon atoms. These have been observed to be in substantial concentrations in flames (Homann, 1998). Studies of cyclopentene flames have shown the importance of RSR chemistry to the formation of benzene and subsequent PAH formation through cyclopentadienyl chemistry (Baroncelli et al., 2020). Earlier studies have also suggested the importance of small RSR in the formation and growth of PAHs (Hansen et al., 2011). Johansson et al. (2017) used aerosol mass spectrometry coupled with tunable vacuum ultraviolet radiation to study soot precursor species at different heights in a premixed flat flame and in a counter-flow diffusion flame fueled by ethylene and oxygen. They found large concentrations of small PAH radicals, which could undergo recombination reactions that result in non-sequential growth processes to larger PAHs that could participate in soot formation. It is worth noting that a recent study by Jacobson et al. (2020) challenges the large presence of aliphatics and oxygenated groups, and re-affirms the large number of peaks that are mainly attributed to circular peri-condensed PAHs. Notably, this study also identifies several PAHs containing pentagonal rings which could lead to curved PAHs as well as localised  $\pi$ -radical PAHs. These species are studied in later chapters of the thesis.

### 2.2.2 Particle Phase measurements of soot and PAHs

Several techniques are also used to analyse soot particles. Such techniques include those that extract soot from the flame by making use of sampling techniques, or those that try to be less intrusive and measure properties in the flame environment, typically by employing optical techniques.

## Background

---

### 2.2.2.1 Optical Diagnostics

*In situ* optical techniques often involve methods such as laser extinction measurements, laser induced incandescence, laser induced fluorescence and X-ray scattering. Starting with laser extinction measurements, these typically make use of a supercontinuum laser, which is then applied to different regions of the flame. The absorbance of the aerosol at different positions can then be measured. A sample experimental set-up is seen in Figure 2.2.

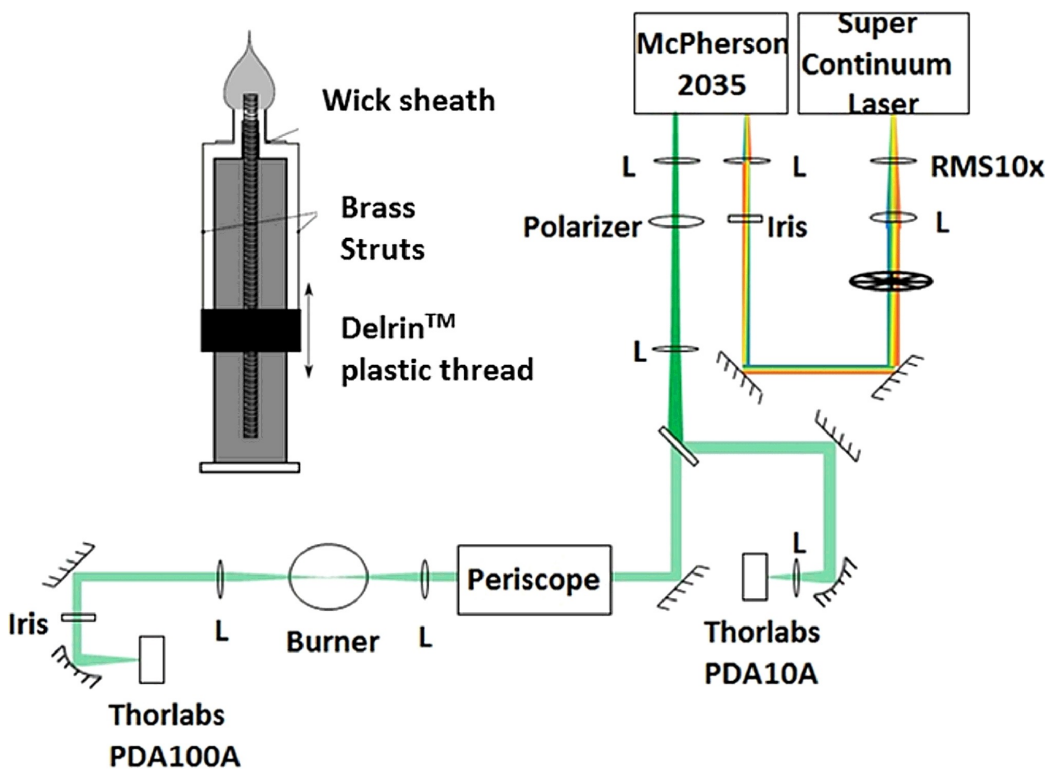


**Figure 2.2:** *Experimental schematic of line of sight laser extinction measurements. This figure is reproduced from Botero et al. (2016b) with permission from Elsevier ©*

Such a set up enables the measurement of the optical band gap (OBG) of the absorbing aerosol, which can be attributed to the PAHs present in the gas phase. The OBG at different positions within flames is then derived by using the Tauc method (Tauc et al., 1966). D'Alessio et al. (1996) assumed an indirect electron transition and observed a range of OBGs in their benzene/air flames depending on

whether the flame was non-sooting (3 eV – 4.6 eV), nearly-sooting (1 eV – 5 eV) or sooting (0.6 eV – 1 eV). [Adkins and Miller \(2015\)](#) performed a similar study on a diluted ethylene/N<sub>2</sub>/air flame but assumed a direct electron transition, finding a much smaller OBG range of 1.85 – 2.35 eV as a result. A similar OBG range of 1.7 – 2.4 eV was found by [Botero et al. \(2016b\)](#) for sooting n-heptane/toluene flames, again assuming a direct transition, as [Botero et al. \(2016b\)](#) noted that using an indirect transition resulted in very low OBG values. Once the OBGs inside a flame are known, the challenge is to correlate the measured values to specific PAH structures present in both soot and the gas phase. [Robertson and O'Reilly \(1987\)](#) have found that sp<sup>2</sup> carbon systems, such as soot, have their electronic properties governed by  $\pi - \pi^*$  interactions such as those in PAHs. Therefore, OBGs measured in flames should be indicative of PAHs, and the measured OBGs can be compared to theoretical predictions to identify which PAHs are present. This is discussed further in Chapter 4. In one such example, [Botero et al. \(2016a\)](#) suggested that the smallest peri-condensed PAHs contributing to the OBG consist of 16 rings.

Another popular optical diagnostic technique is laser induced incandescence (LII). In LII, particles are heated by a laser pulse. As a consequence, the soot nanoparticles emit thermal radiation, which is related to the volume fraction of the particles whilst the decay rate of the signal during cooling is related to the particle surface area and hence the average particle size. Quantitative calibration is typically required by reference to an extinction measurement and the interpreted results depend on the estimated refractive index. LII has been used for the characterisation of primary soot particles in laboratory flames in multiple studies, ([Lehre et al., 2003](#)), in order to derive key properties such as soot volume fraction ([Quay et al., 1994](#); [Vander Wal and Weiland, 1994](#)) as well as soot primary particle size ([Vander Wal et al., 1999](#)). Reviews have confirmed that interpretation of LII measurements is reliant on a few key parameters such as the refractive index ([Michelsen et al., 2007](#)).

A closely related technique is laser induced fluorescence (LIF). This typically makes use of a neodymium-doped yttrium aluminum garnet (Nd:YAG) laser with 263 nm in order to excite the aerosol and measure their emission spectra. By



## Background

---

matching the emission spectra to the fluorescence spectra for individual PAHs, LIF can provide spatially resolved relative concentration of PAHs, making it a powerful technique (D'Anna et al., 2008; Herdman et al., 2011; Sirignano et al., 2017). This is especially useful for non-premixed and turbulent flames. Notably, LIF has provided substantial evidence suggesting the presence of PAH dimers and stacked structures in flames by comparing experimental spectra to those of aromatic excimers (Miller, 2005; Krueger and Blanquart, 2019). Studies have also matched certain fluorescence patterns to the presence of key five-member ring containing species in flames (Liu et al., 2015).

X-ray and neutron diffraction and scattering techniques have also been applied to the study of soot nanoparticles. Early X-ray diffraction studies were used to confirm that PAHs within soot consistently adopt stacked structures (Chen and Dobbins, 2000). Both small angle and wide angle x-ray scattering techniques have been applied to soot particles, with the former considering mainly smaller particles, and the larger being applied to resolve the effects of the chemical structure on the scattering pattern (Hessler et al., 2002; Mitchell et al., 2009). Such studies have provided information on aggregate structure of soot nanoparticles. Similarly, small angle neutron scattering has also been applied to the study of soot, and is notable for being able to investigate systems with low soot volume fraction, and can provide spatially resolved soot particle size distributions (Wang et al., 2002). The scattering also suggested that most of the interference is due to smaller PAHs and particles in the sub-5 nm range, where incipient particle formation is thought to occur (Wang et al., 2002).

Soot nanoparticles are also frequently analysed by means of *ex-situ* techniques. Here, thermophoretic and dilution sampling are used to extract soot samples from a flame by means of a thermophoretic probe, which can then be analysed to determine their chemical composition. Notably, the dilution, extraction, and quenching required to obtain these *ex-situ* samples will inevitably have altered the soot nanoparticles so that they are different to what is in the flame, and so this needs to be taken into account.



### 2.2.2.2 *Ex-situ* spectroscopic techniques

Spectroscopic techniques have frequently been applied to soot samples collected from flames. As mentioned before, the sampling procedure can affect the soot collected, but careful setting of dilution ratios by carrier gas and precise use of small sampling probes have been shown to help ensure that the sampled soot is representative of the soot formed in the flame (Wang, 2011). For example, Dobbins et al. (1995) used laser microprobe mass spectrometry (LMMS) and thermophoretic sampling to study particles at different positions in a non-smoking laminar ethylene–air diffusion flame. The samples collected were mainly small precursor soot particles. These early soot particles were irradiated with a laser to ionise and vaporize molecules from the samples, which were then analysed by TOF-MS, detecting PAHs of mainly 200–300 amu in size at low height above burner and 400–500 amu at high height above burners. At larger height above burners, masses contributing to clusters of moderate PAHs were also detected, ranging in the C50 to C92 range. Dobbins et al. (1995) attributed this to carbonization of soot particles, during which the carbon content of soot particles increases through increase in PAH size and dehydrogenation as soot matures. Further mass spectra analyses of young soot samples conducted by Dobbins et al. (1998) again found PAHs in the 400–500 amu with peaks that suggested peri-condensed PAHs. Further mass spectrometry studies on soot samples have also provided evidence for stacking of PAHs (Happold et al., 2007b; Carbone et al., 2019). Recent mass spectra on soot samples have also shown peaks that can be attributed to resonance-stabilized-radical species, suggesting their potential importance (Johansson et al., 2018).

Raman spectroscopy and Fourier transform infrared spectroscopy (FTIR) have also been frequently applied as a non-destructive way to study extracted soot samples. Raman analysis has been used to identify key bands and fingerprints of soot, that can then be related to crystallite and PAH size (Ferrari and Robertson, 2000). The quantity of interest is the ratio of the D- and G- band intensities, with the D-band arising from a six-member ring breathing mode forbidden in pure graphene. It was found that for larger crystallite sizes, the ratio of intensities is inversely proportional to the crystallite length, whilst for smaller

## Background

---

sizes, the ratio of intensities is proportional to the square of the crystallite size (Ferrari and Robertson, 2000). Further experimental studies have established empirical correlations that are more applicable across the whole crystallite size range. For example, a study by Herdman et al. (2011) used Raman spectroscopy in conjunction with laser-induced incandescence to analyse soot produced in nitrogen-diluted ethylene–air flames. The ratio of D- and G- band intensities in the signature allow correlation to crystallite sizes and the results suggest the presence of PAH molecules within the soot samples with conjugation lengths of 1-2 nm corresponding to masses of 500–1000 amu. FTIR studies have also been used to study the chemical composition of soot particles. FTIR studies by Cain et al. (2010) have also provided quantitative evidence for aliphatic content in soot. Other Raman and FTIR studies have also shown evidence for curved structures and corannulene in soot when combined with HPLC and UV/Visible analyses (A.L. Lafleur, J.B. Howard, J.A. Marr, T. Yapesh, 1993), and have helped characterized soot particles produced in a variety of conditions (Desgroux et al., 2013; Peña et al., 2017).

### 2.2.2.3 *Ex-situ* microscopic techniques

The other main category of *ex-situ* techniques are microscopic techniques, two of the most common being transmission electron microscopy (TEM) and atomic force microscopy (AFM). These techniques allow direct imaging of the nanostructure of various soot nanoparticles, giving them a distinct advantage. A sample TEM image of soot extracted from a low height above burner is given in Figure 2.3.

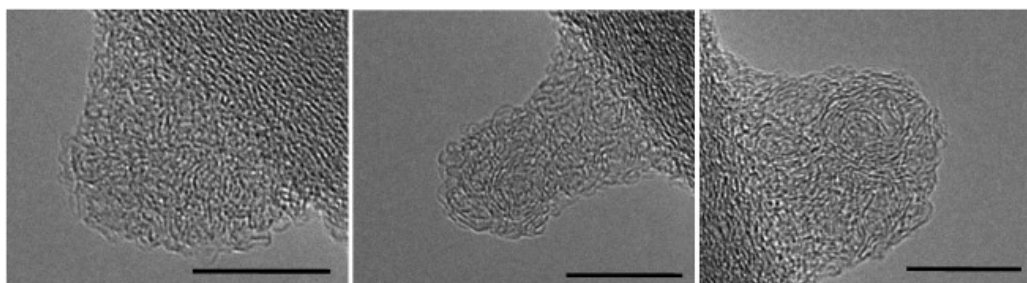


**Figure 2.3:** Sample HRTEM image of soot extracted from a flame. This figure is adapted from Botero et al. (2018) with permission from Elsevier ©

High Resolution TEM (HRTEM) can even give quantitative information about soot nanoparticles, which is highly useful. [Fernandez-Alos et al. \(2011\)](#) demonstrated that HRTEM images could achieve one nanometer resolution, and were able to make use of image analysis algorithms to relate the fringes to the characteristics of the underlying PAH molecules. Improving upon this, fringe analysis has been combined with the aforementioned optical band gap analysis to estimate the size of peri-condensed PAH that matches the imaged fringe lengths ([Botero et al., 2016b](#)) (see Figure 2.3).

HRTEM has shed substantial insight onto the nanostructure and behaviour of soot under a variety of conditions. Early studies of soot confirmed that the oxidation of soot is highly dependent on the nanostructure of the particles [Vander Wal and Tomasek \(2003\)](#). There was also noticeable curvature of the basal planes, which contributed to the soot's reactivity towards oxidation. TEM images have also confirmed that young soot is liquid-like ([Abid et al., 2008, 2009](#)). Studies have also elucidated the difference between young soot, which contains much more amorphous carbon structures, and more mature soot, which is seen to have a graphitic-like shell and an amorphous core, the so-called core-shell nanostructure ([Vander Wal and Tomasek, 2004](#)). Further studies have also confirmed that the formation of the core-shell nanostructure is likely due to graphitisation, where at high temperatures the shell contains longer fringes, and hence larger PAHs, than in the more disordered core ([Botero et al., 2018](#)). Notably, these HRTEM images also showed stacking of PAHs, and a rather moderate size range of peri-condensed PAHs, ranging from 10–20 rings.

Perhaps one of the most important observations from HRTEM images is the persistence of curved fringes in soot. These HRTEM micrographs have been used to suggest curvature in soot and carbon black from bent fringes ([Heidenreich et al., 1968](#); [Vander et al., 2013](#)). This curvature suggests the presence of five-member rings within the PAHs ([Vander Wal and Tomasek, 2004](#)), which then need to be fully integrated into the PAH to induce curvature ([Martin, 2019](#)). Analysis of the length and tortuosity of the fringes has helped quantify the degree of curvature present. Fringe analysis has helped quantify the amount, suggesting >62.5% of all fringes are curved. The tortuosity further suggests the degree of curvature of

## Background

---

the PAHs, which by comparison to simulations, suggests that curved PAHs in early soot particles can contain between 1 and 3 pentagons, a substantial amount. (Botero et al., 2016b; Wang et al., 2017; Martin, 2019; Botero et al., 2018).

Atomic Force Microscopy makes use of a sharp tip to probe the surface of a sample, and can therefore be used to construct a three-dimensional representation of the soot nanoparticle surface. Early AFM studies were used to confirm the presence of very small nanoparticles, which were noticeably susceptible to deformation by the AFM tip, suggesting a lack of rigidity in nascent soot particles (Barone et al., 2003). Further AFM studies have confirmed the liquid-like nanostructure of nascent soot nanoparticles. Recent HR-AFM studies have been able to go even further than just surface analysis by using non-contact methods that use a carbon-monoxide molecular tip to probe the samples. This method has actually been able to achieve bond-scale resolution, making direct images of PAHs within young soot particles a possibility (Schulz et al., 2019; Commodo et al., 2019). An example is shown in Figure 2.4.

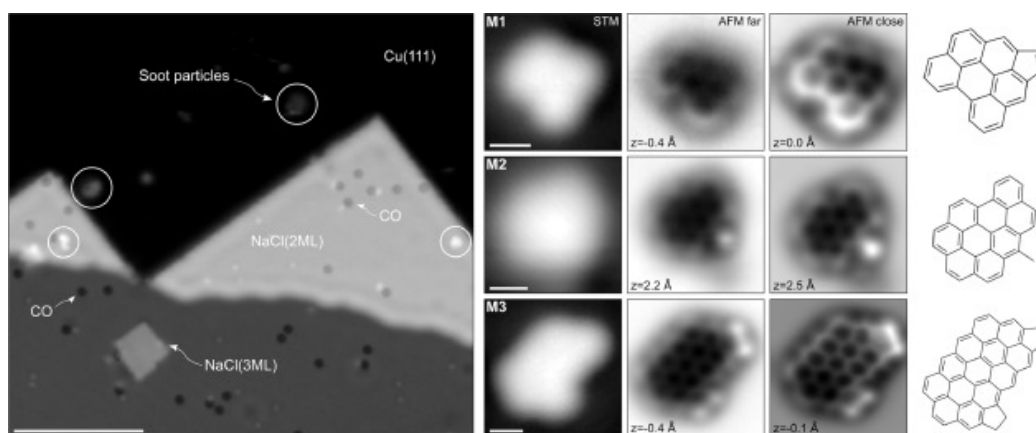


**Figure 2.4:** Sample STM (left) and HR-AFM (right) imaging of young soot particles extracted from a flame. This figure is adapted from Schulz et al. (2019) with permission from Elsevier © (2019)

This huge contribution has allowed much clearer insight into what types of PAHs soot truly contains. There are a remarkable number of PAHs with rim-based pentagonal rings, a large number of  $\pi$ -radical PAHs, as well as several PAHs containing aliphatic chains and cross-links between different PAH units (Schulz

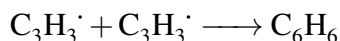
[et al., 2019](#); [Commodo et al., 2019](#)). It is worth noting that curved PAHs could not be imaged, but several of the PAHs that could be imaged contained sites that are likely to lead to the formation of curved PAHs. Several new sites were also imaged that could potentially result in the formation of seven-member rings as well. This study essentially confirms the variety of PAHs that could be relevant to soot formation and that warrant further study.

### 2.3 Formation and Growth of PAHs

Modelling the gas phase formation and growth of PAHs is crucial to modelling soot formation, as it is necessary to ensure the appropriate reaction pathways are included such that relevant PAHs are formed at the necessary timescale and with appropriate concentrations. This is key to modelling soot formation, as the rates of inception are dependent on the gas-phase concentrations of the designated precursor PAHs. As a consequence, new reaction pathways for the formation of PAHs in the gas-phase are under constant study. This section aims to summarize some of the key pathways for PAH formation that are widely included in chemical mechanisms used to model soot formation.

#### 2.3.1 Formation of the first aromatic ring

The first step leading to PAH growth involves the formation of the first aromatic rings. This typically concerns the formation of benzene, with one six-member aromatic ring. Formation of the resonance stabilized cyclopentadienyl radical,  $C_5H_5$  is also crucial for the formation of the first aromatics. Several studies have highlighted that the crucial reaction that drives the formation of benzene is due to C3 chemistry, namely the self-recombination reaction between propargyl ( $C_3H_3$ ) radicals ([D'Anna and Violi, 1998](#); [Hansen et al., 2007](#); [Chu et al., 2019](#)):



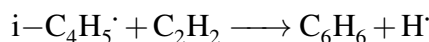
Notably, this recombination reaction produces not only benzene but also another  $C_6H_6$  isomer, fulvene, which is a five-member cyclic compound (a cyclopentadiene) with a methylene substituent. Studies have shown that benzene

## Background

---

is by far the dominant product, which is also aided by the fact that fulvene can easily undergo hydrogen-atom assisted isomerization to the formation of benzene (Hansen et al., 2007). The combination of the propargyl radical with other resonance-stabilized-radicals have also been suggested to be key to formation of the first aromatic rings in C3 chemistry. Notably the reaction of propargyl radicals with 1-methylallenyl radicals has also been seen to contribute substantially to benzene formation in flames (D'Anna and Violi, 1998), as has the propargyl + allyl combination reaction, which was observed to be the dominant contributor to benzene formation in fuel-rich hexene flames (Hansen et al., 2010).

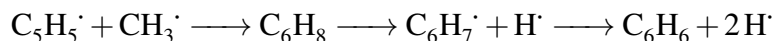
Several studies have also highlighted the role of C4 species in the formation of benzene and its derivatives in flames. Early studies proposed the reaction between 1,3-butadienyl and acetylene as a major contributor to benzene formation (Cole et al., 1984):



Acetylene addition to the *n*-C<sub>4</sub>H<sub>5</sub> isomer has also been seen to contribute to formation of fulvene and benzene, but *n*-C<sub>4</sub>H<sub>5</sub> was also seen to isomerise easily to *i*-C<sub>4</sub>H<sub>5</sub>, and hence the above reaction was concluded to be the more significant C4 contributor to aromatic formation (Senosiain and Miller, 2007). Further C4 reaction pathways to benzene include the addition of acetylene to *n*-C<sub>4</sub>H<sub>3</sub> and *i*-C<sub>4</sub>H<sub>3</sub>, producing phenyl radicals. However, these reactions were seen to be less significant than the reaction between 1,3-butadienyl and acetylene (D'Anna and Violi, 1998). Recent studies have also considered the contribution of the self-combination reaction between C<sub>4</sub>H<sub>4</sub>, which can also be assisted by the presence of molecular hydrogen (Lin et al., 2016). It was noted that one of the dominant products of this reaction is fulvene, and hence such a route could also be important to aromatics formation.

Finally, the role of C5 chemistry in formation of aromatic rings is seen to be substantial during the combustion of fuels containing five-member rings, such as cyclopentene. In this case, the driving reaction is known to be the reaction between the resonantly-stabilized cyclopentadienyl radical,

and the abundant methyl radical (Hansen et al., 2007; Herbinet et al., 2016; Baroncelli et al., 2020):

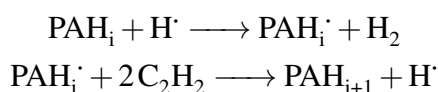


The sequence of steps involves a combination reaction between the cyclopentadienyl radical and methyl radical to form 5-methyl-1,3-cyclopentadiene. This then undergoes hydrogen loss to form the 5-methyl-1,3-cyclopentadiene radical, which then undergoes the so-called ring enlargement reaction to the cyclohexadi-1,3-en-5-yl radical. Finally, another hydrogen loss results in the formation of benzene. This pathway is known to be the dominant pathway for cyclopentene flames.

### 2.3.2 Growth beyond benzene - PAHs

#### 2.3.2.1 HACA

Once the first aromatics form from small hydrocarbon radicals, the formation and growth of PAHs is the next key step to soot. Several processes have been hypothesized to drive PAH growth, but none have been as enduring as the Hydrogen-Abstraction-Carbon-Addition (HACA) mechanism (Wang and Frenklach, 1997; Frenklach, 2002a), which to this day is the main reaction sequence used to model PAH growth. Broadly speaking, the HACA mechanism is a step-wise growth mechanism for PAHs by which a reactive site on the PAH is first activated by a hydrogen abstraction to create a PAH radical. This is followed by carbon addition, typically through acetylene addition, and finishes with cyclization and hydrogen loss to form a larger aromatic. A very simplified way of writing this is:



In reality, potential energy surfaces for HACA sequences are more complex. As an example, the HACA sequence for the formation of naphthalene from benzyl is given in Figure 2.5.



## Background

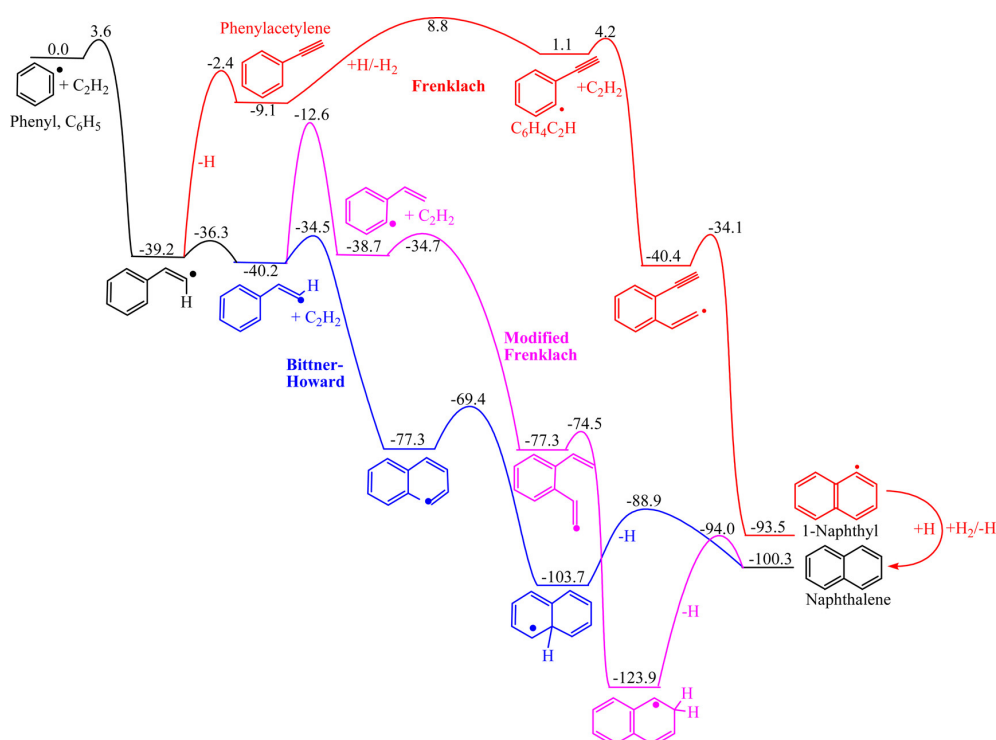


**Figure 2.5:** Potential energy surface for HACA growth from benzene to naphthalene. This figure is adapted from *Mebel et al. (2017)* with permission from the American Chemical Society © (2017)

As one can see, the HACA mechanism from phenyl to naphthalene actually consists of several different pathways, including the Bittner-Howard route by which the second acetylene adds to the the radical site on the first, as well as the modified Frenklach route where the second acetylene adds to the benzene ring. Both end with cyclization and formation of naphthalene. Importantly, the HACA route can also result in the formation of phenylacetylene as a side product, which is a PAH with an aliphatic side chain. Further density functional theory and RRKM studies on the site effect have confirmed that HACA can form these aliphatic side products (*Liu et al., 2019*). This shows the capability of HACA to form aliphatic PAHs that have been observed experimentally.

Additionally, HACA is a crucial mechanism for the formation of five-member rings and subsequent integration of curvature in PAHs. Computational quantum chemical calculations have employed density functional theory to derive potential



## 2.3 Formation and Growth of PAHs

energy surfaces and Rice–Ramsperger–Kassel–Marcus (RRKM) theory/Master Equation simulations to derive rate constants for the growth of naphthalene to three ring aromatics (Kislov et al., 2005; Liu et al., 2019). These studies have both shown that the dominant product from HACA is acenaphthylene, which contains a rim-based five member ring. Furthermore, subsequent curvature has been suggested to be integrated through the HACA mechanism with acetylene addition to an armchair site containing a pentagonal ring (Frenklach and Ebert, 1988; Violi et al., 2004; Violi, 2005a; Whitesides et al., 2009). HACA is also important for the formation and growth of resonantly-stabilized radical PAHs. The formation of the smallest PAH, indene is formed by acetylene addition to the benzyl radical:

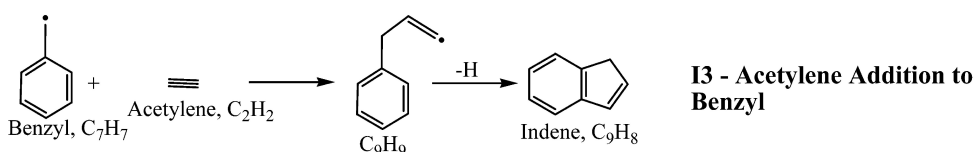


**Figure 2.6:** Formation of indene from benzyl by acetylene addition. This figure is adapted from Mebel et al. (2017) with permission from the American Chemical Society ©

Loss or abstraction of a hydrogen atom from indene results in formation of indenyl, a small resonantly stabilized radical (RSR). Growth by HACA from indenyl leads to larger RSR PAHs that have been seen to match observed peaks in VUV-AMS spectra (Johansson et al., 2018). Recently, (Frenklach and Mebel, 2020) has expanded the scope of HACA, suggesting that this stepwise growth sequence can be initiated not only by hydrogen abstraction, but low barrier hydrogen additions. Such hydrogen additions are key to the production of other classes of PAHs, such as the localised  $\pi$ -radical PAHs formed by the addition of hydrogen onto a rim-based pentagonal ring (Wang, 2011; Frenklach and Mebel, 2020). As such, HACA can be thought of more broadly as hydrogen-activated-carbon-addition, and suggests the possibility of formation of a wide variety of PAHs.

## Background

---

### 2.3.2.2 Other Pathways

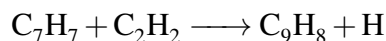
Several other pathways for the formation of small PAHs and their subsequent growth also exist. [Mebel et al. \(2017\)](#) made use of composite quantum chemical methods, density functional theory, and RRKM/master equation simulations to derive the major pathways for the formation of naphthalene and indene, the smallest closed-shell PAHs containing only six-member rings, and a six-member and five-member ring respectively. For naphthalene, the following six pathways were investigated:

- N1: HACA growth from the phenyl radical:  
$$\text{C}_6\text{H}_5 + 2\text{C}_2\text{H}_2 \longrightarrow \text{C}_{10}\text{H}_8 + \text{H}$$
- N2: Vinylacetylene radical addition to phenyl radicals:  
$$\text{C}_6\text{H}_5 + \text{C}_4\text{H}_4 \longrightarrow \text{C}_{10}\text{H}_8 + \text{H}$$
- N3: Cyclopentadienyl radicals/Cyclopentadiene recombination:  
$$\text{C}_5\text{H}_5 + \text{C}_5\text{H}_5 \longrightarrow \text{C}_{10}\text{H}_8 + 2\text{H} / \text{C}_5\text{H}_6 + \text{C}_5\text{H}_5 \longrightarrow \text{C}_{10}\text{H}_8 + 3\text{H}$$
- N4: Benzyl and propargyl radical recombination:  
$$\text{C}_7\text{H}_7 + \text{C}_3\text{H}_3 \longrightarrow \text{C}_{10}\text{H}_8 + 2\text{H}$$
- N5: 1,3-butadiene addition to phenyl radicals:  
$$\text{C}_6\text{H}_5 + \text{C}_4\text{H}_6 \longrightarrow \text{C}_{10}\text{H}_8 + 3\text{H}$$
- N6: methylation of indene/indenyl:  
$$\text{C}_9\text{H}_7 + \text{CH}_3 \longrightarrow \text{C}_{10}\text{H}_8 + 2\text{H} / \text{C}_9\text{H}_8 + \text{CH}_3 \longrightarrow \text{C}_{10}\text{H}_8 + 3\text{H}$$

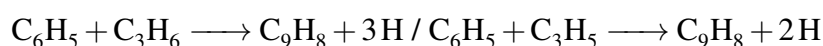
Similarly, for indene, four potential pathways were identified:

- I1: Allene and methylacetylene addition to phenyl:  
$$\text{C}_6\text{H}_5 + \text{C}_3\text{H}_4 \longrightarrow \text{C}_9\text{H}_8 + \text{H}$$
- I2: propargyl addition to benzene or phenyl radicals:  
$$\text{C}_6\text{H}_6 + \text{C}_3\text{H}_3 \longrightarrow \text{C}_9\text{H}_8 + \text{H} / \text{C}_6\text{H}_5 + \text{C}_3\text{H}_3 \longrightarrow \text{C}_9\text{H}_8$$

- I3: Acetylene addition to benzyl:



- I4: Propene / Allyl addition to phenyl :



Under combustion conditions, (Mebel et al., 2017) concluded that for naphthalene pathways N1 and N3 were the most important contributors, with N2 and N4 being secondary contributors. For indene, the main contributors were pathways I1 and I3. However, it was noted that at slightly lower temperatures, pathway N2 becomes significantly more important, due to the initial entrance channel of addition of the RSR vinylacetylene being barrierless. As a result, it was suggested that the addition reactions of radicals like vinylacetylene could provide additional pathways to the growth of larger PAHs. Further computational studies on the subject have shown that molecular growth reactions involving resonance-stabilized-free-radicals like propargyl, cyclopentadienyl, benzyl, allyl, and indenyl can be key to forming larger PAHs with six-member rings, like phenanthrene and pyrene (Sinha and Raj, 2016; Zhao et al., 2019).

Finally, a third pathway of note for molecular weight growth in PAHs consists of cross-link condensation reactions. Density functional theory studies of phenyl, naphthyl, and anthracenyl condensation on naphthalene and anthracene showed that these reactions have modest barriers of activation of around 25 kcal/mol, which is only slightly higher than HACA (Unterreiner et al., 2004). Experimental observations have also provided evidence of crosslinks that rearrange into curved pericondensed structures containing internal pentagonal rings (Baum et al., 1992; Homann, 1998; Scott, 1996; Xue and Scott, 2007), meaning that cross-link condensation pathways can be a pathway to integrating curved species as well.

## 2.4 Inception of soot from PAHs

The transition from the gas-phase regime of PAH formation and growth, to the particle-phase regime of soot formation and particle dynamics, is known as

## Background

inception or nucleation, and, as mentioned previously, is the least well understood part of the soot formation process. It is widely believed that the formation of soot is a second order process, as this is required to explain the bimodal soot particle size distributions that are observed experimentally (Wang and Frenklach, 1997; Wang, 2011). Nevertheless, the mechanism by which PAHs self-assemble to form nascent soot nanoparticles, and even which PAHs are able to initiate inception still remains elusive and is thus the subject of several studies. Several different types of mechanisms have been proposed. These are shown schematically in Figure 2.7.

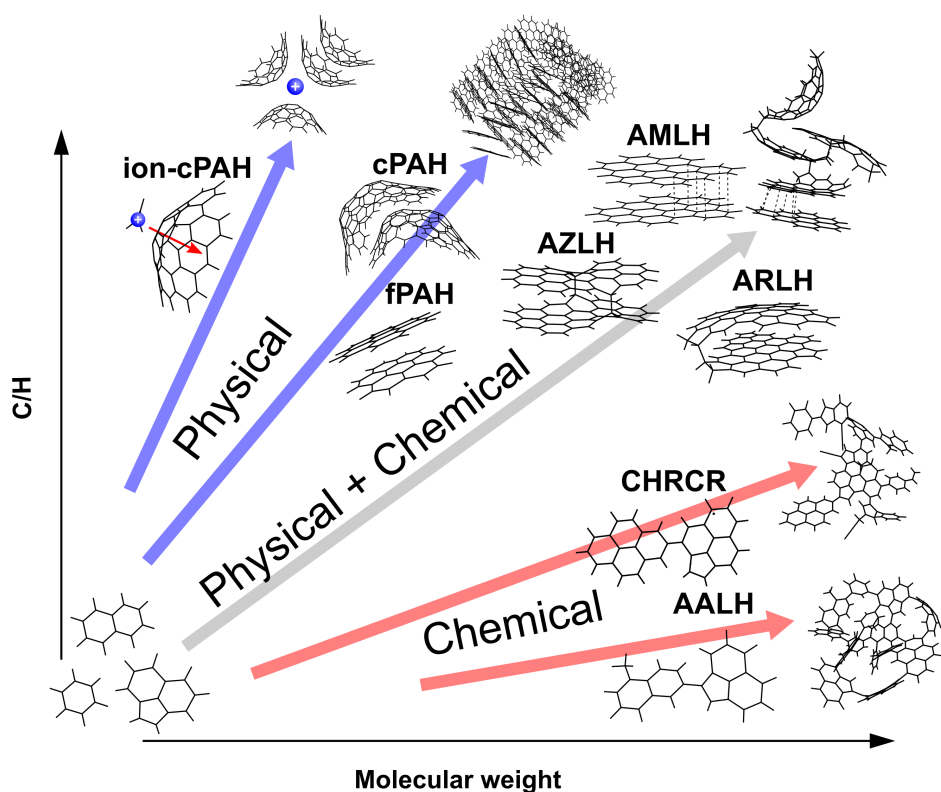


**Figure 2.7:** Various proposed mechanisms for the inception of soot nanoparticles from PAHs. This figure is courtesy of Jacob Martin © and is used with permission.

Broadly speaking, there are three main categories that inception mechanisms fall into.

- 1: Inception by physical or van der Waals interactions between PAHs, or

dispersion interactions between PAHs and other species such as charged ions that are known to have substantial concentrations in flames.

- 2: Inception through chemical reactions, sometimes known as reactive dimerization by which PAHs cluster through formation of bonds.
- 3: Inception by a combination of physical and chemical interactions between PAHs.

### 2.4.1 Inception by physical interactions between PAHs

One of the earliest, and arguably the most longstanding, suggestions of modelling inception was based on physical dimerization between flat, peri-condensed PAHs, with pyrene being a popular choice ([Wang and Frenklach, 1997](#); [Frenklach, 2002a](#); [Wang, 2011](#)). Physical dimerization results in the experimentally observed stacked nanostructures, and physical dimerization is a second order process, both of which are necessary to match experimental observations. Additionally, choosing peri-condensed PAHs is in agreement with the stabilomer analysis of [Stein and Fahr \(1985\)](#), and matches both early and recent mass spectra analyses of soot nanoparticles in flames as discussed previously ([Dobbins et al., 1995](#); [Jacobson et al., 2020](#)).

However, there are several theoretical considerations that cast doubt certainly on pyrene dimerization leading to soot, but also on the possibility of larger peri-condensed PAHs physically dimerizing. For starters, molecular dynamics of peri-condensed PAH clustering and thermodynamic analyses have all suggested that only PAHs of roughly 16-20 rings can actually cluster at flame temperatures ([Totton et al., 2012](#); [Chen et al., 2014a](#); [Sabbah et al., 2010](#)), but these larger PAHs are thought to have too low concentrations for this process to lead to sufficient nucleation flux. It has also been noted that physical dimerization of these flat peri-condensed PAHs can be highly reversible ([Eaves et al., 2015](#)), which sheds some doubt on this being a feasible route to nucleation, which is usually considered irreversible.

A recent suggestion has been the possibility of curved PAHs to nucleate physically. A study by [Martin et al. \(2017b\)](#) found that more curved PAHs have

## Background

---

larger dipole moments due to the  $\pi$ -electron flexoelectric effect. Additionally, by applying strain to corannulene, it was found that the dipole moment increased linearly with the pyramidalization angle, meaning larger curved PAHs can have substantial dipole moments. This could impact their propensity to self assemble, as interactions between permanent dipole moments are significantly stronger and more long range than simple London dispersion forces. However, a follow up work showed that the binding energies computed by DFT for curved PAH dimers are actually very similar to that for flat peri-condensed PAH dimers, due to a cancellation between the enhanced dipole-dipole interaction and the higher steric repulsion due to the curved geometries (Martin, 2019). A molecular dynamics study on the clustering of corannulene, a small curved PAH, found that no meaningful homogeneous clusters could form at 500 K, which was again similar to the results for coronene, a flat peri-condensed PAH of very similar size (Bowal et al., 2019).

However, whilst these studies argue against homogeneous clustering, the electronic structure calculations did also reveal that substantial binding energies were between a curved PAH and the  $C_3H_3^+$  chemi-ion, which is known to be abundant in flames (Hayhurst and Jones, 1987). Indeed, the binding energy predicted by electronic structure calculations between moderately sized curved PAHs of around 15 rings and this chemi-ion was seen to be above 40 kcal/mol, which is likely to be able to withstand high flame temperatures (Martin et al., 2018). Bowal et al. (2019) also found that a substantial number of clusters of corannulene were able to form when a potassium ion was introduced, with the flexoelectric dipole interacting with the charge of the ion, in contrast to purely homogeneous clustering of PAHs. This does suggest that interactions between ions and curved PAHs could be of interest to nucleation.

### 2.4.2 Inception by chemical bonding between PAHs

The second category of inception are those involving chemical bonds. This relies on reactive PAHs clustering by continuous chain reactions, typically through the formation of cross-links or bridge bonds between PAHs. As mentioned previously, Homann (1998) and Siegmann et al. (1995) have both suggested

## 2.4 Inception of soot from PAHs

---

reactive dimerization as a pathway to the inception of soot on the basis of the second maximal peaks appearing in mass spectrometry analysis of soot and flames. However, which PAHs initiate this sequence of chain reactions is uncertain, as there are a wide variety of edge types on PAHs that could potentially react, and hence several different types of mechanisms.

Homann (1998) suggested a 'zipping up' type of mechanism by which aromatic oligomers, or aromers, are produced by the formation of aliphatic cross-links between peri-condensed PAHs, that can then condense further to form larger structures. However, due to the aromatic stability predicted by Stein and Fahr (1985), peri-condensed PAHs are also expected to be less reactive, so it is not clear if such a process generates substantial nucleation flux. An early suggestion on how this could be overcome involves a  $\sigma$ -radical forming on a PAH, for example by abstraction. This radical then attacks a rim five-member ring on another PAH., which is termed the aromatic-aliphatically-linked-hydrocarbon or AALH mechanism of Violi et al. (2002). The five-member ring on a PAH will be less aromatic, and hence have an edge double bond that can be attacked by a  $\sigma$ -radical PAH. However it is uncertain if the rate constants for such a reaction is fast enough for inception to occur on the rapid timescale necessary in flames. Additionally, molecular dynamics studies have shown that the collision efficiency of  $\sigma$ -radical PAHs can be rather low with other closed-shell PAHs (Mao et al., 2018), although more recent studies dispute this (Frenklach and Mebel, 2020). However, it is known that single cross-links between PAHs are also quite susceptible to fragmentation pathways and reversibility (Wang, 2011; Frenklach and Mebel, 2020).

Recently, Frenklach and Mebel (2020) have suggested modifications to the AALH mechanism that could resolve these issues. In particular, whilst the reaction still occurs between a radical PAH and a closed-shell PAH with a rim five-member ring, instead of repeatedly forming a single aliphatic cross-link like in the AALH mechanism, they argue that an 'E-bridge' or doubly linked structure could form, which results in two adjoining five-member rings. Formation of the E-bridge results in a stable structure, does not fragment, and is less reversible. The two adjoining five-member ring structures were also observed experimentally

## Background

---

(Frenklach and Wang, 1991; Commodo et al., 2019). However, it was also noted that the forward rate is still not sufficient to generate nucleation flux on its own. A significant rate pre-exponential factor is necessary to generate sufficient nucleation flux, which was suggested to be achievable by the formation of internal rotors upon collision (Frenklach and Mebel, 2020).

Finally, another reactive pathway to soot formation suggested recently is the clustering of hydrocarbons by radical chain reactions (CHRCR) mechanism (Johansson et al., 2018). The key propagator species in this mechanism are resonantly-stabilized-radical (RSR) PAHs. As an example, it is proposed that an RSR PAH, like indenyl, could react with a  $\sigma$ -radical PAH, like phenyl. This is a barrierless reaction, as is typical of a reaction involving two radicals, and is thus expected to be quick. Once the two species react and form a cross-link, either a loss or abstraction of a hydrogen atom occurs, which results in another RSR PAH that could then react with another  $\sigma$ -radical PAH. This is then thought to occur repeatably until a cluster of PAHs results. Whilst the initial reaction is barrierless, the rate constants for a reaction between an RSR and  $\sigma$ -radical PAH have not been explored, nor has the reversibility, and the sequence still requires abstraction or hydrogen loss reactions to occur. Computation of kinetics and equilibria for these reactions is necessary to further analyse this mechanism.

### 2.4.3 Combined physical and chemical interactions between PAHs

The final category essentially combines the previous two, with PAHs both interacting physically due to dispersion forces, whilst also potentially forming chemical bonds. This is thought to combine the fast second-order dynamic nature of physical inception with the additional thermodynamic stability afforded by chemical bond formation. Examples of this include the aromatic zig-zag linked hydrocarbon (AZLH) mechanism, where linear acene-type PAHs are able to first stack and then form multiple bonds to stabilize the structure (Wang, 2011). It is known that the central rings of acenes are very reactive and longer acenes are essentially di-radical in nature (Ezawa, 2007; Minami et al., 2013). This would promote their ability to cluster in this manner. However, an issue is whether



## 2.4 Inception of soot from PAHs

---

this radical character propagates over the stacked structure and can result in a continuous clustering process. Additionally, it is known that such acenes are not very stable in flames and readily re-arrange to peri-condensed PAHs instead (Stein and Fahr, 1985).

Further mechanisms include the formation of pancake bonds that is possible between resonantly-stabilized-radical PAHs that contain only six-member rings and thus are also known as de-localised  $\pi$ -radical PAHs. An example of this is phenalenyl, which has been observed to form these multicentre  $\pi$ -bonded dimer (Small et al., 2004). Whilst this does enhance the binding energy, calculations for larger delocalised  $\pi$ -radical PAHs have suggested that the enhancement is insufficient to be stable at flame temperatures (Martin et al., 2019b). Finally, a recent study by Martin et al. (2019b) used electronic structure theory with reactivity indices to map the reactivity and bond energies of cross-links between PAHs of different edge types. localised  $\pi$ -radicals on partially saturated rim-based pentagonal rings were seen to be reactive and able to form complexes that  $\pi$ -stacked and covalently bonded at larger sizes. These complexes were named aromatic rim-linked hydrocarbons (ARLH) by Martin et al. (2019b). The bond-and-stacked ARLH compounds did have substantially larger binding energies than AMLH or physically interacting dimers, which suggests a potential avenue to soot nucleation that requires thermodynamic and kinetic analyses to be explored further.

### 2.5 Summary

This section has provided background on the processes leading to the formation of soot in a combustion environment, with a focus on polycyclic aromatic hydrocarbons (PAHs), their formation and growth, and role in forming soot nanoparticles. A survey of experimental techniques as well as growth and formation mechanisms highlights that there is substantial evidence for the presence and formation for a wide variety of PAHs, including standard peri-condensed PAHs, curved PAHs, cross-linked PAHs, and even radical PAHs. The mechanism of inception and which PAHs form soot remain elusive, and several different possibilities are under consideration. Of particular interest are the formation and properties of curved PAHs, cross-linking reactions between PAHs, and  $\pi$ -radical PAHs.

The following chapters of this thesis aim to explore the properties of these PAHs further by use of computational chemistry tools. Chapter 3 provides the theoretical background of these tools. Chapter 4 uses optical band gap analysis to re-affirm what size and types of PAHs match the optical properties of soot and flames. Chapters 5 and 6 look at the thermodynamics and kinetics of curved PAHs namely those of curved PAHs and their interactions with ions, new pathways and rates of the formation of novel classes of these curved PAHs that include seven-member rings. Chapter 7 looks at the properties and concentrations of the localised  $\pi$ -radical PAHs in flames. Finally, chapter 8 computes rate and equilibrium constants for reactions between the various types of PAHs. These studies are done to help provide further insight on how novel PAHs form and whether or not they can ultimately form soot.

# Chapter 3

## Theory and computational methods

*This chapter presents the theoretical concepts underpinning the computational techniques used in this work. This starts with quantum chemistry, where it is explained how the key properties of chemical species can be predicted from first principles. Subsequently, an overview of statistical mechanics, thermodynamics, and transition state theory is given to show how the thermodynamic properties of the species and the rate constant coefficients of chemical reactions can be calculated using information derived from the aforementioned quantum chemistry calculations. Finally, a brief summary of batch reactor simulations is provided to show how such rate processes can be compared.*

### 3 THEORY AND COMPUTATIONAL METHODS

---

The understanding of chemical processes requires the development and collection of the fundamental thermodynamic and kinetic data behind the chemical systems. Whilst experimental techniques are crucial to the development and collection of this thermodynamic and kinetic data, doing so for reactive species can often be prohibitively difficult, as several key species typically exist for extremely short periods or under difficult conditions of very high temperatures and pressures. This can make it very challenging to identify the key intermediates and reaction pathways from experiments alone. With this in mind, theoretical techniques can be a useful supplement or even alternative, by which thermodynamic and kinetic data can be calculated. This work uses quantum chemistry to compute the fundamental molecular properties of chemical species, from which the necessary data may be derived. Several such methods exist, which have varying degrees of accuracy. The following sections present a brief overview of these computational methods and procedures, from their theoretical background to their advantages and limitations.

## 3.1 Quantum chemistry

Quantum chemistry's central aim is to describe the molecular properties of a chemical system from first-principles by solution of the Schrödinger Equation. This section provides an introduction to the key approaches used in solving the the Schrödinger Equation from approximate techniques to computational methods. A more detailed description of these topics can be found in several textbooks, such as [Atkins and Friedman \(2011\)](#), [Cramer \(2013\)](#), [Lewars \(2003\)](#), and [Szabo and Ostlund \(2012\)](#), to name a few.

### 3.1.1 The Schrödinger Equation

The goal of quantum chemistry is to derive the wavefunction  $\Psi(\vec{r}, t)$  of each particle. The wavefunction is a function of the position  $\vec{r}$  and time  $t$ , but most of the methods used in this work are concerned with the time-independent solution, and so  $t$  is omitted for now. The wavefunction provides the information about the quantum state of the system, such as the positions of nuclei and electrons and the energy associated with their particular configuration, but it is not observable

in itself. The physical interpretation of the wavefunction lies in the quantity  $|\Psi|^2$ , which relates to the probability of finding a particle in a given volume. The wavefunction for such particles is in principle found by solution of the Schrödinger Equation. The time-independent Schrödinger Equation for a system consisting of several electrons and nuclei is written as follows:

$$\hat{H}\Psi(\vec{r}, \vec{R}) = E\Psi(\vec{r}, \vec{R}) \quad (3.1)$$

where  $\hat{H}$  is the Hamiltonian operator,  $\Psi$  is the wavefunction of the system,  $\vec{r}$  and  $\vec{R}$  are the positions of electrons and nuclei and  $E$  is the eigenvalue, representing the total energy of the system. The Hamiltonian operator can be written as follows:

$$\hat{H} = \hat{T}_n + \hat{T}_e + \hat{V}_{n-n} + \hat{V}_{n-e} + \hat{V}_{e-e} \quad (3.2)$$

where,  $\hat{T}_n$  and  $\hat{T}_e$  operators represent the kinetic energy of the nuclei and electrons respectively, and  $\hat{V}_{n-n}$ ,  $\hat{V}_{n-e}$  and  $\hat{V}_{e-e}$  represent the potential energy of the nuclei-nuclei, nuclei-electrons and electrons-electrons interactions, respectively. Equation 3.2 neglects relativistic effects, which is a good approximation for non-heavy atoms, namely atoms not belonging to the lanthanides or actinides (Pilar, 2001). Each term in the Hamiltonian can be expanded further. For a system consisting of  $M$  nuclei and  $N$  electrons, the terms in the Hamiltonian can be written as follows when using Hartree atomic units:

$$\begin{aligned} \hat{T}_n &= \sum_{k=1}^M -\frac{1}{2M_k} \nabla_k^2 \\ \hat{T}_e &= \sum_{i=1}^N -\frac{1}{2} \nabla_i^2 \\ \hat{V}_{n-n} &= \sum_{k<l}^M \frac{Z_k Z_l}{|\vec{R}_k - \vec{R}_l|} \\ \hat{V}_{n-e} &= \sum_{k=1}^M \sum_{i=1}^N -\frac{Z_k}{|\vec{R}_k - \vec{r}_i|} \\ \hat{V}_{e-e} &= \sum_{k=1}^M \sum_{i=1}^N \frac{1}{|\vec{r}_i - \vec{r}_j|} \end{aligned} \quad (3.3)$$

### 3 THEORY AND COMPUTATIONAL METHODS

---

where the indices  $k$ ,  $i$ ,  $l$ , and  $j$  refer to the contributions to the potential energy of nuclei, electrons, and nuclei-electron interactions, and the terms  $Z_k$  and  $M_k$  are the charge and mass of the  $k$ th nuclei respectively.

The Schrödinger Equation is only solvable analytically for very simple hydrogen-like atoms. Analytical solutions for multiple electron systems are not possible, and so approximations and numerical techniques become necessary to derive information for larger systems. The first key approximation that is usually made is the Born-Oppenheimer approximation, which essentially neglects coupling between the electrons and nuclei. This approximation argues that since nuclei are so heavy compared to electrons, they effectively appear as stationary particles to the electrons. As a result, the nuclear kinetic energy term,  $\hat{T}_n$ , can be treated as negligible, and the nuclei-nuclei potential energy,  $\hat{V}_{n-n}$ , can be treated to be constant. The Born-Oppenheimer approximation allows the wavefunction of the system to be separated into nuclear and electronic wavefunctions:

$$\Psi = \Psi_e \Psi_n \quad (3.4)$$

This also allows the Hamiltonian operator to be reduced to the electronic Hamiltonian:

$$\hat{H}_e = \hat{T}_e + \hat{V}_{n-e} + \hat{V}_{e-e} \quad (3.5)$$

An electronic Schrödinger Equation is also frequently defined:

$$\hat{H}_e \Psi_e(\vec{r}, \vec{R}) = E_e \Psi_e(\vec{r}, \vec{R}) \quad (3.6)$$

Most computational quantum chemistry approaches centre on solving the electronic Schrödinger Equation, with the nuclei-nuclei potential energy term added in at the very end. Hence, in subsequent discussion of approximate and numerical solution techniques, the subscript  $e$  is omitted.

### 3.1.2 Approximation methods for solving the Schrödinger Equation

Approaches do exist to reduce the multiple-electron problem such as the independent particle model, which defines that each electron moves in its own orbital. This simplifies the many-body problem to a set of one-electron equations. However, the electron-electron repulsion energy  $\hat{V}_{e-e}$ , is not separable, meaning the computation of these interactions still needs to be approximated, either by accounting for an average of the interactions, or only incorporating the most significant interactions. This means mathematical approximations and numerical techniques are still required.

#### Variational methods

One such method is the variational method, which constructs a trial wavefunction,  $\Psi_T$ , composed of several adjustable parameters. Typically, the trial wavefunction is constructed from atomic or molecular orbitals, which are regions having high probability of containing an electron:

$$\Psi_T = f(\phi_1, \phi_2, \dots, \phi_N) \quad (3.7)$$

where  $\phi_i$  is the  $i$ th molecular/atomic orbital. These molecular orbitals are usually expanded in terms of basis functions:

$$\phi_i(c_{i1}, c_{i2}, \dots, c_{ik}) = \sum_{j=1}^k c_{ij} \chi_j \quad (3.8)$$

With  $\chi_j$  and  $c_{ij}$  being the  $j$ th basis function and its  $j$ th expansion coefficient for  $i$ th orbital respectively. Basis functions and basis sets are discussed further in section [3.1.3.3](#).

Once the trial wavefunction is constructed, the average energy of the system with this trial wavefunction can then be computed:

### 3 THEORY AND COMPUTATIONAL METHODS

---

$$E_T = \frac{\langle \Psi_T | \hat{H} | \Psi_T \rangle}{\langle \Psi_T | \Psi_T \rangle} \quad (3.9)$$

The denominator is usually equal to one as most wavefunctions are normalised. Fundamentally, the energy of the trial wavefunction will always be greater than or equal to the ground state energy of the system,  $E_0$ . This means that an optimisation problem is formulated, where the parameters (orbitals) of the trial wavefunction are varied to minimise the energy of the system so that it approaches the ground state energy. This enables the final form of the wavefunction to be determined:

$$E_T = \min_{\phi_i} \{E_T[\Psi_T(\phi_1, \phi_2, \dots, \phi_N)]\} \quad (3.10)$$

#### Perturbation methods

Perturbation methods approximate the solutions to the Schrödinger Equation for a complex system by using a known solution for a simpler system, and adding a perturbation term that accounts for interactions not included in the simple system. The wavefunction for the simple system will obey:

$$\hat{H}^{(0)} \psi_i^{(0)} = E_i^{(0)} \psi_i^{(0)} \quad (3.11)$$

The solution for this system must be known for the perturbation method to work. The Hamiltonian  $\hat{H}^{(0)}$  is then perturbed by an amount, typically represented as  $\lambda$ :

$$\hat{H} = \hat{H}^{(0)} + \lambda \hat{H}' \quad (3.12)$$

Using the perturbed Hamiltonian, one can approximate the solution to the complex system:

$$\hat{H} \Psi_i = E_i \Psi_i \quad (3.13)$$

By using Taylor expansions about the perturbation  $\lambda$  for the Hamiltonian, energies



and wavefunctions:

$$\hat{H}_i = \sum_{j=0}^N \lambda^j \hat{H}_i^{(j)} \quad (3.14)$$

$$E_i = \sum_{j=0}^N \lambda^j E_i^{(j)} \quad (3.15)$$

$$\Psi_i = \sum_{j=0}^N \lambda^j \Psi_i^{(j)} \quad (3.16)$$

This requires the perturbation to be small for the Taylor series expansion to be valid. Substitution of the expansions into the Schrödinger equation for the desired system yields:

$$\sum_{j=0}^N \lambda^j \hat{H}_i^{(j)} \sum_{j=0}^N \lambda^j \Psi_i^{(j)} = \sum_{j=0}^N \lambda^j E_i^{(j)} \sum_{j=0}^N \lambda^j \Psi_i^{(j)} \quad (3.17)$$

Rearrangement in terms of  $\lambda$  and equating coefficients yields the perturbation terms. As an example, the first order perturbation terms are given as:

$$E_i = E_i^{(0)} + \langle \Psi_i^{(0)} | \hat{H}^{(1)} | \Psi_i^{(0)} \rangle \quad (3.18)$$

$$\Psi_i = \Psi_i^{(0)} + \sum_{k \neq i} \Psi_k^{(0)} \frac{\langle \Psi_i^{(0)} | \hat{H}^{(1)} | \Psi_i^{(0)} \rangle}{E_i^{(0)} - E_k^{(0)}} \quad (3.19)$$

Higher order terms can be derived similarly.

### 3.1.3 Computational methods for solving the Schrödinger Equation

The following section presents a brief summary of computational methods that are used to solve the Schrödinger Equation. The methods covered are ones typically employed by modern quantum chemistry software packages, but this is by no

---

### 3 THEORY AND COMPUTATIONAL METHODS

---

means a complete list. The section starts with brief explanation of *ab initio* wavefunction methods, followed by an introduction to density functional theory. The section concludes with a discussion of composite methods that use a mixture of other methods to compute specific properties accurately.

#### 3.1.3.1 Wavefunction-based methods

Several *ab initio* methods have been used to derive approximate solutions to the Schrödinger Equation, from the Hartree-Fock method (Slater, 1951, 1953) to more advanced wavefunction-based methods such as Møller-Plesset perturbation theory and configuration interaction methods. Wavefunction-based methods have the advantage of not relying on empirical-parameters. More advanced methods in this category also systematically approach the exact solution. However, the most accurate methods, such as configuration-interaction methods, tend to be applicable only to small molecules due to the high computational cost.

##### 3.1.3.1.1 Hartree-Fock Theory

As discussed in section 3.1.2, approximating a solution to the Schrödinger Equation to derive electronic properties typically requires the construction of a trial wavefunction, which is then iterated upon to get closer to the true solution. The first robust trial wavefunction developed was proposed by the Hartree-Fock method (Slater, 1951, 1953). The Hartree-Fock method is the foundation for most other advanced methods such as configuration-interaction based methods, and is key to hybrid density functional theory methods as well. The Hartree-Fock method adopts a variational approach, with each electron assumed to inhabit spinorbital,  $\phi_i$ . This essentially invokes the independent particle model, where the electrons are modelled as a combination of the various one-electron wavefunctions. One key approximation made in the Hartree-Fock approach is the mean field approximation, which posits that each electron behaves as if it sees an average potential of all of the other electrons. This essentially omits real exchange correlation between the electrons. With these approximations in

mind, the trial wavefunction is constructed by using a Slater determinant. For a system with  $N$  electrons, the Slater determinant is as follows:

$$\Psi = \frac{1}{\sqrt{N!}} \begin{vmatrix} \psi_1(\vec{r}_1) & \psi_2(\vec{r}_1) & \dots & \psi_n(\vec{r}_1) \\ \psi_1(\vec{r}_2) & \psi_2(\vec{r}_2) & \dots & \psi_n(\vec{r}_2) \\ \dots & \dots & \dots & \dots \\ \psi_1(\vec{r}_N) & \psi_2(\vec{r}_N) & \dots & \psi_n(\vec{r}_N) \end{vmatrix} \quad (3.20)$$

The spinorbital functions  $\psi_i(\vec{r}_i)$  are the product of the orbital functions  $\phi_i(\vec{r}_i)$  and the spin function, which is one of two functions  $\alpha$  or  $\beta$ . The Slater determinant construction includes considerations of spin and also produces an antisymmetric wavefunction, as swapping two electrons transposes the rows and columns which changes the sign of the determinant. Additionally, the Slater determinant also satisfies the Pauli exclusion principle, for if two electrons in the same orbital have identical spins, the columns of the determinant are the same, resulting in a value of zero. To keep the governing Hartree-Fock equations at a manageable size, the spinorbital are chosen to be orthonormal to each other, reducing the number of terms substantially. The final equations that are solved in the Hartree-Fock method are a set of one-electron equations where the Hamiltonian is replaced by a Fock operator:

$$\hat{F}_i = \hat{h}_i + \sum_{j=1}^N (\hat{J}_{ij} - \hat{K}_{ij}) \quad (3.21)$$

With the one-electron Hamiltonian  $\hat{h}_i$  being given by:

$$\hat{h}_i = \hat{T}_{e,i} + \hat{V}_{n-e,i} \quad (3.22)$$

This is essentially the kinetic energy of the electron and Coulombic interaction of a single electron with all present nuclei. The other two terms in the Fock operator,  $\hat{J}_{ij}$  and  $\hat{K}_{ij}$ , account for the electrostatic repulsion between electrons and the electron exchange interaction respectively. However, to compute these terms for each electron spinorbital, one would need to know the solutions for the

### 3 THEORY AND COMPUTATIONAL METHODS

---

spinorbitals of all of the other electrons, which is clearly impossible. As a result, the self-consistent field method (SCF) is adopted, where trial spinorbitals are used to initiate the optimization problem. With each iteration, the spinorbitals are updated and used to compute the wavefunction and hence the average energy of the system, until the change in energy between consecutive iterations falls below a defined threshold, after which a self-consistent field has been found.

For closed-shell systems with a multiplicity of one, restricted Hartree-Fock (RHF) can be used, where the orbital functions are the same for opposite spins and each orbital is doubly occupied. However, for open-shell systems *i.e* free radicals this approach does not work and either restricted open-shell Hartree-Fock (ROHF) or unrestricted Hartree-Fock (UHF) must be adopted instead. In ROHF, partial occupancy of orbitals is allowed, but the orbital functions are still identical for opposite spin electrons. In UHF, the orbital functions for opposite spin electrons are entirely independent. This treatment allows for considerable improvement in the energies estimated for the system, but the method does not preserve the total spin symmetry of the system, and can result in spin contamination. ROHF does preserve the total spin of the system, but tends to give poorer estimates of energy. With modern quantum chemistry software packages incorporating spin annihilation steps to counteract spin contamination, more advanced "Post Hartree-Fock" wavefunction methods tend to be based on UHF. These methods are discussed further in the next section.

#### 3.1.3.1.2 Post Hartree-Fock Methods

The solutions to the Schrödinger Equation provided by the Hartree-Fock method contain significant errors. This is primarily due to mean field approximation. Treating the other electrons as an average potential is insufficient, as in reality each individual electron moves under the influence of the other electrons, in what are known as electron correlation effects. Post-Hartree-Fock methods attempt to improve on the Hartree-Fock method by trying to incorporate correlation effects into the solutions.

### Møller-Plesset Perturbation Theory

Møller-Plesset (MP) Perturbation Theory uses perturbation methods to correct the Hartree-Fock solution to account for primarily dynamic electronic correlation effects (Møller and Plesset, 1934). The unperturbed reference Hamiltonian is taken as the sum of the one-electron Fock operators used in Hartree-Fock (Head-Gordon and Pople, 1988):

$$\hat{H}^{(0)} = \sum_{i=1}^N F_i \quad (3.23)$$

The perturbation term is the difference between the exact Hamiltonian and the reference Hamiltonian. This equals the difference between the electron-electron interaction potential, and the mean-field potential assumed by Hartree-Fock:

$$\hat{H}^{(1)} = \hat{H} - \hat{H}^{(0)} = \sum_{i<j}^N \hat{V}_{e-e,ij} - \sum_{j=1}^N \hat{V}_j^{\text{HF}} \quad (3.24)$$

The zeroth and first order corrections to the energy are equivalent to the Hartree-Fock energy, so corrections to the Hartree-Fock method that include electron correlation are found for second order perturbation theory, termed MP2. MP2 gives reasonable energies for affordable computational costs. More accurate energies can be computed by using higher order perturbation methods, such as MP3, MP4, and MP5, but these methods are significantly more computationally demanding. As such, MP2 tends to be the most widely used of the perturbation methods.

### Configuration Interaction Methods

Configuration interaction methods (CI) (Sherrill and Schaefer, 1995) are an extension to the Hartree-Fock method that tries to correct the correlation energy error. CI methods construct a wavefunction as a linear combination of Slater determinants used in Hartree-Fock, or configuration state functions (CSF), which are then optimized according to the variational principle. This can be written as follows:

### 3 THEORY AND COMPUTATIONAL METHODS

---

$$\Psi = \sum_{k=0}^N C_k \Psi_k, \quad (3.25)$$

with  $\Psi_k$  and  $C_k$  being the  $k$ th determinant or CSF, and the  $k$ th expansion coefficient. The terms in the expansion (*i.e.* each  $C_k \Psi_k$  term) are the different electronic configurations included in the method, with the first typically being the Hartree-Fock term, and subsequent terms representing electronic excitations from ground state to the  $k$ th state. The expansion coefficients are determined variationally in a method analogous to the SCF approach used in the Hartree-Fock method, but the orbitals are kept frozen to those determined by the Hartree-Fock solution.

Including all possible excitations and CSFs within a configuration interaction method does correctly compute the static electron correlation term for one-electron wavefunctions. However, this is computationally prohibitive, and truncated methods are typically used, with the number of excitations defining the order of the method. Typically, this includes single (S), double (D), triple (T) and, at a stretch, quadruple (Q) excitations. As an example, the CISD method is a configuration interaction method that allows single and double excitations of electrons in the ground state. To improve computational cost, excitations beyond the double excitation may be included using a perturbation approach, which is denoted by the letter being in parentheses, *i.e.* CISD(T), which includes the triple excitations using perturbation theory. These truncated CI methods are size inconsistent, meaning the energies for infinitely separated systems are not correctly reproduced as the sum of the energies of the individual entities. To correct for this, [Pople et al. \(1987\)](#) developed quadratic configuration interaction (QCI), which includes terms that are quadratic in the expansion coefficients  $C_k$ .

Other extensions of the CI method include coupled-cluster (CC) methods. These methods allow for consideration of correlation terms due to the products of excitations when compared to the CI technique, and results in improved accuracy. Mathematically, this is the result of using exponential expansions as opposed to linear expansions:

$$\Psi = \exp\left(\sum_{k=0}^N T_k\right) \sum_{k=0}^N \Psi_k \quad (3.26)$$

By making use of the Taylor expansion, this can be written as:

$$\Psi = \sum_{k=0}^N \left(\frac{T_k}{k!}\right) \Psi_k \quad (3.27)$$

Coupled cluster methods are highly accurate and often referred to as the gold standard of computational chemistry. However, the computational cost scales very quickly with the size of system studied, with CCSD(T) scaling with  $N^7$  with  $N$  being the system size, compared to  $N^4$  for Hartree-Fock theory. This is due to the much larger number of expansion terms required. Much like with CI methods, the CC methods are often truncated to only allow certain excitations, with the naming convention being the same as for CI methods as well, *i.e.* CCSD(T) including single and double electron excitations, with triple excitations included using perturbation theory. Even so, CC methods are typically only feasible for very small molecules, such as those with less than 30 atoms.

### **Multiconfiguration SCF Methods**

Multiconfiguration SCF (MCSCF) methods are an extension of CI methods, in which the constraint of freezing the orbitals to the Hartree-Fock solution present in the CI methods is relaxed. This means that the orbitals and expansion coefficients are optimized together for the various electronic states. As a result, MCSCF methods are far more computationally demanding than CI methods.

In practice, most methods introduce some form of truncation to limit the number of terms used in the expansion, such that the computational time becomes more feasible. The first of these methods is the complete active space SCF (CASSCF) method. CASSCF utilizes a user-defined "active space", which specifies the number of electrons and orbitals to include in the optimisation process. The number of determinants introduced in the expansion terms is then determined by the distribution of the selected electrons into the selected orbitals.

### 3 THEORY AND COMPUTATIONAL METHODS

---

The CASSCF method is often used to describe potential energy surfaces for various chemical reactions, and unlike simpler methods, it can describe the wavefunction for bond dissociation processes reasonably well. This is primarily due to the degree of customisation available for constructed wavefunction offered by control of the active space. However, CASSCF methods do not account for electron dynamics, and thus the energies produced are not always reliable, and the method is entirely reliant on choosing an appropriate active space, which typically requires significant knowledge of the process. As such, it is not a method that can be treated as a black box.

To improve upon CASSCF, multi-reference methods are used to account for the dynamic correlation contribution to the energy, whilst using the CASSCF wavefunction as the reference solution. As the name suggests, instead of using one reference configuration (such as the ground state Hartree-Fock solution), multiple electronic configurations are used as references instead, typically including ground and excited states. Examples of multi-reference methods include multi-reference configuration interaction (MRCI) methods ([Shamasundar et al., 2011](#)), which use the CI approach to account for electron dynamics, and CASPT2 ([Celani and Werner, 2003](#)), which uses second order perturbation corrections to account for electron dynamics.

#### 3.1.3.2 Density Functional Theory

Density functional theory (DFT) ([Ziegler, 1991](#)) is a popular computational method in quantum chemistry. In contrast to wavefunction-based methods, DFT centres on the electron probability density,  $\rho(\vec{r})$ . This electron density is computed from the integral over all of the spin coordinates of the electrons,  $s$ , and over two of the three spatial coordinates:

$$\rho(\vec{r}) = N \int \prod_{i=2}^N d\vec{x}_i ds_i |\Psi(\vec{x}_1, \vec{x}_2, \dots, \vec{x}_N)|^2 \quad (3.28)$$

In this definition,  $(\vec{x} \equiv \vec{r}, s)$ , determines the probability of finding any of the  $N$  electrons within a volume element  $d\vec{r}$ . The total number of electrons is retrieved by



the standard approach of integrating the electron density over the volume element:

$$N = \int \rho(\vec{r}) d\vec{r} \quad (3.29)$$

It is worth noting that this electron density is a function only of the three spatial coordinates  $\vec{r}$ , which can offer significant computational advantages over wavefunction based methods, which are a function of  $4N$  variables.

The proof that using the electron density  $\rho(\vec{r})$  can be used to derive the electronic properties of atoms and molecules was demonstrated by Hohenberg and Kohn (Hohenberg and Kohn, 1964). This can be summarised in two main theorems. The first Hohenberg-Kohn theorem states that the ground state properties of a system are a function of the ground state electron density function,  $\rho_0(\vec{r})$ . This means the ground state energy  $E_0$ , must be a function of  $\rho_0(\vec{r})$ . The second Hohenberg-Kohn theorem is essentially a statement of the variational principle, but for DFT:

$$E[\rho(\vec{r})] \geq E[\rho_0(\vec{r})] \quad (3.30)$$

As a result of the theorems, there must exist a functional that maps the ground state electron density to the ground state energy. However, the form of the functional that defines this relation is not known *a priori* for a system containing interacting electrons. To circumvent this, the system containing interacting electrons is treated using a fictitious model system having non-interacting electrons, but the same electron density  $\rho(\vec{r})$ . Using this approach, the energy as a function of electron density may be written as:

$$E[\rho(\vec{r})] = T_s[\rho(\vec{r})] + V_{n-e}[\rho(\vec{r})] + J[\rho(\vec{r})] + E_{xc}[\rho(\vec{r})] \quad (3.31)$$

where  $T_s[\rho(\vec{r})]$  is the kinetic energy of the non-interacting model system and  $J[\rho(\vec{r})]$  is the Coulomb energy functional, both of which are known exactly. Similarly,  $V_{n-e}[\rho(\vec{r})]$  is the nucleus-electron attraction potential functional whose form can be derived given the Born-Oppenheimer approximation. The final term,  $E_{xc}$  is termed the exchange-correlation functional, and accounts for the difference

### 3 THEORY AND COMPUTATIONAL METHODS

---

in kinetic and potential energies between the real interacting-electron system, and the approximate non-interacting electron system:

$$E_{xc}[\rho(\vec{r})] = (T[\rho(\vec{r})] - T_s[\rho(\vec{r})]) + (V_{e-e}[\rho(\vec{r})] - J[\rho(\vec{r})]) \quad (3.32)$$

$$= T_c[\rho(\vec{r})] + \hat{V}_{e-e}[\rho(\vec{r})] \quad (3.33)$$

Again, the exact forms for the residual kinetic energy,  $T_c[\rho(\vec{r})]$  and residual potential energy  $\hat{V}_{e-e}[\rho(\vec{r})]$  are not known, and so developing reasonable approximations and forms for the exchange correlational,  $E_{xc}$  is a key part of DFT.

Once an approximation is made for the exchange correlational term, performing the computations using DFT are analogous to the Hartree-Fock method, with an SCF approach again being adopted. This is known as Kohn-Sham DFT, where the SCF approach is used to minimise the energy with respect to the Kohn-Sham orbitals (Kohn and Sham, 1965). These orbitals are related to the electron density by the following:

$$\rho(\vec{r}) = \sum_i^N |\psi(\vec{r})|^2 \quad (3.34)$$

However, the main challenge for DFT is still developing appropriate methods for the exchange correlational term, or functionals. Since the start of development of DFT, a variety of functionals have been proposed, which are often categorized into different groups.

#### Pure Functionals

Pure functionals strictly use only DFT methods without incorporating other methods. The first and most basic type of functionals invoke the local density approximation (LDA). The LDA method approximates the inhomogeneous system electron density as one consisting of several infinitesimal regions where the electron density is constant. Each of these regions then has its electronic-exchange correlation evaluated as that of a free electron gas. The result

is that LDA functionals depend only on the value of the electron density at the spatial coordinate at which they are being evaluated. The LDA functional is reasonable for systems with slowly varying densities such as solids. It is poor for other systems such as molecules. Generalized gradient approximation (GGA) functionals extend the concept of LDA functionals. In GGA functionals, the electronic-exchange correlation depends on not only the value of the electron density at the spatial coordinate, but also the value of the electron density gradient at this point as well. As a result, GGA methods can give accurate ground state energies and geometries for simple molecules.

#### Hybrid Functionals

Unlike pure functionals, which are strictly DFT-based approaches, Hybrid functionals combine the DFT framework with Hartree-Fock methods in order to achieve more accurate results. These hybrid functionals mix the exact exchange determined by Hartree-Fock methods with the exchange-correlation energies determined by using a density functional. The ratio can be tuned to create different functionals, depending on the properties of interest. Examples of such hybrid functionals include the widely popular B3LYP (Becke, 1993) and B971 (Hamprecht et al., 1998) functionals, which are more general purpose. Functionals are often tailored for accurately determining certain properties. For example, the HSE06 functional makes use of a screen-exchanged Coulomb potential to capture short range interactions, and is often used for computing optical properties of materials and modelling metals (Heyd et al., 2005). The Minnesota family of functionals, such as M06-2X, are meta-GGA functionals that include dependence on the kinetic energy density, and are often used for determining more accurate barrier heights and thermochemistry (Zhao and Truhlar, 2008). All of these functionals are used in this work. Additionally, hybrid functionals can be corrected to include dispersion interactions, namely van der Waals interactions, that are not included in the energies computed by Kohn-Sham DFT. This is typically referred to as dispersion-corrected DFT, and usually computes the dispersion correction by pair-wise interaction corrections that are then added onto the DFT energy (Grimme, 2011).

### 3 THEORY AND COMPUTATIONAL METHODS

---

#### Application of DFT in computational chemistry

Due to the lower computational cost relative to higher-accuracy wavefunction methods, and the availability of a wide range of functionals, DFT has become one of the main work horses of computational chemistry, finding a wide variety of applications (Burke, 2012). In this work for example, it has been used to determine an array of molecular properties, such as optical properties and band gaps that are used in spectroscopic studies, electronic and binding energies that are used to determine thermodynamic stability, and geometries and vibrations of chemical species that are used to study the chemical kinetics of various reactions. Nevertheless, it is worth noting that DFT does have its limitations, as an unwise choice of functional leads to poor results. Additionally, unlike wavefunction methods, DFT methods are not variational, which means that systematic improvements by increasing the basis set are not always found with DFT methods. This is compounded by the fact that no one functional can predict all properties accurately due to the way they are tailor-made, whereas high level post Hartree-Fock methods are generally more accurate at predicting a wider range of properties (Foresman and Frish, 1996). As a result, what is commonly done is using a combination of different functionals for different calculation steps to achieve more accurate results, such as using B3LYP for determining the geometries and vibrations, followed by M06-2X for determining more accurate electronic energies. Sequential calculations with different functionals can often achieve so called chemical accuracy for computations whilst still being computationally feasible.

#### 3.1.3.3 Basis sets

Both Hartree-Fock and DFT methods employ the use of orbitals, which are then used to construct the wavefunction or electron density. These orbitals are usually represented by the linear combination of basis functions, termed the basis set:

$$\phi_i = \sum_{j=1}^k c_{ij} \chi_j \quad (3.35)$$

with  $\phi_i$  being the orbitals,  $c_{ij}$  being the normalization constants, and  $\chi_j$  being the basis functions used to construct the orbitals. The choice of appropriate basis functions to describe the atomic orbitals is key to performing quantum chemistry calculations.

Basis sets are typically denoted by the number and type of basis functions they use to describe the electron orbitals. The simplest basis set is a minimal basis set, in which one basis function is used per electron orbitals. However, describing an orbital with only one basis function is typically insufficient, and typically multiple basis functions are used. Using two basis functions per orbital is termed a double- $\zeta$  (double-zeta) basis set, and similarly using three basis functions is known as a triple- $\zeta$  basis set. In principle, using an infinite number of basis functions, termed the complete basis set limit, would correctly describe an orbital. This is infeasible, practically, and truncation of basis sets does introduce a source of error into the calculations. Typically, to reduce computational cost, a split-valence approach is adopted. Split-valence basis sets use multiple basis functions to describe the valence electrons, as these are usually the important electrons for most chemical phenomena such as bonding and reactions, and then minimal basis functions to describe the core electrons. This is a popular approach adopted in many basis sets.

Several types of basis functions are used in different basis sets. One of the earliest suggested types of basis functions made use of Slater type orbitals (STOs) [Slater \(1951\)](#). These have the general form of:

$$S = N(r - R)^{n-1} e^{-\zeta(r-R)}, \quad (3.36)$$

with  $N$  being a normalization constant,  $n$  being the principle quantum number, and  $r$  being the radial distance, with the centre of the radial coordinate system,  $R$ , conventionally being defined as the atomic nucleus. Slater-type orbitals approximate the shape of atomic orbitals well, but numerical integration involving these orbitals is computationally more demanding. As a result, STOs are rarely used in computational chemistry software.

One of the most popular and widely used functions are Gaussian-type orbitals

### 3 THEORY AND COMPUTATIONAL METHODS

---

(GTOs). As the name suggests, the basis functions are constructed using primitive Gaussian functions:

$$G = M(x - X)^{l_x}(y - Y)^{l_y}(z - Z)^{l_z}e^{-\zeta(r-R)^2}, \quad (3.37)$$

with  $M$  being a normalization constant,  $x$ ,  $y$ ,  $z$ , and  $r$  being the positional coordinates with the centre  $R(X, Y, Z)$  conventionally defined as the coordinates of the atomic nucleus (the nuclear coordinates),  $l_x$ ,  $l_y$ , and  $l_z$  defining the angular momentum and hence the orbital type (i.e.  $l_x + l_y + l_z = 0$  for an s orbital), and  $\zeta$  being a parameter that governs the size of the orbital. Gaussian-type-orbitals are significantly easier to work with when performing numerical integration, and are the basis sets used in this work consist of multiple primitive GTOs.

The first type of basis set used in this work are Pople-type orbitals, which are named with the notation “ $x - yz_wG$ ” and describes the system where the core electron orbitals are approximated by one basis function consisting of  $x$  primitive Gaussian equations, and where the valence electrons are represented using a triple- $\zeta$  basis set, consisting of three basis functions each composed of  $y$ ,  $z$ , and  $w$  basis functions respectively. As an example, one of the most popular basis sets is 6-311+G(d,p), which uses a single basis function of six Gaussians to describe the core electrons, and three basis functions of three, one, and one Gaussian-type-orbitals to describe the valence electrons. The ‘+’ symbol indicates that diffuse functions are included, which are functions with broad tails that are helpful for describing broad electron distributions. They are often used for describing anions, molecular complexes, and radicals. The (d,p) in brackets represents the use of polarisation functions. These functions allow polarisation of the atomic electron density, which again help give a better description of the molecular electronic structure. The d signifies that d orbitals are added to row 1 and row 2 elements, and p orbitals are added to any hydrogens present.

Whilst popular, Pople-type basis sets do not systematically converge to a complete basis set limit as their size increases. As a result, Dunning’s correlation consistent basis sets (Dunning, 1989) are often used as they do systematically approach a CBS limit for wavefunction methods. Dunning-type basis sets are often named

as (aug)-cc-pVnZ. The aug, if added, includes diffuse functions into the basis set, cc stands for correlation-consistent, the p indicates that polarisation functions are included, the V indicates a valence-only basis set, and the nZ denotes a split-valence basis set. n is typically one of D,T,Q,5,and 6, which signifies how many basis functions are used for the valence electrons. For example DZ stands for double-zeta, indicating two basis functions are used for the valence electrons. Similarly, TZ is triple-zeta, so three basis functions are used for valence electrons, and so on for the others. Although not used in this work, it is worth mentioning plane-wave basis sets, where the basis functions of choice consist of plane-wave functions:

$$p = c_G e^{-iG \cdot r}, \quad (3.38)$$

with  $c_G$  being the complex coefficient of the plane-wave,  $G$  being the grid size of the system, and  $r$  being the distance coordinate. Plane-wave basis sets can only be used on a user-defined periodic cell, where the number of plane-waves used is essentially all of the wavevectors that can be placed in the periodic cell. Plane-wave functions are naturally orthogonal, which makes them numerically efficient so long as the number of plane-waves used is manageable. Plane-waves are the basis set of choice for larger systems with naturally periodic behaviour such as solids, as any periodic boundary conditions on the electronic structure of a solid can be inherently achieved with plane-waves. However, it is worth knowing that plane-wave basis sets are typically not used for molecular systems, as to do so requires constructing an artificial periodic cell around the molecule, resulting in a large number of plane-wave basis functions being used to describe what is effectively empty space.

### 3.1.3.4 Composite Methods

Composite methods aim to compute accurate energies and thermodynamic properties of molecular systems in a computationally affordable framework. As the name suggests, composite methods often involve performing several

### 3 THEORY AND COMPUTATIONAL METHODS

---

computations using various levels of theory, that is different methods and basis sets. The results of these different calculations are then combined to extrapolate to an accurate value for the quantity of interest. These methods rely on assuming that the contributions of the various electronic effects are additive, that is they can be added individually to a given reference energy (Weber and Wilson, 2015). Typically, a set of main group species whose energies have well-known experimentally determined energies are used to calibrate these composite methods, with the aim of composite methods typically being to reproduce the energies of these reference species with a mean absolute error of no more than 1 kcal/mol (Curtiss et al., 1991). This is often termed chemical accuracy. Various series of composite methods are used, that adopt different approaches and combinations of methods to achieve said chemical accuracy. Some of the most popular are the following:

Gaussian- $n$  or  $G_n$  methods consist of a series of methods (with  $n$  being 1,2,3, and 4) of increasing accuracy (Pople et al., 1989; Curtiss et al., 1991, 1998, 2007) with the original G1 method being developed by Pople et al. (1989), and the most recent being the G4 method. The principle underlying the different  $G_n$  methods is the same and relies on cancellation of the systematic errors in the various levels of theory that comprise these composite methods. The components of each  $G_n$  method are different, but typically each component is included for a specific purpose. For example, in the G4 method, the geometries and vibrations are obtained using the B3LYP functional and the 6-31G(2df,p) basis set, the basis set extrapolation energy is computed using HF/aug-cc-PVQZ and HF/aug-cc-PV5Z, the polar, diffuse and large basis set effects are computed by using MP2 energies and a variety of basis sets and correlation effects are included using CCSD(T)/6-31G(d). This illustrates how several different *ab initio* calculations can be used to construct composite methods. It is worth noting that in the case of  $G_n$  methods, the process is not entirely *ab initio*, as an empirical correction term is also included.

Complete-Basis set (CBS) methods adopt the approach of using multiple calculations to get an estimate of the energy if one were to construct a wavefunction with an infinite number of basis functions (an infinitely large



basis set). This is achieved by running a sequence of calculations, each with a progressively large basis set, and then using an extrapolation formula to estimate what the result would be if an infinite basis set was used. An example of a popular CBS method is the CBS-QB3 method ([Montgomery et al., 1999](#)).

The Weizmann-n or Wn methods are composite methods consisting of various couple cluster methods, utilizing primarily CCSD and CCSD(T) methods whilst also using sequential basis sets to extrapolate to the infinite basis set limit like the CBS methods. The Wn methods typically achieve the highest degree of accuracy, owing to them relying on high-level wavefunction methods. This does also mean they are significantly more expensive computationally, and are limited to small molecules as a result.

## 3.2 Statistical Thermodynamics

A key component to modelling chemical systems is the determination of thermochemical data such as enthalpy, entropy, Gibbs free energy, and heat capacities for the various chemical species in said system. For large macroscopic systems, classical thermodynamics is applicable, but in this work, the systems of interest are typically of the molecular scale, where quantum effects and molecular theory are important and classical thermodynamics is no longer sufficient. Another framework to compute the macroscopic properties of many-particle systems like molecules from their microscopic properties is therefore necessary. Statistical thermodynamics provides this framework by adopting a probabilistic approach. By making use of statistical thermodynamics, the microscopic properties of molecules such as energy levels, geometries, and vibrations that are determined experimentally or by quantum chemistry, may be used to compute macroscopic thermodynamic quantities. The key concepts enabling this are that of the partition function and the Boltzmann distribution.

The following section presents a brief summary of the main aspects of statistical thermodynamics used in this work to derive thermodynamic properties and rate constants from computational quantum chemistry calculations. This starts with a description of the partition function and Boltzmann distribution, followed by

### 3 THEORY AND COMPUTATIONAL METHODS

---

a summary of the key components required to determine a molecular partition function. The section closes with the determination of thermodynamic properties from the partition function. Throughout, the ideal gas law is assumed, which assumes no interactions (and hence independence) between individual particles of a system. Properties are also derived at thermodynamic equilibrium. More detailed descriptions of statistical thermodynamics may be found in standard textbooks, such as [Atkins and Friedman \(1997\)](#) or [McQuarrie and Simon \(1999\)](#).

#### 3.2.1 Partition Functions

The key concepts of statistical thermodynamics are the partition function and the Boltzmann distribution. As statistical thermodynamics relies on a probabilistic approach, the Boltzmann distribution is crucial as it describes the probability of a system being in different states. A system's probability of being in these different states is a function of the energy required to access these states and hence the temperature of the system. The accessibility of these states is given by the partition function. For a molecule, the energy levels of the system,  $\epsilon_i$ , either determined experimentally or from computational chemical methods, are used to build the partition function as follows:

$$q(V, T) = \sum_{i=1}^N g_i \exp\left(-\frac{\epsilon_i}{k_B T}\right), \quad (3.39)$$

where  $V$  and  $T$  are the volume and temperature,  $\epsilon_i$  are the energy levels, with degeneracy  $g_i$  (the number of states with the same energy),  $k_B$  is the Boltzmann constant, and  $N$  is the total number of energy levels. The contributions to the molecular partition function come from the various modes, namely the translational, vibrational, rotational, and electronic modes. Typically, to determine the molecular partition function, one makes the assumptions to treat the molecule as an ideal gas of non-interacting particles, and the rigid rotor harmonic oscillator (RRHO) approximation, which states that the modes of motion that contribute to the partition function are independent of one another, thus allowing them to be treated separately. The RRHO approximation is almost always invoked, as it results in a simple way to derive the molecular partition function and gives

reasonably accurate results. By the RRHO approximation, the energy of a molecule at state  $i$  is given by:

$$\varepsilon_i = \varepsilon_i^T + \varepsilon_i^V + \varepsilon_i^R + \varepsilon_i^E \quad (3.40)$$

Substitution of the above into equation 3.39 yields an expression for the total molecular partition function:

$$q = q_T q_V q_R q_E \quad (3.41)$$

The individual translational, vibrational, rotational, and electronic partition functions can then be solved for as discussed in the next sections.

### 3.2.1.1 Translational Partition Function

The energy levels necessary to construct the translational partition function are derived from solving the Schrödinger equation for a particle confined in a cubic box of volume  $V = a^3$ :

$$\varepsilon_{n_x, n_y, n_z}^T = \frac{\pi^2 \hbar^2}{2ma^2} (n_x^2 + n_y^2 + n_z^2) \quad n_x, n_y, n_z = 1, 2, 3, \dots, \quad (3.42)$$

Where  $\hbar$  is the Planck's constant  $h$  divided by  $2\pi$ ,  $m$  is the mass of the particle, and  $n_x$ ,  $n_y$ , and  $n_z$  are the quantum numbers for the corresponding Cartesian directions. These energy levels can then be substituted into equation 3.39, which, after noting that  $n_x = n_y = n_z$  will hold for the cubic box case, yields:

$$q_T = \left[ \sum_{n=1}^{\infty} \exp\left(-\frac{\pi^2 \hbar^2 n^2}{2k_B T m a^2}\right) \right]^3 \quad (3.43)$$

With the assumption of tightly packed energy levels, this sum can be replaced with an integral that can be found to be:

### 3 THEORY AND COMPUTATIONAL METHODS

---

$$q_T = \left[ \int_0^\infty \exp\left(-\frac{\pi^2 \hbar^2 n^2}{2k_B T m a^2}\right) \right]^3 = \left( \frac{mk_B T}{2\pi \hbar^2} \right)^{\frac{3}{2}} V \quad (3.44)$$

This defines the translational partition function contribution to the molecular partition function. It is worth noting that the volume contributes to the translational partition function and thus an equation of state is needed when evaluating this. As mentioned previously, the ideal gas law is assumed and so the volume  $V$  is given by the standard expression  $\frac{k_B T}{P}$ .

#### 3.2.1.2 Vibrational Partition Function

The energy levels for the vibrational partition function are derived from the solution of the Schrödinger equation for a harmonic oscillator, in which a particle oscillates in a parabolic potential well. The resulting energy levels are equally spaced and singly degenerate, and are given by the following:

$$\epsilon_n^V = \left(n + \frac{1}{2}\right) h \nu_i \quad n = 0, 1, 2, \dots, \quad (3.45)$$

where  $n$  is the quantum number, and  $\nu_i$  is the vibrational frequency of the  $i$ th normal mode. Even at  $n = 0$ , the energy of the harmonic oscillator is not zero, but instead equal to  $\frac{1}{2} h \nu_i$ . This is termed the zero-point energy, representing the fact that the system will always have non-zero energy, even at 0 K due to quantum fluctuations. To derive the partition function, one again substitutes the above energy levels into equation 3.39:

$$q_{V,i} = \sum_{n=0}^{\infty} \exp\left(-\frac{\left(n + \frac{1}{2}\right) h \nu_i}{k_B T}\right) \quad (3.46)$$

Due to the quantum number taking integer values, the above is a geometric series, and, given that the argument of the exponent will always be less than or equal to zero, the infinite geometric series may be simplified to:

$$q_{V,i} = \frac{\exp\left(-\frac{h\nu_i}{2k_B T}\right)}{1 - \exp\left(-\frac{h\nu_i}{k_B T}\right)} \quad (3.47)$$

The number of vibrational modes,  $N_V$  for a polyatomic molecule is equal to the number of vibrational degrees of freedom. For a linear molecule,  $N_V$  is equal to  $3N - 5$ , whereas for a nonlinear molecule,  $N_V$  is equal to  $3N - 6$ , with  $N$  being the number of atoms in the molecule. The total vibrational partition function is then given by the product of all of the individual vibrational partition functions:

$$q_V = \prod_{i=1}^{N_V} q_{V,i} = \prod_{i=1}^{N_V} \frac{\exp\left(-\frac{h\nu_i}{2k_B T}\right)}{1 - \exp\left(-\frac{h\nu_i}{k_B T}\right)} \quad (3.48)$$

This gives the vibrational partition function contribution to the molecular partition function.

### 3.2.1.3 Rotational Partition Function

The rotational energy levels can be derived by solving the Schrödinger equation for a freely rotating molecule and using the concept of a rigid rotor. The solution is different for linear and nonlinear molecules. For a linear molecule, the energy levels are:

$$\epsilon_J^R = \frac{\hbar^2}{2I} J(J+1) \quad J = 0, 1, 2, \dots, \quad (3.49)$$

with  $I$  being the moment of Inertia about a particular axis, and  $J$  is the angular momentum quantum number. The factor  $\frac{\hbar^2}{2I}$  is also known as the rotational constant,  $B$ . Typically, the bonds in a molecule are assumed to be fixed, which means  $B$  is constant. For a non-linear molecule, the rotational energy levels are given by:

### 3 THEORY AND COMPUTATIONAL METHODS

---

$$\epsilon_J^R = \frac{J_x^2}{2I_x} + \frac{J_y^2}{2I_y} + \frac{J_z^2}{2I_z} \quad J_x = J_y = J_z = 0, 1, 2, \dots, \quad (3.50)$$

To derive the rotational partition functions, the above energy levels can be substituted into the partition function equation. The degeneracy of the rotational energy levels,  $g_J$  is given by  $2J + 1$ , and the number of these energy levels must be further scaled by a symmetry factor  $\sigma$ . The rotational symmetry factor is the number of indistinguishable orientations a molecule can adopt when rotated about its centre of mass, and essentially corrects for over-counting states with identical symmetry. Once again, assuming tightly packed energy levels, the partition functions can be computed by an integral, yielding the following:

$$q_R = \frac{2Ik_B T}{\sigma \hbar^2} \quad (3.51)$$

for linear molecules, and:

$$q_R = \frac{(8\pi^3 I_x I_y I_z)^{1/2} (k_B T)^{3/2}}{\sigma \pi \hbar^3} \quad (3.52)$$

for non-linear molecules. Often, a rotational temperature,  $\Theta_{rot,i}$  is defined for convenience:

$$\Theta_{rot,i} = \frac{\hbar^2}{2I_i k_B} \quad i = \{x, y, z\} \quad (3.53)$$

If the temperature is large compared to this rotational temperature, then the assumption of tightly packed energy levels is a reasonable one. This is usually the case and the above expressions for the partition function can then be used.

#### 3.2.1.4 Electronic Partition Function

Unlike the other contributions, there is no simple derivable expression for the electronic energy levels. The electronic energy levels have to be determined by solving the electronic Schrödinger equation (through the methods described in the

previous sections). Once the energy levels are determined, the electronic partition function is of the standard form:

$$q_E = \sum_{n=0}^{\infty} g_n^E \exp\left(-\frac{\epsilon_n^E}{k_B T}\right) \quad (3.54)$$

By convention, the electronic energy levels are computed relative to the ground state energy ( $n = 0$ ), whose energy is therefore taken as zero. Electronic energy levels are usually widely separated, especially compared to translational, vibrational, and rotational energy levels. As a result, the energy gap between the ground state and higher excited states is large enough that the excited state contribution to the electronic partition function is small enough to be neglected:

$$q_E \approx g_0^E \quad (3.55)$$

The ground state degeneracy  $g_0^E$ , is equal to the spin multiplicity, defined as  $2S + 1$  where  $S$  is the spin operator. By this definition, the spin multiplicity is 1 for a singlet spin state (no unpaired electrons), 2 for a doublet spin state (one unpaired electron), and so on. This approximation is usually sufficient, and excited states typically only need to be accounted for at very high temperatures, where the Boltzmann energy,  $k_B T$ , is comparable to the excitation energy required to access the excited state.

### 3.2.1.5 Internal Rotational Partition Function

The previous expressions for the vibrational and rotational partition functions are valid under the RRHO assumptions. Whilst this is often sufficient, more accurate results do require the correction of these partition functions for non-ideal effects. In the case of the vibrational partition function, low frequency modes are not approximated well by the RRHO assumption. Typically, these low frequency modes are better treated by internal rotation partition functions and rotational-vibrational couplings (Pitzer and Gwinn, 1942), which then replace the vibrational partition function for the low frequency mode. The expression for a

### 3 THEORY AND COMPUTATIONAL METHODS

---

hindrance partition function for a 1-D hindered internal rotation was developed by [Pitzer and Gwinn \(1942\)](#):

$$q_H = \sqrt{\frac{I_r k_B T}{2\pi \hbar^2}} \int_0^{\frac{2\pi}{\sigma}} \exp\left(\frac{-V(\theta)}{k_B T}\right) d\theta, \quad (3.56)$$

where  $\theta$  is the torsional dihedral corresponding to the internal rotor,  $V(\theta)$  is the potential energy of the internal rotation,  $\sigma$  is the symmetry number for the rotation, and  $I_r$  is the reduced moment of inertia. Typically, the potential energy is fitted to a Fourier series:

$$V(\theta) = \frac{a_0}{2} + \sum_{i=1}^N \{a_i \cos(i\theta) + b_i \sin(i\theta)\}, \quad (3.57)$$

with  $N$  being the number of expansion terms, and  $a_i$  and  $b_i$  being the Fourier coefficients. In the case of symmetric tops, the Fourier series can be simplified to:

$$V(\theta) = \frac{V_0}{2}(1 - \cos(\sigma\theta)), \quad (3.58)$$

with  $V_0$  as the barrier to the rotation. Typically, to derive the potential energy surface for the rotation, one must run a series of constrained geometry optimisations, where the torsional angle  $\theta$  is fixed to different values that span  $2\pi$ . The energy at each constrained geometry can then be obtained once the optimisation is complete, giving the potential energy surface.

A molecule can have several internal rotors, which if coupled would require simultaneous scanning along all internal rotor angles. This would result in a multi-dimensional potential energy surface, which very quickly becomes computational infeasible to fully represent. As a result, the assumption of uncoupled 1-D rotations is widely adopted, where each torsion potential can be determined individually.

Further approximations are also possible. At very high temperatures, the hindered rotor partition function will approach the free rotor limit:



$$q_F = \frac{1}{\sigma} \sqrt{\frac{I_r k_B T}{2\pi \hbar^2}} \quad (3.59)$$

This expression does not require the determination and fitting of the hindrance potential.

### 3.2.1.6 Anharmonic Partition Function

The assumption of harmonic frequencies in the harmonic oscillator function can also lead to significant errors in the vibrational partition function and the zero point energy. This can be due to anharmonic effects being neglected, which can cause errors as high as a factor of four (Bross et al., 2019). Typically, the anharmonic correction is expressed as a multiplier to the RRHO partition function:

$$q = f_{\text{vib}} q_{\text{RRHO}} \quad (3.60)$$

The correction factor  $f_{\text{vib}}$  can be derived by several methods. Most modern quantum chemistry codes can compute anharmonic effects using second order vibrational perturbation theory (VPT2) (Nielsen, 1951). The correction of the partition function and zero-point energy based on these anharmonic effects can be performed in several ways. One such approach adopted in Multiwell is to use the anharmonic coefficient matrix,  $X_{ij}$ , which can be derived from experiments or VPT2 results (Barker et al., 2017b). The anharmonic coefficient matrix  $X_{ij}$  contains the results the anharmonic contribution of frequency  $i$  to frequency  $j$ . If separable degrees of freedom are assumed, the anharmonic coefficient matrix is diagonal and reducible to just  $X_i$ . With this, the vibrational energy levels are corrected to:

$$\epsilon_{n,anh}^V = \left(n + \frac{1}{2}\right) h\nu_i + X_i \left(n + \frac{1}{2}\right)^2 h\nu_i \quad n = 0, 1, 2, \dots, \quad (3.61)$$

The higher order term is the result of the perturbational approach, and is also non-zero at quantum number 0, thereby introducing an additional term into the

### 3 THEORY AND COMPUTATIONAL METHODS

---

zero-point energy. Substitution of the corrected energy terms into the expression for the partition function gives:

$$q_{V,anh,i} = \sum_{n=0}^{\infty} \exp\left(-\frac{(n + \frac{1}{2})h\nu_i + X_i(n + \frac{1}{2})^2 h\nu_i}{k_B T}\right) \quad (3.62)$$

As this is no longer a simple geometric series, the expression cannot be simplified in the same way as before, but the total anharmonic vibration partition function is still given by the products of the individual vibration partition functions :

$$q_{V,anh} = \prod_{i=1}^{N_V} q_{V,anh,i} = \prod_{i=1}^{N_V} \sum_{n=0}^{\infty} \exp\left(-\frac{(n + \frac{1}{2})h\nu_i + X_i(n + \frac{1}{2})^2 h\nu_i}{k_B T}\right) \quad (3.63)$$

This enables the computation of a partition function that incorporates anharmonic corrections.

#### 3.2.2 Deriving thermodynamic properties from the partition functions

In the previous subsection, the molecular partition function was derived. However, this is for an individual particle, whereas a system will have an ensemble of particles. In the case of a monatomic gas, the system is one consisting of  $N$  different indistinguishable particles, where each particle will have the same partition function as before. The global partition function,  $Q$  is thus given by:

$$Q(V, T, N) = \frac{q^N(V, T)}{N!} \quad (3.64)$$

This is effectively the product of the individual partition functions,  $q$ , with the factor of  $N!$  being a combinatorial correction to ensure that identical states where any indistinguishable particles are swapped are not over-counted. Thermodynamic properties, such as the heat capacities,  $C_p$  and  $C_v$ , entropy,  $S$ , absolute enthalpy,  $H$ , and Gibbs free energy,  $G$ , can be computed in terms of the partition functions and its derivatives, in conjunction with Stirling's approximation. The expressions are:

### 3.2 Statistical Thermodynamics

---

$$S = k_B T \left( \frac{\partial \ln Q}{\partial T} \right)_{N,V} + k_B \ln Q = N k_B \left[ \frac{\partial (T \ln q)}{\partial T} - \ln N + 1 \right] \quad (3.65)$$

$$C_v = N k_B T \left( \frac{\partial^2 (T \ln q)}{\partial T^2} \right) \quad (3.66)$$

$$C_p = C_v + N k_B \quad (3.67)$$

$$\Delta H(T) = \int_0^T C_p dT = \frac{N k_B T^2}{q} \left( \frac{\partial q}{\partial T} \right) + N k_B T \quad (3.68)$$

$$G = H - TS \quad (3.69)$$

$$U = k_B T^2 \left( \frac{\partial (\ln q)}{\partial T} \right) \quad (3.70)$$

$$A = U - TS \quad (3.71)$$

Molar thermodynamic properties are widely used, in which case the number of particles  $N$  is equal to the Avogadro's constant  $N_A$ .

It is also possible to relate the equilibrium constant,  $K$  of a reaction to the partition functions of the participating species. This will be illustrated for a gas-phase reaction. First, the standard molar Gibbs free energy,  $G_m^\circ(T)$ , can be computed in terms of the standard molar partition function,  $q_m^\circ$  as follows:

$$G_m^\circ(T) = G_m^\circ(0) - RT \ln \frac{q_m^\circ}{N_A} \quad (3.72)$$

The Gibbs Free energy of reaction and the equilibrium constant,  $K$ , are related by the expression:

$$\Delta G_r = -RT \ln K \quad (3.73)$$

### 3 THEORY AND COMPUTATIONAL METHODS

---

If one considers a generic reaction:



The change in Gibbs Free energy for this reaction is given by:

$$\Delta G_r = cG_{c,m}^\circ(T) + dG_{d,m}^\circ(T) - aG_{a,m}^\circ(T) - bG_{b,m}^\circ(T) \quad (3.75)$$

$$= cG_{c,m}^\circ(0) + dG_{d,m}^\circ(0) - aG_{a,m}^\circ(0) - bG_{b,m}^\circ(0) \quad (3.76)$$

$$- RT \left[ c \ln \frac{q_{c,m}^\circ}{N_A} + d \ln \frac{q_{d,m}^\circ}{N_A} - a \ln \frac{q_{a,m}^\circ}{N_A} + b \ln \frac{q_{b,m}^\circ}{N_A} \right] \quad (3.77)$$

The first term,  $cG_{c,m}^\circ(0) + dG_{d,m}^\circ(0) - aG_{a,m}^\circ(0) - bG_{b,m}^\circ(0)$ , is the difference in ground state energies between the products and reactants, and is essentially the 0 K correction term. Calling this  $\Delta_r E_0$  and manipulating the logarithms allows the equilibrium constant to be derived as:

$$K = \frac{(q_{C,m}/N_A)^c (q_{D,m}/N_A)^d}{(q_{A,m}/N_A)^a (q_{B,m}/N_A)^b} \exp\left(\frac{-\Delta_r E_0}{RT}\right) \quad (3.78)$$

### 3.3 Transition State Theory

Transition state theory (TST) is a widely popular and powerful methodology to estimate rate parameters of elementary chemical reactions from properties derived using first-principle calculations. Originally developed by [Eyring \(1935\)](#) based on steady-state analyses, various forms of TST have been developed for the application of computing rate constants for different reactions under certain assumptions. Several detailed publications of the development and application transition state theory are available ([Evans and Polanyi, 1935](#); [Laidler and King, 1983](#); [Truhlar et al., 1996](#)), so only a brief summary is provided here.

Transition state theory relies on the concepts of a phase space, which consists of all positions and momenta of the molecular system. Any molecular state is

defined by a point on this phase space. This allows an elementary reaction to essentially be defined as a trajectory which starts in the reactants region of the phase space and moves towards the products region of the phase space. One of the key assumptions of TST is that the reactant region and the product region are separated by the dividing surface, which in TST is known as the transition state. Locating and describing the properties of the dividing surface is essential to the TST framework.

It is also assumed that a trajectory which starts from the reactants and crosses this dividing surface will either thermalise or reach the product state and not re-approach the dividing surface. This is deemed the no recrossing assumption, in which the transition state is the critical point of the reaction after which products will form. In reality, re-crossing occurs and so the reactive flux is overestimated by TST. As a consequence, when using TST, great care is taken into finding a dividing surface that minimises the reactive flux.

Other assumptions made by TST include the assumption that the reactants are in equilibrium, either on a fixed-temperature basis which is deemed canonical TST, or on a fixed-energy basis which is deemed microcanonical TST. Finally, it is also assumed that the electron dynamics during the transition from the reactant space to product space is much faster than nuclear dynamics during the same transition, which is again the Born-Oppenheimer approximation and means branching of the potential energy surface due to non-adiabatic effects may be neglected. With these approximations, the molecular properties of reactants and transition states may be used to compute rate constants using TST for different ensembles.

#### 3.3.1 Canonical Transition State Theory

In canonical transition state theory, (CTST), the dividing surface is varied such that the reactive flux is minimised at a given temperature. The rate constant for the reaction corresponding to the trajectory and dividing surface in question is given by the following expression:

$$k(T) = \frac{k_B T}{h} \frac{q^\ddagger(\mathbf{v} \neq \mathbf{v}^\ddagger)}{q^R} \exp\left(-\frac{E_0^\ddagger}{k_B T}\right), \quad (3.79)$$

### 3 THEORY AND COMPUTATIONAL METHODS

---

where  $k(T)$  is the rate constant as a function of temperature,  $q^\ddagger$  and  $q^R$  are the partition functions of the transition state and the reactants, and  $E_0^\ddagger$  is the threshold energy, defined as the difference in the ground state electronic energy between the transition state and the reactants at 0 K. The  $(\nu \neq \nu^\ddagger)$  denotes that when computing the partition function for the transition state, the transition state's imaginary vibrational frequency,  $\nu^\ddagger$ , is excluded from the transition state's vibrational partition function as it corresponds to the motion along the reaction coordinate that characterizes the transition state. For simplicity, just  $q^\ddagger$  is used to represent the partition function of the transition state in subsequent statements of transition state theory. This expression corresponds to having a single dividing surface at the given temperature, namely the transition state, and deriving the reactive flux from the ratio of accessible states of the transition state to the accessible states of the reactants at said temperature. This does assume that there is a singular transition state for all possible energies, and the use of partition functions also assumes that the underlying distribution of energy states is that of a Boltzmann distribution.

The above expression is often corrected for several factors, including quantum mechanical tunneling, symmetry factors of the reaction, and the presence of optical isomers. With these corrections, a more typical expression for the rate constant from CTST is given by:

$$k(T) = \kappa \frac{k_B T}{h} \frac{\sigma^\ddagger}{\sigma^R} \frac{m^R}{m^\ddagger} \frac{q^\ddagger(\nu \neq \nu^\ddagger)}{q^R} \exp\left(-\frac{E_0^\ddagger}{k_B T}\right), \quad (3.80)$$

where  $\kappa$  is the tunneling correction factor,  $\sigma^\ddagger$  and  $\sigma^R$  are the external symmetry factors of the transition state and reactants, and  $m^\ddagger$  and  $m^R$  are the number of optical isomers of the reactants and products.

#### 3.3.2 Microcanonical Transition State Theory

In microcanonical transition state theory, ( $\mu$ TST), the dividing surface is varied such that the reactive flux is minimised at a given energy. The rate constant in the microcanonical ensemble is given by the Rice-Ramsperger-Kassel-Marcus

(RRKM) theory expression (Rice and Ramsperger, 1927; Kassel, 1928; Marcus, 1952):

$$k(E) = \frac{N^\ddagger(E - E_0)}{h\rho_R(E)}, \quad (3.81)$$

where  $k(E)$  is now the rate constant as a function of energy,  $N^\ddagger(E - E_0)$  is the number of states of the dividing surface with energy less than the threshold energy  $E_0$ , and  $\rho_R(E)$  is the density of states (number of states per unit energy) of the reactants. These quantities are typically computed by using inverse Laplace transforms of the corresponding partition functions or by direct counting algorithms. The thermal rate constant,  $k(T)$  is then found by averaging  $k(E)$  over an energy distribution.

The microcanonical formulation of TST has several advantages. The thermal rate constants can be averaged over any energy distribution, not just the Boltzmann distribution. The computed rate constants are also more accurate, as there is more control and refinement over the position of the dividing surface. Furthermore, the microcanonical treatment also allows consideration of a distribution of angular momenta, where some energy states are not allowed due to angular momentum restrictions. This is often called  $J$ -resolved microcanonical TST, where the rate is now given by:

$$k(E, J) = \frac{N^\ddagger(E - E_{0,J}, J)}{h\rho_R(E, J)} \quad (3.82)$$

Resolution of the rate constants at the energy level also enable consideration of collisional effects, which are key to describing pressure dependent unimolecular reactions, and considerations of angular momentum are often important for computing the rates of barrierless reactions.

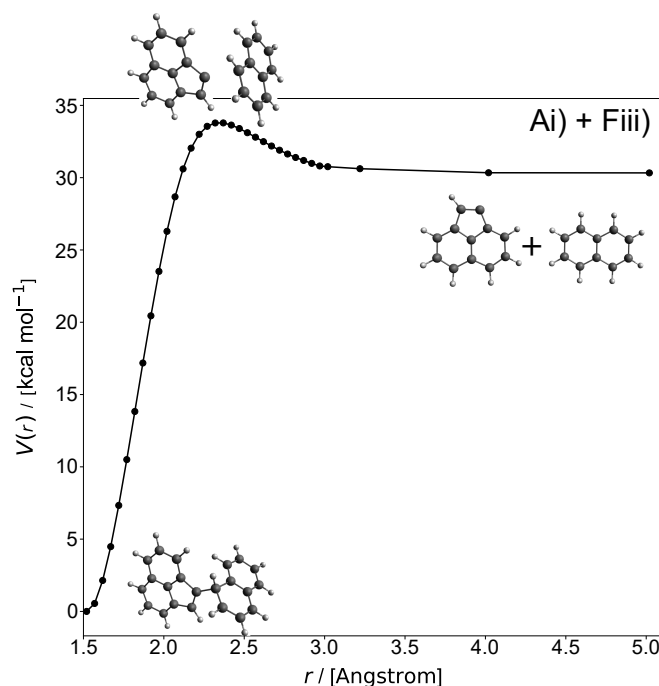
#### 3.3.3 Reactions with Barriers

Figure 3.1 shows an illustrative one-dimensional potential energy surface of a reaction containing a barrier, with the reaction coordinate taken as the bond length.

### 3 THEORY AND COMPUTATIONAL METHODS

---

In actuality, a potential energy surface is a multi-dimensional surface with several reaction coordinates, but a simplified treatment using one reaction coordinate is frequently adopted.



**Figure 3.1:** Sample 1-D potential energy surface for an aromatic decomposition reaction with a barrier.

There exists a maximum (saddle point in the multi-dimensional potential energy surface) of the barrier that is higher in energy than both the reactants and products. This configuration is the transition state geometry of the reaction. Since this transition state exists along the minimum energy pathway, computing the rate constant via TST is straightforwardly done by setting the position of the dividing surface to correspond to the transition state position. This is valid as the energetic barrier present means that the reactive flux is going to be much lower at this geometry than other positions along the pathway. Typically, the transition state geometry for such reactions is similar to the reactants, with most bond lengths and angles being within the standard values aside from the key one, in this case the distance between the two fragments of the aromatic molecule. As a consequence, this inter-fragment distance is taken as the reaction coordinate. The existence of



such a transition state is typically referred to as a "tight" transition state. In reality, the exact position of the minimal rate dividing surface may not be exactly at the position of the transition state, and varies with temperature and energy. These effects can be taken into account with variational transition state theory, discussed later, but can be safely neglected for "tight" transition states with sufficiently high barriers.

### 3.3.4 Barrierless Reactions

Figure 3.2 shows an illustrative potential energy surface of a reaction without a barrier.

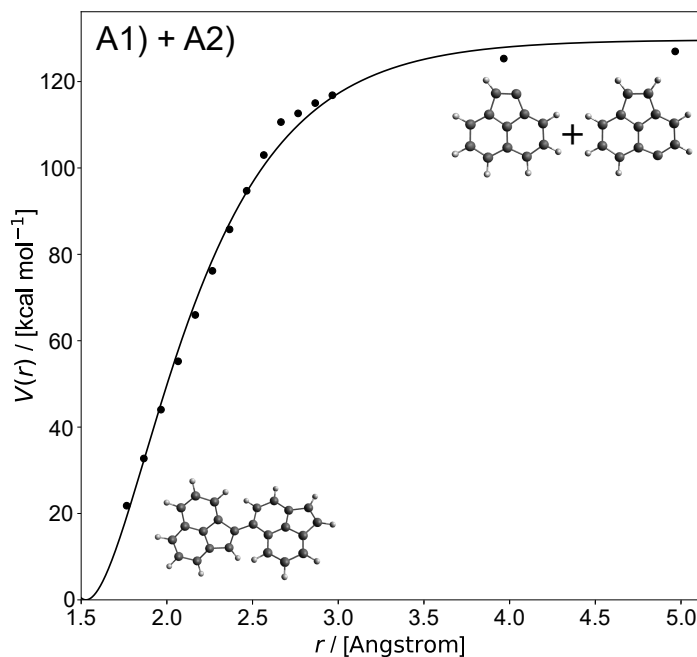


**Figure 3.2:** Sample potential energy surface for a barrierless aromatic decomposition reaction.

Reactions such as unimolecular decomposition or radical-radical recombination are quite frequently barrierless, showing no clear saddle point along the minimal energy pathway. This makes computing the rate constant using TST significantly more challenging, as the dividing surface can no longer simply be placed at the top of the barrier when there is none. Barrierless reactions are usually treated

### 3 THEORY AND COMPUTATIONAL METHODS

---

with a variational approach (Bao and Truhlar, 2017), which varies the position of the dividing surface to locate the position that minimises the reactive flux as required. This is known as Variational Transition State Theory (VTST). Typically, the position of the dividing surfaces results in large separations between the reactants, with this being temperature and energy dependent as well. This is typically referred to as a "loose" transition state to indicate that the position of the dividing surface moves. As a result, several approximations are made regarding the partition functions and states of these loose transition states.

#### 3.3.4.1 Variational Transition State Theory

As mentioned, variational transition state theory is typically used for reactions without a tight transition state, or barrierless reactions. Like TST, VTST also has canonical and microcanonical forms. In canonical variational transition state theory (CVTST), one computes the rate constant for several trial dividing surfaces using canonical TST. The expression for the trial rate constants is the same as before, and can be written as a function of the position of the dividing surface,  $s$

$$k_{\text{trial}}^{\text{CVTST}}(T, s) = \frac{k_B T}{h} \frac{q_{\text{trial}}^\ddagger(s)}{q^R} \exp\left(-\frac{V_{\text{trial}}^\ddagger(s)}{k_B T}\right), \quad (3.83)$$

with  $q_{\text{trial}}^\ddagger(s)$  and  $V_{\text{trial}}^\ddagger(s)$  being the partition function and ground state energy relative to the reactants at the position of the trial dividing surface  $s$ . As explained, the actual rate constant from CVTST will minimise the reactive flux:

$$k^{\text{CVTST}}(T) = \min_s \{k_{\text{trial}}^{\text{CVTST}}(T, s)\}, \quad (3.84)$$

such that if the minimum is at  $s = s^*$ , the rate constant computed by CVTST is given by:

$$k^{\text{CVTST}}(T) = \frac{k_B T}{h} \frac{q^\ddagger(s = s^*)}{q^R} \exp\left(-\frac{V^\ddagger(s = s^*)}{k_B T}\right) \quad (3.85)$$

Similarly, in microcanonical VTST ( $\mu$ VTST), the rate constant is a function of the

energy and the trial position:

$$k_{\text{trial}}^{\mu\text{VTST}}(E, s) = \frac{N_{\text{trial}}^{\ddagger}(E - E_0, s)}{h\rho_R(E)} \quad (3.86)$$

If one is resolving the rate constant at the angular momentum level, then typically, the rate constant is averaged over the angular momentum first, before minimising the energy-resolved rate constant as with CVTST:

$$k^{\mu\text{VTST}}(E) = \min_s \{k_{\text{trial}}^{\mu\text{VTST}}(E, s)\} \quad (3.87)$$

To obtain the thermal rate constant, one needs to average over the distribution of energy as with  $\mu\text{TST}$ .

#### 3.3.4.2 Other methods

Other theoretical frameworks other than VTST are also commonly applied to compute rate constants for barrierless reactions. A much simpler approach than VTST is the Gorin Model ([Gilbert and Smith, 1990](#)), whilst some reactions require more advanced frameworks than VTST, such as variable-reaction-coordinate transition state theory (VRC-TST) ([Klippenstein, 1991](#); [Georgievskii and Klippenstein, 2003](#); [Klippenstein et al., 2006](#)).

In the Gorin Model, the conserved (vibrational) modes of motion of the transition state are taken as those of the separated fragments or reactants, and are assumed to be constant along the potential energy surface of the reaction. The transitional (rotational and translational) modes of motion corresponding to the transition between reactants and products are approximated by free or sinusoidally hindered rotations, and the interaction potential between the fragments is usually approximated as a Morse potential. These approximations make computing the rate constant in a Gorin Model framework much simpler, as the partition functions and modes of vibration can be computed using standard expressions and, aside from the mode of transition, do not change as a function of the position of the dividing surface. This means the Gorin Model can be very useful for quick

### 3 THEORY AND COMPUTATIONAL METHODS

---

estimates of rate constants, but they can result in substantial overestimates due to the inherent assumptions.

In VRC-TST, the reactive flux is also minimised with respect to a set of dividing surfaces along the reaction coordinate, but the definition of the reaction coordinate is much more flexible. The reaction coordinate is representative of the separation between the reacting fragments, but the pivot points for the dividing surfaces can be placed at the centre of mass between the reacting fragments, or along the bond length of the breaking bond, or often a combination of both. This flexible definition of the reaction coordinate allows greater accuracy in describing the potential energy surface of the reaction and improves the computed rate constants. The modes and states of the dividing surfaces are computed using direct counting algorithms for the vibrational modes and Monte-Carlo evaluation of phase space integrals for the rotational and translational modes. The rate constant is then given by optimizing the position and relative separation of the pivots.

#### 3.3.5 Tunneling Corrections

As mentioned previously, when computing rate constants using TST, a tunneling correction factor has to be applied to the rate constants, as represented by the transmission coefficient  $\kappa$ . The tunneling correction is a quantum mechanical effect. Classically, particles with an energy below a potential barrier would be reflected, meaning reactants with energies lower than the barrier height cannot reach the products region. However, quantum mechanically, there is a non-zero probability that a particle with lower energy than the barrier could tunnel through said barrier. This effect can be significant particularly for small atom transfer reactions, and is not accounted for in transition state theory as the Born-Oppenheimer approximation neglects the kinetic energy of nuclei. As a consequence, the rate constant must be increased to account for quantum mechanical effects enabling reactants to form products even when their energy is lower than the barrier height. To derive the correction factor due to tunneling, one assumes a shape for the potential,  $V(x)$ , and then solves the one-dimensional, time-independent Schrödinger Equation for a particle with this potential:

### 3.3 Transition State Theory

---

$$-\frac{\hbar}{2m} \frac{d^2}{dx^2} \psi(x) + V(x)\psi(x) = E\psi(x) \quad (3.88)$$

One of the most popular tunneling corrections is the Wigner tunneling correction (Wigner, 1932). This assumes a parabolic form for the potential  $V(x)$ , and whilst the one-dimensional Schrödinger Equation is not analytically solvable, a perturbative expansion enables the tunneling correction factor to be approximately derived as:

$$\kappa_W = 1 - \frac{1}{24} \left( \frac{\hbar |\nu^\ddagger|}{k_B T} \right)^2 \quad (3.89)$$

with  $\nu^\ddagger$  being the magnitude of the imaginary frequency of the transition state. The Wigner correction is the first correction term in the perturbative expansion, and as a result is only valid for small tunneling corrections (Bell, 1959). Nevertheless, its simplicity in evaluation makes it easy to apply as a first estimate.

Another very popular tunneling correction is the Eckart tunneling correction (Truhlar and Kuppermann, 1971). In this case, the potential is given by:

$$V(x) = -\frac{\hbar}{2m} \left[ \frac{A \exp(x)}{1 + \exp(x)} + \frac{B \exp(x)}{(1 + \exp(x))^2} \right], \quad (3.90)$$

with  $A$  and  $B$  being parameters. If  $A$  is zero, the potential is the symmetric Eckart potential, and if  $A$  is non-zero, the potential is the asymmetric Eckart potential. In this case, the one-dimensional Schrödinger Equation is analytically solvable, and the microcanonical correction factor can be derived as:

### 3 THEORY AND COMPUTATIONAL METHODS

---

$$\kappa_E(E) = 1 - \frac{\cosh(2\pi a - 2\pi b) + \cosh(2\pi d)}{\cosh(2\pi a + 2\pi b) + \cosh(2\pi d)} \quad (3.91)$$

$$2\pi a = \frac{2\sqrt{\alpha_1 \xi}}{\alpha_1^{-1/2} + \alpha_2^{-1/2}} \quad (3.92)$$

$$2\pi b = \frac{2\sqrt{|(\xi - 1)\alpha_1 + \alpha_2|}}{\alpha_1^{-1/2} + \alpha_2^{-1/2}} \quad (3.93)$$

$$2\pi d = 2\sqrt{\left|\alpha_1 \alpha_2 - \frac{4\pi^2}{16}\right|} \quad (3.94)$$

$$\alpha_1 = 2\pi \frac{W_1^\ddagger}{h\nu^\ddagger} \quad (3.95)$$

$$\alpha_2 = 2\pi \frac{W_2^\ddagger}{h\nu^\ddagger} \quad (3.96)$$

$$\xi = \frac{E}{W_1}, \quad (3.97)$$

with  $W_1$  and  $W_2$  being the threshold energies for the reactants and products, respectively. Retrieving the thermal tunneling correction factor requires an integral over the energy distribution:

$$\kappa_E(T) = \exp\left(\frac{W_1^\ddagger}{k_B T}\right) \int_0^\infty \kappa_E(E) \exp\left(-\frac{E}{k_B T}\right) dE \quad (3.98)$$

The Eckart correction is generally a better approximation than the Wigner correction, as it includes information on the reactants, transition state, and products in the computation. However, for small tunneling corrections, the Eckart and Wigner corrections yield very similar results. This is typically the case for reactions with very large barriers, and at higher temperatures.

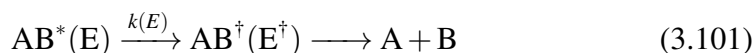
#### 3.3.6 Pressure Dependence

The previously discussed approaches can be used to compute rates in the high-pressure limit. However, in the case of unimolecular reactions, the molecule typically needs to be ‘activated’ by collisions with a third-body species. In this case, the rate constant is dependent on the concentration of these

### 3.3 Transition State Theory

---

colliders, and hence the pressure of the system. As a consequence, bimolecular recombination reactions are often also pressure-dependent as reverse reactions of unimolecular decomposition reactions. Several different methodologies to treat pressure dependence exist, ranging from the simple Lindemann and Lindemann-Hinshelwood theories to full Master Equation simulations (Miller et al., 2000; Miller and Klippenstein, 2000, 2006). A popular framework is to apply RRKM theory to compute pressure dependent rate constants of unimolecular decompositions. In this schematic, a molecule is first activated by collisions with a third-body species, and then forms a complex, before decomposing to form the product:



In this case,  $dk_a$  is the rate of activation due to collision with a third body, and  $\omega$  is the collision frequency. Assuming that the activated molecule,  $AB^*$  is in steady state, one can derive its concentration as:

$$[AB^*(E)] = \frac{dk_a(E)/\omega}{1 + k(E)/\omega} [AB] \quad (3.102)$$

The ratio  $dk_a(E)/\omega$  is essentially the equilibrium constant of the activation energy, and can be thought of as the probability distribution of energy transfer within the energy range of  $E$  to  $E + dE$ :

$$dk_a(E)/\omega = P(E)dE \quad (3.103)$$

The microcanonical rate constant for the decomposition is given by  $k(E)[AB^*(E)]$ . The pressure-dependent, thermal RRKM rate constant for the decomposition is given by substituting the expression for  $dk_a(E)/\omega$  into the expression for  $[AB^*(E)]$  and then integrating over all possible energy levels:

### 3 THEORY AND COMPUTATIONAL METHODS

---

$$k_{uni}(T, P) = \int_0^{\infty} \frac{k(E)P(E)dE}{1 + k(E)/\omega} \quad (3.104)$$

The pressure dependence is captured in the collision frequency  $\omega$ .  $\omega$  is computed from:

$$\omega = k_{coll}[M] \quad (3.105)$$

Where  $k_{coll}$  is the collision rate, and is typically computed from collisions of Lennard-Jones particles.

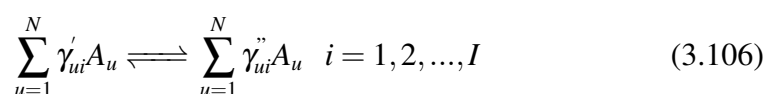
This approach is sufficient provided the reaction has sufficiently strong collisions and an energy barrier. For multi-channel and low-barrier reactions, it is necessary to use the master equation approach, where the interactions between several energy-dependent collisional energy transfers and energy-dependent chemical reactions are treated and used to derive phenomenological rate constants.

## 3.4 Kinetic Simulations and Sensitivity Analysis

Kinetic simulations are useful tools that enable the analysis of reaction mechanisms under different conditions such as temperature, pressure, and reactor volume. They can give insight into which reactions and chemical species are preferred in a mechanism under given conditions. Additionally, a sensitivity analysis can be used to identify the response of the concentration of key species to rate constant parameters.

### 3.4.1 Kinetic Simulations

Kinetic simulations essentially solve the chemical reactions defined in a given mechanism. A set of chemical reactions can be denoted as follows ([Leon et al., 2019](#)):





### 3.4 Kinetic Simulations and Sensitivity Analysis

---

where  $A_u$  are the chemical species involved in the reaction,  $\gamma'_{ui}$  and  $\gamma''_{ui}$  are the forward and reverse stoichiometric coefficients of species  $u$  participating in reaction  $i$ ,  $N$  is the number of species participating in reaction  $i$ , and  $I$  is the total number of reactions.

The rate of progress,  $z_i$  of reaction  $i$  is then given by:

$$z_i = k_i \prod_{j=1}^N c_j^{\gamma'_{ji}} - \frac{k_i}{K_{ci}} \prod_{j=1}^N c_j^{\gamma''_{ji}}, \quad (3.107)$$

with  $k_i$  being the forward rate constant of reaction  $i$ , and  $K_{ci}$  is the equilibrium constant for reaction  $i$  and  $c_j$  is the concentration of species  $j$ . Using the progress variable, the net production rate of species  $u$  is given by:

$$\dot{\omega}_u = \sum_{i=1}^I (\gamma''_{ui} - \gamma'_{ui}) z_i \quad (3.108)$$

Substitution of 3.107 into 3.108 yields:

$$\dot{\omega}_u = \sum_{i=1}^I \left( k_i \prod_{j=1}^N \gamma''_{uj} c_j^{\gamma'_{ji}} + \gamma'_{ui} \frac{k_i}{K_{ci}} \prod_{j=1}^N c_j^{\gamma''_{ji}} \right) \quad (3.109)$$

$$- \sum_{i=1}^I \left( k_i \prod_{j=1}^N \gamma'_{uj} c_j^{\gamma'_{ji}} + \gamma''_{ui} \frac{k_i}{K_{ci}} \prod_{j=1}^N c_j^{\gamma''_{ji}} \right) \quad (3.110)$$

The first and second terms in parentheses correspond to the generation and loss of species  $u$ , respectively. Reaction mechanisms are typically constructed in terms of elementary reactions, in which case most reactions will be first order with respect to all participating species. The expression for  $\dot{\omega}_u$  can be rearranged to give:

$$\dot{\omega}_u = G_u - L_u c_u \quad (3.111)$$

This work uses constant volume, constant-temperature, simulations in a 0D homogeneous reactor. In this case, a mass-balance gives the kinetic equations

### 3 THEORY AND COMPUTATIONAL METHODS

---

to be solved for the simulation:

$$\frac{dc_u}{dt} = \dot{\omega}_u = G_u - L_u c_u \quad (3.112)$$

#### 3.4.2 Sensitivity Analysis

The impact of the model parameters on key response variables are commonly assessed using a sensitivity analysis ([Warnatz and Dibble, 2006](#)). It tracks the response of the key outputs of a given model to the parameters used in said model. When applied to kinetic simulations, it is frequently used to see how the concentrations of the species of interest in the mechanism are impacted by the rate constants of the reactions. The sensitivity analysis enables the identification of reactions that need particular attention to achieve a high quality model. These reactions will thus need their rate constants determined with the highest level of accuracy and certainty, as they have the biggest impact on the results.

In the case of kinetic simulations, the normalised sensitivity coefficient is usually computed as:

$$S_{ki}(t) = \frac{X_i}{Y_k} \frac{\partial Y_k(t)}{\partial X_i}, \quad (3.113)$$

where  $S_{ki}$  is the sensitivity of response  $Y_k$  to a change in variable  $X_i$ . To compute sensitivities to rate constants, the rate-constant typically has a multiplier applied to either increase or decrease the constant. As noted above, these normalised sensitivity coefficients are a function of time. To remove the time dependence, one can use the maximum sensitivity coefficient, or the steady state sensitivity coefficient. In this work, these two definitions coincided, and so the time independent sensitivity coefficient is given by:

$$S_{ki} = \max_t \{S_{ki}(t)\} \quad (3.114)$$

## Chapter 4

# Optical band gap of cross-linked, curved, and radical polyaromatic hydrocarbons

*In this chapter, the optical band gaps (OBGs) of polycyclic aromatic hydrocarbons (PAHs) crosslinked via an aryl bond, curved via pentagon integration and with radical character are computed using density functional theory. Pericondensed aromatics with different symmetries are calculated providing new scaling relationships. Crosslinks are observed to cause a small decrease in the OBGs of the monomers, saturating after 3–4 crosslinks. Curvature in PAHs is shown to increase the optical band gap due to the resulting change in hybridisation of the system, but this increase saturated at larger sizes. The effect of  $\sigma$ -radicals on the optical band gap was also shown to be negligible, however,  $\pi$ -radicals were found to decrease the band gap by  $\sim 0.5$  eV. These findings are discussed in the context of understanding the molecular species involved in soot formation.*

### Collaborative Contributions

The work presented in this chapter has been published in *Physical Chemistry Chemical Physics* and includes contributions from co-authors. Jochen Dreyer performed the UV/Visible spectroscopy measurements with the author. Jacob Martin assisted in analysis of the results. The other authors helped edit the manuscript. The DFT calculations, figure preparation, and writing of the manuscript were done by the author.

### 4.1 Introduction

The difficulty of modelling inception and gas-phase chemistry necessitates the use of diagnostic techniques to determine what polycyclic aromatic hydrocarbons (PAHs) may be involved in particulate formation. One property of particular interest for PAHs is the optical band gap (OBG). Previous studies reported the OBG at different positions within flames by using laser extinction and the Tauc method (Tauc et al., 1966). D'Alessio et al. (1996) assumed an indirect electron transition and observed a range of OBGs in their benzene/air flames depending on whether the flame was non-sooting (3 eV – 4.6 eV), nearly-sooting (1 eV – 5 eV) or sooting (0.6 eV – 1 eV). Adkins and Miller (2015) performed a similar study on a diluted ethylene/N<sub>2</sub>/air flame but found a much smaller OBG range of 1.85 – 2.35 eV while assuming that the extinction corresponded to a direct transition. A similar OBG range of 1.7 – 2.4 eV was found by Botero et al. (2016a) for sooting n-heptane/toluene flames, again assuming a direct transition.

Once the OBGs inside a flame are known, the challenge is to correlate the measured values to specific PAH structures present in both soot and the gas phase. Robertson and O'Reilly (1987) have found that sp<sup>2</sup> carbon systems, such as soot, have their electronic properties governed by  $\pi - \pi^*$  interactions such as those in PAHs. Therefore, OBGs measured in flames should be indicative of PAHs. Robertson and O'Reilly (1987) used Hückel molecular orbital theory calculations and showed that the OBG scales with  $M^{-\frac{1}{2}}$ , where  $M$  is the number of aromatic rings in the carbon system for clusters of diamond-like-carbon. Adkins and Miller then performed density functional theory (DFT) calculations to obtain

the OBG of moderately-sized peri-condensed PAHs in the  $D_{2h}$  point group, by approximating the OBG as the energy between the highest occupied molecular orbital (HOMO) and lowest unoccupied molecular orbital (LUMO) transition (Adkins and Miller, 2015). These results were correlated to OBG measurements in a diluted ethylene/ $N_2$ /air flame, indicating peri-condensed PAHs comprised of 10–20 rings. This is in agreement with simulations performed by Yapp et al. (2016) on the same flame, using a stochastic population balance model to resolve the PAHs in the gas phase and soot. An OBG profile was calculated based on the obtained PAH compositions, and a comparison to experiments and HRTEM images obtained by Botero et al. (2016a) suggested that the smallest peri-condensed PAHs contributing to the OBG consist of 16 rings.

However, more complex structures such as curved and cross-linked PAHs as well as PAHs containing aliphatic side-chains might be present in flames. In a further study, Adkins and Miller (2017) computed the OBG of several hundred PAHs of different topologies using time-dependent density functional theory (TD-DFT), including different benzenoid PAHs, acenes and structures with pentagonal rings. The calculated OBGs of these species were correlated with the number of rings for a more comprehensive OBG taxonomy of PAHs. For the curved PAHs, they found that curvature increases the OBG due to  $\sigma$  interactions, but this was secondary to molecular size effects from the number of rings. A direct quantification of how the curvature impacts the OBG was not made. Reports that include OBGs of cross-linked PAHs are even scarcer, being limited to mainly asphaltene structures (Ruiz-Morales, 2002). The aforementioned studies were also primarily limited to closed-shell PAHs, whereas there has been recent interest in radical PAHs, especially resonance stabilised or  $\pi$ -radical PAHs and their role in soot formation (Johansson et al., 2018).

Even though the understanding of the correlation between PAH size, structure and OBG has advanced substantially, it was primarily based on computational studies. Previously, TD-DFT calculations have used the B3LYP functional due to its widespread applicability, but the accuracy of B3LYP and other functionals has not been explored for PAHs.

**The purpose of this chapter** is twofold. First, experimental UV-visible

spectroscopy OBG measurements of a selection of small PAHs are used to evaluate the performance of DFT calculations with different functionals in predicting the OBG of PAHs. The selected experimental test set PAHs have different structures, including cross-links, peri-condensed species, acenes, and species with pentagonal rings, to represent some of the main PAH classes potentially involved in soot formation. The different hybrid functionals were benchmarked against the experimental results to identify the most suitable one. Second, the best performing functional was used to elucidate the effect of various PAH characteristics, such as size and symmetry, cross-linking by aliphatic bond formation, curvature, and radical character on their OBG.

## 4.2 Materials and Methods

### 4.2.1 Ultraviolet-visible spectroscopy

The optical band gap of 18 different small PAHs and benzene were measured by means of ultraviolet-visible (UV-Vis) spectroscopy. These were chosen to represent a range of structures, namely peri-condensed (benzene to perylene), linear acenes (benzene to tetracene), cross-linked (phenyls) and pentagon-containing PAHs (fluorene and acenaphthylene).

UV-Vis absorption spectra of PAHs dissolved in cyclohexane were recorded. Cyclohexane was chosen as it is transparent in the wavelength range of interest, is capable of dissolving PAHs and is expected to cause minimal solute-solvent interactions as it is non-polar. The impact of cyclohexane as a solvent on PAH band gap was confirmed to be minimal by performing band gap calculations with cyclohexane as an implicit solvent as discussed in the next section. PAH concentrations of  $10^{-5}$ – $10^{-4}$  M were used to minimise PAH-PAH interactions and to keep the maximum absorbance below 1.5 AU. These low concentrations are used to ensure that the measured absorbance is representative of the PAH and not an aggregated cluster by keeping interactions low. The solution was placed in a quartz cuvette with 1 cm path-length and the sample's UV-Vis spectra were measured between 200–800 nm using an Agilent Cary 8453 spectrometer using a

step size of 0.5 nm with 0.5 s per step. The optical band gap was determined from plots of absorbance vs wavelength using the absorption edge method (Caglar et al., 2007). This method has found wide use in optical characterisation of organic thin films by UV-Vis spectroscopy, such as in Costa et al. (2016).

### 4.2.2 Density Functional Theory

Optimised geometries of the PAHs were determined using the 6-311G(d,p) basis set and the B3LYP hybrid functional. This combination has been shown to provide accurate molecular geometries in other works (Plumley and Dannenberg, 2011). Single point DFT calculations were then performed on these geometries using the same 6-311G(d,p) basis set and different hybrid exchange-correlation functionals. This included widely used hybrid functionals with exact exchange (HSE06, B3LYP, B971, PBE0, and B972), functionals including long-range interaction parameters and dispersion corrections (CAM-B3LYP and  $\omega$ -B97XD) and the Minnesota functional M06. The initial test calculations were performed on naphthalene, biphenyl and fluorene to identify the most suitable functional. These were chosen to cover the flat, cross-linked and pentagonal categories and are economic enough for timely DFT calculations. The theoretical optical band gap is estimated as the HOMO-LUMO gap determined from the single point calculation. This is the result of the ground single point calculation. TD-DFT calculations are used to confirm that the main contribution to the lowest lying excited state is the HOMO-LUMO gap and to compare the electronic structure determined by DFT to more advanced electronic structure calculations. DFT has been used in previous works by Adkins and Miller (2015) to compare to optical absorption measurements in flames. The HOMO-LUMO gap and the onset of optical absorption in PAHs are both determined by the  $\pi - \pi^*$  transition, so it is expected that the DFT calculated HOMO-LUMO gap should correlate with the absorption edge measurements, as suggested in other works (Caglar et al., 2007; Costa et al., 2016). Still, it should be noted that the HOMO-LUMO gap is not an exact estimate of the optical band gap, but using the HOMO-LUMO gap of constituent PAHs to understand the optical absorption measurements of carbon nanomaterials is well established in the combustion community (Robertson and

## 4 CHAPTER 4

---

O'Reilly, 1987; Adkins and Miller, 2015, 2017). It should also be noted that not all states are bright, particularly for the high symmetry PAHs. Still, it should be noted that HOMO-LUMO gaps tend to be an overestimate compared to vertical excitation energies from higher level methods, so these values are an estimate for the optical band gap. With this in mind, the accuracy of the different functionals was quantified by comparing the percentage error between the computed ( $E_{g,DFT}$ ) and experimental OBG ( $E_{g,Exp}$ ):

$$P.E. = \frac{E_{g,DFT} - E_{g,Exp}}{E_{g,Exp}}. \quad (4.1)$$

Once the best functional was identified, the OGBs of some larger, cross-linked, curved, and radical PAHs were also calculated. The cross-linked PAHs consisted of naphthalene, pyrene, coronene and ovalene monomer units connected by aliphatic bonds in para-geometries. To investigate the effect of curvature, constrained geometry optimisations were performed on corannulene, a small, curved molecule with a central pentagonal ring and five outer hexagonal rings. The constrained geometry optimisation fixed the value of the dihedral angles between the pentagonal plane of corannulene and the hexagons beneath, thereby varying the curvature of the corannulene molecule. The impact of the cyclohexane was also briefly considered using the SCRF solvation model for cyclohexane (Tomasi et al., 2005). Compared with the vacuum calculations the resulting HOMO-LUMO gaps were impacted minimally, with the solvent calculations giving 3.44 eV vs. 3.42 eV in vacuum for pyrene and both calculations giving 3.44 eV for corannulene. All DFT calculations were performed using Gaussian09 (Gaussian Inc.) (Frisch et al., 2009) except for the corannulene geometry optimisations, which were performed using Gaussian03 (Frisch et al., 2004) to use the constrained geometry optimisation implemented in this version of the program.



## 4.3 Results and discussion

### 4.3.1 Choice of functional

In order to quantify the accuracy of the considered DFT functionals, the percentage errors (PE) between simulated and measured OBGs was calculated for three representative PAHs (naphthalene, biphenyl and fluorene), shown in in Figure.4.1. All functionals overpredict the OBG of the three PAHs when compared to the experiments. The simulated OBG of naphthalene is more accurate than that of biphenyl and fluorene. All functionals predict a larger OBG for fluorene than for naphthalene, whereas the measured OBG is 4.2 eV for naphthalene and 4.1 eV for fluorene. This indicates that the B3LYP/6-311G(d,p) level of theory used for the geometry optimisation might be less accurate for the complex non-planar structures of the cross-linked biphenyl and five-ring containing fluorene. Amongst the considered functionals, HSE06 results in the most accurate OBGs with an average P.E. of 7%. This is supported by a similar DFT study performed on semiconductors (Clark and Robertson, 2010). The next best performing functional is the widely used B3LYP with an average PE of 20%. Functionals such as the CAM-B3LYP and  $\omega$ -B97XD overestimate the OBG significantly. The reason for this is that they are parametrised to give orbital energies for accurately calculating the transport gap, which includes the energy to create an unbound electron-hole pair, rather than the OBGs (Salzner and Aydin, 2011). The computed OBG values are also in agreement with the current literature. For example, the OBG of 4.85 eV for naphthalene predicted using B3LYP and the 6-311G(d,p) basis set is very similar to the 4.75 eV reported for B3LYP and the similar 6-31+G(d,p) basis set (Costa et al., 2016).

The experimental OBGs of 18 PAHs and benzene were compared to the DFT predictions obtained with the most accurate functional to further evaluate the applicability of HSE06 for PAH OBG simulations (Fig. 4.2). Overall, there is good agreement between the simulated and measured OBGs for all PAH geometries considered (see Table A.2 for full list). The largest deviation between the computational and experimental OBG is observed for tetracene, at

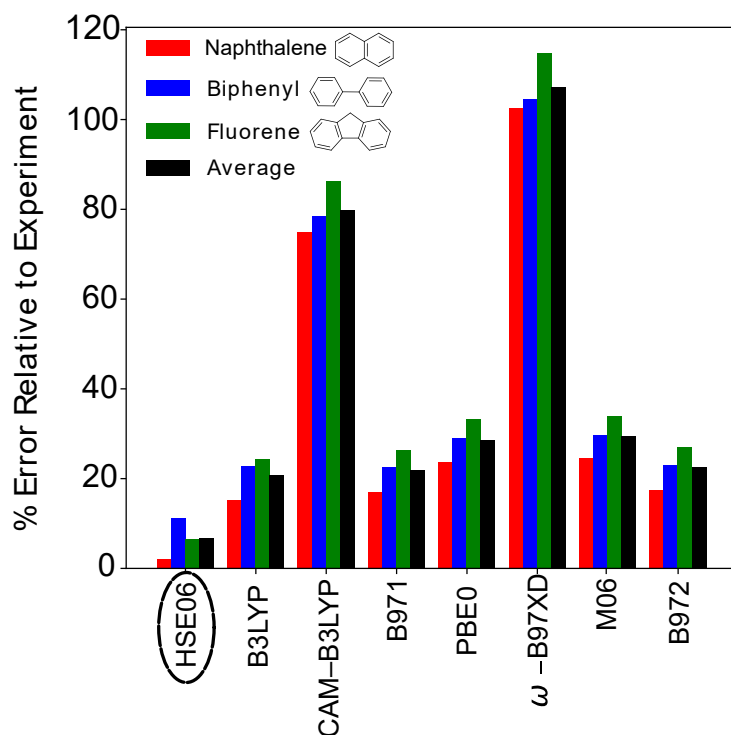


**Figure 4.1:** Comparison of the percentage errors between the OBGs obtained from experimental UV-Vis absorption experiments and DFT simulations using different hybrid functionals. Also shown are the structures of the three PAHs we tested.

a percentage error of 11 % and absolute error of 0.3 eV. The absolute OBG values are also in good agreement with previous studies. For example, DFT predicts OBGs of 2.89 eV for perylene, 3.84 eV for chrysene and 2.33 eV for tetracene while the semi-empirical ZINDO/S predicted 2.82 eV, 3.86 eV and 2.81 eV respectively (Ruiz-Morales, 2002). Even though the DFT and semi-empirical OBGs are very similar, semi-empirical methods can struggle with more complex organic structures outside their parametrisation (Andreu et al., 2001). Therefore, DFT with a combination of the HSE06 functional and 6-311G(d,p) basis set is suitable for OBG calculations of PAHs.



## 4 CHAPTER 4

---

functional has been found to give reasonable predictions for both the band gap of low band gap semiconductors by [Garza and Scuseria \(2016\)](#) as well as for optical properties of larger carbon nanotube and graphene nanoribbon structures by [Barone et al. \(2011\)](#). Therefore, the values for larger PAHs in the following section are provided as a prediction of further trends.

Similarly, open shell systems are more prone to requiring many spin configurations to describe their electronic structure. This limitation can be explored by comparing the excitation energies computed by HSE06 to those performed by [Sandoval-Salinas et al. \(2019\)](#). They used restricted active space configuration interaction (RAS-CI) calculations to compute the excitation to the lowest lying excited states for phenalenyl and triangulene, which were found to give excellent agreement with multireference calculations performed by [Das et al. \(2016\)](#). Comparing the vertical excitation energies of the two lowest states for phenalenyl in [Sandoval-Salinas et al. \(2019\)](#) to those computed by the level of theory used here, good agreement is found with the excitations being 2.82 eV in and 3.05 eV in this work compared to 2.76 eV and 3.04 eV respectively. Similarly, good agreement is also found for the low-lying singlet and triplet-state vertical excitation energies for triangulene, with the values in this work being 0.52 eV and 2.71 eV in this work compared to 0.57 and 2.82 eV respectively in [Sandoval-Salinas et al. \(2019\)](#) Comparison with [Das et al. \(2016\)](#) for the quartet–quartet vertical excitation energy gap of a triangulene with 10 rings again suggests reasonable agreement: 2.8 eV in this work compared to 3.3, 3.1, and 3.0 eV for CASSCF, MR-CISD, and MR-CISD+Q methods respectively in theirs. This comparison suggests that the HSE06 functional is providing reasonable predictions for small to moderate radical and multi-radical triangulenes. For larger triangular and hexagonal graphene nano-islands as well as other graphene structures, screen-based DFT methods, similar to the ones employed in HSE06, have been shown to describe the spin states in the ground state correctly ([Fernández-Rossier and Palacios, 2007](#); [Gillen and Robertson, 2010](#)). However, as was the case for closed-shell PAHs, the accuracy of prediction of optical properties for larger radical species is expected to wane, but they are included in this work for completeness.

### 4.3.3 Trends for Flat PAHs of varying symmetry

With the accuracy of the DFT method shown, the OBGs of additional PAHs were simulated. These included PAHs that are expected to form during hydrocarbon combustion but are difficult to acquire commercially. Previous studies have shown that molecule size, typically quantified by the number of benzenoid rings  $M$ , is the determining factor of the optical band gap (Robertson and O'Reilly, 1987; Adkins and Miller, 2017). The DFT results show that the OBGs of the acenes decrease more rapidly with  $M$  than for  $D_{2h}$  and  $D_{6h}$  peri-condensed PAHs (Fig. 4.3), which is in agreement with previous reports (Adkins and Miller, 2017). The smaller OBG of acenes for a given  $M$  can hereby be explained by their Clar structures. They only have one clar sextet, making them electronically more similar to graphene than the peri-condensed PAHs. The correlation between the OBG and  $M$  of the three PAH classes follows the reported inverse power law, namely  $a \cdot M^{-1/2} + b$  (Robertson and O'Reilly, 1987), or  $c \cdot M^d$  (Adkins and Miller, 2017), with  $a$ ,  $b$ ,  $c$  and  $d$  being fitting parameters. For  $D_{2h}$  peri-condensed PAHs, the current DFT simulations result in  $c = 5.621$  and  $d = -0.376$ , similar to  $c = 5.978$  and  $d = -0.327$  reported previously (Adkins and Miller, 2017). The power-law fit for acenes gives  $c = 6.479$  and  $d = -0.732$ , again similar to  $c = 8.913$  and  $d = -0.891$  in Adkins and Miller (2017). The effect of symmetry is also very apparent, with the lowest symmetry group, the  $C_{2v}$  acenes possessing substantially lower OBGs than the more symmetric  $D_{2h}$  and  $D_{6h}$  peri-condensed PAHs. There is also a noticeable difference between the  $D_{2h}$  and  $D_{6h}$  species, highlighted by the 7-ring  $D_{6h}$  coronene having a slightly higher OBG than the much smaller 4-ring  $D_{2h}$  pyrene.

Figure 4.3 also gives some indication of which isolated PAHs have OBGs within the range of those observed in flames for the different symmetry groups. For  $D_{2h}$  peri-condensed species, the flame region of OBGs includes isolated PAHs with 14-24 rings. For  $D_{6h}$  peri-condensed species, the reported OBG range in flames correlates to approx. 19-20 rings (the size of circumcoronene) and extends well past circumcircumcoronene (37 rings) to species containing hundreds of rings. However, the latter are likely larger than what can be expected to form in a flame from HRTEM studies (Botero et al., 2016a). For acenes, the flame region of OBGs

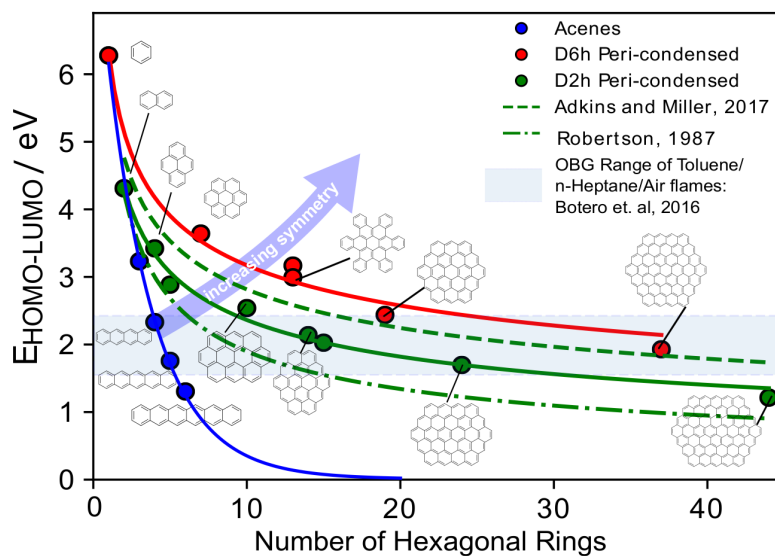


**Figure 4.3:** Plot of the optical band gap of PAHs against number of rings,  $M$ . Previous literature results from similar fittings done by Adkins and Miller [Adkins and Miller \(2017\)](#) and Robertson [Robertson and O'Reilly \(1987\)](#) are also shown.

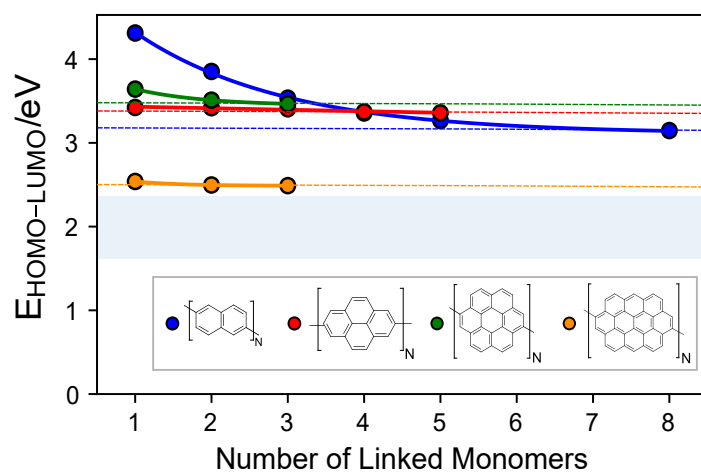
includes isolated PAHs only 4–5 rings in size. It should also be noted that PAH clusters have OBGs approximately 1 eV lower than their isolated counterparts ([Adkins et al., 2017](#)). Thus for a given OBG measured inside the flame, the PAH size that can be assigned to it decreases if a PAH cluster was measured. Acene clusters are therefore unlikely because the constituting PAHs would be too small to form a condensed phase in a flame and are not thermally stable ([Totton et al., 2012](#); [Elvati and Violi, 2013](#)). However, species such as ovalene ( $D_{6h}$  peri-condensed) and hexabenzocoronene ( $D_{2h}$  peri-condensed) might be large enough to incept and their clusters would result in OBGs similar to what was measured in flames.

#### 4.3.4 Trends for cross-linked PAHs

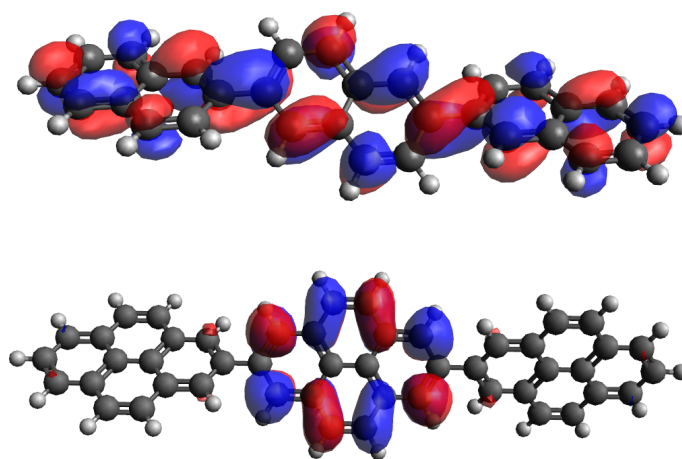
The variation in OBG for flat PAHs is well known in the literature. Less is known about the effect of cross-linking on the OBG of PAHs. Cross-linking reactions between PAHs has been observed in flames and hypothesised as a possible route for soot particle inception via chemical clustering ([Mao et al.,](#)

2017; Richter and Howard, 2000; Bachmann et al., 1996). Cross-linking also can be a mechanism of carbonisation of soot nanoparticles, as bridge forming between PAHs requires the release of hydrogen from the PAH, thereby increasing the carbon-to-hydrogen ratio. The following calculations aim to probe the effect of such cross-linking reactions on the OBG of complex PAHs. Since the agreement between HSE06/6-311G(d,p) DFT calculations and experiments is good for the smaller cross-linked PAHs, the DFT calculations were therefore extended to larger and more complex cross-linked PAHs. The variation in the OBG with increasing number of homogeneous cross-linked PAHs was further studied by performing DFT calculations of naphthalene, pyrene, coronene, and ovalene, cross-linked in the para-position, that is forming linear chains. This is seen in Figure 4.4a. The homogeneous cross-linked structures vary in size from the respective monomer to the octamer for naphthalene, the pentamer for pyrene, and the trimer for coronene and ovalene.

The results suggest that cross-linked structures of moderate PAHs have a reduced OBGs that reach an asymptote. When naphthalene is the repeat unit, there is a significant reduction in the OBG of  $\approx 1.1$  eV for 8 monomers. However, when larger PAHs such as pyrene, coronene, and ovalene are the repeat units, the final reduction of the OBG is only around 0.1 eV. In contrast, previous studies found that clustering by physical agglomeration of PAHs effects a decrease in OBG of approximately 1 eV even for PAHs as large as ovalene, which is not the case here (Adkins et al., 2017). The observed trends can be explained by considering the change of the relevant orbitals when the monomer size increases. The LUMO of p-ternaphthyl extends across all three naphthalene units, thus each one contributes to the LUMO energy and consequently the OBG. For p-terpyrenyl, the DFT calculations indicate that the LUMO is localised onto only the central pyrene, and the addition of further pyrene monomers has little influence on its LUMO (Fig. 4.4b). Similar observations are made for the HOMOs of these two molecules. For larger p-naphthyls, the orbital localisation can also be observed. This indicates that the number of monomers required for orbital localisation depends on the size of the monomers. Therefore, the localisation of orbitals is a function of monomer size and number, explaining the observed asymptotes in Fig. 4.4a. The impact of



(a)



(b)

**Figure 4.4:** a) Plot of optical band gap against number of linked monomers for homogeneous aromers. An exponential decay curve has been fitted to guide the eye, with the dashed lines representing the expected asymptotic gap value. The blue shaded region represents flame optical band gap measurements from [Botero et al. \(2016a\)](#) b) LUMO orbitals of *p*-ternaphthyl (top) and *p*-terpyrenyl (bottom).



longer aliphatic chains was not explored in detail due to their insulating nature. However, as an example, the HOMO-LUMO gap for two pyrenes joined via a four-carbon aliphatic bridge was computed to be 3.41 eV compared with 3.42 eV for pyrene alone. Therefore, it is expected that longer aliphatic bridges will also have a minimal impact on the OBG.

It should be noted that the asymptotic OBGs of all cross-linked species are higher than the OBGs observed in ethylene and toluene flames by [Adkins and Miller \(2015\)](#) or [Botero et al. \(2016a\)](#). This agrees with previous studies for pyrene and coronene that suggested that such clusters are unlikely to be in flames ([Lowe et al., 2015](#)) and hence it is understandable that their OBG does not match those measured in flames. However, even for the case of ovalene, the asymptotic OBG is higher than those observed in flames. In contrast, physical clusters of ovalene were seen to have OBGs that are in the range of those observed in such sooting flames ([Adkins et al., 2017](#)). Thus homogeneous chemical clustering by cross-linking would require larger PAH monomers than homogeneous physical clustering to match the observed OBGs in flames.

The effect of cross-linking between different PAHs on the OBG was also explored computationally. Heterogeneous cross-linked structures of naphthalene, pyrene, coronene, and ovalene were chosen in order to use the same monomer PAHs as the homogeneous case. This is presented in [Figure 4.5](#).

[Figure 4.5](#) would suggest that the optical band gap of heterogeneously cross-linked PAHs is strongly correlated with the optical band gap of the largest monomer PAH fragment within the PAH. In other words, the OBG of the heterogeneously cross-linked PAHs is controlled by the largest PAH/lowest OBG of the monomer PAH fragments in the molecule. This is clearly seen for cross-linked structures between naphthalene and a larger PAH, with species (c), (g), and (j) having OBG values very close to the larger PAH of pyrene, coronene, and ovalene respectively. Similarly, all heterogeneous cross-linked structures which contain ovalene have OBGs very close to ovalene, although there is a slight reduction suggesting that there may be a minute amount of spread of the HOMO and LUMO orbital across the aliphatic cross-link. However, there are complications for PAHs that have coronene as the largest fragment cross-linked

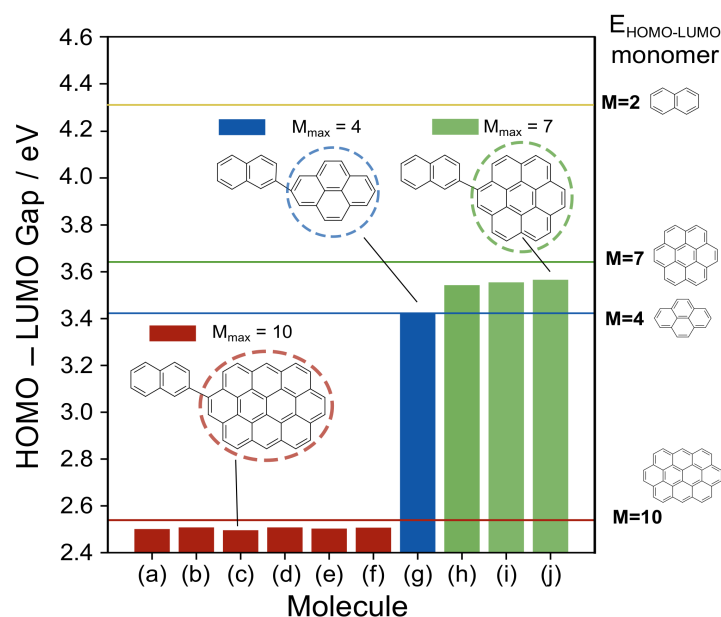


**Figure 4.5:** Optical band gap of cross-linked structures of naphthalene, pyrene, coronene, and ovalene.  $M_{\max}$  is defined as the number of rings in the largest PAH monomer fragment in the cross-linked PAH (blue for pyrene, green for coronene, red for ovalene). The horizontal lines on the bar plot show the optical band gap of the 4 different monomer PAHs for reference.

to a pyrene fragment. In this case, the OBG of pyrene and coronene are quite close (3.64 and 3.42 eV respectively), and the OBG of the cross-linked PAHs are  $\approx 3.55$  eV, which is nearer to the average of the OBGs of pyrene and coronene. Nevertheless, using the OBG of coronene is still clearly a reasonable approximation for molecules (h), (i), and (j).

In addition to the localisation effect in cross-linked PAHs, the formation of a cross-link introduces another degree of freedom in the PAH, namely the rotation of the monomer fragments about the cross-link axis. Tuning of such electronic and optical properties by twisting fragments in a polymer has been seen experimentally, for example in  $\text{TiO}_2$  based-dyes for solar cell applications (Zhang et al., 2019). Particularly at the higher temperatures experienced in flames, it may be the case that a cross-linked PAH will be able to adopt several rotational conformers, resulting in a spread of the OBG. The upper bound of this effect can

be seen by considering the rotation of the two phenyl fragments in biphenyl. As the cross-linked PAH with the smallest individual monomer fragments, biphenyl is expected to be able to rotate with the most ease and therefore have the largest spread in its OBG. This effect was explored by means of a relaxed scan of the biphenyl molecule with the dihedral angle of the cross-link bridge used as the scan coordinate. The minimum energy geometry and optical band gap were then determined for each rotational conformer along the scan point.

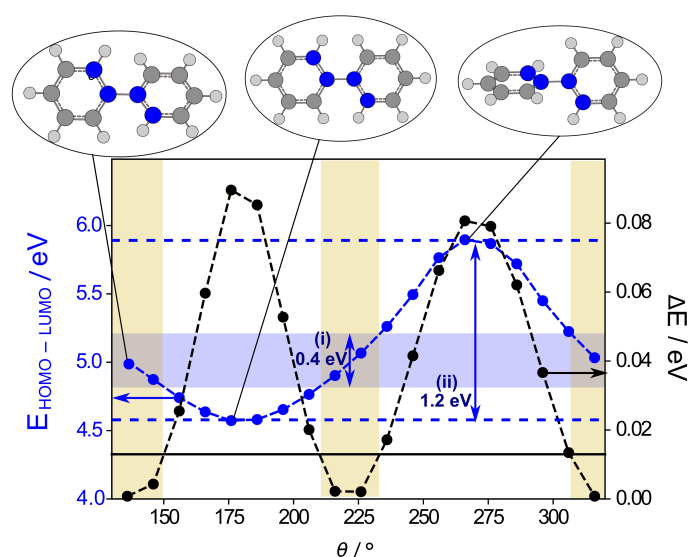


**Figure 4.6:** Optical band gap and change in energy of biphenyl rotational conformers as a function of the dihedral angle,  $\theta$ . Examples of some of the rotational conformers in the scan are illustrated in the plot, with the atoms comprising the dihedral angle  $\theta$  highlighted in blue. The beige and blue shaded regions represent the rotational conformers accessible at 298K and their corresponding OBG values.

Figure 4.6 suggests that some spread in the OBG is expected for cross-linked PAHs due to their ability to rotate. Rotational conformers are deemed to be accessible if the deviation between the energy of the conformer and that of the equilibrium biphenyl geometry was less than or equal to the Boltzmann thermal energy,  $k_B T$ . At 298 K, the regions shaded in beige are accessible to biphenyl, resulting in a modest spread in optical band gap of 0.4 eV. At a temperature of 1500 K, typical of those in flames, all conformers are expected to be accessible, as

## 4 CHAPTER 4

---

$k_B T$  has a value of 0.13. Thus, in flames, biphenyl could have an optical band gap spread of 1.3 eV. This spread corresponds to a maximum decrease in the OBG of 0.37 eV compared to biphenyl's equilibrium geometry, and a maximum increase of 0.93 eV. As a result, rotation appears to favor an increase in the OBG over the equilibrium value in the case of biphenyl. This increase in OBG is significant enough that it would have to be considered when making optical measurements at higher temperatures. However, it should also be noted that biphenyl represents the cross-linked PAH that is most likely to rotate. Larger cross-linked PAHs are unlikely to have so many rotational conformers accessible due to the additional energy required, and so the spread in optical band gap expected would be lower. It is also expected that the more cross-links that form, the more difficult it will be for internal rotations about the cross-link to occur, meaning the increase in OBG due to rotation is likely mainly significant for smaller cross-linked PAHs as opposed to those with larger monomers or multiple cross-links.

To summarise, for cross-linking between PAHs, the OBG can be approximated by the OBG of the largest monomer in the system. The rotation of monomer fragments about a cross-link was seen to result in a significant spread in the optical band gap of biphenyl, and resulted in a net increase in the optical band gap of biphenyl when considering all conformers. However, this was noted to be an upper bound as larger cross-linked PAHs and clusters of such PAHs are expected to require greater energy to effect internal rotation, and so the effect is hypothesised to be significant only for smaller cross-linked PAHs. These results suggest that forming a cluster of PAHs by continuous cross-linking would require larger PAHs present than for physical clustering to explain the lower OBG regimes measured in flames, as there is no additional reduction in OBG due to forming a network of PAHs like there is for physical clustering.

### 4.3.5 Trends for curved PAHs

Finally, the effect of pentagons and curvature on the OBG of PAHs is investigated. Curved PAHs form via the integration of interior pentagons into their geometry. This can occur, for example, from zig-zag edge oxidation of a PAH ([Singh and Frenklach, 2016](#)). Understanding how pentagonal rings and curvature

affect the OBG is desired, as the presence of pentagonal-ring containing curved PAHs such as fullerene and corannulene has been observed in soot and flames ([A.L. Lafleur, J.B. Howard, J.A. Marr, T. Yapesh, 1993](#)) and may contribute to OBG measurements. Therefore, it is useful to understand what sort of pentagonal-ring structures would have OBGs similar to those observed in flames. For example, fluorene and acenaphthylene have quite different OBGs (4.1 and 3.6 eV respectively) despite having similar structures. This can be explained by aromatic differences as Zdetsis and Economou recently found a correlation between aromaticity and OBG ([Zdetsis and Economou, 2016](#)). The position of the pentagon is very different in acenaphthylene and fluorene, resulting in them having different Clar sextets. By calculating the aromatic fluctuation index ([Matito et al., 2005](#)) of the rings in both fluorene and acenaphthylene using Multiwfn ([Lu and Chen, 2012](#)), it is found that the hexagonal rings in fluorene are significantly more aromatic than their counterparts in acenaphthylene, as acenaphthylene has one Clar sextet shared between its two hexagonal rings. The differences in aromaticity between fluorene and acenaphthylene help explain their difference in OBG.

The comparison between experiments and DFT simulations for fluorene and acenaphthylene indicate that HSE06/6-311G(d,p) gives reasonably accurate OBGs for PAHs containing 5-member rings. The comparison of these two molecules suggests that slight differences in pentagon position can have significant impacts on aromaticity and the OBG. Such differences are likely to be of even more importance when the PAHs are curved due to internal pentagon integration. For example, a recent study by [Martin et al. \(2017b\)](#) found that more curved PAHs have larger dipole moments due to the  $\pi$ -electron flexoelectric effect. Additionally, by applying strain to corannulene, they found that the dipole moment increased linearly with the pyramidalisation angle, showing that curvature can have a significant impact on the properties of PAHs. Previous studies have suggested similar ideas, with [Adkins and Miller \(2017\)](#) finding that curvature effects are generally secondary to those of size and shape for larger PAHs. However, it would be useful to establish the optical band gap ranges in which PAH curvature has a significant effect. To do this, the OBG of a set of

## 4 CHAPTER 4

curved PAH species of varying size, symmetry, and number of pentagons (and therefore curvature) was computed using the same levels of theory as before. This set of PAHs was previously studied by [Martin et al. \(2017b\)](#) to elucidate the effect curvature and size had on dipole moment. This is seen in Figure 4.7.

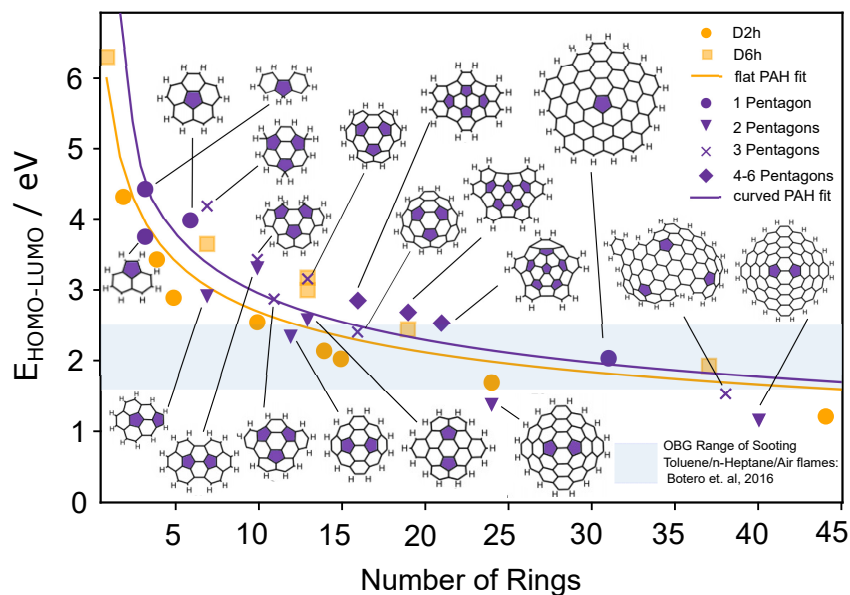


**Figure 4.7:** Optical band gap of curved PAHs with a varying number of rings. The blue shaded region corresponds to measurements from [Botero et al. \(2016a\)](#). The PAHs are numbered according to the number of pentagons they contain. The lines shown are power-law fittings, comparing the fit to all the peri-condensed flat PAHs calculated in section 3.2. The full list of curved PAHs studied is taken from [Martin et al. \(2017b\)](#).

Due to the curved PAHs having different number of pentagons, the symmetry of the curved PAHs are quite different. Therefore when comparing to flat peri-condensed PAHs, the power-law fitting in Figure 4.7 was done for the combined set of  $D_{2h}$  and  $D_{6h}$  PAHs previously computed in Figure 4.3. It is worth noting that the OBG of curved PAHs is plotted against the number of rings, and not an explicit description of curvature such as the pyramidalisation angle, as the use of number of rings makes it easier to compare the OBGs of curved and flat PAHs directly. However, the more pentagons a curved PAH, the more curved it is ([Martin et al., 2017b](#)), and this is shown in Figure 4.7. Figure 4.7 helps

establish some guidelines on when the effect of curvature impacts the OBG of peri-condensed PAHs. For smaller PAHs (and therefore higher OBG values), the effect of curvature is important, and arguably of similar significance to the size and symmetry effects, even given the expected error in the DFT calculations. This appears to be the case up until around PAHs of size 15-20 rings. In this smaller PAH range, one can also see that the 2-pentagon PAHs have lower OBGs that are very similar to the  $D_{2h}$  flat PAHs. The  $\geq 3$  pentagon containing curved PAHs can be seen to have OBGs that are similar and even exceeding that of the highly symmetric  $D_{6h}$  PAHs in the same size range. As a result, if one takes an OBG of 2.4 eV, corresponding to the upper limit of that measured by [Botero et al. \(2016a\)](#) in flames, one can see that a flat peri-condensed PAH would be expected to be around 12–13 rings to give this, whilst a curved PAH would need to be around 16–17 rings to give the same value. Typically, the OBGs measured in flames are related to the size of the peri-condensed species, which led to the conclusion that modest sized PAHs such as ovalene could be present in soot ([Adkins and Miller, 2015](#); [Adkins et al., 2017](#)). However, the above analysis suggests the same higher OBG mode could similarly be attributed to curved PAHs of larger sizes which could have increased dispersion interactions. This larger OBG mode in flames is generally attributed to nascent soot as opposed to more mature soot, so the results here also suggest that consideration of larger curved PAH species may be relevant to nascent soot conditions.

Figure 4.7 also confirms that the effect of curvature on the OBG is also finite, namely that it becomes less significant as the PAHs get larger. After PAHs grow enough, size is clearly the more important factor impacting OBG. At the lower OBG mode of around 1.7 eV, one would expect the flat and curved PAHs to be of roughly the same size. This would suggest that the decrease in OBG as soot matures cannot be attributed to potential curvature integration after soot formation, but due to other mechanisms, such as growth of PAHs. This is in agreement with HRTEM results of [Botero et al. \(2018\)](#), who found that curvature is less important in more mature soot.

To understand why the effect of curvature seems to become less relevant for larger species, it is helpful to consider what happens if curvature is reduced in a PAH



## 4 CHAPTER 4

by applying strain. For example, by considering the smallest PAH with a fully integrated pentagon, corannulene, and constraining it to have varying degrees of curvature, one can see the variance in optical band gap solely with respect to curvature. To do this, the curvature of corannulene was varied by fixing the value of the dihedral angles during geometry optimisation. The OBG was then calculated as with the other PAHs.

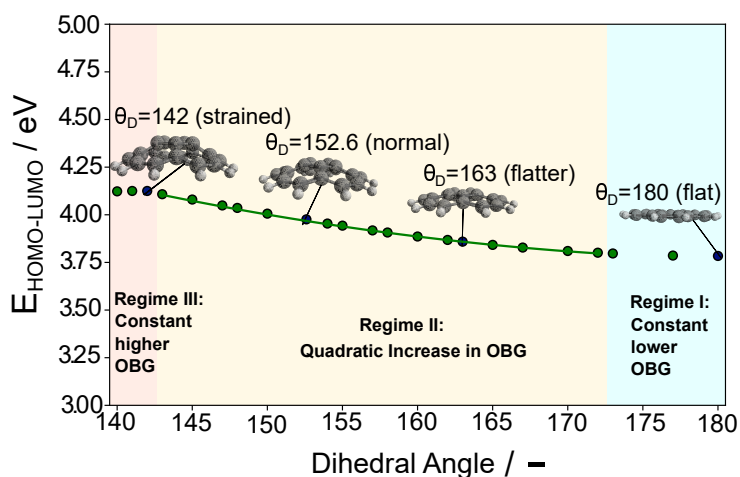


**Figure 4.8:** Plot of the OBG of corannulenes subjected to different amounts of strain.

Figure 4.8 shows the variance in the OBG of corannulene as it is subjected to different degrees of strain. Flat corannulene has dominantly  $\pi$  character, and has the lowest optical band gap, which is consistent with smaller flat PAHs having lower band gaps than curved ones. As the corannulene is strained into a curved geometry, its OBG increases as more  $\sigma$  character is introduced into the  $\pi$ -bonding due to the change from  $sp^2$  to  $sp^3$  hybridisation (Martin et al., 2017a,b). This agrees with observations made by Jäger et al. (2009). Three distinct regimes are seen in Figure 4.8. The first is for the very flat corannulenes, where the OBG is constant. The dihedral angle needs to reach  $175^\circ$  before an increase in OBG is observed. Then, the OBG increases in a quadratic manner with the dihedral angle, suggesting a reasonably strong dependence on curvature of the OBG. The overall increase in OBG between the flat geometry and the curved saturation geometry is 0.4 eV, which is similar to the difference seen between smaller/moderate flat and curved PAHs in Figure 4.7. One can also see that once a dihedral angle of



around  $142^\circ$  is reached, there is no further change in the OBG, meaning additional curvature no longer increases the optical band gap. The corannulene molecule under strain shows that there is a limit to the amount that curvature impacts the optical band gap in PAHs, which could also explain why larger curved PAHs have similar optical band gaps to larger flat PAHs. Even though the larger curved PAHs in this case are more curved than corannulene, it would seem that their optical band gap is already saturated by the size of the PAH and adding curvature is less important. For small and moderate PAHs, this is not the case, and adding curvature effects a noticeable change in optical band gap due to the  $\sigma$ -character.

### 4.3.6 Trends for open-shell PAHs

#### 4.3.6.1 $\sigma$ -radical PAHs

The previous sections considered PAHs of various geometries, but all structures were closed-shell species, so the impact of radical nature on the OBG is now explored. Firstly, a single hydrogen was removed from the acene,  $D_{2h}$ , and  $D_{6h}$  PAHs studied in the first section. This forms an open-shell PAH  $\sigma$ -radical, with one radical site. Such PAHs are of interest as they are formed during the HACA mass growth process (Wang and Frenklach, 1997; Frenklach, 2002a). Soot is also known to possess several radical sites on its surface (Howard, 1991) that have ramifications for surface growth and oxidation processes of such particles as well as PAHs in the gas phase (Liu et al., 2019; Frenklach, 2019). The effect of radicals on optical properties of PAHs is thus important to take into account. The effect of the radical site and its position in the PAH on the OBG is then compared to the closed-shell counterpart, using the same computational methods as before. This is seen in Figure 4.9.

Figure 4.9 suggests that there is almost no difference between the OBG of a single radical site open-shell PAHs and their closed-shell counterparts, as most of the simulated points lie on the  $y = x$  line. This is true even given the expected error in the DFT calculations of  $\approx 0.1$  eV when comparing to UV/Visible spectroscopy. The position of the radical site on the PAH also seems to have almost no impact, as this would appear on Figure 4.9 as a scatter of points lying on the same vertical

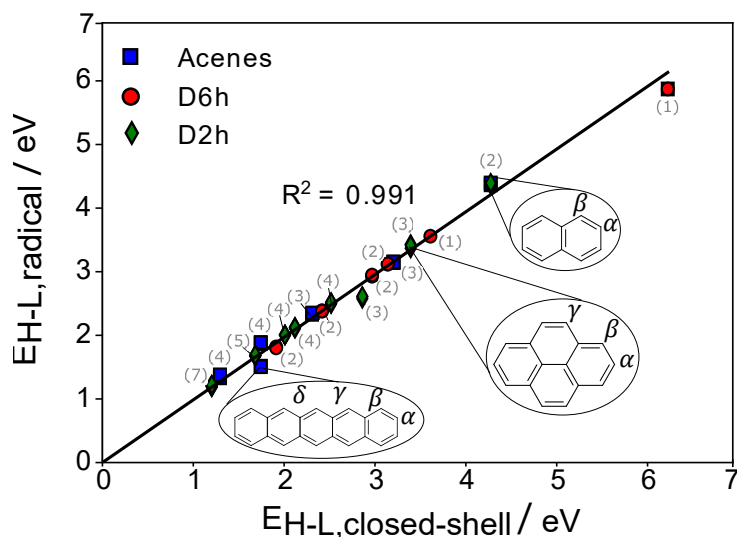


**Figure 4.9:** Comparison between the OBG of open-shell flat PAHs containing one radical site and their closed-shell counterparts. The gray numbers represent the number of unique radical sites the PAH in question possess. Examples are given for naphthalene (2), pyrene (4), and pentacene (5) with each unique potential radical site demarcated with a Greek letter. The straight line plotted represents the open and closed-shell counterparts having the same OBG.

line, but most points for the different radical sites are near indistinguishable. This was due to the minimal impact on the HOMO and LUMO energies which are  $\pi$ -orbitals that are orthogonal to the low lying  $\sigma$ -orbitals responsible for the carbon hydrogen bonding. There was a very slight shift towards lower orbital energies for the case of the radical, but this is negligible compared to the magnitude of the HOMO and LUMO energies. The orbital densities make it clear that since removing a hydrogen removes a  $\sigma$ -bond and not a  $\pi$ -bond, the aromatic network of the PAH is conserved, leading to the OBG being invariant to this change. Therefore, it can be stated that the OBG of a  $\sigma$ -radical PAH and its corresponding closed shell PAH are likely identical.

The one exception to the above rule in the DFT calculations appears to be pentacene, where two distinct points are identified, with one representing the  $\alpha$  and  $\beta$  sites and the other representing the  $\gamma$  and  $\delta$  sites. Strangely, no other acene radicals have this bi-modal OBGs, even the larger hexacene, so it could well be an artifact of the DFT calculation. Nevertheless, the average of the two pentacene radical OBGs is approximately equal to the OBG of closed-shell pentacene. Therefore, the approximation that the OBG of a  $\sigma$ -radical flat PAH is the same as the closed shell PAH is reasonable. From a flame diagnostics perspective, this means that OBG measurements in flames could be attributed to either closed or  $\sigma$  open-shell PAHs. Much like how the degree of cross-linking is not reflected in the OBG, neither is the  $\sigma$  radical character of the soot/gas-phase present.

### 4.3.6.2 $\pi$ -radical PAHs

Another key category of PAH species include resonance-stabilised radical (RSR) PAHs such as indenyl RSRs, peri-condensed RSRs, cyclopentamethylene RSRs, and triangulene RSRs. Resonance-stabilised radical species are known to form from reactions of unsaturated hydrocarbons (Mebel and Kaiser, 2015), and play important roles in the initial formation chemistry of smaller gas-phase PAHs (Sinha and Raj, 2016; Zhao et al., 2018). Recently, RSR PAHs have been proposed as potential precursors to the formation of soot, initiated first by growth of RSRs by HACA or vinyl addition followed by radical-chain reactions resulting in an incipient soot particle consisting of several RSR and closed-shell PAHs covalently linked (Johansson et al., 2018; Wang, 2011; Richter and Howard, 2000). Understanding how the optical band gap of RSR PAHs compares to their closed shell counterparts can help shed light on the differences in properties between these two classes and what this could mean for soot formation. To do so, the OBG of several different classes of RSR PAHs was computed. These include four categories of RSR PAHs. The first are those formed from growth of indenyl which are hypothesised as seed radical for PAHs (Johansson et al., 2018). The second is the traditional odd-number carbon peri-condensed radicals which have been seen in mass-spectra analyses of PAHs in flames (Bachmann et al., 1996; Homann, 1998). The third is PAHs containing pentagonal rings and

## 4 CHAPTER 4

methylene groups, which have been observed in young soot particles by atomic force microscopy (Schulz et al., 2019). Finally, the fourth category consists of triangulene-like PAHs. This is seen in Figure 4.10.

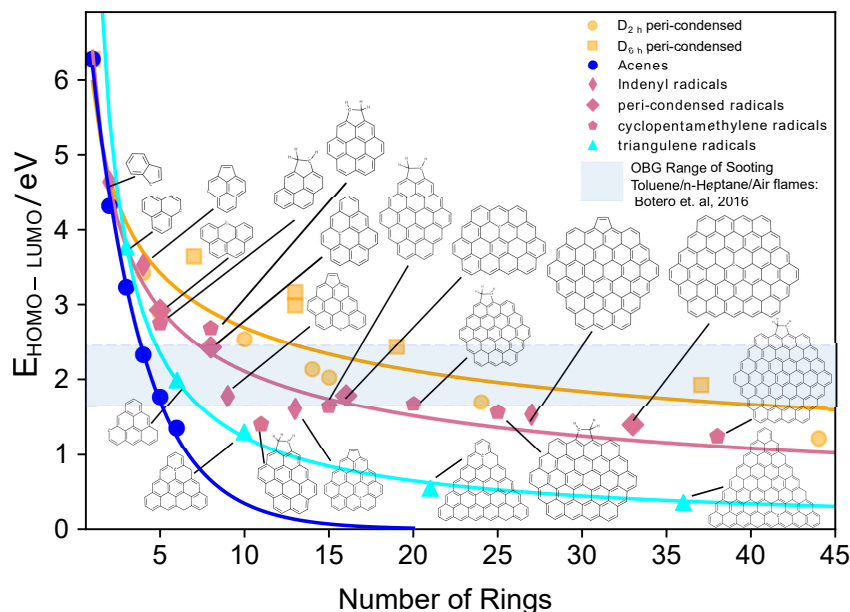


**Figure 4.10:** Optical band gap of different resonance-stabilised-radical (RSR) PAHs as compared to closed-shell peri-condensed PAHs and acene series PAHs. The RSR PAHs include peri-condensed, indenyl-like, triangulene, and cyclopentamethylene RSR PAHs. The lines shown are power-law fittings, comparing the fits to all the peri-condensed flat PAHs calculated in section 3.2.

Figure 4.10 suggests that resonance-stabilised radical PAHs have lower optical band gaps than closed-shell peri-condensed PAHs or their  $\sigma$  radicals on average. The triangulenes in particular have much lower OBGs than the other types of resonantly stabilised radicals. This is in spite of the fact that triangulenes have higher symmetry than the other  $\pi$ -radical PAHs and higher symmetry typically leads to larger OBG values. However, the triangulenes are also noted to typically possess bi-radical character as well as potential non-Kekulé structures that contribute to their energetics and optical properties as nano-graphene structures (Yeh and Chai, 2016). In the context of soot, triangulenes with OBG values in the range of 1.7 - 2.4 eV are expected to be very small, around 5-8 rings. Much like the acenes, these triangulenes are not expected to be very stable at flame temperatures.

For the rest of the RSR PAHs, the size-range of PAHs that match the optical band gaps observed in sooting flames is significantly more narrow. At the upper end of 2.4 eV, the size of RSR PAHs is estimated to be  $\approx 9$  rings, significantly smaller than flat peri-condensed PAHs (12-13 rings), and curved peri-condensed PAHs ( $\approx 16$  rings). The lower end of 1.7 eV corresponds to a RSR PAH of size around 16 rings, suggesting that in general the RSR PAHs in soot would have to be smaller than other types of PAHs to explain the same OBG measurements. Given that such small PAHs are unlikely to be able to cluster physically, it would be expected that the RSR PAHs would need to cluster covalently to be stable, which is consistent with the recent hypothesis of [Johansson et al. \(2018\)](#).

## 4.4 Conclusions

The accuracy of different functionals for Density Functional Theory (DFT) calculations of the optical band gap (OBG) of PAHs was evaluated by comparison with experimentally determined values. The results indicate that HSE06 gives the most accurate OBG values compared to other functionals, especially for smaller PAHs including cross-linked and curved PAHs. Certain popular hybrid functionals were seen to significantly overestimate the OBG due to being parametrised to give the transport gap. The HSE06 functional was further used for calculating the OBG of larger and more complex PAHs. The observed inverse power-law correlation of the OBG with number of rings was in agreement with previous reports. In case of homogeneous cross-linked PAHs, it was shown that orbital localisation effects cause an asymptotic decrease in the OBG with increasing number of monomers. This effect was especially pronounced for larger PAH monomers. For cross-linking between two different PAHs, the OBG was shown to reflect the OBG of the largest monomer PAH and not the average of the monomers.

The effect of PAH curvature was also studied by first comparing the OBG of peri-condensed curved PAHs with varying number of pentagons to the OBG of flat peri-condensed PAHs. These calculations suggested that PAH curvature is important when considering the higher value OBGs measured in flames, as

## 4 CHAPTER 4

---

curved PAHs are expected to be larger than flat ones for these higher OBG values. However, for lower OBG ranges or larger sizes, it was seen that flat and curved PAHs essentially converge to the same number, so this range cannot be explained by curvature effects. By inducing strain in corannulene, a small curved PAH, it was found that the difference in OBG between a flat corannulene and a highly strained corannulene is 0.4 eV, but there is a limit to how much curvature changes the OBG. This helped explain why larger flat and curved PAHs have similar OBG values.

Finally, the effect of radical character on the OBG of PAHs was considered.  $\sigma$ -radical PAHs were seen to have the same OBG as their equivalent closed-shell structure, regardless of the location of the radical site as well. On the other hand,  $\pi$ -radical PAHs were seen to have significantly lower optical band gaps than flat peri-condensed species of the same size, meaning that smaller  $\pi$ -radicals may also be important PAHs to consider. Further steps involve understanding the kinetics and thermodynamics of the formation of larger curved and  $\pi$ -radical PAHs under flame conditions.

## Chapter 5

# Investigating the polarity of curved PAHs at flame conditions

*In this chapter, the polarity of curved aromatics in flame conditions is investigated using electronic structure calculations and transition state theory. The barriers and rates of inversion for curved PAHs of varying sizes are computed. A transition is observed for smaller curved aromatics between 11–15 ( $\approx 0.8$  nm) rings where the increasing strain introduced from the pentagonal ring increases the inversion barrier leading to rigidity. This is seen to be a function of the degree of curvature, as represented by the number of pentagons. Ab initio quantum molecular dynamics of a 1 nm curved PAH and  $C_3H_3^+$  chemi-ion suggest molecular dipole fluctuations of  $\pm 0.5$ –1 debye compared to the equilibrium 5 debye, indicating persistent polarity at 1500 K. The curved PAH and  $C_3H_3^+$  chemi-ion remain bound throughout the dynamics, suggesting that interactions between curved PAHs and chemi-ions may be relevant for soot formation.*

### Collaborative Contributions

The work presented in this chapter has been published in *Combustion and Flame* and is an equal collaboration with Jacob Martin. Jacob Martin performed the *ab initio* molecular dynamics (MD) simulations and conducted the analysis for these MD simulations. The electronic structure and rate calculations were performed by the author. The writing of the manuscript and preparation of the figures were done jointly by Jacob Martin and the author.

### 5.1 Introduction

Curved PAHs have long been suggested as precursors to soot formation (Baum et al., 1992; Homann, 1998). A small curved PAH (cPAH), corannulene has been extracted from soot (Lafleur et al., 1993; Wu et al., 2016) and the synthesis of closed cage fullerenes molecules in low pressure benzene flames has been observed (Gerhardt et al., 1987; Richter et al., 1997).

Detailed electronic structure calculations on curved PAHs have shown that curved PAHs possess significant dipole moments due to the flexoelectric effect (4–6 debye for species found in early soot) (Martin et al., 2017d; Martin, 2019). Further work showed that the dimerisation energy of cPAHs with 1–2 pentagons is comparable to that of similar sized planar PAHs. The calculations also suggested that for a PAH to become flexoelectric, more than six aromatic rings are required. However, electrostatic interactions between permanent dipoles range significantly farther than dispersion interactions, suggesting that the permanent dipoles possessed by curved PAHs may play a role in the stability of early soot clusters (Martin et al., 2018).

In particular, it has been hypothesised that the interaction of curved PAHs with charged species in flames could impact soot formation. Substantial binding energies in excess of 40 kcal/mol between curved PAHs and an abundant chemi-ion in sooting hydrocarbon flames, cyclopropenyl ( $C_3H_3^+$ ) have been observed (Martin, 2019)). Chemi-ions are produced in significant concentrations in flames and their correlations with soot formation have long been known (Calcote et al., 1988; Lawton and Weinberg, 1969; Hayhurst and Jones, 1987;



Fialkov, 1997), such as the impact of electric fields (Mayo and Weinberg, 1970; Saito et al., 1999; Park et al., 2014) and the addition of alkali metal ions (Place and Weinberg, 1966; Di Stasio et al., 2011; Simonsson et al., 2017).

One significant issue surrounding ionic routes to soot nucleation is how persistent the polarities of curved PAHs are at the temperatures of sooting flames. For example, if curved PAHs could invert rapidly, this would likely impede their ability to form a stable complexes. Additionally, fluctuations of the dipole moment at flame temperatures could mean that the dipole moment decreases, thereby mitigating the importance of this property that curved PAHs possess. The small cPAH corannulene is well known to rapidly invert at room temperature with an experimental inversion barrier of 10.2 kcal/mol (Scott et al., 1992) and computed barrier of 11.5 kcal/mol (Seiders et al., 2001). This barrier is significantly lower than the strain energy anticipated in corannulene, namely 24 kcal/mol (Sun et al., 2006), and is attributed to the planar transition state that increases  $\pi$ -electron delocalisation decreasing the barrier by 11 kcal/mol (Dobrowolski et al., 2011). Soon after corannulene was found to invert rapidly at room temperature, it was also found that addition of a single extra pentagonal ring on the rim doubles the inversion barrier (Abdourazak et al., 1993). Calculations of larger cPAH have found a non-planar S-shaped transition state that considerably increases the inversion barrier with a one pentagon 10 ring PAH having an inversion barrier of 56 kcal/mol while two pentagon >14 ring species having inversion barriers of >100 kcal/mol (Wu et al., 2013).

**The purpose of this chapter** is to determine how persistent the polarities of curved PAHs are at flame temperatures and to study the interaction of an ion with a dipolar cPAH. The rate of inversion is computed for a range of cPAH revealing the size required for inhibition of inversion in flame conditions. *Ab initio* molecular dynamics simulations are used to track the fluctuation of the dipole moment of a curved PAH and study the dynamics of a chemi-ion interacting with the cPAH over two picoseconds.

## 5.2 Methodology

Figure 5.1 shows the curved PAHs chosen for this study. These include the smallest curved PAH, corannulene **1**. Additionally, curved PAHs of the size seen in early soot particles 0.9–1.2 nm were also studied. This includes a fifteen-ring structure with a single pentagonal ring and a five member bay site **2** and the same single pentagon structure with the closure of the bay site **3**. Additionally, a two-pentagon containing 15 ring cPAH **4** suggested from HRTEM imaging of early soot nanoparticles (Martin et al., 2018), and a three-pentagon containing cPAH, **5**, are also provided. For each of the largest cPAH we also added/removed a hydrogen to the site specified to consider the effect of a  $\pi$ -radical on the rate of inversion.

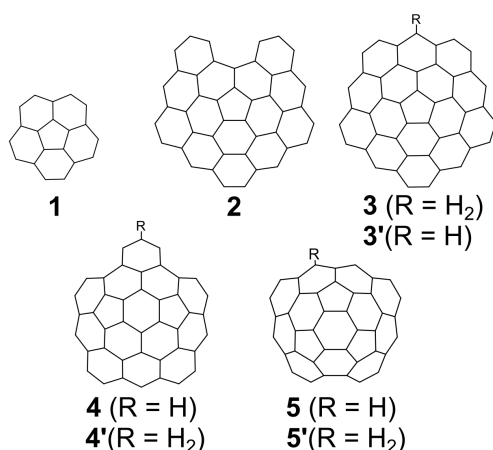


**Figure 5.1:** Curved PAH molecules chosen in this study with 3-5 chosen from a previous study by Martin (2019).

The energies and frequencies of the minimum energy and transition state structures of the curved PAHs were computed using the hybrid density functional B3LYP/6-311+G(d,p) level of theory. This has been found to correctly describe the equilibrium geometry of curved arenes compared with crystal structures and the inversion dynamics of these systems (Wu et al., 2013). For all geometries located by DFT, the frequencies were checked to ensure the calculation had found the appropriate energy minima and transition states. To obtain a more accurate estimate of the energies of the minima and the transition state,

single point energy calculations using the Minnesota hybrid density functional M06-2X/6-311g(d,p) were performed on the optimised geometries. This has been shown to give accurate energies for reactions involving PAHs (Hou and You, 2017). Energies are reported with the zero point energy correction included from the B3LYP/6-311+G(d,p) level of theory.

The rate of inversion was calculated using canonical transition state theory as implemented within the THERMO package of the Multiwell software (Barker, 2001, 2009; Barker et al., 2017b). In this case the barriers of inversion are high and pressure dependence was not considered, so canonical transition state theory was considered sufficient over more sophisticated methods such as variational transition state theory and RRKM/Master Equation calculations. Due to the larger size of the 15 ring PAHs, the source code had to be modified to include more vibrational and rotational degrees of freedom than the default 150 implemented in Multiwell. Additionally, tunneling was not treated by the standard unsymmetrical Eckart tunneling in THERMO as the very large barriers of inversion led to some numerical difficulties with this tunneling form. Instead, tunneling effects were treated by means of the Wigner correction. For the rate calculations in this work, the obtained Wigner tunneling corrections were extremely close to one, which is expected given the large reactants and high energy barriers.

*Ab initio* molecular dynamics (AIMD) techniques were used to study the thermal fluctuation of the dipole moment of the curved PAHs. These methods have been used previously in combustion to study the dimer lifetimes of pyrene using a semi-empirical quantum theory, an example of which is Born-Oppenheimer molecular dynamics (BOMD). In BOMD, nuclei are treated as classical ions with the forces on these ions computed on the basis of electronic structure theory calculations.

$$\partial E/\partial \mathbf{R} = \langle \Psi | \partial H / \partial \mathbf{R} | \Psi \rangle + \langle \partial \Psi / \partial \mathbf{R} | H | \Psi \rangle + \langle \Psi | H | \partial \Psi / \partial \mathbf{R} \rangle, \quad (5.1)$$

The first term is the Hellmann-Feynman force and the second and third term are the "Pulay" forces (Schlegel et al., 2001). BOMD performs a self-consistent field calculation at each time step, which is usually prohibitively expensive for

larger molecular systems. One successful simplification to this is the atom-density matrix propagation (ADMP) method, which propagates the electronic structure using an extended Lagrangian coupled to the nuclear positions via a fictitious mass. This significantly reduces the computational cost, and is similar to the Car-Parrinello method. However for ADMP, the density matrix is propagated instead of the Kohn-Sham orbitals and atom-centred Gaussian basis functions are used instead of plane wave basis functions (Schlegel et al., 2001). These features of ADMP allow any hybrid density functional theory to be used to generate the density matrix and provides better separation between the electronic and nuclear degrees of freedom. ADMP has been found to accurately follow the fully converged Born-Oppenheimer MD, provided small time steps are used (Schlegel et al., 2001; Iyengar et al., 2001; Schlegel et al., 2002; Li et al., 2008). ADMP has been applied in describing gas interactions with aromatic macrocycles (Das and Chattaraj, 2014) and has recently been used to model the formation of covalent bonds between pyrene dimers (Observatory et al., 2018). A similar method using converged semi-empirical PM3 simulations has also been employed in combustion research to study PAH dimerisation at flame temperatures by Schuetz and Frenklach (2002); Wong et al. (2009).

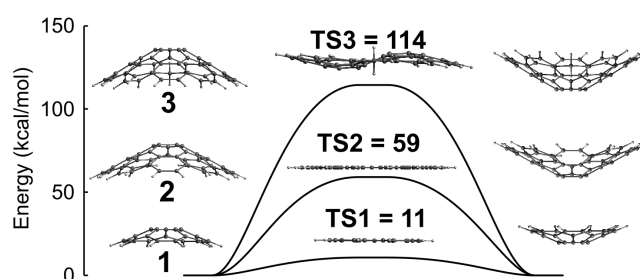
For the AIMD simulations, the B97D/6-31G(d) level of theory was used, which is a smaller but more computationally manageable level of theory. The GGA density functional theory with dispersion correction B97D (Grimme, 2006) has performed well compared with benchmark coupled cluster calculations for cation-benzene clusters and dimers of corannulene (error < 1 kcal/mol B97D/cc-pVTZ) (Janowski et al., 2011; Neves et al., 2011; Martin et al., 2018). For the molecular system **4** a dipole moment of 5.00 debye was calculated, which is slightly below (<4%) the value calculated at a higher level of theory 5.32 debye (Martin (2019)). The method used here computes binding energies of 40.9 kcal/mol, which is larger than that calculated at a higher level of theory B97D/cc-pVTZ = 38.1 kcal/mol but should provide preliminary insight into the dynamics of the system (Martin, 2019). In simulating the  $C_3H_3^+$  -**4** system, there was minimal impact of the fictitious mass on the energetics, as others have also documented (Schlegel et al., 2002) and therefore the default mass of 100 amu was used. A timestep of 0.1 fs

was employed to ensure energy conservation during the simulation. No angular momentum was included in the system to provide a better understanding of the vibrational degrees of freedom. Gaussian 16 was used for all of the electronic structure and AIMD calculations (Frisch et al., 2016).

## 5.3 Results and discussion

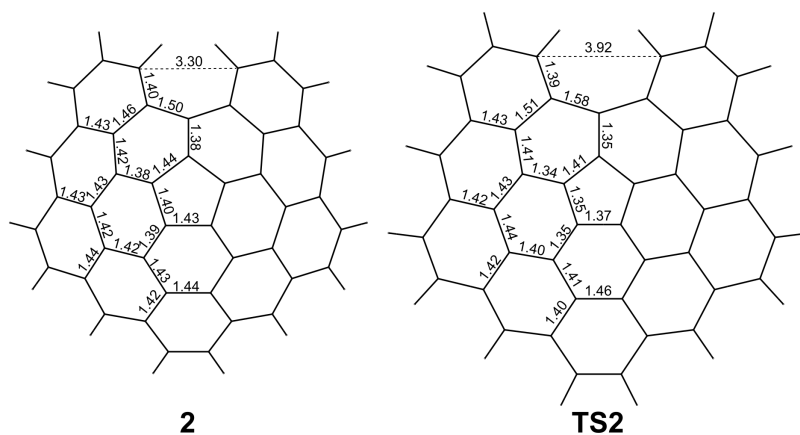
### 5.3.1 Inversion of curved PAH at flame temperatures and timescales

The energies and geometries of the transition state for inversion of molecules **1**, **2** and **3** are displayed in Figure 5.2. For the smallest structure corannulene **1** the barrier is low at 11 kcal/mol, due to the planar transition state. Enlarging the PAH so that it was similar in size to those found in soot **2** increases the inversion barrier considerably, raising it to 59 kcal/mol. The transition state was still found to be planar for this geometry.



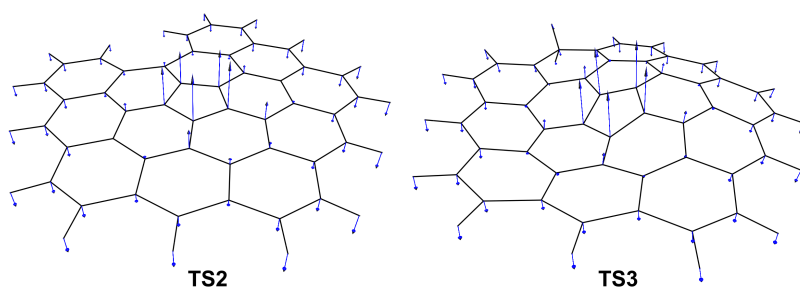
**Figure 5.2:** Energies and geometries of the inversion transition states.

Figure 5.3 shows the bond lengths of the equilibrium geometry and the transition state showing the considerable strain in the system. There is a notable reduction in bond lengths at the pentagonal site. For the bay site, there is a considerable increase in the distance between the bay exterior carbons, 3.30 Å to 3.92 Å and a lengthening of the bonds around the baysite 1.50 Å to 1.58 Å. This flattening expands the exterior rings and compresses the interior carbon network and is consistent with strain from  $\sigma$ -bonding.



**Figure 5.3:** Geometries of molecule **2** at equilibrium and at the transition state **TS2**.

Closing the bay site of **2** to form species **3** nearly doubles the inversion barrier. Figure 5.2 shows the S-shaped transition state formed due to this bay closure. It is important to note that for the S-shaped transition state, the inversion still involves all core carbon atoms flipping from one side to the other. Figure 5.4 shows the imaginary frequency associated with the planar transition state for **2** and the S-shaped transition state for **3**. The main difference in the transition state is the warped nature of **TS3** with the skeletal strain essentially disrupting the planar  $\pi$ -bonding network. This interplay between planarity and curvature in small pentagon containing PAHs has been observed previously by [Martin et al. \(2018\)](#).



**Figure 5.4:** Molecular geometries with blue arrows indicating the relative amplitude and direction of the imaginary vibrations associated with the transition states of molecules **2** and **3**.

Increasing the number of pentagons increases the barrier to inversion. Figure 5.5 shows the transition state energies and geometries for cPAH containing one **3**, two **4** and three **5** pentagonal rings. A modest increase is seen between one and two pentagonal rings from 114 to 138 kcal/mol respectively. Integration of three pentagonal rings significantly increases the inversion barrier with molecule **5** barrier rising to 360 kcal/mol. The transition state geometries are heavily strained and S-shaped thus significantly disrupting the  $\pi$ -bonding.

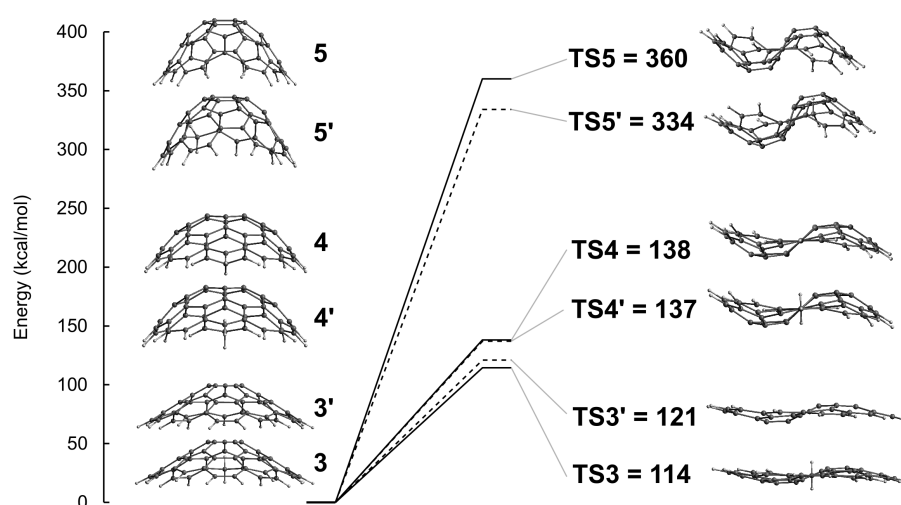


**Figure 5.5:** Inversion barriers and molecular geometries for molecules **3**, **4** and **5** as well as their  $\pi$ -radicals **3'**, **4'** and **5'** dashed line.

Minimal changes in the inversion barrier were seen for the  $\pi$  radicals compared with the closed shell structures. In the case of **TS3'**, there is even an increase in the inversion barrier. A possible explanation is that the loss of hydrogen leads to an increased aromaticity and stability of the transition state. This suggests that the aromaticity is more important than the  $\pi$  radical nature. Little change was seen for the two pentagon containing molecule's transition state **TS4/TS4'**. The most strained structure, **5**, has the most significant radical effect decreasing the barrier for inversion by 26 kcal/mol, but this is near negligible given how high the barriers are.

The geometries and frequencies calculated were used to compute the inversion rate for the species in Figure 5.1. The reciprocal of the inversion rate constant

was used,  $1/k = \tau$ , which can be thought of as a characteristic time for inversion, as a function of the temperature. The characteristic time can be compared to the time scale of soot formation, which in a premixed flame ranges from micro to milliseconds [Frenklach \(2002b\)](#). Any characteristic time below a millisecond could be important for early soot formation, as above this value no inversion can occur on the time scale of soot formation. Another distinction can be made considering the temperature in the flame where soot forms which are near 1500 K ([Wang, 2011](#)). Figure 5.6 shows that only corannulene has considerable low temperature inversion **1**, which is a well known result experimentally verified by [Scott et al. \(1992\)](#). Molecule **2** is able to invert at high temperatures only. However, for the other PAHs, the temperature required for them to invert during soot formation timescales is much too high, and it is more likely that the molecules would break down before this threshold was reached. The same is true for radicals of these PAHs.

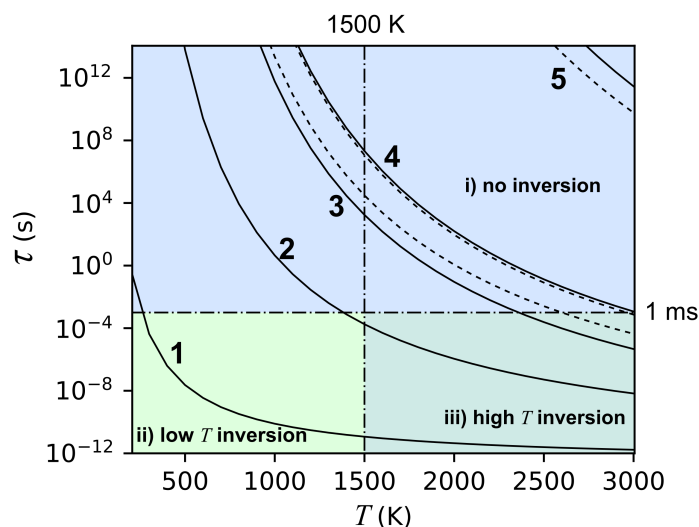


**Figure 5.6:** Characteristic time for inversion for the species shown in Figure 5.1 with  $\pi$ -radicals shown in dashed line.

In order to extend this analysis to consider the onset of rigidity in smaller curved PAH, the size dependency of the inversion is explored. This was achieved by using the exponential relationship between the characteristic time and the barrier for inversion calculated for the species in Figure 5.1, to determine a barrier of 66.3



## 5.3 Results and discussion

**Table 5.1:** Inversion barriers  $E_{inv}$  (kcal/mol), values from the Arrhenius fitting of the form  $k = A \exp(-E_a/k_bT)$  ( $s^{-1}$  and kcal/mol), the rate of inversion at 1500 K ( $cm^3 mol^{-1} s^{-1}$ ) and the characteristic time,  $\tau = 1/k$ , at 1500 K (s).

| Species | $E_{inv}$ | $A$                   | $E_a$ | Rate at 1500 K         | $\tau$ at 1500 K        |
|---------|-----------|-----------------------|-------|------------------------|-------------------------|
| 1       | 11        | $3.76 \times 10^{12}$ | 11.2  | $8.62 \times 10^{10}$  | 11.6 ps                 |
| 2       | 59        | $3.10 \times 10^{12}$ | 60.0  | $5.62 \times 10^3$     | 180 $\mu$ s             |
| 3       | 114       | $5.64 \times 10^{13}$ | 116.5 | $5.76 \times 10^{-4}$  | 1737 s                  |
| 3'      | 121       | $1.70 \times 10^{13}$ | 121.6 | $3.28 \times 10^{-5}$  | $30.5 \times 10^3$ s    |
| 4       | 138       | $1.09 \times 10^{13}$ | 139.6 | $4.74 \times 10^{-8}$  | $21.1 \times 10^6$ s    |
| 4'      | 137       | $1.47 \times 10^{13}$ | 138.7 | $8.65 \times 10^{-8}$  | $11.6 \times 10^6$ s    |
| 5       | 360       | $1.32 \times 10^{15}$ | 365.5 | $6.82 \times 10^{-39}$ | $1.50 \times 10^{38}$ s |
| 5'      | 334       | $8.07 \times 10^{14}$ | 339.3 | $2.69 \times 10^{-35}$ | $36.2 \times 10^{33}$ s |

kcal/mol that would provide a characteristic time of 1 ms at 1500 K. This allows incorporation of inversion barriers previously calculated by others at similar levels of theory (Biedermann et al., 1999; Chen et al., 2014b) to provide a more complete picture of when inversion will be halted at flame temperatures under the timescales of interest. Figure 5.7 shows the inversion barrier for different species as a function of the total number of hexagonal and pentagonal rings. It is important to note that a pentagonal ring in this context is defined as an internal pentagon surrounded by 5 hexagonal rings or an exterior pentagon that has  $>3$  neighbouring hexagonal rings that are adjacent to each other. This definition was utilized in a previous study of Gaussian curvature and the integration of curvature (Yapp et al., 2017a; Martin et al., 2018).

Three different size ranges were found for the inversion behaviour of pericondensed cPAH. For  $6 \leq N_{rings} < 11$  inversion occurs rapidly at flame temperature. For  $11 \leq N_{rings} \leq 15$  inversion does not occur for species with  $\geq 2$  pentagonal rings but is possible for species containing a single pentagonal ring. For  $15 < N_{rings}$ , the PAH structures are stable to inversion and remain curved during the entirety of soot formation.

Considering the impact of inversion on soot formation a few conclusions can be drawn. For small curved PAH, inversion is expected to be an important

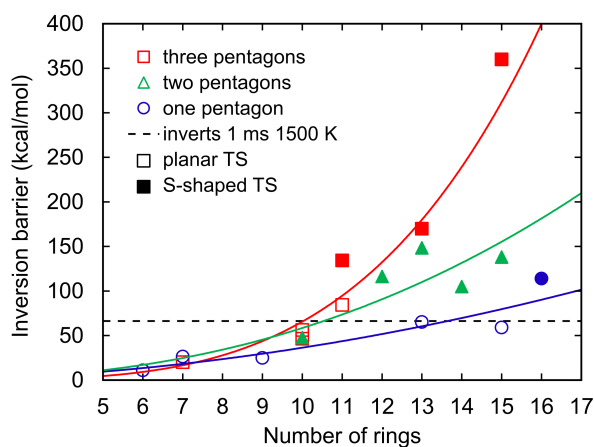


**Figure 5.7:** Inversion barrier as a function of the number of rings for structures in this work and from previously studied cPAH (Biedermann *et al.*, 1999; Chen *et al.*, 2014b). The dashed line highlights the inversion barrier 66.3 kcal/mol which provides a characteristic time of 1 ms at 1500 K from our calculations.

consideration. A PAH like corannulene will invert rapidly under flame conditions, which will result in a cancelling out of the flexoelectric dipole moment effects. This is somewhat seen in the similar vapour pressure of perylene and corannulene (Chickos *et al.*, 2002). Addition of rings increases the inversion barrier. For the size of PAH seen in early soot particles, the inversion is not rapid enough to be important at flame temperatures and timescales. The  $\pi$ -radical nature does not significantly lower the barrier for inversion indicating that size and curvature dictate inversion dynamics more than radical character.

Further work is needed to understand the rate of inversion of cPAH inside clusters as barriers for inversion of cPAH have been found to decrease in the presence of a planar PAH (Karton, 2014; Denis, 2015) or in different molecular environments (Juríček *et al.*, 2014). However, it is worth noting that these effects were only seen for small curved PAH with planar transition states. It appears that the transition from planar to S-shaped transition states determines when the cPAH becomes rigid at flame temperatures. This can be seen in Figure 5.7 where the larger barriers for inversion are predominately for those species with S-shaped transition states (denoted by filled symbols).

While it seems unlikely inversion will occur for cPAH found in early soot particles the suggestion of an interaction with a chemi-ion needs to be considered to see if it can catalyse an inversion. This will be considered for molecule **4** in the presence of  $C_3H_3^+$ . Figure 5.8 shows the barrier for inversion, which was lowest when going from the convex arrangement to the transition state **4+**(. The transition state energy barrier was similar, 140 kcal/mol, compared to without an ion, 138 kcal/mol, indicating the presence of the ion has a minimal effect on the inversion barrier and therefore the dynamics of the bowl.

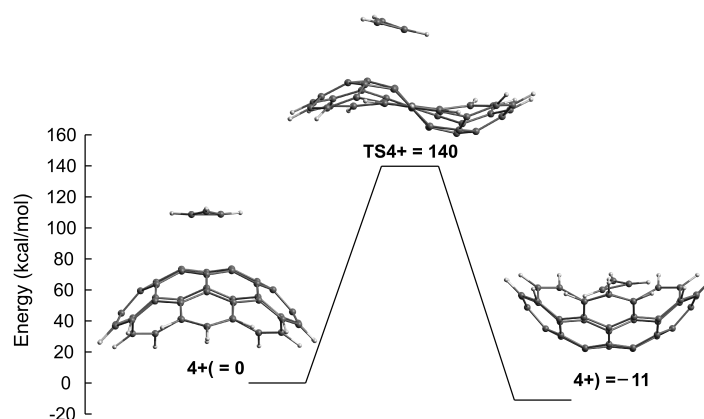


**Figure 5.8:** Barrier for inversion for molecule **4** in the presence of an ion.

### 5.3.2 Fluctuations of the dipole moment

AIMD simulations were performed in order to consider the fluctuations of the dipole moment of a cPAH at temperatures in the flame where soot inception occurs. A chemi-ion was also included to gain insight on the impact of high temperatures on the flexoelectric dipoles of these curved PAHs and the curved PAH - chemi-ion dynamics. As the inversion dynamics are minimally impacted by the chemi-ion, these two phenomena can be considered independently of inversion. The chemi-ion was placed on the top surface of the bowl as this is the expected binding site for an ion, as the flexoelectric dipole will align to interact with the positive charge. The simulation was run for half a picosecond in order for the thermal energy to equilibrate and stabilize. Subsequently, the dynamics of molecule **4** and the chemi-ion  $C_3H_3^+$ , **4+**(, was followed over 2 ps.

Figure 5.9 shows the trajectory of the atomic positions over the first picosecond. Concentrating on the cPAH fluctuations, it is seen that the carbon atoms near the middle of the aromatic plane have a reduced range of motion compared to the rim atoms on the PAH. The main low frequency vibrations observed are bending mode vibrations on the edge, occurring with a frequency of 250–350 femtoseconds (fs). This vibration will impact the local flexoelectric dipole moment. Instead of calculating the dipole moment at every time step, which would have been prohibitively slow, geometries were chosen over one of these bending modes and single point energy calculations were performed on the cPAH to compute the dipole moment (Figure 5.9b). The equilibrium dipole moment was 5.00 Debye and therefore the dipole moment is found to fluctuate by  $\pm 0.5$ – $1.0$  Debye, or  $\pm 10$ – $20\%$ . This analysis showed that at temperatures in the flame where soot

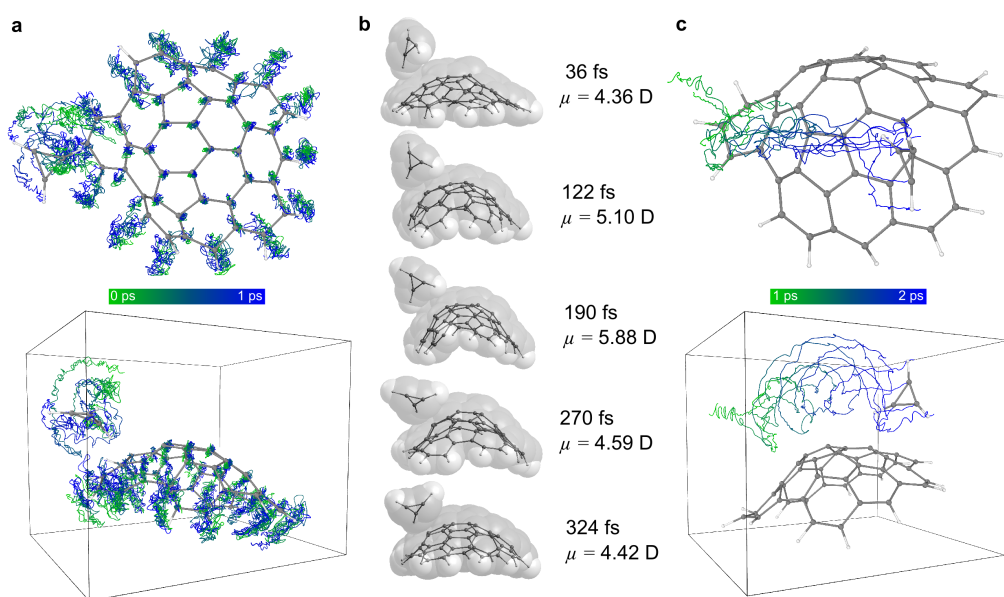


**Figure 5.9:** Dynamics of molecule 4 and the chemi-ion. a) dynamics of the complex over the first picosecond shown with a line at each atom with the geometry at 1 ps shown with a ball and stick model. b) Fluctuation of the bowl during a low frequency bending mode vibration. The dipole moment was calculated for the bowl fragment. c) dynamics of the complex over the second picosecond with the geometry shown with the ball and stick model for the final structure at 2 ps.

forms large cPAH have a persistent polarity that does not decrease substantially during thermal excitation.

The movement of the chemi-ion was then considered in the presence of the cPAH. While the equilibrium geometry shows a binding site above the out of plane carbon atoms, the chemi-ion was found to move freely across the surface from the top of the bowl to the edge of the bowl. Figure 5.9a shows the chemi-ion trapped at the rim of the cPAH for the first picosecond. This is likely due to the charge concentration at the edge of the PAH, where it is known that an induced dipole forms on rim carbon atoms due to charge partitioning in C–H bonds (Martin et al., 2017c). The binding of the chemi-ion does not appear to be influenced strongly by the bending mode of the cPAH as seen in Figure 5.9b. Figure 5.9c shows the movement of the chemi-ion across the top surface of the cPAH interacting with the pentagonal carbon atoms where the flexoelectric effect is greatest (Martin et al., 2017d).

Further work is required on the dynamics of a curved PAH -ion system, with this work only considering a combination of a moderately sized curved PAH with the  $C_3H_3^+$  ion. There are several other combinations, some potentially important ones being the  $CHO^+$  - curved PAH combination as well as smaller cPAH with chemi-ions.

The main conclusions about dipole fluctuations observed for molecule **4** are suggested to hold for all cPAH with a large inversion barrier, namely above the 66 kcal/mol threshold described earlier. However, other suggested ionic interactions, such as with  $CHO^+$ , may interact more strongly with a cPAH than  $C_3H_3^+$  (Chen and Wang, 2017), and such could result in a different effect. Additionally, this study of chemi-ion-cPAH interactions does not capture long term dynamics for accurate statistics of the chemi-ion cPAH system, and more computationally efficient methods are necessary to explore longer dynamics.

The impact of rotational degrees of freedom was also neglected in order for the fluctuations in dipole moments for cPAH to be more clearly observed. However, rotational effects are expected to enhance binding if anything, as has been previously found for homogeneous dimers of planar PAHs (Schuetz and Frenklach, 2002; Wong et al., 2009). The movement of the chemi-ion across

the surface of the bowl and rim provides an opportunity for reactions with the rim carbon atoms (Chen and Wang, 2017). These reactions would result in a positively charged PAH, which have been observed previously using mass spectrometry (Homann, 1998), and could be of importance.

### 5.4 Conclusions

In this chapter, it has been demonstrated that curved PAHs of around 15 rings in size with 2 pentagonal rings are unable to invert at flame temperatures. It is therefore expected that these curved PAHs are persistently polar at flame temperatures. The transition from invertible to rigid at 1500 K for cPAH was found to be between 11 and 15 rings and often corresponded to a S-shaped transition state as opposed to planar transition states for PAHs that could readily invert.  $\pi$ -radicals and chemi-ions were not found to influence the inversion barrier substantially. *Ab initio* MD simulations were used to study the fluctuation of the dipole moment for molecule **4** at flame temperatures. The dipole moment was found to fluctuate, by  $\pm 10$ -20%, suggesting curved PAHs will still have substantial dipole moments even in flame conditions. Dynamics between a chemi-ion and curved PAH was also briefly studied. The chemi-ion mainly interacted with the pentagonal atoms on the curved PAH due to the flexoelectric effect as well as the rim due to charge concentration. These results indicate that the polarity of curved PAH is substantial even at flame conditions and may be important to consider in soot formation.

## Chapter 6

# Kinetics of seven-member ring bay closures in PAHs

*In this chapter, the kinetics of seven-member ring formation in PAHs containing a five-member ring is studied by density functional theory. The pathways studied include integration of a seven-member ring by the hydrogen-abstraction-acetylene-addition (HACA) mechanism for two different PAHs, one closed shell and one resonance-stabilised-radical (RSR) PAH. The rate of seven-member ring formation by HACA was seen to be faster for the RSR PAH. Formation of a seven member ring by bay closure processes facilitated through hydrogen abstraction, hydrogen addition, carbene formation, and direct cyclisation were also studied for two PAHs. The rate constants determined for the pathways were then used in kinetic simulations in 0D homogeneous reactors to compare the pathways, highlighting the importance of hydrogen abstraction based pathways, and carbene pathways at higher temperature. The formation of seven-member rings occurred within 1 ms for all cases studied, suggesting that seven-member ring formation in PAHs containing a five-member ring is possible at flame temperatures.*

### Collaborative Contributions

The work presented in this chapter has been published in *Combustion and Flame* and is primarily a collaboration with Gustavo Leon. Gustavo Leon performed the gas-phase kinetic simulations in a 0D homogeneous reactor and also analysed and prepared the figures relating to these simulations with the author. Gustavo Leon also helped edit the rest of the manuscript. The electronic structure calculations, rate calculations, figure preparation and manuscript writing were done by the author.

### 6.1 Introduction

Several studies have focused on the integration of curvature into graphenic PAHs, by focusing on the mechanisms by which a pentagonal or five-member ring could form. Such studies have included the five-member bay-capping reaction determined by [You et al. \(2011\)](#), which was then used in a kinetic Monte Carlo (KMC) simulation to show curvature occurring during singular PAH growth ([Whitesides and Frenklach, 2010](#)). The formation of curved PAHs has also been seen in KMC-molecular dynamics studies by [Violi et al. \(2004\)](#) as well as by [Raj et al. \(2009\)](#) and [Yapp et al. \(2017b\)](#), where bay-capping and five-member ring migration reactions were seen to be key to curvature integration. Other pathways to five-member ring formation and integration include those based on cyclodehydrogenation. This was studied computationally by density functional theory (DFT) calculations on various pathways including hydrogen addition, hydrogen abstraction, and carbene formation, all followed by bay closures ([Violi, 2005b](#)). Recent work has also shown five-member ring addition can occur by reaction between an aryl radical and allenes ([Zhao et al., 2019](#)). The resulting curved PAHs have been seen to possess strong permanent dipole moments due to the flexoelectric effect which could have implications for their ability to interact with ions in flames ([Martin et al., 2017b, 2018; Martin, 2019](#)). Curved PAHs with five-member rings have also been seen to be more reactive with regards to both oxidation ([Raj et al., 2013; Singh and Frenklach, 2016](#)) and recently growth by HACA ([Raj et al., 2013; Raj, 2019](#)).



However, less focus has been given to PAHs containing seven-member rings. Whilst five-member ring PAHs result in bowl shaped structures with positive Gaussian curvature, seven-member ring PAHs result in saddle-shaped structures that have negative Gaussian curvature. Distorted nano-graphenes containing seven-member rings have been synthesized by several methods (Márquez et al., 2018; Mughal and Kuck, 2012). In addition, the formation of five-seven member ring defect pairs is key to forming closed fulleroid structures (Schwerdtfeger et al., 2015) and can occur by the Stone-Wales transformation (Eggen et al., 1996; Ewels et al., 2002; Ma et al., 2009), although these transformations are typically slow at flame conditions (Scott, 1996). The formation of seven member rings by sequential HACA additions in small PAHs has also been considered by Kislov et al. (2013). In addition, it has been found that net negative curvature and hence seven-member ring formation is key to forming disordered 3D graphene sheets, a nanostructure key to several carbon materials such as charcoal and activated carbon (Martin et al., 2019a). In particular, Martin et al. (2019a) found that chains of alternating five-member and seven-member rings resulted in line dislocations between the six-member rings of graphene, and this was required for the 3D graphene nanostructure to form. NMR studies on nanoporous carbons for a variety of applications such as batteries and supercapacitors have also shown that these carbons contain curved domains with both five and seven member rings (Forse et al., 2014, 2015). Seven-member ring formation has also been seen in tight-binding molecular dynamics studies of benzene combustion and soot particles at higher temperatures, as well as in molecular dynamics studies of trace-metal assisted soot formation (Mao et al., 2017; Mao and Luo, 2019; Saha et al., 2010). Ricca et al. (2011) also computed the infrared spectra of PAHs with five-seven member ring pairs and found that the PAH spectra are shifted due to this defect and could be important for class A astronomical spectra.

Formation of seven-member rings and coupled five-seven-member pairs in PAHs is therefore of interest for carbon nanomaterials in a variety of fields but kinetic studies of how this could occur are sparse. Therefore, **the purpose of this chapter** is to computationally explore the possibility of seven-member ring formation by a variety of mechanisms considered previously for five and six member ring

formation in PAHs by means of density functional theory and transition state theory calculations. Kinetic simulations in a 0D reactor at concentrations of species typical in flames and a variety of temperatures are then performed to see which routes are more important and how likely seven-member ring formation could be under flame conditions.

### 6.2 Methodology

In this chapter, seven-member ring formation was considered to occur in two overarching categories. The first is by the HACA mechanism which underpins PAH growth and has been shown to be key to integrating five-member rings into flat PAH systems (Frenklach et al., 1985; Frenklach, 2002a; Raj, 2019). This was studied for two PAHs, A and B seen in Fig. 6.1. In both cases, the seven-member ring is formed by the HACA process acting on a bay site next to a five-member ring. PAH B also contains an odd-number of carbon atoms, making it a resonance-stabilised radical (RSR) PAH, which has recently been suggested as potential precursors for soot nanoparticle formation in flames (Johansson et al., 2018). A jump process illustration of the formation of seven-member rings by HACA are seen in Fig. 6.2. The second category of seven-member ring formation studied in this work is by bay closure reactions. This was also studied for two PAHs, C and D also seen in Fig. 6.1, with the required seven-member bay again adjacent to a five-member ring. PAHs containing sites similar to these have also recently been observed in early soot imaged by high resolution atomic force microscopy (Commodo et al., 2019), so studying the kinetics of seven-member ring formation could be of interest in soot as well.

There are four possible pathways by which the seven-member bay closure can occur. The first three involve an initial step, namely hydrogen abstraction, hydrogen addition, or formation of a carbene, followed by cyclisation and hydrogen loss to complete the bay closure. The fourth pathway involves the direct cyclisation occurring right away, followed by subsequent hydrogen loss. Jump process illustrations of these pathways are given in Fig. 6.3.

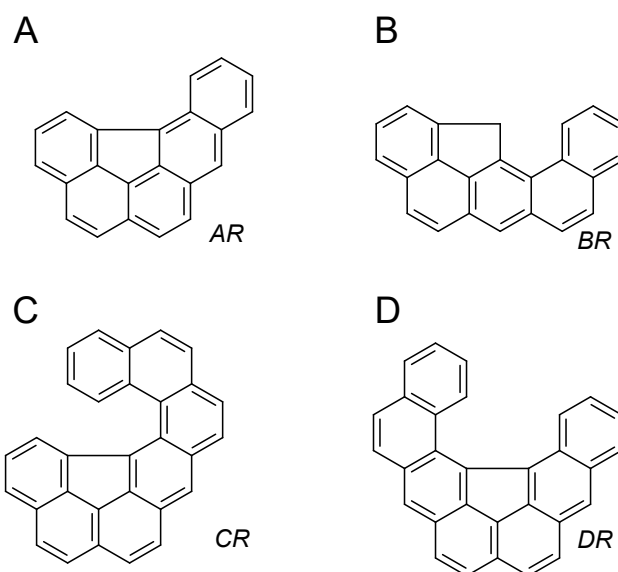
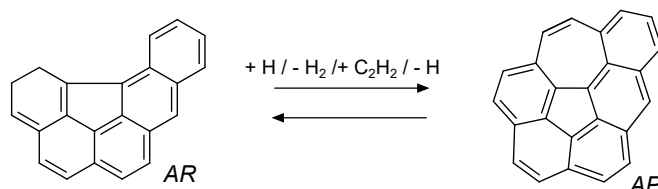


**Figure 6.1:** The starting PAH reactants which can integrate seven-member rings studied in this work. PAHs A and B can form a seven-member ring by the HACA mechanism. PAHs C and D can form a seven-member ring by bay closure reactions.

Formation of R7 on PAH A



Formation of R7 on PAH B

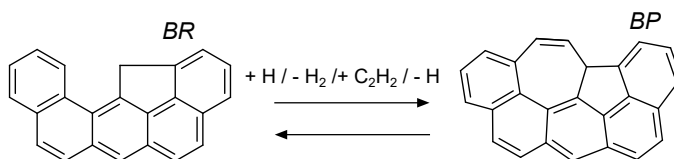


**Figure 6.2:** Jump process illustrating formation of seven-member ring by HACA acting on PAH A and B.

The formation of a seven-member ring without an adjacent five-member ring has not been considered in this work. Nevertheless, the integration of five-seven-member ring pairs into graphenic substrates is a key line dislocation

## 6 CHAPTER 6

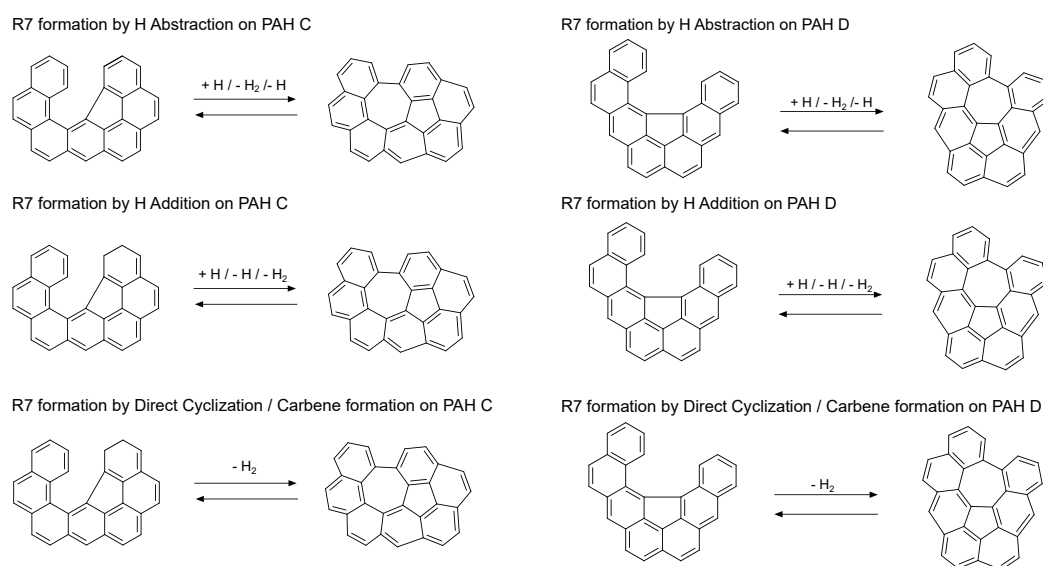


**Figure 6.3:** *Jump process illustrating formation of seven-member ring by various bay closures in PAH C and D above.*

in the formation of 3D graphenic structures as well as fulleroids as mentioned previously (Martin et al., 2019a). All ten routes to seven-member ring formation were explored further computationally by means of density functional theory and rate constant calculations, followed by kinetic simulations performed at conditions relevant to flames. This is done in order to gain some insight on the likelihood of PAHs with seven-member rings forming in flames.

### 6.2.1 Density Functional Theory calculations

The potential energy surfaces of the HACA and bay closure reactions considered in this study were constructed by first performing geometry optimisations and frequency calculations at the B3LYP/6-311+G(d,p) level of theory for all reactants, intermediates, transition states and products. The B3LYP functional has been shown to give reasonable geometries for systems concerning polycyclic aromatic hydrocarbons (Violi, 2005b; Kislov et al., 2005). For transition states, the vibrational frequencies were checked to ensure that only one imaginary frequency was present and that this vibrational mode corresponded to the reaction in question. In addition, since several studies have reported that

B3LYP underpredicts the barrier heights of such organic reactions (Temelso et al., 2006; Hou and You, 2017), single point energies were also calculated for all species using the modern density functional M06-2X and with Dunning’s cc-pVTZ basis set. This functional has been shown to give improved energy estimates for reactions involving hydrogen abstraction from various PAHs (Hou and You, 2017). It is worth mentioning that PAH B is an RSR, and as such the pathways computed involve radical-radical reactions. Such reactions can require multireference methods, but due to the computational restrictions, the M06-2X functional was used for this pathway as well. It has also been previously shown that the M06-2X functional gives very good descriptions of the energetics of bond dissociation in which two radicals are produced. This was seen to be true for a variety of hydrocarbons and hydrocarbon derivatives, and hence the M06-2X functional is adopted in this work (Zhao and Truhlar, 2008). In general, the barriers predicted by B3LYP were lower compared to those of M06-2X, as expected. All density functional theory calculations were performed using the Gaussian 16 program suite (Frisch et al., 2016).

### 6.2.2 Computation of rate constants

The energetics and molecular properties computed by the DFT calculations were then used for the rate constant calculations. Rate constants were determined by means of canonical transition state theory as implemented in the Arkane package within the Reaction Mechanism Generator (RMG) software (Gao et al., 2016). Transition state theory was used as the reactions studied in this work have appreciable barriers, and so more sophisticated methods such as variational transition state theory were not used in this work. Nevertheless, it is likely that the rates reported here will be an overestimate as a result. The rate constant is therefore given by the standard transition state expression:

$$k = \frac{k_B T}{h} \frac{q^\ddagger}{\prod_i^{n_{\text{reactants}}} q_i} \exp\left(\frac{-\Delta E_0}{RT}\right) \quad (6.1)$$

where  $k$  is the rate constant,  $k_B$  is the Boltzmann constant,  $T$  is temperature,  $h$

---

is Planck's constant,  $q$  is the total partition function, and  $\Delta E_0$  is the classical barrier height. The partition functions for all species were computed using the Rigid-Rotor, Harmonic-Oscillator (RRHO) model. To account for quantum tunneling effects, the simple Wigner correction was employed (Wigner, 1932), giving the tunnelling correction factor,  $C_W$  as follows:

$$C_W = 1 - \frac{1}{24} \left( \frac{h\nu^\ddagger}{k_B T} \right)^2 \quad (6.2)$$

with  $\nu^\ddagger$  being the magnitude of the imaginary frequency of the transition state. The Eckart tunneling correction is also commonly used (Truhlar and Kuppermann, 1971), but the difference between the Eckart and Wigner correction in this case was negligible. In the temperature range used for the 0D reactor simulations, the tunneling factors are between 1.03 at 1000 K and 1.01 at 2500 K for both Eckart and Wigner tunneling corrections. The rate constants were computed at a range of temperatures (200 K to 3000 K) and then fitted to the modified Arrhenius expression, again as implemented in Arkane:

$$k = A \left( \frac{T}{T_0} \right)^n \exp \left( \frac{-E_A}{RT} \right) \quad (6.3)$$

In all the rate constants here, sufficient fits could be obtained with  $T_0$  taken as 1 K, allowing one less parameter to be used. Even though the reaction pathways studied in this work contain several unimolecular reactions, pressure dependence was not considered. Generally, pressure dependence is less likely for larger species, such as the PAHs studied here as there are several more modes available for the randomisation of the internal energy from collisions. To check this, pressure-dependent rate constants were computed for the main unimolecular reactions in the HACA pathway for PAH A, including the bay closures in AS2a and AS2b to form AS3a and AS3b as well as hydrogen loss from AS3a and AS3b to form product AP. RRKM theory as implemented in KiSThelp (Canneaux et al., 2014) was used for the calculations, with nitrogen as the bath gas and collisional

parameters of PAHs estimated based on their molecular weight using the results of Wang and Frenklach (1994):

$$\sigma = 1.234(M_w^{0.33}) \quad (6.4)$$

$$\frac{\epsilon}{k_B} = 37.15(M_w^{0.58}) \quad (6.5)$$

The rate constants as a function of temperature and pressure are plotted below.

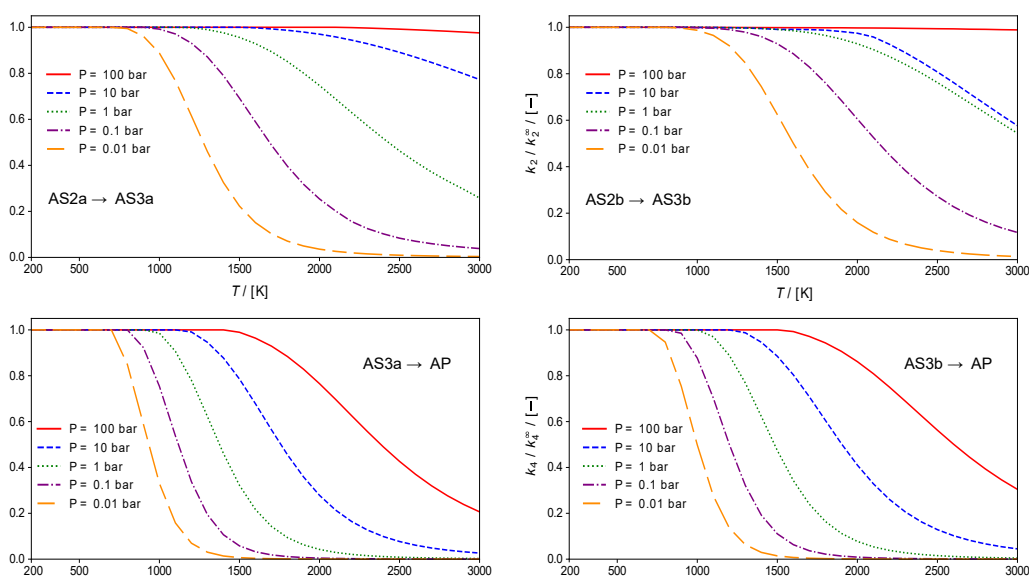


**Figure 6.4:** Falloff curves for the pressure-dependent rate constants of the unimolecular reactions in the HACA pathway for PAH A as computed by RRKM theory with tight transition states.

The calculations suggest that these unimolecular reactions are weakly pressure dependent. For the bay closures of AS2a and AS2b, the closure rate constants are at 96% and 99% of their high pressure limits at 1500 K and 1 bar. The rate constants of hydrogen losses from AS3a and AS3b are at 32% and 47% of their high pressure limits at 1500 K and 1 bar. As such, pressure dependence was not considered further in this work.

### 6.2.3 Kinetic simulations

The rate constants provide a first estimate on the time scale required for the formation of seven-membered rings in the presence of combustion species. However, the different reaction pathways affecting a starting site compete with each other making it difficult to determine the likeliness of each one. To estimate the conditions under which pathway is favoured, a set of kinetic simulations in a 0D isothermal reactor model were used. The simulations were performed using both the B3LYP/6-311G+(d,p) and the M06-2X/cc-pVTZ levels of theory. For each case a reaction time of 100 ms was used under a pressure of 1 atm and temperatures of 1000, 1500, 2000, and 2500 K. The mole fractions for all cases were assumed to be  $10^{-5}$  for the starting PAH,  $10^{-3}$  H, 0.1 H<sub>2</sub>, 0.1 C<sub>2</sub>H<sub>2</sub> and the rest of N<sub>2</sub> which resemble typical flame conditions. Using an identical mole fraction of the starting PAH allows a straightforward comparison of the time required for each studied reaction to happen and the net rates of formation for the seven-member ring containing curved products.

## 6.3 Results and Discussion

### 6.3.1 Potential Energy Surfaces

The potential energy surfaces computed at the B3LYP/6-311+G(d,p) were constructed for all ten pathways. Optimised geometries at this level of theory are also shown for all species in each pathway. The energies computed using the single point energy calculations at the M06-2X/cc-pVTZ level of theory are shown in parentheses and in red in the potential energy surfaces.

Every species and transition state is given a name shown in italics next to the structure in the potential energy surface figures. The naming convention is as follows: The first capital letter refers to the initial PAH (A, B, C or D). This is followed by either S for species or TS for transition state. The next number refers to which intermediate or transition state it is along the pathway, and the final lowercase letter refers to the type of pathway and route, as in most cases there



are two routes for each type of pathway (abstraction, addition, carbene formation, direct cyclisation). In this case, a and b are for hydrogen abstraction based routes, c and d are for hydrogen addition based routes, e and f are for carbene based routes, and g and h are for direct cyclisation routes. For simplicity, the PAH reactants and products are denoted by AR and AP, BR and BP, CR and CP, and DR and DP as these structures are shared between multiple pathways. As an example, the first intermediates in PAH C forming a seven-member ring facilitated by hydrogen abstraction will have the names CS1a and CS1b for the two different routes.

In the subsequent discussions of the pathways, the M06-2X/cc-pVTZ energies are used as these were used for the computation of the rate constants in the kinetic simulations. Comparing the two levels of theory, it seems that B3LYP tends to predict lower barriers for hydrogen abstractions, with most abstractions in this work having barriers between 12-14 kcal/mol compared to 16-19 kcal/mol predicted by M06-2X. This agrees with previous findings for hydrogen abstractions (Hou and You, 2017). Similarly, B3LYP tends to predict lower barriers for hydrogen addition and direct cyclisation processes in this work compared to M06-2X. However, for processes involving hydrogen migration or loss, B3LYP sometimes predicts slightly higher barrier than M06-2X. Nevertheless, it is observed that the barriers predicted by M06-2X and B3LYP are generally similar, as are the predicted trends. Comparison of the barrier heights computed at the M06-2X/cc-pVTZ level of theory for hydrogen abstraction by H atoms and acetylene addition in this work to those computed at the G3(MP2,CC) level of theory by (Kislov et al., 2005) also shows reasonable agreement, with the G3 calculations suggesting abstraction barriers between 16-18 kcal/mol, very similar to this work. The acetylene addition barriers in (Kislov et al., 2005) are predicted to be between 2 and 6 kcal/mol compared to 4 to 8 kcal/mol in this work, again suggesting reasonable agreement.

### 6.3.1.1 PAH A - HACA growth pathways a and b

Figure 6.5 presents the potential energy diagram for HACA growth on PAH A resulting in the formation of a seven-member ring adjacent to a five-member ring,

or a 7-5 ring pair. The first step in this process is hydrogen abstraction from one of the two edge carbons in the bay site next to the five-member ring, resulting in a radical site. The barriers for the two abstractions are very similar, at 18.4 and 17.3 kcal/mol for the sites using M06-2X. The two radicals AS1a and AS1b can interconvert by hydrogen migration, as indicated by the  $\updownarrow$ . This is described further in section 6.3.1.12 for all PAHs, as the transition states for this have higher relative energies. The next step involves acetylene ( $C_2H_2$ ) addition to the formed radical site. Again the addition step has very similar and rather low barriers for the two routes, requiring 5.8 and 4.7 kcal/mol. From here, AS2a and AS2b, three sub-pathways are possible. For the first sub-pathway, the last two steps are seen to have significantly higher barriers than the first two. The cyclisations have barriers of 26.0 and 31.2 kcal/mol, followed by hydrogen loss with barriers of 27.4 and 29.1 kcal/mol to complete the seven-member ring formation. The overall formation process is exothermic, releasing 33.2 kcal/mol, and little difference is seen between the two routes. An alternative route to achieve the bay closure is presented in Figure 6.6. Here, the hydrogen migrates towards the acetylene from the PAH, requiring larger barriers of 27 and 33.5 kcal/mol for the two pathways. The subsequent cyclisations have very low barriers of 4.5 and 2.5 kcal/mol, but in both cases the final hydrogen loss requires overcoming a much larger barrier of 45.7 and 45.5 kcal/mol, which would suggest this pathway is less preferable. Formation of ethynyl-substituted side products ASPa and ASPb is also possible by hydrogen loss from AS2a and AS2b, and is shown in Figure 6.7. This hydrogen loss does have a large barrier of 41.1 and 41.5 kcal/mol for the two cases, but is a one step process.

## 6.3 Results and Discussion

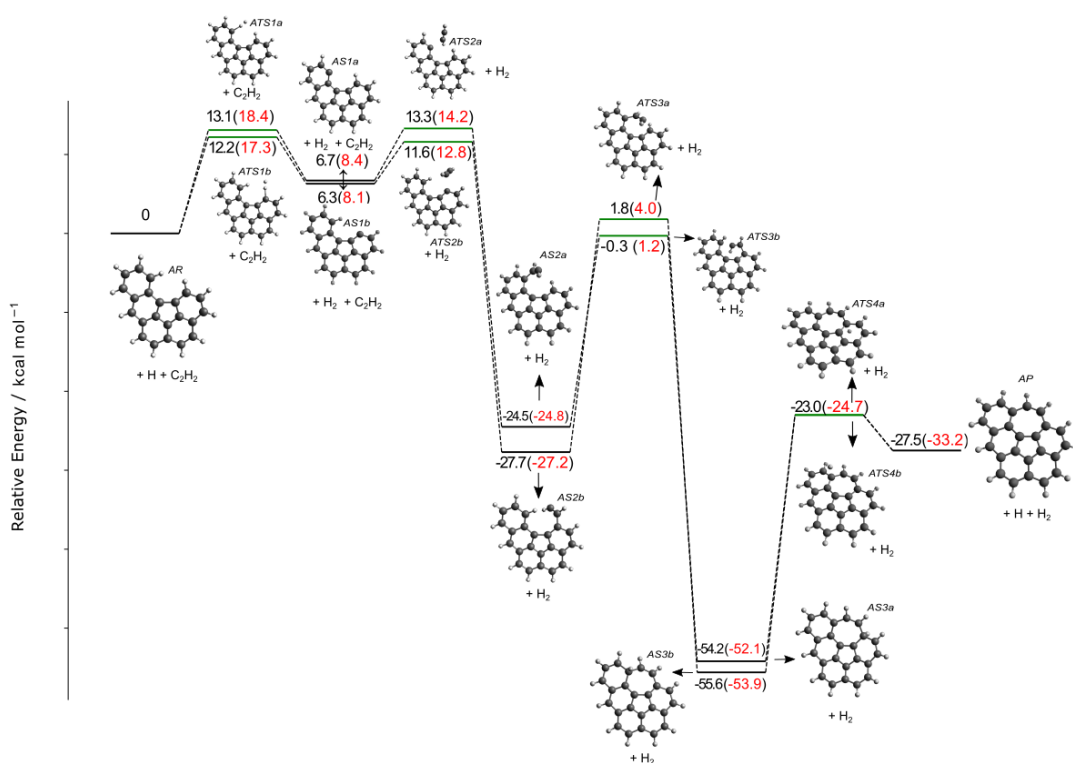


**Figure 6.5:** Potential energy surface for the formation of a seven-member ring by HACA on PAH A at 0 K. The relative energy of the different species are computed at both the M06-2X/cc-pVTZ and B3LYP/6-311+G(d,p) level of theory.

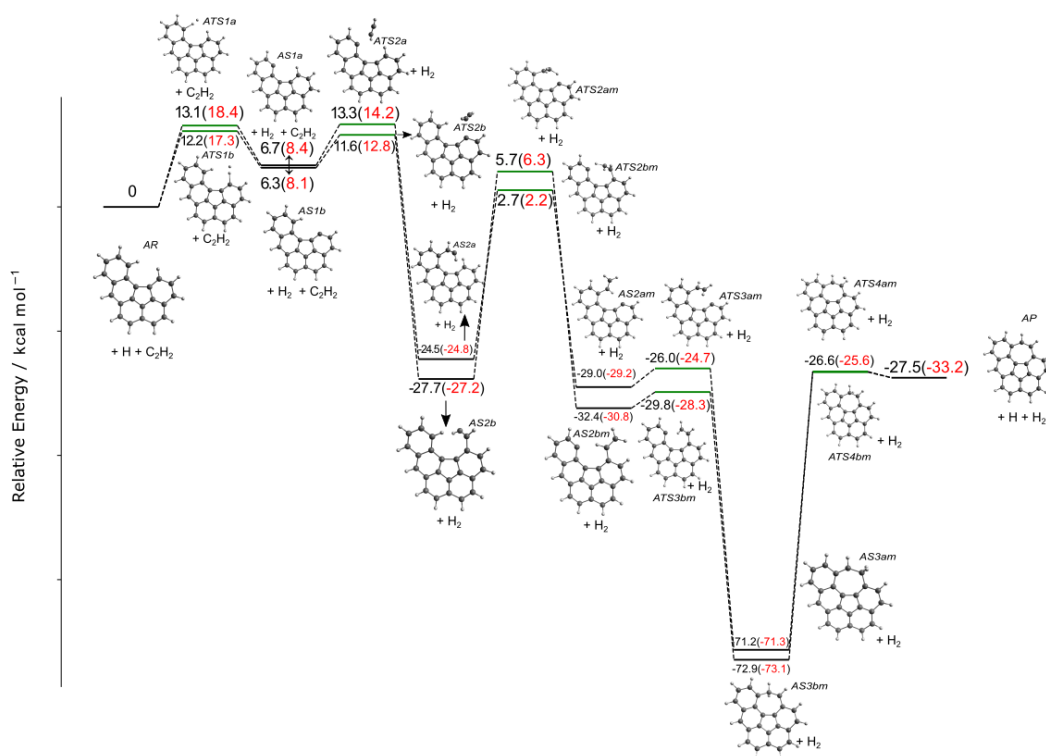


**Figure 6.6:** Potential energy surface for the formation of a seven-membered ring by HACA followed by hydrogen migration to the acetylene group on PAH A at 0 K. The relative energy of the different species are computed at both the M06-2X/cc-pVTZ and B3LYP/6-311+G(d,p) level of theory.

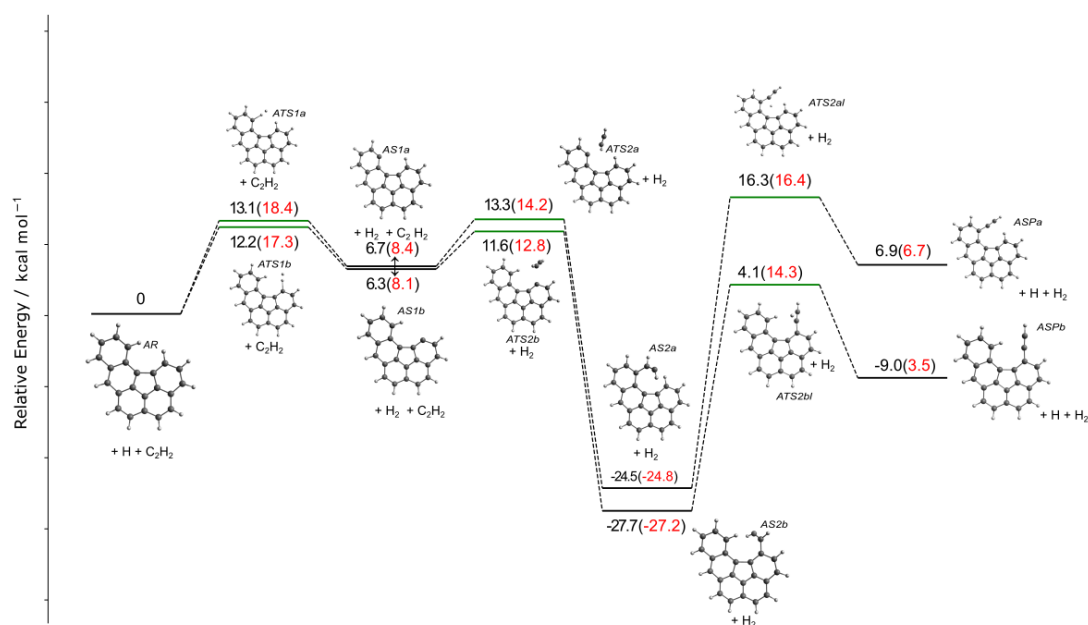


**Figure 6.7:** Potential energy surface for the formation of ethynyl-substituted products by HACA on PAH A at 0 K. The relative energy of the different species are computed at both the M06-2X/cc-pVTZ and B3LYP/6-311+G(d,p) level of theory.

### 6.3.1.2 PAH B - HACA growth pathways a and b

Figure 6.8 presents the potential energy diagram for HACA growth on PAH B. The required steps are the same as for PAH A: hydrogen abstraction followed by acetylene addition, ring cyclisation, and then hydrogen loss to finish the process. However, of note here is that PAH B contains an odd number of carbon atoms and is a RSR PAH and provides a point of comparison to PAH A, a closed-shell species. As with PAH A, there are two carbons on which the the initial hydrogen abstraction may occur, either next to the five-member or 6-member ring, resulting in two routes. This first abstraction step again has very similar barriers of 16 and 18.6 kcal/mol for the two routes, and are also similar to the hydrogen abstraction step for PAH A. The barriers predicted by M06-2X are also slightly higher than those by B3LYP, which is consistent with PAH A. In both abstraction cases, the resulting radical is a triplet, which was found to have lower energy than the singlet state. Additionally, the triplet state remains energetically favoured

over the singlet throughout all the pathways for PAH B in this case, and no inter-crossing was predicted by the single-reference DFT method in this work. However, unlike PAH A, the two acetylene addition steps have quite different barriers of 8.5 kcal/mol and 4.7 kcal/mol, with acetylene addition next to the five-member ring being more difficult. The difference is even more significant for the cyclisation, with the barrier for the cyclisation adjacent to the five-member ring being 20.3 kcal/mol whilst it is only 3.2 kcal/mol for the cyclisation next to the 6-member ring route. Nevertheless, the cyclisation appears to be substantially easier for PAH B than PAH A in both cases. The hydrogen loss steps have higher barriers for both routes being 30.9 and 23.5 kcal/mol. These barriers are also very similar to the hydrogen loss barriers for PAH A. For both PAH A and PAH B the hydrogen loss has the largest barrier. Again, the overall formation process for the seven-member ring is exothermic, releasing 45.3 kcal/mol in this case. As with PAH A, PAH B can undergo bay closure by the hydrogen migrating to the acetylene from the adjacent site on the PAH before cyclisation occurs. In this case, the migration barriers for the two routes are significantly lower than PAH A at 12.9 kcal/mol and 20.7 kcal/mol respectively. The cyclisation barriers are higher than PAH A at 4.9 and 6.5 kcal/mol, but the final hydrogen loss is again substantially easier than PAH A at 28.9 and 30.9 kcal/mol, which would suggest this pathway may be more important than for PAH A. PAH B can also form various side products. Hydrogen loss from BS2a and BS2b produce ethynyl-substituted PAHs like with PAH A, but this requires overcoming a high barrier of 38.4 kcal/mol. BS2b can also undergo a direct ring-enlargement by which the five-member ring is converted into a seven-member ring ([Fascella et al., 2005](#)). The first step involves the acetylene bonding to the five-member ring to create a four-member ring, with a barrier of 25 kcal/mol. The adjacent four-member and five-member rings then fuse to create a seven-member ring, with a moderate barrier of 13.2 kcal/mol. This results in a product with a seven-member ring as well, but noticeably not adjacent to a five-member ring.

## 6.3 Results and Discussion

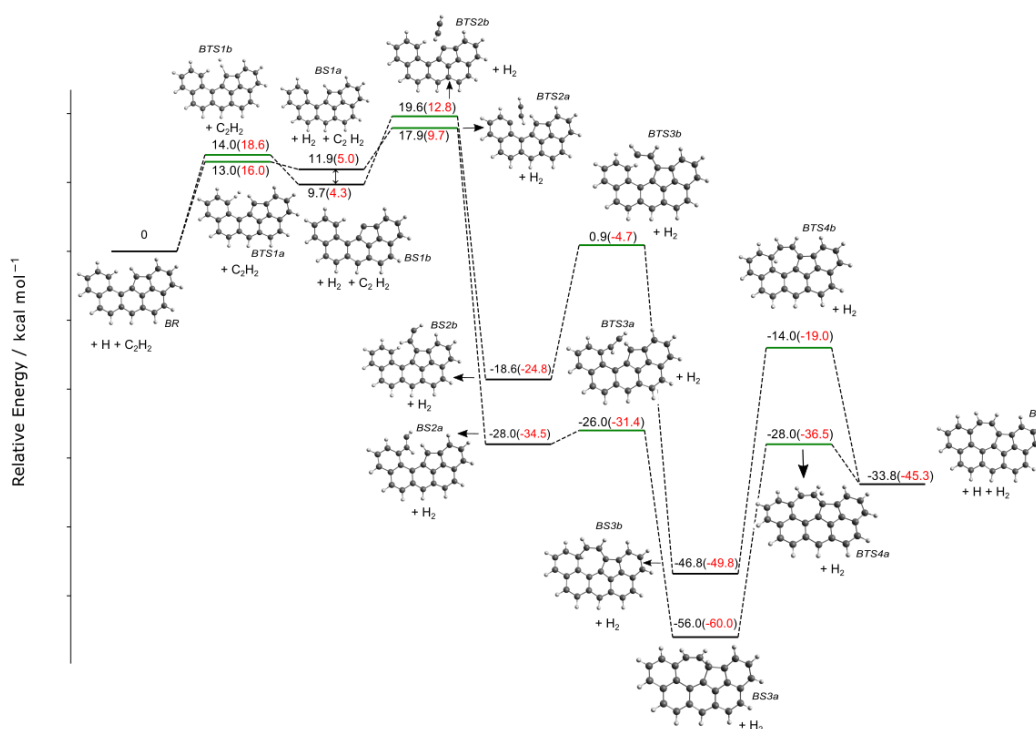


**Figure 6.8:** Potential energy surface for the formation of a seven-member ring by HACA on PAH B at 0 K. The relative energy of the different species are computed at both the M06-2X/cc-pVTZ and B3LYP/6-311+G(d,p) level of theory.

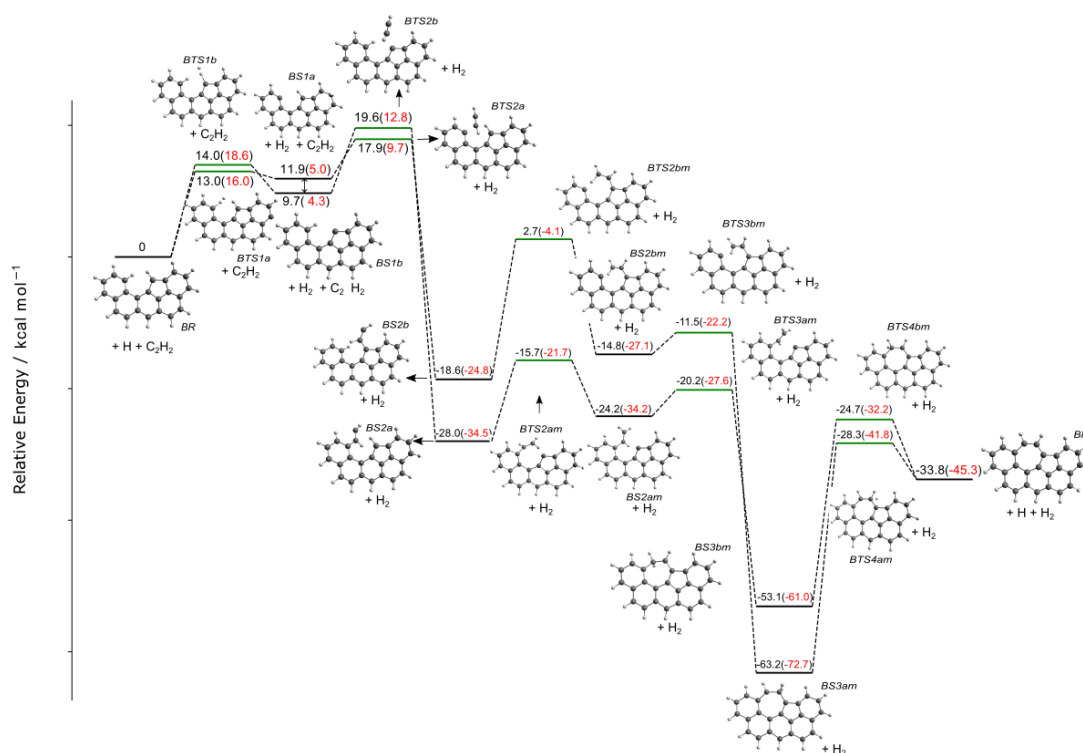


**Figure 6.9:** Potential energy surface for the formation of a seven-member ring by HACA followed by hydrogen migration to the acetylene group on PAH B at 0 K. The relative energy of the different species are computed at both the M06-2X/cc-pVTZ and B3LYP/6-311+G(d,p) level of theory.



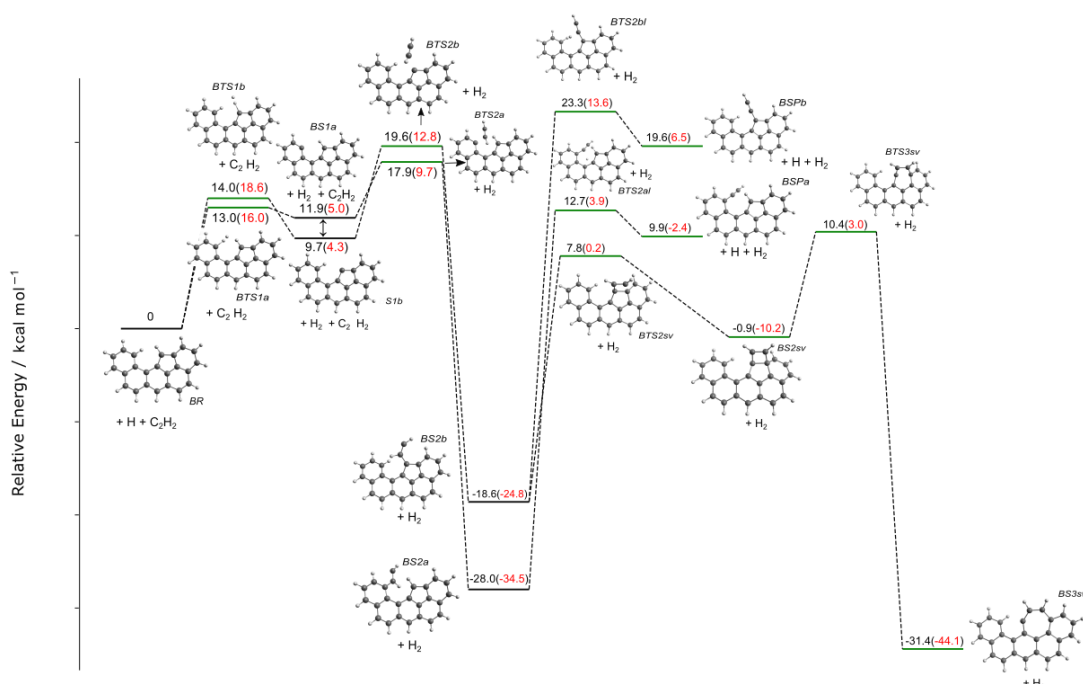


**Figure 6.10:** Potential energy surface for the formation of byproducts of HACA on PAH B at 0 K. The relative energy of the different species are computed at both the M06-2X/cc-pVTZ and B3LYP/6-311+G(d,p) level of theory.

### 6.3.1.3 PAH B - Rearrangement of five-seven-member ring pair to hexagons

The product of the HACA process on PAH B, BP is able to have its five-seven member ring pair converted to a six-six member ring pair through a similar mechanism by which azulene is converted to naphthalene as described by Long et al. (2018). This is presented in Figure 6.11. First, hydrogen addition occurs on the seven-member ring, with a small barrier of 3.6 kcal/mol. This hydrogen then migrates to the five-member-seven-member ring edge, which requires a large barrier of 41.1 kcal/mol and is by far the highest barrier in this pathway. From there, the five-seven member ring pair is converted into a six-member ring and five-member ring partitioned by a triangular structure, with a barrier of 9.3 kcal/mol. The five-member ring and triangle then fuse to form the second six-member ring, with a very low barrier of 3.8 kcal/mol, and being nearly 30 kcal/mol downhill. Finally, the hydrogen is ejected with a barrier of 16 kcal/mol.

## 6 CHAPTER 6

It is worth noting that a similar rearrangement is not possible with the other products AP, CP, or DP, because the five-seven member pairs in these structures are enclosed by more six-member rings.

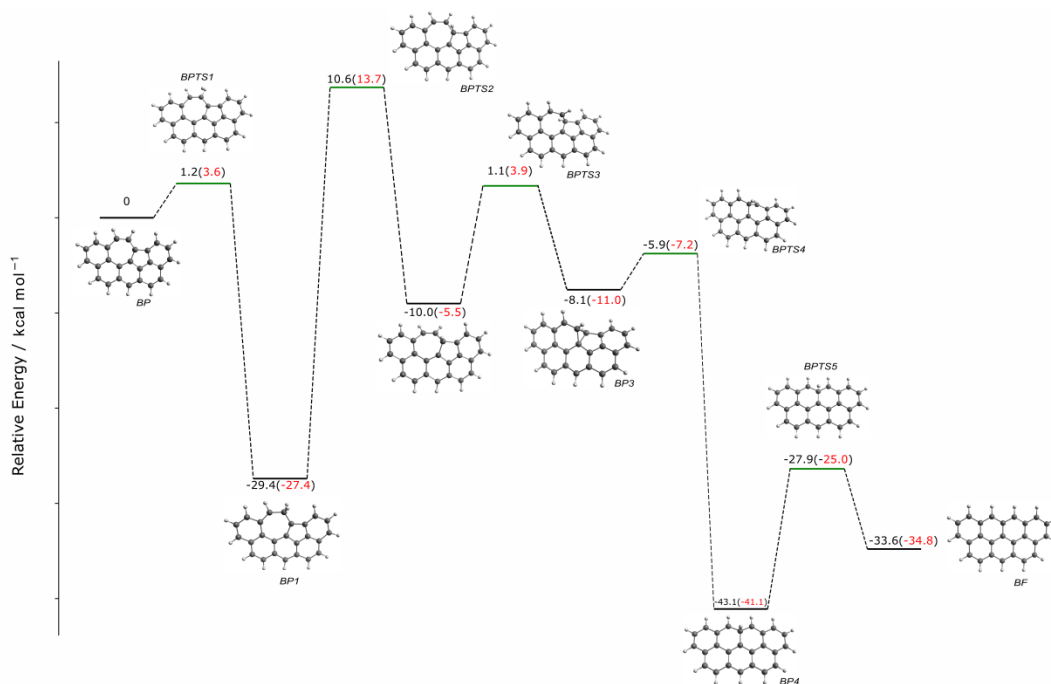


**Figure 6.11:** Potential energy surface for the formation of byproducts of HACA on PAH B at 0 K. The relative energy of the different species are computed at both the M06-2X/cc-pVTZ and B3LYP/6-311+G(d,p) level of theory.

### 6.3.1.4 PAH C - H-abstraction facilitated bay closure pathways a and b

Figure 6.12 presents the potential energy diagram for H abstraction facilitated seven-member ring bay closure in PAH C. This pathway consists of three steps: H abstraction followed by cyclisation and finally hydrogen loss to complete the closure. The barrier for the abstraction step is nearly identical for both potential sites, at 17.3 and 17.6 kcal/mol. This value is very similar to hydrogen abstractions from PAHs a and b as well. The cyclisation steps have substantially different barriers of 7.0 and 13.1 kcal/mol, with the cyclisation being easier when the initial abstraction occurs on the ring adjacent to the five-member ring. The hydrogen loss

step has similar barriers, being 31.9 and 29.7 kcal/mol. This is once again the step with the highest barrier and also has barriers similar to those seen for hydrogen losses from PAHs a and b. However, the overall process for the bay closure is endothermic requiring 10.1 kcal/mol in this case compared to the exothermicity of the HACA routes.

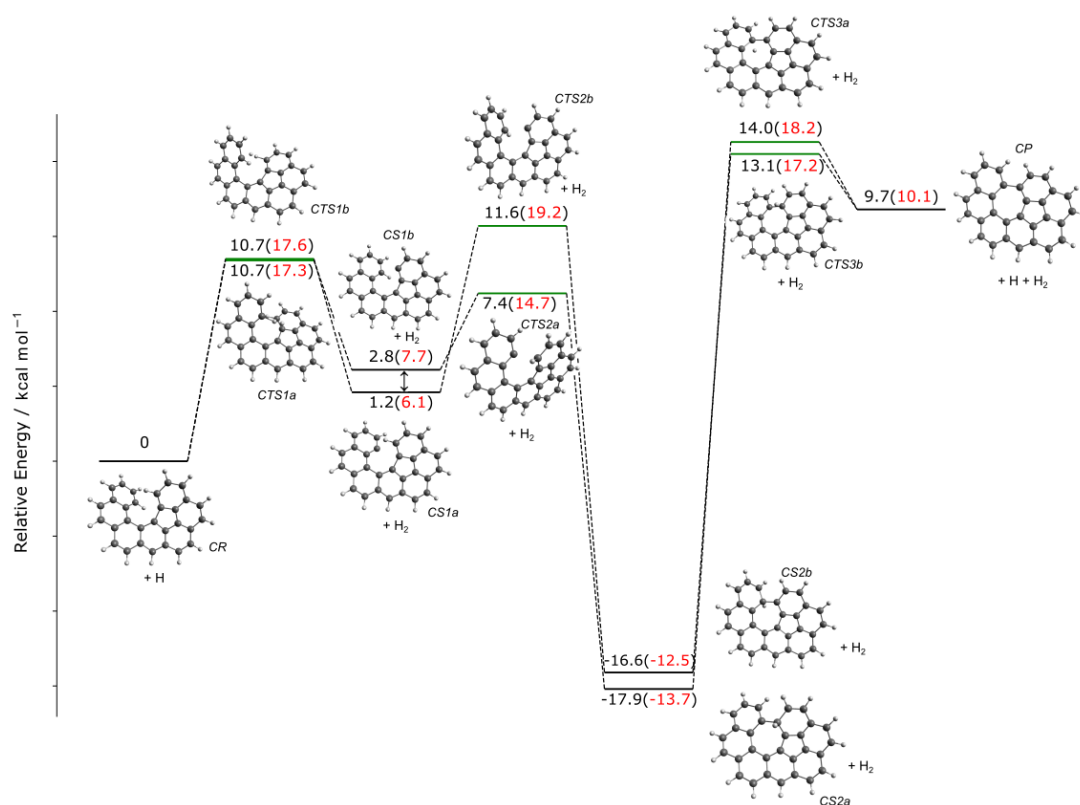


**Figure 6.12:** Potential energy surface for the formation of a seven-member ring by hydrogen abstraction (pathways a and b) followed by cyclisation and bay closure in PAH C at 0 K. The relative energy of the different species are computed at both the M06-2X/cc-pVTZ and B3LYP/6-311+G(d,p) level of theory.

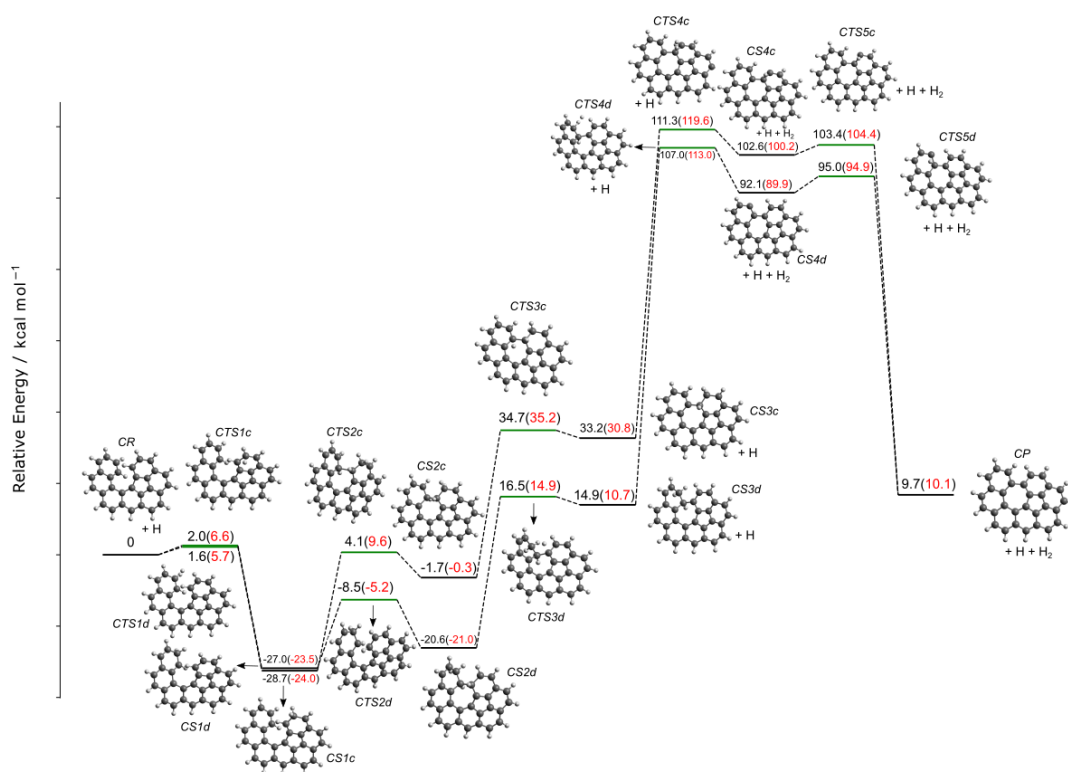
### 6.3.1.5 PAH C - H-addition facilitated bay closure pathways c and d

Figure 6.13 presents the potential energy diagram for H addition facilitated seven-member ring bay closure in PAH C. The steps in this pathway consists of hydrogen addition to the carbon atom, cyclisation, loss of a hydrogen atom, further

## 6 CHAPTER 6

---

loss of two hydrogen atoms as H<sub>2</sub>, and finally hydrogen migration to complete the closure. The initial hydrogen addition step requires low barriers for both sites, at 6.6 and 5.7 kcal/mol. The B3LYP barriers in this case are lower, at 2.2 and 2.6 kcal/mol, suggesting that hydrogen addition predictions are underestimated like those those for hydrogen abstraction. The cyclisation step has quite different barriers of 18.3 and and 33.6 kcal/mol. This results in a high energy and low energy route, with the high energy route starting with hydrogen addition to the carbon nearer the five-member ring. The hydrogen loss steps have similar barriers of 35.4 and 35.9 kcal/mol for the two routes, which is similar to hydrogen losses seen for previous processes. The H<sub>2</sub> loss step has by far the highest barriers for both routes. The barrier is for the low energy route is actually higher in this case, at 102.3 kcal/mol compared to 88.8 kcal/mol for the higher energy route. The final hydrogen migration has a very low barrier, being 4.1 kcal/mol for the high energy route and 5.0 kcal/mol for the low energy route. Clearly, the feasibility of this route is limited by the very large barriers required to overcome for the H<sub>2</sub> loss.



**Figure 6.13:** Potential energy surface for the formation of a seven-member ring by hydrogen addition (pathways c and d) followed by cyclisation and bay closure in PAH C at 0 K. The relative energy of the different species are computed at both the M06-2X/cc-pVTZ and B3LYP/6-311+G(d,p) level of theory.

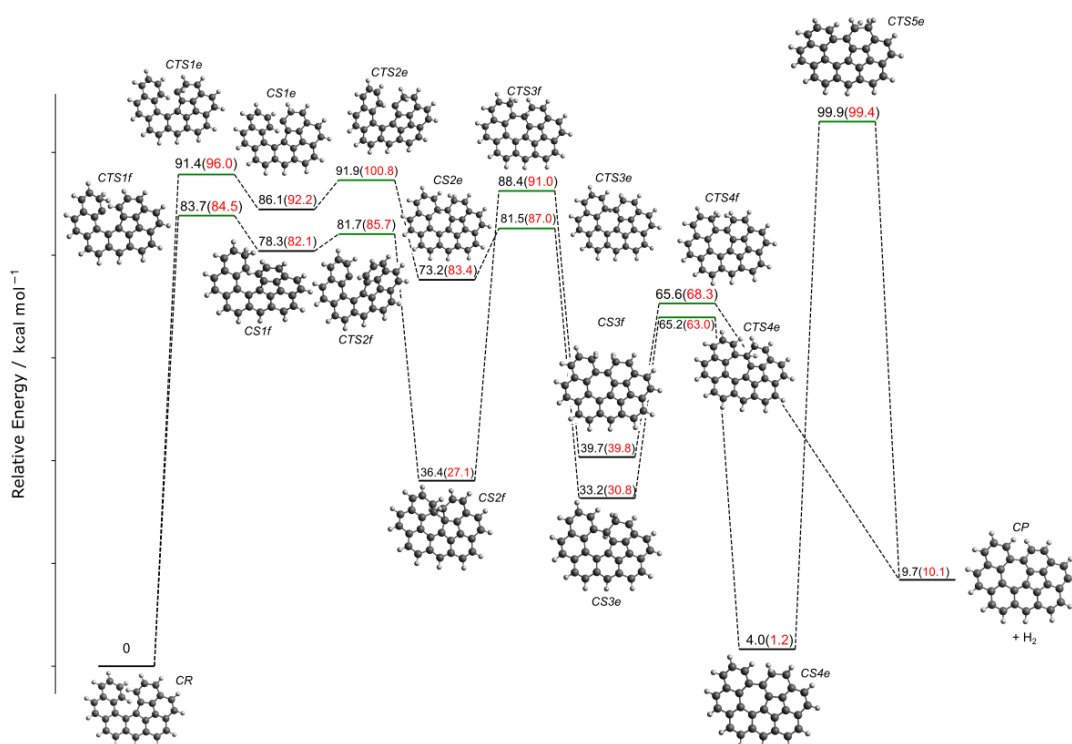
### 6.3.1.6 PAH C - Carbene facilitated bay closure pathways e and f

Figure 6.14 presents the potential energy diagram from carbene formation facilitated seven-member ring bay closure in PAH C. The steps in this pathway consists of carbene formation by hydrogen migration from the bay, cyclisation, several hydrogen migrations, and then finally the loss of two hydrogen atoms as H<sub>2</sub>. The initial hydrogen migration step requires very high barriers for both potential carbenes, at 84.5 and 96.1 kcal/mol. The subsequent bay closures both have low barriers of 8.6 and 3.6 kcal/mol. However, the resulting structures after the bay closures are quite different, with one structure forming a triangle connecting two 6-member rings at a much lower energy and the other forming

## 6 CHAPTER 6

---

the heptagon directly with a much higher energy. In the path where the heptagon forms immediately, two hydrogen migrations are required for the hydrogen to get into position to undergo H<sub>2</sub> loss with hydrogen on the carbene site. These have a low barrier of 3.7 kcal/mol followed by a more difficult migration with 32.2 kcal/mol. The final H<sub>2</sub> loss step has a very large barrier of 98.1 kcal/mol, similar to the barriers seen for H<sub>2</sub> loss in the hydrogen addition pathway. In the other path, a hydrogen migration is required to break the triangle and form the heptagon after the cyclisation, which requires a quite large barrier of 64.0 kcal/mol compared to the hydrogen migrations in the other path. However, the final H<sub>2</sub> loss in this pathway is much easier, requiring a moderate barrier of 28.5 kcal/mol. This may be the case as the H<sub>2</sub> loss occurs across an armchair site as opposed to a free edge in the first pathway.



**Figure 6.14:** Potential energy surface for the formation of a seven-member ring by carbene formation (pathways e and f) followed by cyclisation and bay closure in PAH C at 0 K. The relative energy of the different species are computed at both the M06-2X/cc-pVTZ and B3LYP/6-311+G(d,p) level of theory.

### 6.3.1.7 PAH C - Direct cyclisation bay closure pathway g

Figure 6.15 presents the potential energy diagram for direct cyclisation seven-member ring bay closure in PAH C. This is by far this simplest pathway, requiring only a cyclisation followed by H<sub>2</sub> loss. The initial cyclisation has a very large barrier of 101.7 kcal/mol, which is understandable as there is no aromatic stability to drive the bay to close as there would be with a 6-member bay closure Xue and Scott (2007). The cyclisation could only happen in the cis-orientation in this case as the trans structure was found to be unstable. The H<sub>2</sub> loss has a moderate barrier of 20.7 kcal/mol, which again occurs in an armchair site and is similar to the armchair hydrogen loss seen in the carbene route for PAH C.

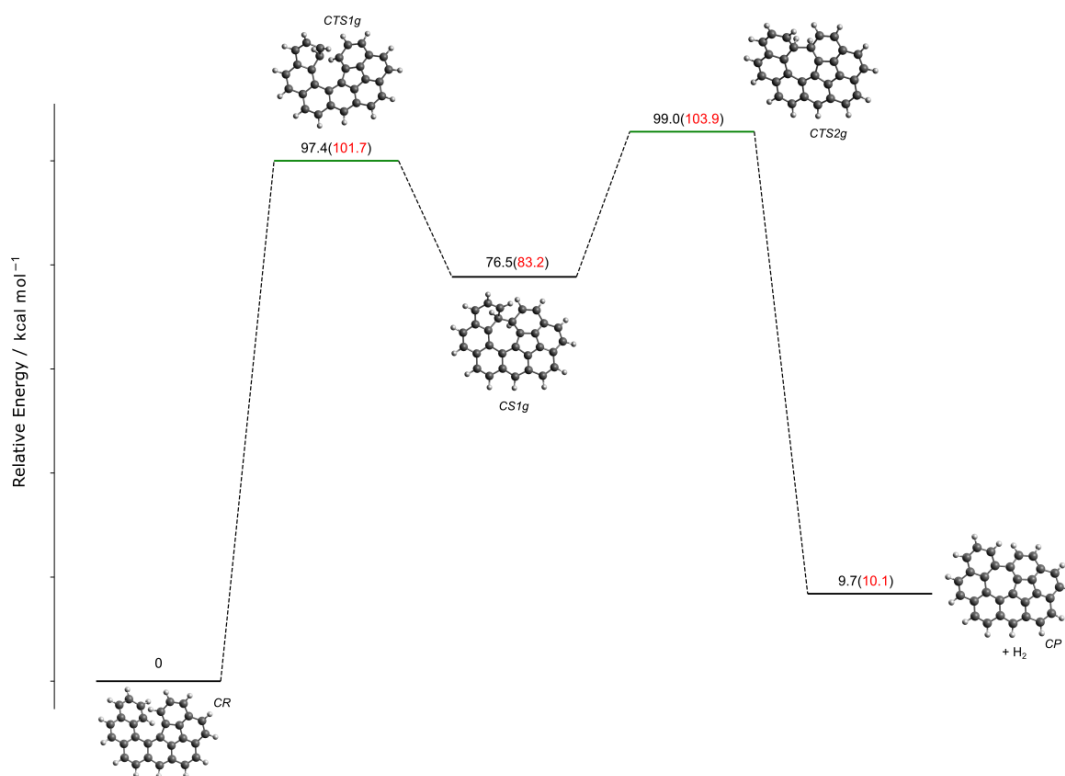


**Figure 6.15:** Potential energy surface for the formation of a seven-member ring by direct cyclisation (pathway g) and bay closure in PAH C at 0 K. The relative energy of the different species are computed at both the M06-2X/cc-pVTZ and B3LYP/6-311+G(d,p) level of theory.

### 6.3.1.8 PAH D - H-abstraction facilitated bay closure pathways a and b

Figure 6.16 presents the potential energy diagram for H abstraction facilitated seven-member ring bay closure in PAH D. The steps in this pathway are identical to those seen for PAH C. The barrier for the first abstraction step is very similar for both sites, at 18.1 kcal/mol and 17.7 kcal/mol. These barriers are similar to abstractions from PAHs A, B, and C. The cyclisation steps in this PAH have similar barriers of 7.1 and 4.9 kcal/mol, in contrast to PAH C where the cyclisations had very different barriers depending on where the initial hydrogen abstraction occurred. The hydrogen loss steps again have the largest barriers in the process, and have close barriers of 32.6 and 32.0 kcal/mol. This is very similar to what was observed for PAH C. The overall process is endothermic with 9.0



kcal/mol which is again very similar to PAH C.

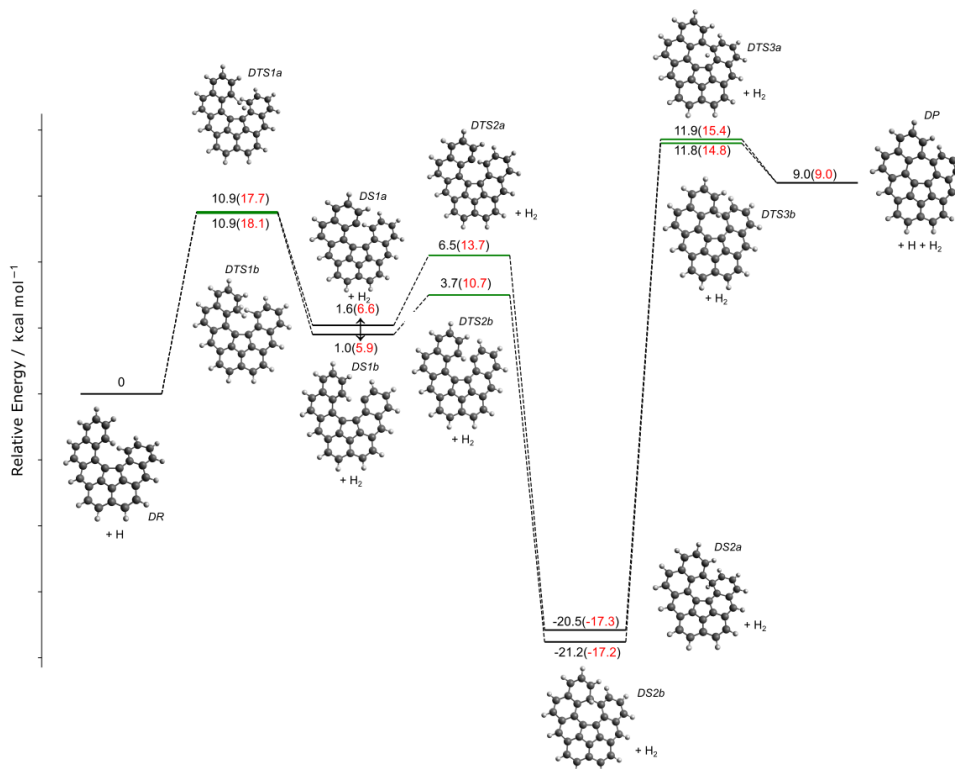


**Figure 6.16:** Potential energy surface for the formation of a seven-member ring by hydrogen abstraction (pathways a and b) followed by cyclisation and bay closure in PAH D at 0 K. The relative energy of the different species are computed at both the M06-2X/cc-pVTZ and B3LYP/6-311+G(d,p) level of theory.

### 6.3.1.9 PAH D - H-addition facilitated bay closure pathways c and d

Figure 6.17 presents the potential energy diagram for H addition facilitated seven-member ring bay closure in PAH D. The steps in this pathway are again identical to those seen for PAH C. The barriers also follow a similar trend to what was seen with PAH C. The initial hydrogen additions have very low barriers of 5.0 and 5.5 kcal/mol similar to what was observed with PAH C. The cyclisations have moderate barriers of 20.9 and 22.3 kcal/mol. The hydrogen loss steps again have barriers similar for the other routes, at barriers of 35.7 kcal/mol and 34.4 kcal/mol, whilst the H<sub>2</sub> loss steps have extremely large barriers of 100 and 99.1 kcal/mol

similar to other barriers for H<sub>2</sub> loss at a free edge. Finally, the last hydrogen migrations have low barriers of 2.8 and 3.7 kcal/mol which is similar to what is seen for PAH C as well. The only significant difference between PAH C and D is that the cyclisation steps in pathways c and d have very similar barriers whereas the barriers were quite different between pathways c and d in PAH C.

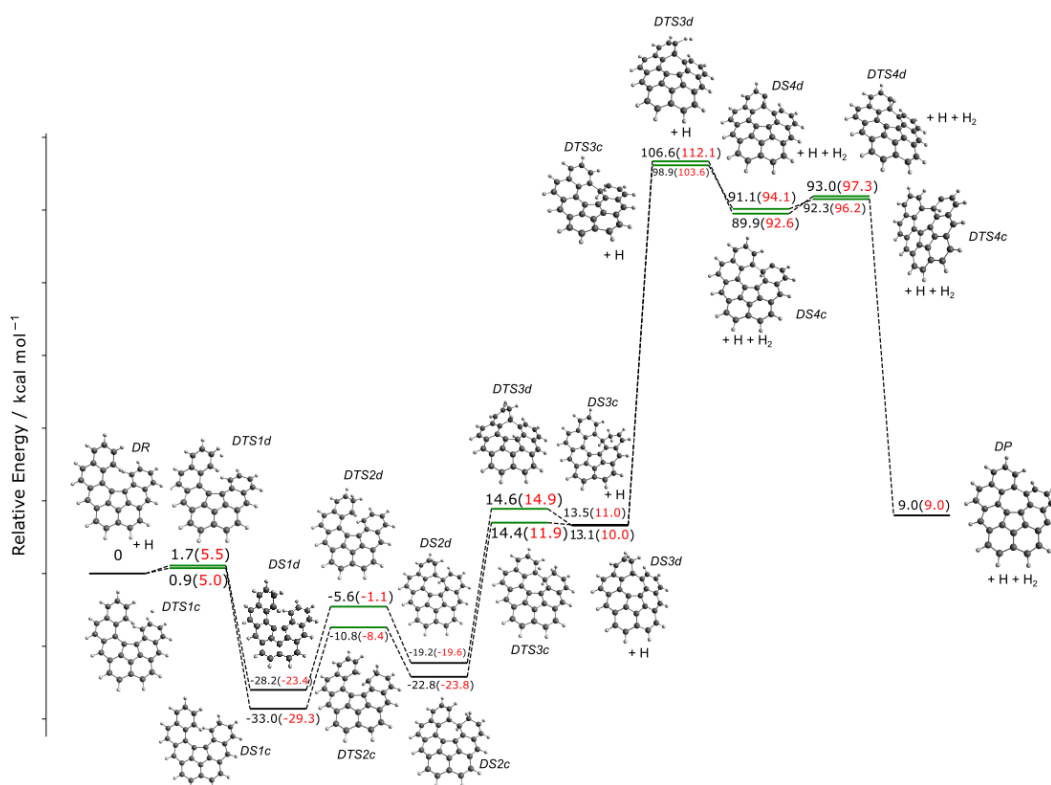


**Figure 6.17:** Potential energy surface for the formation of a seven-member ring by hydrogen addition (pathways c and d) followed by cyclisation and bay closure in PAH D at 0 K. The relative energy of the different species are computed at both the M06-2X/cc-pVTZ and B3LYP/6-311+G(d,p) level of theory.

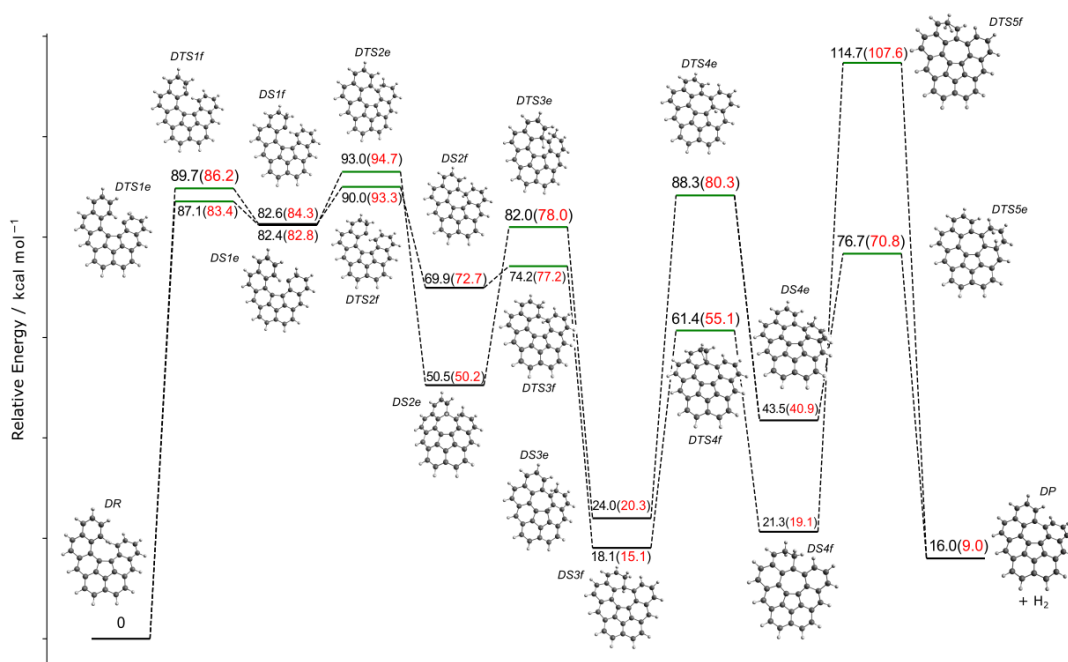
### 6.3.1.10 PAH D - Carbene facilitated bay closure pathways e and f

Figure 6.18 presents the potential energy diagram from carbene formation facilitated seven-member ring bay closure in PAH D. The steps in this pathway are essentially the same as for PAH C, as are the general trends and values for barriers.

## 6.3 Results and Discussion

---

The initial hydrogen migration step to form the carbene site again has very high barriers for both potential carbenes, at 83.4 and 86.2 kcal/mol. The subsequent cyclisations have much lower barriers of 11.9 and 8.9 kcal/mol, although these are noticeably larger than those for PAH C. Additionally, in this case the resulting structures after the bay closures are very similar, but they do have quite different energies at 72.7 and 50.2 kcal/mol respectively. For the higher energy structure, the first migration has a very low barrier of 4.6 kcal/mol. This is followed by a hydrogen migration with a much larger barrier of 40.0 kcal/mol. The final H<sub>2</sub> loss occurs across a free edge and has a characteristically high barrier of 88.5 kcal/mol, similar to what was seen for PAH C. The lower energy pathway has an initial migration with a moderate barrier of 27.8 kcal/mol, which is again followed by a much more difficult migration requiring 60.0 kcal/mol. These barriers are higher than the high energy pathway, but as a consequence, the final H<sub>2</sub> migration occurs across an armchair configuration, and has a much lower 29.9 kcal/mol barrier as a result.



**Figure 6.18:** Potential energy surface for the formation of a seven-member ring by carbene formation (pathways e and f) followed by cyclisation and bay closure in PAH D at 0 K. The relative energy of the different species are computed at both the M06-2X/cc-pVTZ and B3LYP/6-311+G(d,p) level of theory.

### 6.3.1.11 PAH D - Direct cyclisation bay closure pathways g and h

Figure 6.19 presents the potential energy diagram for direct cyclisation seven-member ring bay closure in PAH D. This is the one pathway where PAH D is completely different to PAH C. The initial direct cyclisation has a very high barrier of 98.2 kcal/mol, which is very similar to what was seen for PAH C. However, H<sub>2</sub> loss immediately after cyclisation does not appear to occur in this case, and instead several hydrogen migrations are required until H<sub>2</sub> loss can occur much like the carbene routes. In one case, only one hydrogen migration with a barrier of 43.5 kcal/mol is necessary before H<sub>2</sub> loss can occur across an armchair configuration, requiring a lower barrier of 23.4 kcal/mol. In the other case, a long series of increasingly difficult hydrogen migrations are required, with the first having a barrier of 14.5 kcal/mol, the next two having moderate barriers of

25.8 and 29.1 kcal/mol and the last having a much higher barrier of 59.4 kcal/mol. The final H<sub>2</sub> loss is also across a free edge, meaning its barrier is much higher at 82.9 kcal/mol, consistent with other losses seen across a free edge or on a singular carbon.

Across all pathways, general observations are that abstraction-based pathways are limited by the hydrogen atom loss step, hydrogen addition pathways are limited by H<sub>2</sub> loss, and carbene and direct cyclisation pathways are limited by the initial carbene formation or cyclisation steps, as well as H<sub>2</sub> loss when it occurs across a free edge.

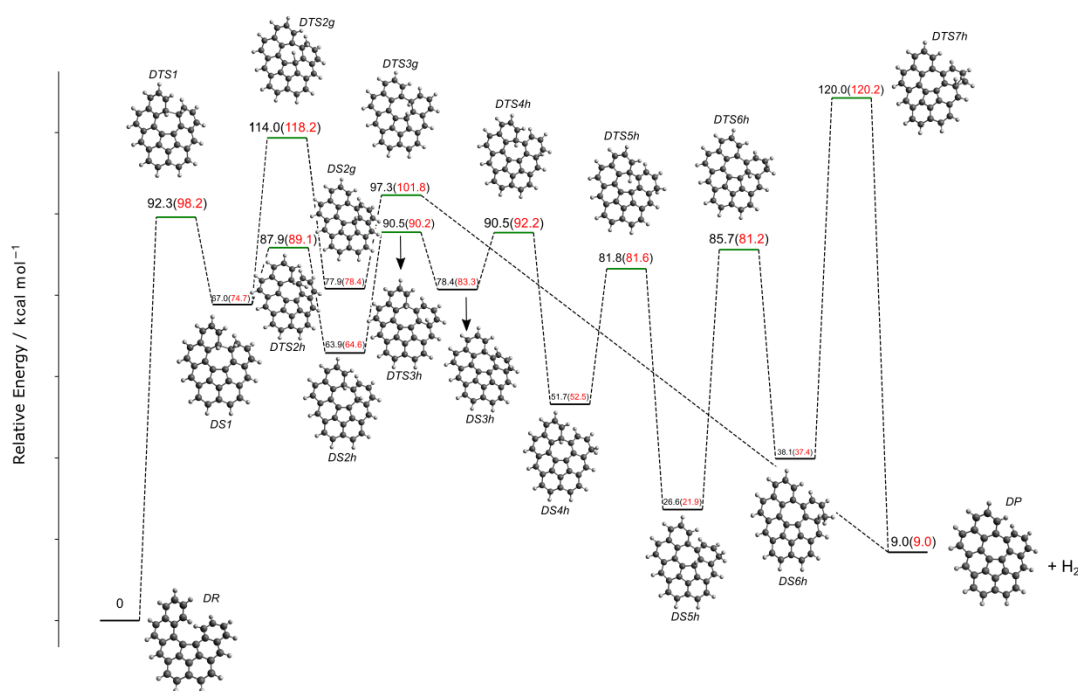


**Figure 6.19:** Potential energy surface for the formation of a seven-member ring by direct cyclisation (pathways g and h) and bay closure in PAH D at 0 K. The relative energy of the different species are computed at both the M06-2X/cc-pVTZ and B3LYP/6-311+G(d,p) level of theory.

### 6.3.1.12 All PAHs - conversion between hydrogen-abstracted radicals

Figure 6.20 presents the hydrogen migration reactions that convert between the initial radicals formed by hydrogen migration, *i.e.* conversion between AS1a

## 6 CHAPTER 6

and AS1b. There is quite a spread of barriers, with the migration in PAH A having a very large barrier of 45.9 kcal/mol and thus unlikely. For PAHs B and C, the barriers 27.9 kcal/mol and 27.3 kcal/mol which is significantly easier than for PAH, but still substantial. For PAH D, the barrier is rather moderate at 13.2 kcal/mol. However, in all cases, the barrier for acetylene addition or cyclisation after hydrogen abstraction is substantially lower than the intramolecular hydrogen migration, and so this path switching is not expected to impact the formation of the seven-member ring.

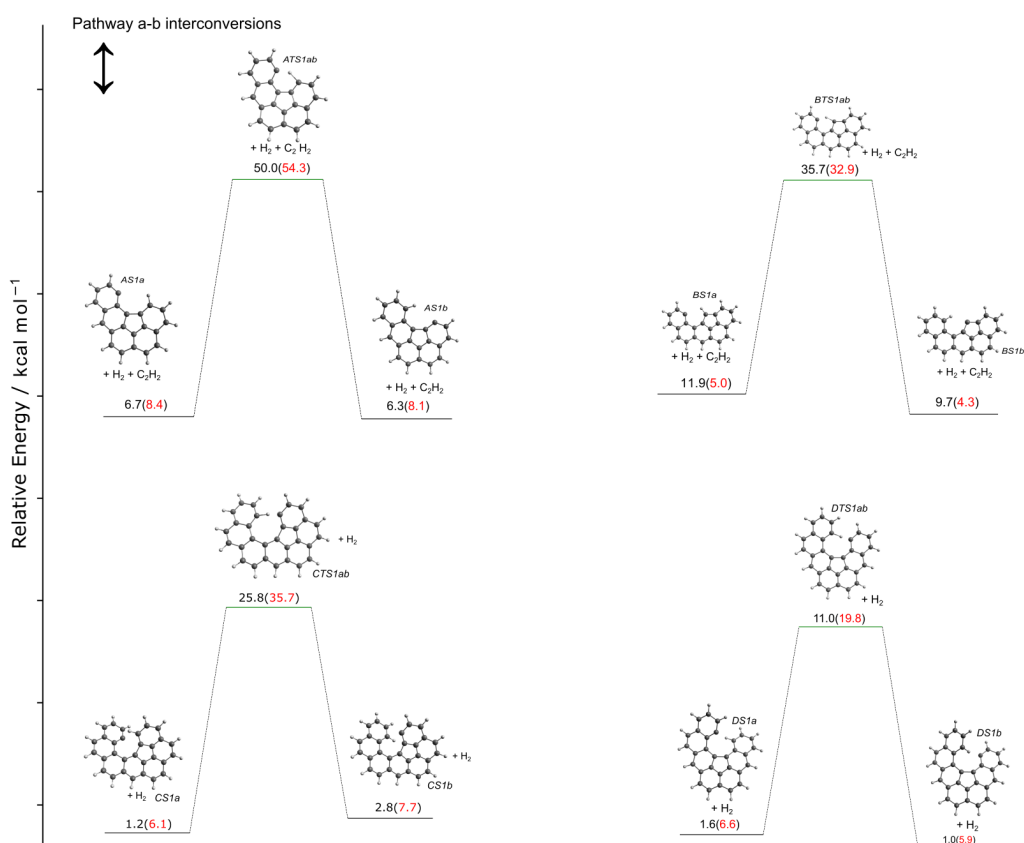


**Figure 6.20:** Potential energy surfaces at 0 K for the conversions of radicals between pathways a and b in HACA and hydrogen abstraction pathways. The relative energy of the different species are computed at both the M06-2X/cc-pVTZ and B3LYP/6-311+G(d,p) level of theory.

### 6.3.2 Rate Constants

The modified Arrhenius parameters,  $A$ ,  $n$ , and  $E_A$  are displayed in Table 6.1. These are fitted to the rate constants calculated at the M06-2X/cc-pVTZ//B3LYP/6-311G(d,p) level of theory. The uncertainty in the rate constants is estimated as  $\pm 2$  kcal/mol in the activation energy, owing to the likely uncertainty in the barrier heights predicted by the M06-2X functional (Hou and You, 2017).

**Table 6.1:** Arrhenius fittings for the rate constants for all pathways studied. Rates are computed at the M06-2X/cc-pVTZ//B3LYP/6-311G(d,p) level of theory. The units are cm, kcal, mol, K, and s.

| Number | Reaction  | $A$                   | $n$  | $E_A$ |
|--------|---|-----------------------|------|-------|
| 1a     | AR + H $\rightarrow$ AS1a + H <sub>2</sub>              | $5.90 \times 10^7$    | 1.85 | 17.12 |
| -1a    | AS1a + H <sub>2</sub> $\rightarrow$ AR + H              | $1.21 \times 10^5$    | 2.23 | 7.72  |
| 1b     | AR + H $\rightarrow$ AS1b + H <sub>2</sub>              | $5.31 \times 10^7$    | 1.86 | 16.12 |
| -1b    | AS1b + H <sub>2</sub> $\rightarrow$ AR + H              | $9.16 \times 10^4$    | 2.28 | 7.01  |
| 1ab    | AS1a $\rightarrow$ AS1b                                 | $7.81 \times 10^{10}$ | 0.44 | 41.76 |
| -1ab   | AS1b $\rightarrow$ AS1a                                 | $6.23 \times 10^{10}$ | 0.48 | 42.04 |
| 2a     | AS1a + C <sub>2</sub> H <sub>2</sub> $\rightarrow$ AS2a | $1.345 \times 10^3$   | 2.57 | 4.94  |
| -2a    | AS2a $\rightarrow$ AS1a + C <sub>2</sub> H <sub>2</sub> | $2.37 \times 10^{12}$ | 0.71 | 39.67 |
| 2b     | AS1b + C <sub>2</sub> H <sub>2</sub> $\rightarrow$ AS2b | $3.52 \times 10^3$    | 2.60 | 4.00  |
| -2b    | AS2b $\rightarrow$ AS1b + C <sub>2</sub> H <sub>2</sub> | $4.74 \times 10^{12}$ | 0.70 | 40.80 |
| 3a     | AS2a $\rightarrow$ AS3a                                 | $1.96 \times 10^{11}$ | 0.11 | 25.33 |
| -3a    | AS3a $\rightarrow$ AS2a                                 | $3.41 \times 10^{11}$ | 0.63 | 53.37 |
| 3b     | AS2b $\rightarrow$ AS3b                                 | $1.13 \times 10^{11}$ | 0.13 | 30.51 |
| -3b    | AS3b $\rightarrow$ AS2b                                 | $2.38 \times 10^{11}$ | 0.60 | 57.90 |
| 4a     | AS3a $\rightarrow$ AP + H                               | $1.77 \times 10^{10}$ | 1.09 | 27.15 |
| -4a    | AP + H $\rightarrow$ AS3a                               | $5.32 \times 10^7$    | 1.51 | 7.10  |
| 4b     | AS3b $\rightarrow$ AP + H                               | $1.51 \times 10^{10}$ | 1.08 | 28.84 |
| -4b    | AP + H $\rightarrow$ AS3b                               | $5.84 \times 10^7$    | 1.53 | 7.08  |

Continued on next page.

## 6 CHAPTER 6

*Continued from previous page.*

| Number | Reaction  | $A$                   | $n$  | $E_A$ |
|--------|---|-----------------------|------|-------|
| 2am    | AS2a $\rightarrow$ AS2am                                | $1.83 \times 10^{11}$ | 0.37 | 25.83 |
| -2am   | AS2am $\rightarrow$ AS2a                                | $3.59 \times 10^{10}$ | 0.53 | 29.67 |
| 2bm    | AS2b $\rightarrow$ AS2bm                                | $8.16 \times 10^{10}$ | 0.37 | 32.09 |
| -2bm   | AS2bm $\rightarrow$ AS2b                                | $4.64 \times 10^9$    | 0.48 | 35.31 |
| 3am    | AS2am $\rightarrow$ AS3am                               | $8.54 \times 10^{11}$ | 0.05 | 4.25  |
| -3am   | AS3am $\rightarrow$ AS2am                               | $1.57 \times 10^{11}$ | 0.48 | 45.50 |
| 3bm    | AS2bm $\rightarrow$ AS3bm                               | $1.03 \times 10^{11}$ | 0.04 | 2.30  |
| -3bm   | AS3bm $\rightarrow$ AS2bm                               | $1.56 \times 10^{12}$ | 0.60 | 43.35 |
| 4am    | AS3am $\rightarrow$ AP + H                              | $1.02 \times 10^9$    | 1.22 | 40.86 |
| -4am   | AP + H $\rightarrow$ AS3am                              | $3.91 \times 10^8$    | 1.53 | 3.62  |
| 4bm    | AS3bm $\rightarrow$ AP + H                              | $1.21 \times 10^{10}$ | 1.30 | 42.21 |
| -4bm   | AP + H $\rightarrow$ AS3bm                              | $3.02 \times 10^8$    | 1.53 | 3.43  |
| 2al    | AS2a $\rightarrow$ ASPa + H                             | $8.36 \times 10^9$    | 1.41 | 35.85 |
| -2al   | ASPa + H $\rightarrow$ AS2a                             | $5.30 \times 10^8$    | 1.53 | 5.50  |
| 2bl    | AS2b $\rightarrow$ ASPb + H                             | $4.30 \times 10^9$    | 1.44 | 36.12 |
| -2bl   | ASPb + H $\rightarrow$ AS2b                             | $3.41 \times 10^8$    | 1.56 | 6.50  |
| 1a     | BR + H $\rightarrow$ BS1a + H <sub>2</sub>              | $6.59 \times 10^7$    | 1.77 | 14.77 |
| -1a    | BS1a + H <sub>2</sub> $\rightarrow$ BR + H              | $1.15 \times 10^5$    | 2.31 | 8.82  |
| 1b     | BR + H $\rightarrow$ BS1b + H <sub>2</sub>              | $1.48 \times 10^7$    | 1.86 | 17.07 |
| -1b    | BS1b + H <sub>2</sub> $\rightarrow$ BR + H              | $5.91 \times 10^4$    | 2.23 | 11.87 |
| 1ab    | BS1a $\rightarrow$ BS1b                                 | $3.86 \times 10^{11}$ | 0.35 | 24.41 |
| -1ab   | BS1b $\rightarrow$ BS1a                                 | $1.39 \times 10^{11}$ | 0.54 | 23.66 |
| 2a     | BS1a + C <sub>2</sub> H <sub>2</sub> $\rightarrow$ BS2a | $3.89 \times 10^3$    | 2.59 | 4.01  |
| -2a    | BS2a $\rightarrow$ BS1a + C <sub>2</sub> H <sub>2</sub> | $6.51 \times 10^{12}$ | 0.71 | 45.04 |
| 2b     | BS1b + C <sub>2</sub> H <sub>2</sub> $\rightarrow$ BS2b | $1.10 \times 10^3$    | 2.58 | 7.65  |
| -2b    | BS2b $\rightarrow$ BS1b + C <sub>2</sub> H <sub>2</sub> | $2.89 \times 10^{12}$ | 0.71 | 38.30 |

Continued on next page.



## 6.3 Results and Discussion

*Continued from previous page.*

| Number | Reaction                    | $A$                   | $n$  | $E_A$ |
|--------|-----------------------------|-----------------------|------|-------|
| 3a     | BS2a $\rightarrow$ BS3a     | $5.75 \times 10^{11}$ | 0.07 | 2.98  |
| -3a    | BS3a $\rightarrow$ BS2a     | $1.74 \times 10^{12}$ | 0.42 | 29.04 |
| 3b     | BS2b $\rightarrow$ BS3b     | $5.10 \times 10^{11}$ | 0.14 | 19.74 |
| -3b    | BS3b $\rightarrow$ BS2b     | $9.94 \times 10^{11}$ | 0.41 | 45.26 |
| 4a     | BS3a $\rightarrow$ BP + H   | $3.21 \times 10^{10}$ | 0.96 | 23.13 |
| -4a    | BP + H $\rightarrow$ BS3a   | $1.29 \times 10^8$    | 1.51 | 7.42  |
| 4b     | BS3b $\rightarrow$ BP + H   | $3.59 \times 10^{11}$ | 0.60 | 30.05 |
| -4b    | BP + H $\rightarrow$ BS3b   | $6.26 \times 10^8$    | 1.38 | 24.51 |
| 2am    | BS2a $\rightarrow$ BS2am    | $1.67 \times 10^{11}$ | 0.48 | 20.79 |
| -2am   | BS2am $\rightarrow$ BS2a    | $1.73 \times 10^{10}$ | 0.80 | 22.17 |
| 2bm    | BS2b $\rightarrow$ BS2bm    | $7.02 \times 10^{10}$ | 0.71 | 12.92 |
| -2bm   | BS2bm $\rightarrow$ BS2b    | $4.80 \times 10^{10}$ | 0.75 | 11.61 |
| 3am    | BS2am $\rightarrow$ BS3am   | $1.51 \times 10^{12}$ | 0.07 | 5.00  |
| -3am   | BS3am $\rightarrow$ BS2am   | $4.00 \times 10^{11}$ | 0.48 | 50.81 |
| 3bm    | BS2bm $\rightarrow$ BS3bm   | $1.00 \times 10^{12}$ | 0.10 | 6.42  |
| -3bm   | BS3bm $\rightarrow$ BS2bm   | $2.13 \times 10^{12}$ | 0.37 | 33.75 |
| 4am    | BS3am $\rightarrow$ BP + H  | $2.37 \times 10^9$    | 1.18 | 30.77 |
| -4am   | BP + H $\rightarrow$ BS3am  | $3.53 \times 10^8$    | 1.49 | 3.44  |
| 4bm    | BS3bm $\rightarrow$ BP + H  | $1.74 \times 10^{10}$ | 0.96 | 28.25 |
| -4bm   | BP + H $\rightarrow$ BS3bm  | $2.06 \times 10^8$    | 1.51 | 12.44 |
| 2al    | BS2a $\rightarrow$ BSPa + H | $4.30 \times 10^9$    | 1.40 | 39.04 |
| -2al   | BSPa + H $\rightarrow$ BS2a | $2.44 \times 10^8$    | 1.52 | 6.04  |
| 2bl    | BS2b $\rightarrow$ BSPb + H | $3.20 \times 10^9$    | 1.48 | 39.19 |
| -2bl   | BSPb + H $\rightarrow$ BS2b | $2.77 \times 10^8$    | 1.52 | 5.30  |
| 2bsv   | BS2b $\rightarrow$ BS2sv    | $3.02 \times 10^{11}$ | 0.30 | 35.35 |
| -2bsv  | BS2b $\rightarrow$ BS2sv    | $1.32 \times 10^{12}$ | 0.34 | 10.10 |

*Continued on next page.*

## 6 CHAPTER 6

*Continued from previous page.*

| Number | Reaction                                   | $A$                   | $n$   | $E_A$ |
|--------|--|-----------------------|-------|-------|
| 3bsv   | BS2sv $\rightarrow$ BS3sv                  | $2.28 \times 10^{12}$ | 0.27  | 13.29 |
| -3bsv  | BS2sv $\rightarrow$ BS3sv                  | $8.85 \times 10^{10}$ | 0.47  | 46.88 |
| 1p     | BP + H $\rightarrow$ BP1                   | $3.48 \times 10^8$    | 1.49  | 3.44  |
| -1p    | BP1 $\rightarrow$ BP + H                   | $2.34 \times 10^9$    | 1.18  | 30.77 |
| 2p     | BP1 $\rightarrow$ BP2                      | $2.12 \times 10^{10}$ | 0.67  | 40.32 |
| -2p    | BP2 $\rightarrow$ BP1                      | $8.39 \times 10^{11}$ | 0.29  | 18.61 |
| 3p     | BP2 $\rightarrow$ BP3                      | $1.03 \times 10^{12}$ | 0.15  | 9.25  |
| -3p    | BP3 $\rightarrow$ BP2                      | $1.87 \times 10^{12}$ | 0.32  | 15.04 |
| 4p     | BP3 $\rightarrow$ BP4                      | $6.65 \times 10^{12}$ | -0.13 | 4.09  |
| -4p    | BP4 $\rightarrow$ BP3                      | $1.52 \times 10^{12}$ | 0.00  | 34.08 |
| 5p     | BP4 $\rightarrow$ BF + H                   | $1.13 \times 10^{10}$ | 1.00  | 15.65 |
| -5p    | BF + H $\rightarrow$ BP4                   | $2.82 \times 10^8$    | 1.36  | 35.44 |
| 1a     | CR + H $\rightarrow$ CS1a + H <sub>2</sub> | $4.20 \times 10^7$    | 1.87  | 16.00 |
| -1a    | CS1a + H <sub>2</sub> $\rightarrow$ CR + H | $2.79 \times 10^5$    | 2.06  | 7.54  |
| 1b     | CR + H $\rightarrow$ CS1b + H <sub>2</sub> | $3.59 \times 10^7$    | 1.87  | 16.21 |
| -1b    | CS1b + H <sub>2</sub> $\rightarrow$ CR + H | $2.93 \times 10^5$    | 2.04  | 9.32  |
| 1ab    | CS1a $\rightarrow$ CS1b                    | $7.83 \times 10^{10}$ | 0.83  | 22.80 |
| -1ab   | CS1b $\rightarrow$ CS1a                    | $9.61 \times 10^{10}$ | 0.81  | 24.36 |
| 2a     | CS1a $\rightarrow$ CS2a                    | $6.74 \times 10^{11}$ | 0.17  | 6.94  |
| -2a    | CS2a $\rightarrow$ CS1a                    | $1.65 \times 10^{12}$ | 0.39  | 28.64 |
| 2b     | CS1b $\rightarrow$ CS2b                    | $5.12 \times 10^{11}$ | 0.26  | 12.94 |
| -2b    | CS2b $\rightarrow$ CS1b                    | $1.08 \times 10^{12}$ | 0.54  | 31.94 |
| 3a     | CS2a $\rightarrow$ CP + H                  | $6.05 \times 10^9$    | 1.22  | 31.47 |
| -3a    | CP + H $\rightarrow$ CS2a                  | $1.37 \times 10^8$    | 1.46  | 6.78  |
| 3b     | CS2b $\rightarrow$ CP + H                  | $4.39 \times 10^9$    | 1.32  | 29.31 |
| -3b    | CP + H $\rightarrow$ CS2b                  | $9.41 \times 10^7$    | 1.49  | 24.14 |

Continued on next page.

## 6.3 Results and Discussion

*Continued from previous page.*

| Number | Reaction                     | $A$                   | $n$  | $E_A$  |
|--------|------------------------------|-----------------------|------|--------|
| 1c     | CR + H → CS1c                | $2.48 \times 10^8$    | 1.54 | 5.53   |
| -1c    | CS1c → CR + H                | $2.29 \times 10^{10}$ | 1.00 | 30.41  |
| 1d     | CR + H → CS1d                | $2.28 \times 10^8$    | 1.52 | 4.57   |
| -1d    | CS1d → CR + H                | $1.71 \times 10^{10}$ | 1.01 | 29.00  |
| 2c     | CS1c → CS2c                  | $2.26 \times 10^{11}$ | 0.19 | 33.08  |
| -2c    | CS2c → CS1c                  | $2.25 \times 10^{11}$ | 0.43 | 9.69   |
| 2d     | CS1d → CS2d                  | $5.54 \times 10^{11}$ | 0.02 | 17.98  |
| -2d    | CS2d → CS1d                  | $1.49 \times 10^{12}$ | 0.40 | 16.05  |
| 3c     | CS2c → CS3c + H              | $8.55 \times 10^9$    | 1.08 | 35.25  |
| -3c    | CS3c + H → CS2c              | $2.21 \times 10^8$    | 1.56 | 3.28   |
| 3d     | CS2d → CS3d + H              | $3.21 \times 10^{10}$ | 1.14 | 36.00  |
| -3d    | CS3d + H → CS2d              | $2.26 \times 10^8$    | 1.55 | 3.11   |
| 4c     | CS3c → CS4c + H <sub>2</sub> | $1.18 \times 10^9$    | 1.65 | 86.44  |
| -4c    | CS4c + H <sub>2</sub> → CS3c | $2.35 \times 10^5$    | 1.97 | 17.19  |
| 4d     | CS3d → CS4d + H <sub>2</sub> | $1.47 \times 10^9$    | 1.59 | 102.07 |
| -4d    | CS4d + H <sub>2</sub> → CS3d | $2.63 \times 10^5$    | 1.87 | 20.77  |
| 5c     | CS4c → CP                    | $7.55 \times 10^{11}$ | 0.39 | 4.13   |
| -5c    | CP → CS4c                    | $4.66 \times 10^{10}$ | 0.88 | 94.28  |
| 5d     | CS4d → CP                    | $1.49 \times 10^{12}$ | 0.39 | 4.82   |
| -5d    | CP → CS4d                    | $1.70 \times 10^{11}$ | 0.82 | 84.72  |
| 1e     | CR → CS1e                    | $8.03 \times 10^{10}$ | 0.90 | 95.83  |
| -1e    | CS1e → CR                    | $4.40 \times 10^{11}$ | 0.36 | 3.38   |
| 1f     | CR → CS1f                    | $1.06 \times 10^{11}$ | 0.80 | 84.26  |
| -1f    | CS1f → CR                    | $5.49 \times 10^{11}$ | 0.34 | 2.01   |
| 2e     | CS1e → CS2e                  | $8.03 \times 10^{11}$ | 0.01 | 8.46   |
| -2e    | CS2e → CS1e                  | $1.90 \times 10^{12}$ | 0.22 | 17.91  |

Continued on next page.

## 6 CHAPTER 6

*Continued from previous page.*

| Number | Reaction                                   | $A$                   | $n$   | $E_A$  |
|--------|--|-----------------------|-------|--------|
| 2f     | CS1f $\rightarrow$ CS2f                    | $1.00 \times 10^{12}$ | -0.01 | 3.47   |
| -2f    | CS2f $\rightarrow$ CS1f                    | $2.17 \times 10^{12}$ | 0.56  | 59.28  |
| 3e     | CS2e $\rightarrow$ CS3e                    | $5.76 \times 10^{11}$ | 0.39  | 0.87   |
| -3e    | CS3e $\rightarrow$ CS2e                    | $1.05 \times 10^{11}$ | 0.90  | 53.50  |
| 3f     | CS2f $\rightarrow$ CS3f                    | $3.06 \times 10^{11}$ | 0.82  | 63.56  |
| -3f    | CS3f $\rightarrow$ CS2f                    | $1.51 \times 10^{10}$ | 0.67  | 50.31  |
| 4e     | CS3e $\rightarrow$ CS4e                    | $8.87 \times 10^{10}$ | 0.64  | 31.31  |
| -4e    | CS4e $\rightarrow$ CS3e                    | $1.73 \times 10^{10}$ | 0.71  | 60.65  |
| 4f     | CS3f $\rightarrow$ CP + H <sub>2</sub>     | $4.48 \times 10^9$    | 0.71  | 27.10  |
| -4f    | CP + H <sub>2</sub> $\rightarrow$ CS3f     | $2.33 \times 10^5$    | 1.74  | 55.10  |
| 5e     | CS4e $\rightarrow$ CP + H <sub>2</sub>     | $3.91 \times 10^{09}$ | 1.27  | 97.14  |
| -5e    | CP + H <sub>2</sub> $\rightarrow$ CS4e     | $2.45 \times 10^5$    | 2.00  | 86.40  |
| 1g     | CR $\rightarrow$ CS1g                      | $1.53 \times 10^{11}$ | 0.52  | 101.74 |
| -1g    | CS1g $\rightarrow$ CR                      | $2.86 \times 10^{12}$ | 0.37  | 18.93  |
| 2g     | CS1g $\rightarrow$ CP + H <sub>2</sub>     | $2.83 \times 10^{10}$ | 1.02  | 19.73  |
| -2g    | CP + H <sub>2</sub> $\rightarrow$ CS1g     | $4.37 \times 10^4$    | 2.16  | 90.76  |
| 1a     | DR + H $\rightarrow$ DS1a + H <sub>2</sub> | $2.77 \times 10^7$    | 1.91  | 16.31  |
| -1a    | DS1a + H <sub>2</sub> $\rightarrow$ DR + H | $4.21 \times 10^4$    | 2.26  | 8.71   |
| 1b     | DR + H $\rightarrow$ DS1b + H <sub>2</sub> | $2.84 \times 10^7$    | 1.91  | 16.74  |
| -1b    | DS1b + H <sub>2</sub> $\rightarrow$ DR + H | $5.33 \times 10^4$    | 2.26  | 9.85   |
| 1ab    | DS1a $\rightarrow$ DS1b                    | $5.04 \times 10^{10}$ | 0.80  | 8.79   |
| -1ab   | DS1b $\rightarrow$ DS1a                    | $6.14 \times 10^{10}$ | 0.81  | 9.48   |
| 2a     | DS1a $\rightarrow$ DS2a                    | $4.70 \times 10^{11}$ | 0.14  | 7.01   |
| -2a    | DS2a $\rightarrow$ DS1a                    | $1.48 \times 10^{12}$ | 0.37  | 31.35  |
| 2b     | DS1b $\rightarrow$ DS2b                    | $6.60 \times 10^{11}$ | 0.08  | 4.76   |
| -2b    | DS2b $\rightarrow$ DS1b                    | $5.13 \times 10^{12}$ | 0.34  | 28.48  |

Continued on next page.

## 6.3 Results and Discussion

*Continued from previous page.*

| Number | Reaction                                 | $A$                   | $n$  | $E_A$  |
|--------|--|-----------------------|------|--------|
| 3a     | DS2a $\rightarrow$ DP + H                | $6.42 \times 10^9$    | 1.09 | 32.34  |
| -3a    | DP + H $\rightarrow$ DS2a                | $1.69 \times 10^8$    | 1.52 | 5.07   |
| 3b     | DS2b $\rightarrow$ DP + H                | $2.06 \times 10^{10}$ | 1.10 | 31.91  |
| -3b    | DP + H $\rightarrow$ DS2b                | $1.73 \times 10^8$    | 1.49 | 4.54   |
| 1c     | DR + H $\rightarrow$ DS1c                | $2.94 \times 10^8$    | 1.53 | 4.06   |
| -1c    | DS1c $\rightarrow$ DR + H                | $1.95 \times 10^{10}$ | 1.07 | 34.30  |
| 1d     | DR + H $\rightarrow$ DS1d                | $2.39 \times 10^8$    | 1.51 | 4.36   |
| -1d    | DS1d $\rightarrow$ DR + H                | $1.89 \times 10^{10}$ | 0.98 | 28.70  |
| 2c     | DS1c $\rightarrow$ DS2c                  | $7.96 \times 10^{11}$ | 0.43 | 20.65  |
| -2c    | DS2c $\rightarrow$ DS1c                  | $2.76 \times 10^{12}$ | 0.43 | 15.70  |
| 2d     | DS1d $\rightarrow$ DS2d                  | $5.72 \times 10^{11}$ | 0.13 | 21.98  |
| -2d    | DS2d $\rightarrow$ DS1d                  | $2.17 \times 10^{12}$ | 0.50 | 18.75  |
| 3c     | DS2c $\rightarrow$ DS3c + H              | $4.15 \times 10^{10}$ | 1.08 | 35.82  |
| -3c    | DS3c + H $\rightarrow$ DS2c              | $3.72 \times 10^8$    | 1.53 | 0.00   |
| 3d     | DS2d $\rightarrow$ DS3d + H              | $1.60 \times 10^{10}$ | 1.05 | 34.30  |
| -3d    | DS3d + H $\rightarrow$ DS2d              | $1.83 \times 10^8$    | 1.54 | 3.65   |
| 4c     | DS3c $\rightarrow$ DS4c + H <sub>2</sub> | $1.87 \times 10^9$    | 1.67 | 92.61  |
| -4c    | DS4c + H <sub>2</sub> $\rightarrow$ DS3c | $2.48 \times 10^5$    | 1.93 | 7.39   |
| 4d     | DS3d $\rightarrow$ DS4d + H <sub>2</sub> | $1.67 \times 10^9$    | 1.62 | 102.02 |
| -4d    | DS4d + H <sub>2</sub> $\rightarrow$ DS3d | $5.68 \times 10^5$    | 1.92 | 15.60  |
| 5c     | D4c $\rightarrow$ DP                     | $4.52 \times 10^{11}$ | 0.35 | 1.73   |
| -5c    | DP $\rightarrow$ DS4c                    | $2.07 \times 10^{11}$ | 0.76 | 83.49  |
| 5d     | DS4d $\rightarrow$ DP                    | $7.60 \times 10^{11}$ | 0.39 | 0.17   |
| -5d    | DP $\rightarrow$ DS4d                    | $8.17 \times 10^{10}$ | 0.78 | 85.59  |
| 1e     | DR $\rightarrow$ DS1e                    | $1.60 \times 10^{11}$ | 0.78 | 83.23  |
| -1e    | DS1e $\rightarrow$ DR                    | $3.05 \times 10^{11}$ | 0.29 | 0.08   |

Continued on next page.

## 6 CHAPTER 6

*Continued from previous page.*

| Number | Reaction                               | $A$                   | $n$  | $E_A$ |
|--------|--|-----------------------|------|-------|
| 1f     | DR $\rightarrow$ DS1f                  | $1.16 \times 10^{11}$ | 0.84 | 86.01 |
| -1f    | DS1f $\rightarrow$ DR                  | $4.95 \times 10^{11}$ | 0.33 | 1.48  |
| 2e     | DS1e $\rightarrow$ DS2e                | $2.49 \times 10^{11}$ | 0.12 | 11.62 |
| -2e    | DS2e $\rightarrow$ DS1e                | $1.47 \times 10^{12}$ | 0.68 | 45.09 |
| 2f     | DS1f $\rightarrow$ DS2f                | $5.74 \times 10^{11}$ | 0.04 | 8.72  |
| -2f    | DS2f $\rightarrow$ DS1f                | $2.16 \times 10^{12}$ | 0.29 | 18.61 |
| 3e     | DS2e $\rightarrow$ DS3e                | $1.40 \times 10^{11}$ | 0.58 | 27.01 |
| -3e    | DS3e $\rightarrow$ DS2e                | $3.26 \times 10^{10}$ | 0.73 | 56.81 |
| 3f     | DS2f $\rightarrow$ DS3f                | $9.90 \times 10^{11}$ | 0.33 | 2.85  |
| -3f    | DS3f $\rightarrow$ DS2f                | $1.02 \times 10^{11}$ | 0.87 | 57.11 |
| 4e     | DS3e $\rightarrow$ DS4e                | $5.52 \times 10^{10}$ | 0.85 | 59.32 |
| -4e    | DS4e $\rightarrow$ DS3e                | $7.57 \times 10^{10}$ | 0.67 | 38.56 |
| 4f     | DS3f $\rightarrow$ DS4f                | $6.16 \times 10^{10}$ | 0.78 | 39.25 |
| -4f    | DS4f $\rightarrow$ DS3f                | $9.57 \times 10^{10}$ | 0.70 | 35.20 |
| 5e     | DS4e $\rightarrow$ DP + H <sub>2</sub> | $6.21 \times 10^9$    | 0.85 | 28.61 |
| -5e    | DP + H <sub>2</sub> $\rightarrow$ DS4e | $2.16 \times 10^5$    | 1.80 | 58.70 |
| 5f     | DS4f $\rightarrow$ DP + H <sub>2</sub> | $3.48 \times 10^9$    | 1.29 | 87.43 |
| -5f    | DP + H <sub>2</sub> $\rightarrow$ DS4f | $1.70 \times 10^5$    | 2.09 | 95.63 |
| 1      | DR $\rightarrow$ DS1                   | $9.28 \times 10^{10}$ | 0.26 | 96.39 |
| -1     | DS1 $\rightarrow$ DR                   | $3.41 \times 10^{12}$ | 0.14 | 22.26 |
| 2g     | DS1 $\rightarrow$ DS2g                 | $5.37 \times 10^{10}$ | 0.75 | 42.64 |
| -2g    | DS2g $\rightarrow$ DS1                 | $1.86 \times 10^{10}$ | 0.46 | 38.89 |
| 2h     | DS1 $\rightarrow$ DS2h                 | $2.75 \times 10^{11}$ | 0.47 | 13.93 |
| -2h    | DS2h $\rightarrow$ DS1                 | $1.16 \times 10^{11}$ | 0.62 | 24.20 |
| 3g     | DS2g $\rightarrow$ DP + H <sub>2</sub> | $1.07 \times 10^{11}$ | 0.53 | 22.31 |
| -3g    | DP + H <sub>2</sub> $\rightarrow$ DS2g | $1.06 \times 10^5$    | 1.94 | 89.66 |

Continued on next page.

*Continued from previous page.*

| Number | Reaction                               | $A$                   | $n$  | $E_A$  |
|--------|--|-----------------------|------|--------|
| 3h     | DS2h $\rightarrow$ DS3h                | $1.01 \times 10^{11}$ | 0.71 | 25.39  |
| -3h    | DS3h $\rightarrow$ DS2h                | $2.06 \times 10^{11}$ | 0.47 | 6.41   |
| 4h     | DS3h $\rightarrow$ DS4h                | $2.07 \times 10^{11}$ | 0.47 | 8.36   |
| -4h    | DS4h $\rightarrow$ DS3h                | $5.21 \times 10^{10}$ | 0.73 | 39.11  |
| 5h     | DS4h $\rightarrow$ DS5h                | $1.64 \times 10^{11}$ | 0.61 | 28.35  |
| -5h    | DS5h $\rightarrow$ DS4h                | $9.36 \times 10^{10}$ | 0.77 | 59.04  |
| 6h     | DS5h $\rightarrow$ DS6h                | $4.51 \times 10^{10}$ | 0.91 | 58.69  |
| -6h    | DS6h $\rightarrow$ DS5h                | $3.93 \times 10^{10}$ | 0.80 | 43.03  |
| 7h     | DS6h $\rightarrow$ DP + H <sub>2</sub> | $6.30 \times 10^{09}$ | 1.19 | 81.67  |
| -7h    | DP + H <sub>2</sub> $\rightarrow$ DS6h | $1.99 \times 10^5$    | 2.09 | 108.19 |

### 6.3.3 Kinetic simulations in a 0D homogeneous reactor

This section presents the results of the kinetic simulations of the seven-member ring formation studied in this work using the M06-2X/cc-pVTZ level of theory. As discussed in previous sections, the rates for the B3LYP/6-311+G(d,p) level predicted very similar trends but generally the rates had higher absolute values for hydrogen abstractions, additions, and cyclisations and lower values for hydrogen migrations or losses. Figure 6.21 shows this for the seven-member ring formation on PAH A by a HACA sequence. The results from using the M06-2X/cc-pVTZ level are shown in a continuous line and the B3LYP/6-311G+(d,p) level in a dashed line. Since we expect the M06-2X/cc-pVTZ level of theory to give more accurate predictions for PAH chemistry we focus mostly on the kinetic simulations using these rate constants.

Figure 6.21 shows the results for the kinetic simulation for the seven-member ring formation on PAH A by a HACA sequence. This addition shows a rather weak temperature dependency with the reactant mole fraction decreasing after

## 6 CHAPTER 6

---

1 ms for all cases and the corresponding products being formed after this time. The reversibility of this reaction system can also be observed in Figure 6.21, with the conversion towards products being reduced at higher temperatures. The heptagon containing species appears to be the dominant product under the conditions studied with the total mole fraction of the ethynyl-substituted products being at least an order of magnitude lower at all temperatures even though the the ethynyl-substituted products are present in higher concentrations at higher temperatures. Both pathways contribute towards the formation of the given products.



## 6.3 Results and Discussion

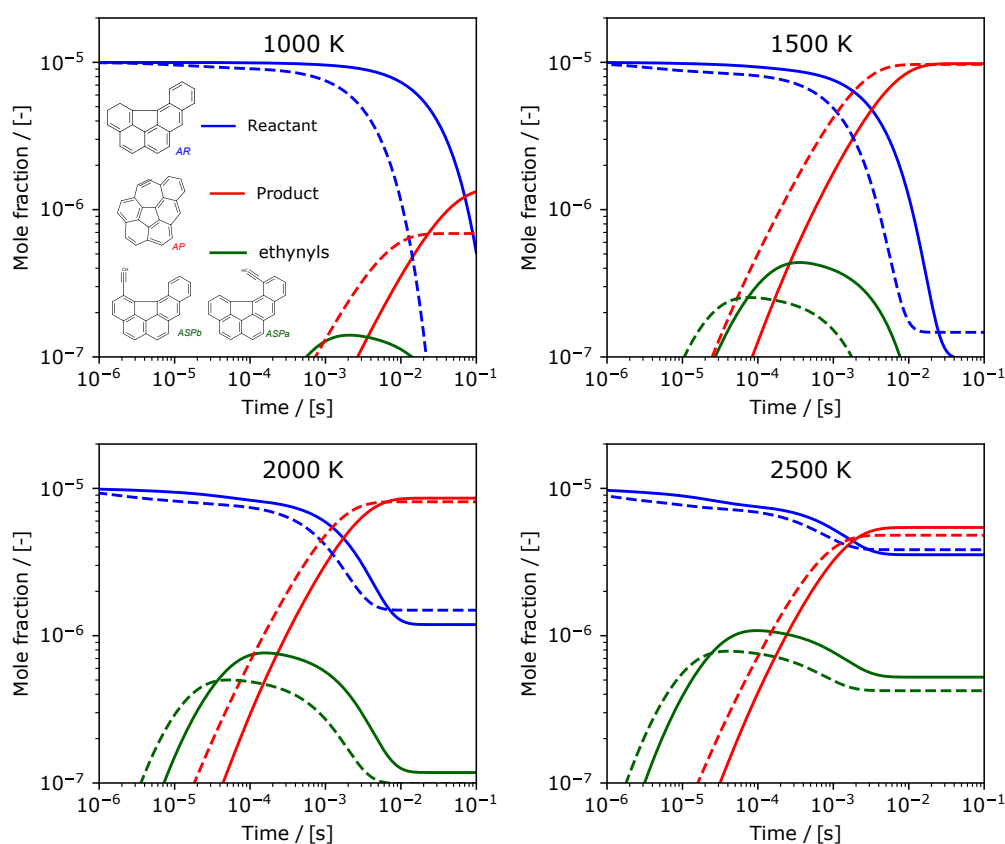


**Figure 6.21:** Kinetic simulation for the HACA seven-member ring formation on PAH A at different temperatures. The figure shows the results for the rate constants at the M06-2X/cc-pVTZ level of theory in a continuous line and the B3LYP/6-311G+(d,p) in a dashed line. The sum of the two ethynyl side products is plotted. The contribution of both HACA pathways studied are included together in this figure.

Figure 6.22 shows the results for the seven-member ring formation on PAH B by a HACA sequence followed by the rearrangement towards species BF, an RSR PAH with only six-member rings. For all the conditions studied, the five-seven-member ring pair containing product, BP, appears to be an important intermediate that is likely to be observed at typical flame timescales of 1 ms. This product proceeds to rearrange into BF via hydrogen addition at all conditions, with BF becoming the dominant product at longer timescales as well as higher temperatures. The ethynyl-substituted PAHs are observed at high temperatures, but its concentration

## 6 CHAPTER 6

is again orders of magnitude lower than BP or BF. This acetylene addition shows a stronger temperature dependency with the mole fraction of reactant decreasing earlier in the high temperature simulations. Figure 6.22 shows in dashed lines the mole fractions of the PAH reactant and products when only the high energy pathway, where the acetylene adds to the five-member ring (pathway a) is considered. Similarly, the dotted lines is for when only the low energy pathway where the acetylene adds to the six-member ring (pathway b). Pathway a appears to dominate the ring formation for this process in all the conditions studied.

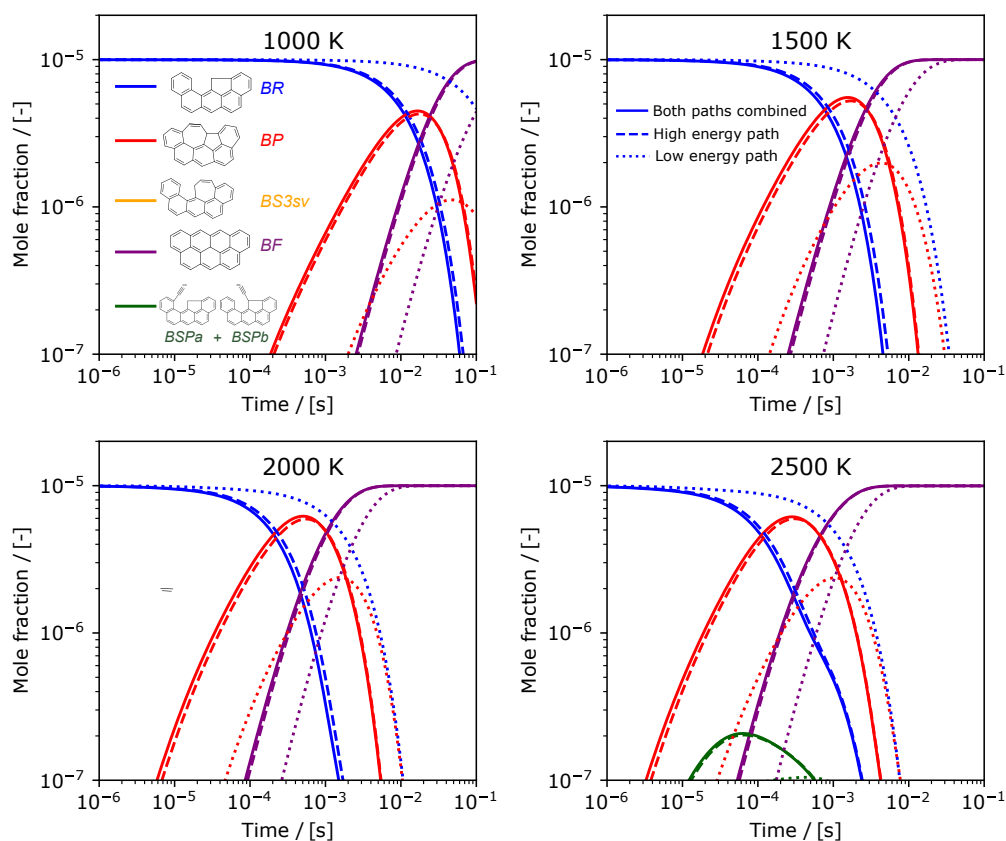


**Figure 6.22:** Kinetic simulation of the HACA seven-member ring formation on PAH B at different temperatures. Continuous lines show both pathways consuming the starting PAH simultaneously. Dashed lines show high energy pathway only. Dotted lines show low energy pathway only.

The main explanation for this seems to be differences in the rate constants for the HACA sequences of both pathways. The hydrogen abstraction for the high energy pathway is faster than that of pathway b as can be seen on the left panel of Figure 6.23. However, the acetylene addition rate constant for pathway a is lower in magnitude than that of pathway b. However, the reverse rate constant for pathway b is at least three orders of magnitude higher than the forward rate constant at high temperatures. In the case of pathway a, the trend is similar but the forward and reverse rate constants are separated by only an order of magnitude making this addition faster as can be seen in the right panel of Fig. 6.23.

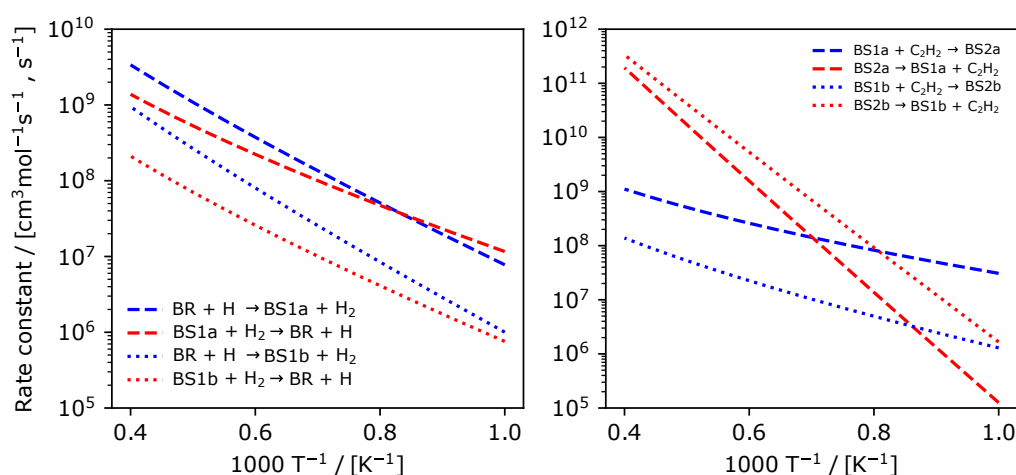


**Figure 6.23:** Forward and reverse rate constants of hydrogen abstraction (left) and acetylene addition (right) for pathway a (dashed lines) and pathway b (dotted lines) on PAH B. Units are  $\text{cm}^3 \text{mol}^{-1} \text{s}^{-1}$  for bimolecular reactions and  $\text{s}^{-1}$  for unimolecular reactions.

In the case of bay closure reactions, the pathways presented in this work can be of importance under different conditions. Figure 6.24 shows the results of kinetic simulations for the consumption of PAH C to form a seven-member ring product through all the different pathways (a to h) simultaneously. Figure 6.24 shows that the hydrogen abstraction bay cyclisation is the route that contributes the most towards the consumption of the starting PAH for temperatures under 2000 K. However, at temperatures around 2500 K the carbene route becomes the dominant pathway with a smaller contribution from the hydrogen abstraction route. This is

## 6 CHAPTER 6

in agreement with Xue and Scott (2007) that suggested the carbene route as the most likely explanation to bond formation in PAH bay sites in the absence of radicals and high temperatures. The hydrogen addition bay closure and the direct cyclisation appear to be of less importance at the conditions studied. Figure 6.24 also shows that the timescale for the bay closure reaction for PAH C is lower than that of a carbon addition (*e.g.* the time for reactants to be consumed in Figures 6.21 and 6.22). A PAH containing a site like this will more likely form a seven-member ring before further carbon additions at neighbouring sites.

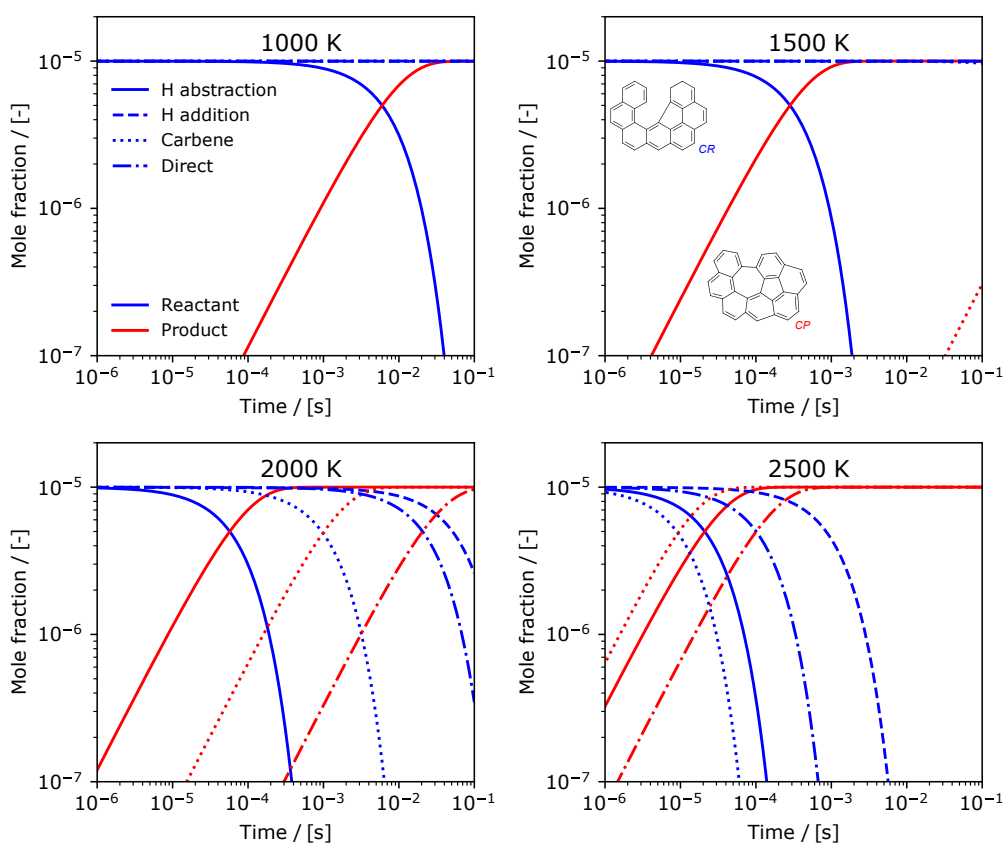


**Figure 6.24:** Kinetic simulations for the seven-member bay closure of PAH C at different temperatures. Each simulation is shown in different line pattern. Solid lines show hydrogen abstraction initiated bay closure, dashed lines show hydrogen addition assisted bay closure, dotted lines show the carbene cyclisation and dash-dotted lines show the direct cyclisation.

Figure 6.25 shows the results of the kinetic simulations of each available pathway consuming PAH D. The behaviour observed for this site is similar to that of PAH C. The figure shows that the hydrogen abstraction bay closure is the route that contributes the most towards the consumption of the starting PAH for temperatures under 2500 K. After this temperature, the carbene route becomes the fastest pathway to produce a seven-member ring, although the contribution from the hydrogen abstraction route is still significant. The hydrogen addition bay closure and the direct cyclisation for this site also appear to be slower for the conditions studied. The timescales for the bay closure for this site appear to be a few milliseconds slower than those of PAH C.

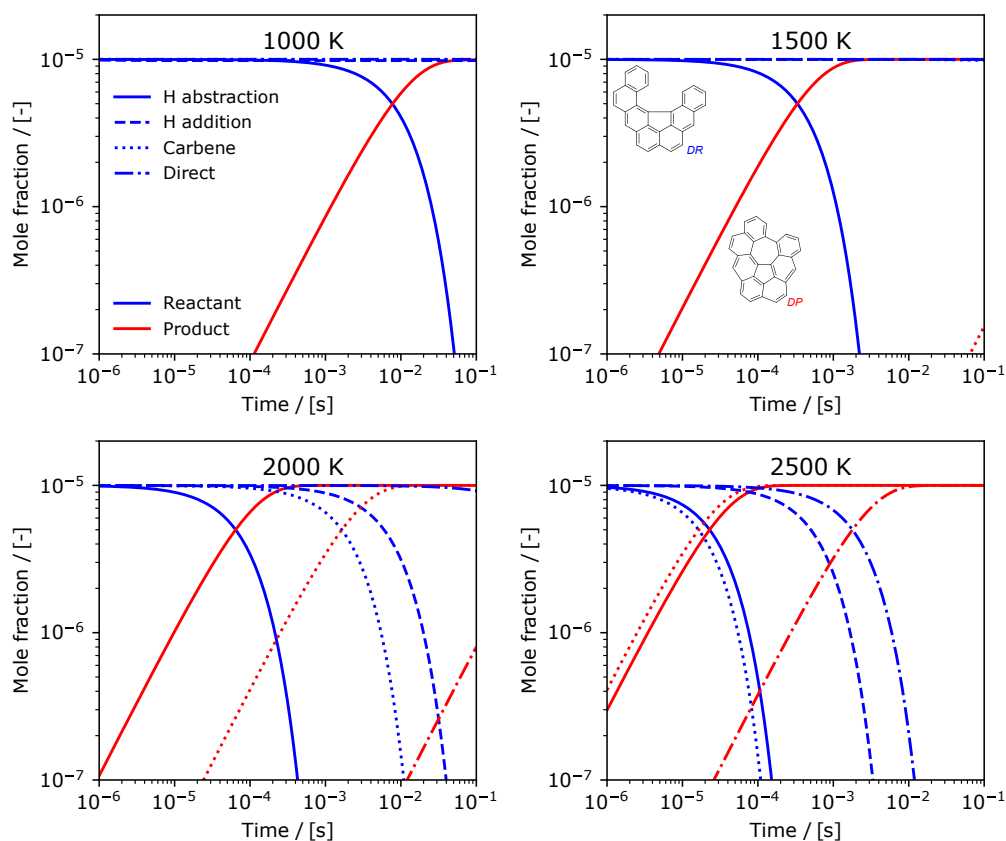


**Figure 6.25:** Kinetic simulations of the seven-member bay closure for PAH D at different temperatures. Each simulation is shown in different line pattern. Solid lines show hydrogen abstraction initiated bay closure, dashed lines show hydrogen addition assisted bay closure, dotted lines show the carbene cyclisation and dash-dotted lines show the direct cyclisation.

## 6.4 Conclusions

In this work, the kinetics of forming a seven member ring adjacent to a five member ring in PAHs have been studied by means of *ab initio* density functional theory calculations and kinetic simulations of 0D reactors at standard flame concentrations and a variety of temperatures. Density functional theory calculations were performed using the B3LYP/6-311+G(d,p) level of theory for

## 6.4 Conclusions

---

all geometry optimizations and frequency calculations. Additional single point energy calculations were performed at the M06-2X/cc-pVTZ level of theory in order to improve the estimates of energies and barrier heights for the computation of rate constants. In general, the barriers predicted by B3LYP and M06-2X are similar, with B3LYP tending to predict lower barriers for most processes.

The computed potential energy surfaces for the two HACA growths show that the formation of a seven member ring in a closed shell PAH (PAH A) and a resonance-stabilised radical PAH (PAH B) follows the same general trends even though the reaction energies are different. In both cases, the loss of hydrogen was seen to be the most difficult step. However, for PAH A, which carbon initially had its hydrogen abstracted was seen to be less significant compared to PAH B, where a clear high energy pathway and low energy pathway could be identified.

The computed potential energy surfaces for the four bay closure routes for PAH C and PAH D were seen to be generally similar for the hydrogen abstraction and addition routes, with atomic hydrogen and H<sub>2</sub> losses seen to be the most difficult steps. For both routes and PAHs, there was not much dependence on the initial carbon attacked by the hydrogen radical. The bay closures via carbene formations for PAH C and PAH D both required several hydrogen migrations to occur before H<sub>2</sub> and there was a noticeable difference depending on which carbon atom forms the initial carbene site, again resulting in higher energy and lower energy routes. The direct cyclisation was the one route where PAH C and PAH D are completely different, with PAH C able to undergo H<sub>2</sub> loss directly after cyclisation, but PAH D requiring several migrations before this can occur.

The kinetic simulations in 0D homogeneous reactors for PAH A showed that the trends in predicted product formation are the same for both the B3LYP/6-311+G(d,p) and M06-2X/cc-pVTZ computed energies, with the seven-member ring containing product formation being slower for the latter level of theory. This is expected given the higher predicted barriers and lower rate constants. In addition, both pathways contributed to the product formation, which is expected as they were rather similar. The kinetic simulations for PAH B show that the high energy pathway is the main contributor to the product formation, due to the lower reversibility of the acetylene addition step. For the bay closures, the

## 6 CHAPTER 6

---

hydrogen abstraction facilitated bay closure was seen to be the main contributor to seven-member ring formation at 1000, 1500, and 2000 K. At 2500 K, the carbene route becomes the dominant contributor, suggesting this pathway could be important at very high temperatures. In general, the HACA growth and bay closure processes did occur to some extent at all temperatures, suggesting seven-member ring formation in PAHs already containing five-member rings could be important.



## Chapter 7

# Modelling the properties and concentration of localised $\pi$ -radicals in flames

*The impact of localised  $\pi$ -radicals on soot formation is explored by considering their electronic structure and computing their relative concentrations in flame conditions by means of batch reactor simulations with flame concentrations of  $H^\bullet$  and  $H_2$ . It is seen that low temperatures ( $<1000$  K) favor the fully saturated rim-based pentagonal ring. Soot nucleation temperatures (1000–1500 K) promote the formation of localised  $\pi$ -radicals on rim-based pentagonal rings. These localised  $\pi$ -radicals are in higher concentration than aryl-type radicals at these temperatures, consistent with recent experimental observations. Higher temperatures favor the  $\sigma$ -radical and the concentration of the localised  $\pi$ -radical on rim-based pentagons becomes negligible. A kinetic Monte Carlo treatment of multiple sites indicates that multiple localised  $\pi$ -radicals are possible on a single molecule suggesting localised  $\pi$ -radicals on rim-based pentagonal rings may be relevant to soot formation in flames.*

### Collaborative Contributions

The work presented in this chapter has been accepted for publication in *Proceedings of the Combustion Institute* and is primarily a collaboration with Jacob Martin and Gustavo Leon. Jacob Martin performed the spin density and Clar analyses. Gustavo Leon performed the kinetic Monte Carlo simulations. The electronic structure calculations, kinetic simulations, rate calculations were performed by the author. The analysis of results and preparation of figures was done collaboratively between Jacob Martin, Gustavo Leon, and the author. The manuscript was written by the author, with Jacob Martin and Gustavo Leon also helping in editing the manuscript.

### 7.1 Introduction

The reactivity of observed edges of PAHs was recently mapped using electronic structure theory with reactivity indices (Martin et al., 2019b). It was found that localised  $\pi$ -radicals on rim-based pentagonal rings that are partially saturated/protonated (previously explored computationally for edge rearrangements (Whitesides and Frenklach, 2010)) are quite reactive. This enables complexes that are both  $\pi$ -stacked and covalently bonded, forming a rim-bond on the face of the aromatic species. These complexes are called aromatic rim-linked hydrocarbons (ARLH). The importance of localised  $\pi$ -radicals in soot formation was first introduced by Wang at the 2010 International Symposium on Combustion (Wang, 2011), where he considered a separate localisation mechanism based on diradical systems such as acenes (Wang, 2011; Koley et al., 2012).

HR-AFM of aromatic soot precursors showed the presence of these partially saturated sites as well as fully saturated rim-based pentagons (Commodo et al., 2019). This would suggest that a partial equilibrium exists between rim-based pentagonal rings and hydrogen radicals in flames, potentially leading to significant concentrations of reactive localised  $\pi$ -radicals. The concentration of another radical – the  $\sigma$ -radical – was computed by Howard (1991), where the edges

of these aromatic species were considered to be in partial equilibrium with  $\text{H}^\bullet$  and  $\text{H}_2$  in the flame. On average, 2–3  $\sigma$ -radicals were found to be present in each  $\approx 670$  Da aromatic species. However, no similar analysis exists for partially saturated rim-based pentagonal rings. **The purpose of this chapter** is to first explore the localisation of  $\pi$ -radicals. A reaction mechanism and rates are then calculated for partially saturated rim-based pentagonal rings. Batch reactor simulations using kinetic equations and Monte Carlo methodologies are then used to explore the concentration of these reactive  $\pi$ -radicals in flames.

## 7.2 Methodology

### 7.2.1 Computational Chemistry Methods

Geometry optimizations and vibrational frequency calculations were performed using the hybrid density functional B3LYP and the 6-311G(d,p) basis set for all chemical species and transition states. Transition states were confirmed to have one imaginary frequency corresponding to the reaction in question. The energies of all major species and transition states were further refined using the composite CBS-QB3 method, as well as the composite G4MP2 and hybrid DFT method M06-2X for comparative purposes. All quantum chemistry calculations were performed using the Gaussian 16 program ([Frisch et al., 2016](#)).

### 7.2.2 Rate Constant Calculations

#### 7.2.2.1 Reactions with Barriers

The rate constants of all reactions with a well-defined transition state and barrier were estimated using conventional transition state theory as implemented in the Arkane package within Reaction Mechanism Generator ([Gao et al., 2016](#)). The rates were computed using the standard transition state expression:

$$k = \frac{k_B T}{h} \frac{q^\ddagger}{\prod_i^{n_{\text{reactants}}} q_i} \exp\left(\frac{-\Delta E_0}{RT}\right), \quad (7.1)$$

where  $k$  is the rate constant,  $k_B$  is the Boltzmann constant,  $T$  is temperature,  $h$  is Planck's constant,  $q$  is the total partition function, and  $\Delta E_0$  is the classical barrier height. The partition functions for all species were computed using the Rigid-Rotor, Harmonic-Oscillator (RRHO) model, with frequencies and rotations determined at the B3LYP/6-311G(d,p) level of theory. To account for quantum tunneling effects, the simple Wigner correction was employed (Wigner, 1932), giving the tunnelling correction factor,  $C_W$  as follows:

$$C_W = 1 - \frac{1}{24} \left( \frac{h\nu^\ddagger}{k_B T} \right)^2, \quad (7.2)$$

with  $\nu^\ddagger$  being the magnitude of the imaginary frequency of the transition state. The Eckart tunneling correction is also commonly used (Truhlar and Kuppermann, 1971), but the difference between the Eckart and Wigner correction in this case was negligible, with both predicting tunneling corrections of around 1.2 at 300 K and negligible tunneling correction at the higher temperatures.

Subsequently, the rates computed for acenaphthylene(A2R5) were assumed to be the same for a larger aromatic, acecoronene (A7R5), which is a coronene with a rim-based pentagonal ring. In order to show that this assumption is reasonable, some rates were recalculated for A7R5 and compared to those computed for A2R5. Since the CBS-QB3 calculations have too large a memory requirement for a molecule such as acecoronene, the rates were computed using energies, geometries, and vibrational frequencies derived at the B3LYP/6-311G(d,p) level of theory. In this case, the reactions chosen were hydrogen abstraction from, addition to, and migration on A7R5, representing the three main categories of hydrogen-PAH reactions studied in this work. Figure 7.1 presents the Arrhenius plots of these three processes for A2R5 and A7R5. Little difference is seen between the smaller and larger aromatic rates. Hence, it is expected that the rates

calculated for A2R5 in this work should scale for larger PAHs with rim-based pentagonal rings as well.

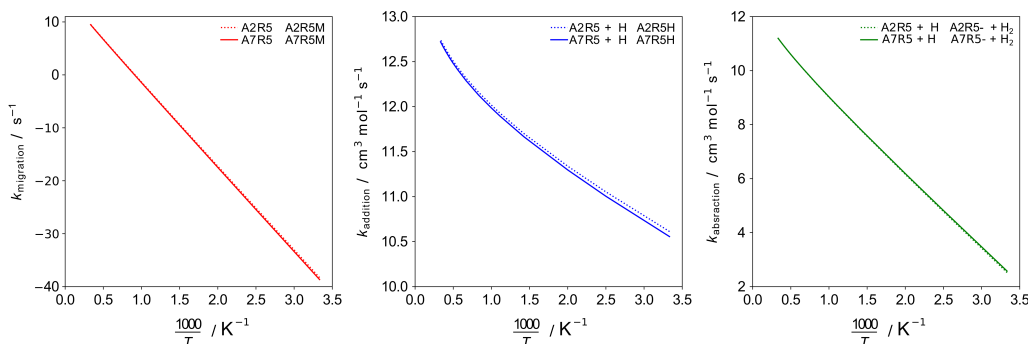


**Figure 7.1:** Temperature dependent rate constant for acenaphthelene A2R5 and coronene A7R5 for some critical reactions in the reaction mechanism.

### 7.2.2.2 Barrierless reactions

In the case of the three barrierless reactions, there is no tight transition state, and application of transition state theory is not possible. To estimate the rate constants for these reactions, two methods were tested. The first was the application of RRKM theory with a simple Gorin Model, as implemented in the Unimol software (Rynefors, 1982). The second was the use of momentum-resolved variational transition state theory (VTST) as implemented in ktools (Barker et al., 2017a). The unimolecular decomposition rates were determined using these methods, and the radical recombination rate was determined from the equilibrium constant for the overall reaction.

For the collisional parameters, the Lennard-Jones parameters of the PAHs were estimated from their molecular weight,  $M_w$ , based on the correlations of Wang et al. (Wang and Frenklach, 1994):

$$\sigma = 1.234(M_w^{0.33}) \quad (7.3)$$

$$\frac{\epsilon}{k_B} = 37.15(M_w^{0.58}) \quad (7.4)$$

For the energy transfer parameters, a standard exponential-down form was adopted:

$$\alpha = \alpha_0 \left( \frac{T}{298} \right)^n, \quad (7.5)$$

with  $\alpha_0$  taken as  $300 \text{ cm}^{-1}$  and  $n$  taken as 0.85.

### 7.2.2.2.1 Gorin Model calculations

In the Gorin model, the internal motion of the transition state is given by the vibrations and rotations of the separated fragments of the product, and the potential energy between the separated fragments needs to be provided. In this case, the free-rotor approximation was used for the rotations of the loose transition states. The potential energy surfaces for the barrierless reactions were determined using a relaxed scan at B3LYP/6-311G(d,p) level of theory. This was then used to fit a Morse potential for the interaction between the separated fragments to use in the Gorin/RRKM computations.:

$$E(r) = D_e [1 - \exp[-\beta(r - r_{\text{eq}})]]^2, \quad (7.6)$$

with  $D_e$  being the bond dissociation energy,  $r$  the reaction coordinate,  $r_{\text{eq}}$  the equilibrium distance, and  $\beta$  the steepness of the potential energy function. The fitted Morse potentials are presented in Figure 7.2.

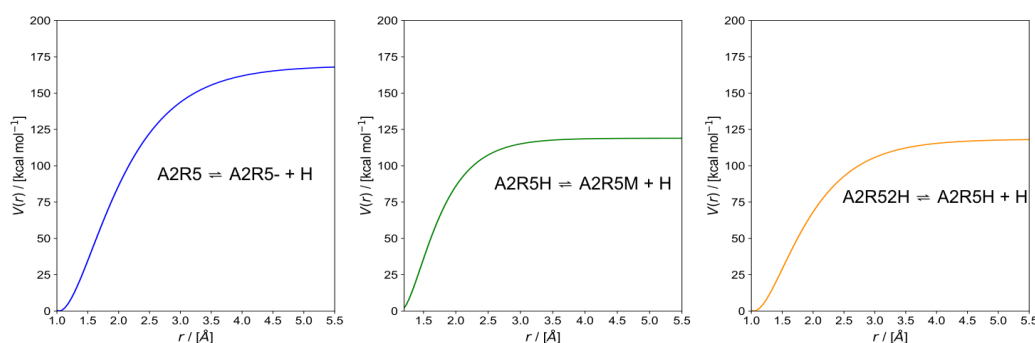


**Figure 7.2:** Fitted Morse potentials for barrierless reactions. The interaction potential energy surfaces were fitted to the B3LYP/6-311G(d,p) level of theory.

The geometries, frequencies, and rotations of the reactants and products were taken from the optimised structures at the B3LYP/6-311G(d,p) level of theory, consistent with the methodology for the reactions with barriers.

#### 7.2.2.2.2 VTST calculations

The VTST calculations performed in this work follow the angular-momentum resolved microcanonical variational transition state theory (J-resolved VTST) implemented in ktools. The canonical rate constants are then computed by a 2D averaging over both the angular momentum and energy microcanonical rate constants (Barker et al., 2017a). For these calculations, nine trial transition states were taken from a relaxed potential energy surface scan at the B3LYP/6-311G(d,p) level of theory, with the coordinate being the carbon-hydrogen bond distance. This is the same scan used to derive the potential energy surface for the Morse potential fits in Figure 7.2. Frequencies and rotations were calculated for each trial transition state by extracting each trial geometry and running a frequency calculation again using B3LYP/6-311G(d,p). Energies of each trial transition state relative to the reactant PAH were also taken at this level of theory, as well the energies of the separated H radical and PAH fragments. The numerical parameters for the energy and angular momentum density of states integration were taken from Akbar Ali and Barker (2015). Namely, this involves

an energy grain of  $10 \text{ cm}^{-1}$  and maximum energy of  $20000 \text{ cm}^{-1}$ , as well as an angular momentum grain of  $1 \text{ cm}^{-1}$  and maximum angular momentum of  $1000 \text{ cm}^{-1}$ . These are essentially the standard recommended parameters. Little variance was seen in the rate constants based on these parameters.

Figure 7.3 compares the three barrierless reaction rate constants computed using the RRKM theory framework and the simple Gorin model with those computed using the variational transition state theory (VTST) framework.

In general, the Gorin model over-predicts the rate constants compared with the more accurate VTST method, possibly because one of the fragments of the product (the PAH radical) is very large and similar to the reactant PAH. The rates predicted by the Gorin Model were hence deemed unreliable, and the VTST rates were used instead.

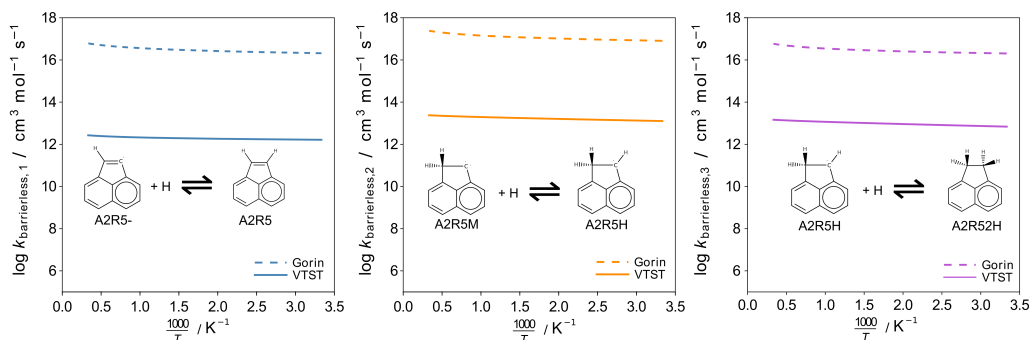


**Figure 7.3:** Temperature dependent rate constant for the three barrierless reactions computed using the Gorin model and variational TST (VTST).

### 7.2.3 Spin-density calculations and Clar analysis

The electron spin density,  $\rho^s(\mathbf{r})$ , is computed from the difference between the spin density of the  $\alpha$  and  $\beta$  electron spin densities:

$$\rho^s(\mathbf{r}) = \rho^\alpha(\mathbf{r}) - \rho^\beta(\mathbf{r}). \quad (7.7)$$

It is widely used as a metric to locate reactive sites and compute degrees of localisation within molecules, finding widespread use in open-shell DFT



calculations. A recent study of diradicals has demonstrated the applicability of spin density studies to determine reactivity on other aromatic species (Stuyver et al., 2019) and a similar approach is adopted here.

The Clar analysis is a qualitative method to determine the reactivity of fused polycyclic aromatics. It centres around aromatic  $\pi$ -sextets that are defined as ‘six  $\pi$ -electrons localised in a single benzene-like ring separated from adjacent rings by formal CC single bonds’ (Solà, 2013). Configurations are sought with the maximum number of sextets with double bonds or a radical placed in the remaining positions. Algorithms for automatically computing the Clar structure are described in various works, such as in Liu and Green (2019).

### 7.2.4 Kinetic Simulations

Kinetic simulations were performed in a 0-D isothermal reactor using Cantera (Goodwin et al., 2009) at a pressure of 1 atmosphere and initial mole fractions of  $10^{-5}$ , 0.001, and 0.1 for acecoronene, H, and H<sub>2</sub> with the rest as N<sub>2</sub>. These are representative of typical concentrations of these species in flames (Raj, 2019). The rates for the reactions of the five-membered ring in acenaphthylene were used, as it was seen that these are likely very similar to those for the five-membered ring in acecoronene.

### 7.2.5 Kinetic Monte Carlo Simulations

In addition, two kinetic Monte Carlo (KMC) simulations were conducted to study the effect of multiple five-membered rings on the formation of localised  $\pi$ -radical sites using the five-membered ring as the reactive site. Coronenes with two and three rim based five-member rings were selected as the starting PAHs for each KMC simulation. In this model, there are five site types used to study the formation of localised  $\pi$ -radicals and other intermediate species formed in the activation process. These site types cover the degree of saturation of the rim-based five-membered rings in the PAH, and are R5, R5-, R5H, R5M and R52H. Only the 18 reactions involving the localised  $\pi$ -radical were included as jump processes for these sites, with the rates given in Table 7.1.

The site specific reaction rate is computed as:

$$r_i = k_i \times [A] \times N_{\text{site},i}, \quad (7.8)$$

where  $r_i$  is the site specific reaction rate for reaction  $i$  with rate constant  $k_i$ ,  $[A]$  is the concentration of the gas phase species involved in the reaction and  $N_{\text{site},i}$  is the number of sites present in the PAH that can undergo reaction  $i$ .

Other important physics for PAHs have been neglected in the model to focus solely on the kinetics of localised  $\pi$ -radicals. Particle processes such as coagulation, sintering or condensation were not considered. This way the PAHs are not interacting with each other and only undergo gas-phase reactions. Other important surface reactions, such as HACA growth or acetylene desorption are not included. Although this is a large simplification, it allows the number of carbon atoms in all the simulated PAHs to be constant and only the radical behaviour due to hydrogen atoms be explored, which is the focus of this work.

The initial concentrations, and pressure were the same as for the 0-D kinetic simulations with a temperature of 1000 K. An ensemble of 100,000 PAHs was used per simulation to achieve statistical significance.

## 7.3 Results and discussion

### 7.3.1 Localisation of $\pi$ -radicals

Localisation of  $\pi$ -radicals is driven by aromaticity. We will highlight this by considering the spin density interpreted through a Clar analysis for  $\pi$ -radical doublet spin states.

Figure 7.4 shows the spin density isosurface as well as the value of the spin density for the most spin-rich site. The phenylmethyl radical [Fig. 7.4 a)] shows the most significant spin density on the methyl site. A Clar analysis would suggest that the phenyl ring contains an aromatic sextet (“six  $\pi$ -electrons localised in a single benzene-like ring separated from adjacent rings by formal CC single

bonds” (Solà, 2013)) with the radical residing solely on the methyl group. Spin density is seen within the aromatic ring suggesting other minor Clar resonance structures, however the Clar structure shown is found to dominate suggesting that the aromaticity of the ring is maximised when the  $\pi$ -radical is localised to the methyl site. Similarly with the fluorenyl radical, shown in figure 7.4 b), the major Clar structure suggests two sextets with the radical localised to the pentagonal ring, which is seen in the spin density. A Clar analysis of the cyclopentamethyl radical shown in Figure 7.4 c), the focus of this paper, would suggest a traveling sextet across the two six-membered rings with the radical localised on the unsaturated pentagonal ring site. The spin density suggests that some minor delocalisation is occurring to the  $\beta$ -site from the primary radical site on the aromatic edge due to minor Clar structures (Martin et al., 2019b). The fact that this site is not significantly delocalised past the  $\beta$ -site is seen from the lack of change in the spin density after enlarging the aromatic network [Fig. 7.4 d)]. Furthermore, no significant change is seen for the same  $\pi$ -radical site on the curved aromatic corannulene in Figure 7.4 e).

Figure 7.4 f) – j) shows the impact of delocalisation on  $\pi$ -radicals. However, it is still seen that aromaticity drives the location of the delocalised  $\pi$ -radical. For indenyl [Fig. 7.4 f)] the Clar analysis provides one sextet with a radical in resonance between two sites, with spin density showing that the radical is indeed split. Protonation of a benzene ring [Fig. 7.4 g)] again suggests three locations for the  $\pi$ -radical beginning to become delocalised. Phenalenyl [Fig. 7.4 h)], the prototypical six-membered ring delocalised  $\pi$ -radical, has the radical split over six sites, still driven by aromaticity. The Clar analysis shows one sextet with the radical residing on the zig-zag edge with six resonance structures suggesting significant delocalisation. Enlarging the aromatic network in this case [Fig. 7.4 i) and j)] leads to a delocalisation of the  $\pi$ -radical with some minor localisation on zig-zag edges, which can be justified by a major Clar structure with the radical centered on these edges. Therefore, the  $\pi$ -radical can be either localised or delocalised depending on the aromatic topology, which can be rationalized by aromaticity rules.

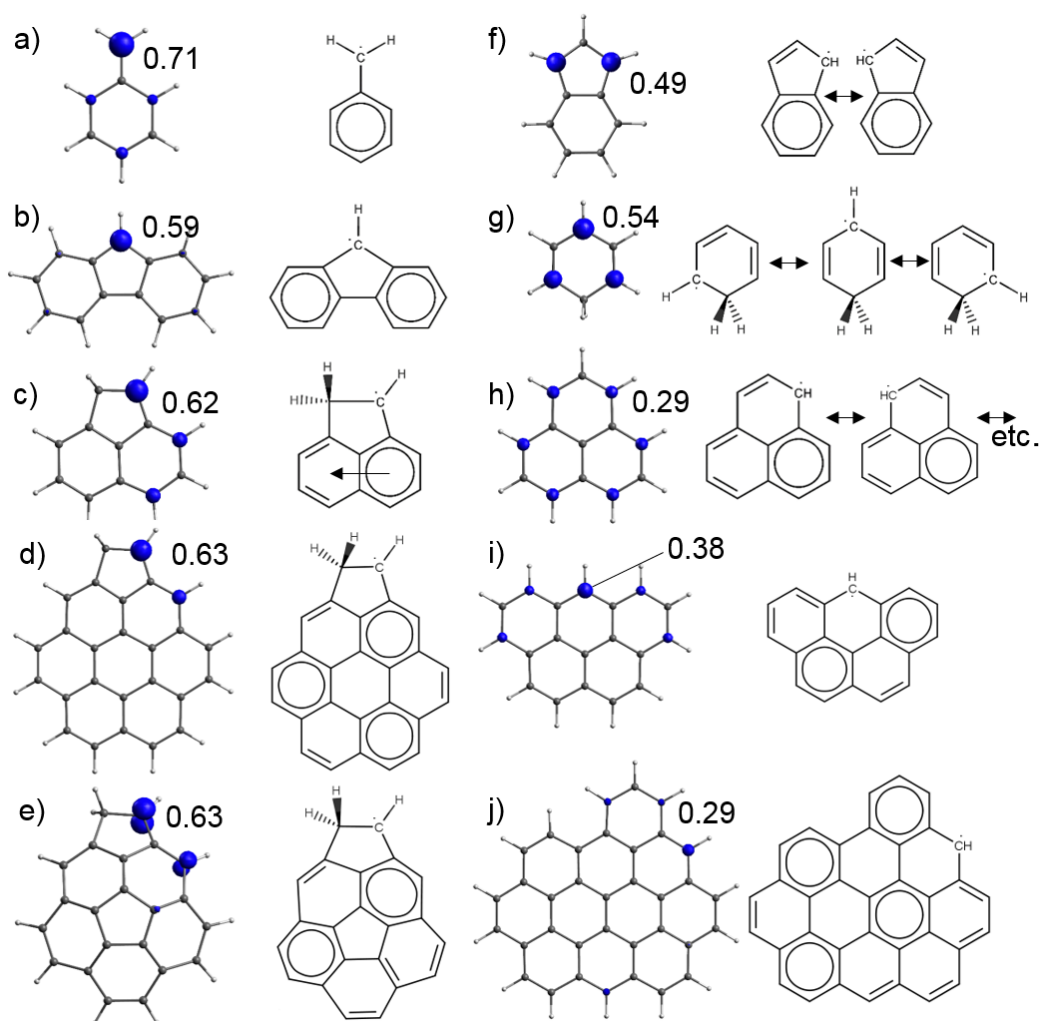


**Figure 7.4:** Spin density isosurface=0.025 shown on the molecular geometry with the Clar analysis. The spin density of the most spin rich carbon site is also shown indicating the degree of localisation.

### 7.3.2 Reaction mechanism for localised $\pi$ -radicals on rim-based pentagonal rings

Entropic considerations suggest that hydrogen addition would be unfavored at high temperatures due to 1) the reverse reaction leading to two species, and 2) the hydrogen addition reactions having a larger pre-exponential factor, as the additions can occur from above and below the aromatic plane, whereas hydrogen

## 7.3 Results and discussion

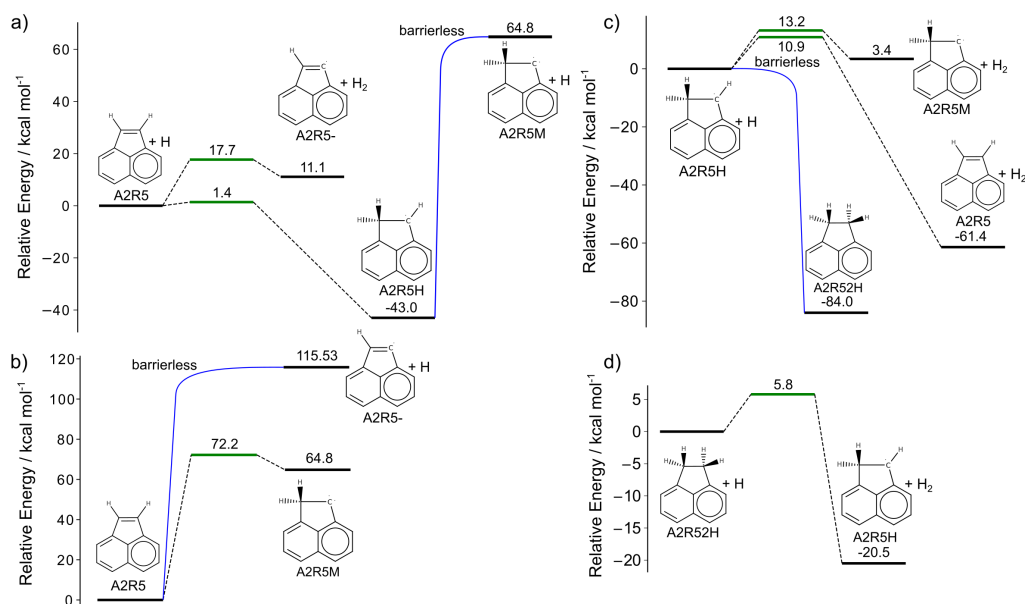


**Figure 7.5:** Potential energy surfaces for the reactions on five-membered rings in acenaphthylene leading to the formation of localised  $\pi$ -radicals on rim-based pentagonal rings at 0 K. Energies are computed at the CBS-QB3//B3LYP/6-311G(d,p) level of theory.

abstraction requires a collision directly along the C–H bond in order to form the radical. At flame temperatures this paints a picture of rapid hydrogen addition and removal during soot formation, requiring a detailed mechanism to reveal the concentration of reactive localised  $\pi$ -radicals on rim-based pentagonal rings. It should be mentioned that systems with diradical character are not considered in this study (Wang, 2011; Koley et al., 2012).

Figure 7.5 presents the potential energy surfaces for the reactions of acenaphthalene (A2R5) that could lead to the formation of the localised  $\pi$ -radical A2R5H, a  $\sigma$ -radical (A2R5-), as well as a fully hydrogenated five-membered ring (A2R52H). Starting from A2R5 as the reactant in Figure 7.5 a), A2R5- can be produced through hydrogen abstraction by an H radical, which proceeds with a moderate barrier of 17.7 kcal/mol. This is similar to values reported for hydrogen abstraction by H radicals on PAHs using the G3(MP2,CC) composite method (Hou and You, 2017). Hydrogen can also attack the five-membered ring

on A2R5, resulting in the localised  $\pi$ -radical, A2R5H. This process has a very low barrier of 1.4 kcal/mol, and releases 43 kcal/mol of energy, meaning it is expected to be preferred at low temperatures. Finally, A2R5H can undergo a hydrogen loss process, the reverse of the barrierless A2R5M and hydrogen radical recombination reaction. The reaction energy for the hydrogen loss in this case is high as expected, at 108 kcal/mol. In Figure 7.5 b), A2R5<sup>-</sup> can also be formed by a hydrogen loss from A2R5. Again, the reverse process of the A2R5<sup>-</sup> and hydrogen radical recombination is barrierless. This hydrogen loss also has a very high reaction energy of 115.5 kcal/mol. A2R5 can also undergo a hydrogen migration to form A2R5M, but this requires a large barrier (72.2 kcal/mol) to be overcome in order for the migration to proceed, with a small reverse barrier. Both of these processes are expected to be unfavorable at flame temperatures (Violi, 2005b; Frenklach, 2019). In Figure 7.5 c), the localised  $\pi$ -radical A2R5H can have hydrogen abstraction by H radicals occur at both carbons along the five-membered ring peripheral free edge. One abstraction results in the formation of A2R5M, requiring a barrier of 13.2 kcal/mol, with a reaction energy of 3.4 kcal/mol. The other abstraction requires a barrier of 10.9 kcal/mol and re-produces A2R5, with a reaction energy of -61.4 kcal/mol. Between the two abstraction processes, the production of A2R5 has a slightly lower barrier and proceeds to a lower energy product, so it is expected that A2R5 will be preferentially formed over A2R5M by abstraction. Alternatively, the H radical can undergo a barrierless recombination reaction with the localised  $\pi$ -radical A2R5H to form the protonated A2R52H. With a reaction energy of -84.0 kcal/mol, this is expected to be the competing route with abstraction, producing A2R5. Finally, Figure 7.5 d) presents hydrogen abstraction by H radicals on either of the fully saturated carbon sites in A2R52H, resulting in the re-formation of A2R5H. This hydrogen abstraction has a much lower barrier than those seen for the abstractions on A2R5 or A2R5H, at just 5.8 kcal/mol. This abstraction also proceeds downhill in energy with a decrease in 20.5 kcal/mol, which is also in contrast to the A2R5 and A2R5H abstractions. This abstraction provides a return path to the localised  $\pi$ -radical. The rate constants for the reactions presented in the potential energy surface in Figure 7.5 and their reverse reactions were computed in the temperature range 300 – 2000 K and at the high pressure limit. The rate constants were then fitted to the modified Arrhenius

form, with the parameters given in Table 7.1.

**Table 7.1:** Modified Arrhenius rate parameters for the localised  $\pi$ -radical mechanism. The units are kcal/mol, K,  $\text{cm}^3\text{mol}^{-1}\text{s}^{-1}$  and  $\text{s}^{-1}$ .

| Reaction                       | A                    | n     | E      |
|--------------------------------|----------------------|-------|--------|
| <i>With Barrier</i>            |                      |       |        |
| A2R5+H→A2R5-+H <sub>2</sub>    | $1.99 \cdot 10^8$    | 1.88  | 16.76  |
| A2R5-+H <sub>2</sub> →A2R5+H   | $7.08 \cdot 10^5$    | 2.11  | 4.89   |
| A2R5+H→A2R5H                   | $1.63 \cdot 10^9$    | 1.51  | 0.77   |
| A2R5H→A2R5+H                   | $1.93 \cdot 10^{10}$ | 1.24  | 44.66  |
| A2R5→A2R5M                     | $2.65 \cdot 10^{11}$ | 0.70  | 71.85  |
| A2R5M→A2R5                     | $3.19 \cdot 10^{11}$ | 0.40  | 6.88   |
| A2R5H+H→A2R5M+H <sub>2</sub>   | $7.29 \cdot 10^7$    | 1.48  | 11.84  |
| A2R5M+H <sub>2</sub> →A2R5H+H  | $4.85 \cdot 10^5$    | 1.89  | 7.49   |
| A2R5H+H→A2R5+H <sub>2</sub>    | $2.17 \cdot 10^7$    | 1.86  | 9.24   |
| A2R5+H <sub>2</sub> →A2R5H+H   | $1.20 \cdot 10^5$    | 2.56  | 69.86  |
| A2R52H+H→A2R5H+H <sub>2</sub>  | $4.42 \cdot 10^7$    | 1.83  | 4.33   |
| A2R5H+H <sub>2</sub> →A2R52H+H | $2.41 \cdot 10^6$    | 1.78  | 24.28  |
| <i>Barrierless</i>             |                      |       |        |
| A2R5→A2R5-+H                   | $2.87 \cdot 10^{15}$ | -0.32 | 117.47 |
| A2R5-+H→A2R5                   | $4.90 \cdot 10^{11}$ | 0.21  | 0.00   |
| A2R5H→A2R5M+H                  | $4.61 \cdot 10^{15}$ | -0.35 | 109.87 |
| A2R5M+H→A2R5H                  | $1.19 \cdot 10^{13}$ | 0.09  | 0.28   |
| A2R52H→A2R5H+H                 | $1.89 \cdot 10^{16}$ | -0.40 | 86.38  |
| A2R5H+H→A2R52H                 | $6.95 \cdot 10^{12}$ | 0.10  | 0.35   |

To examine the accuracy of the rate coefficients calculated above, one can compare the rate constants for the hydrogen abstraction by H radicals to those previously calculated by the authors (Hou and You, 2017), where the rate of abstraction from A2R5 was calculated. The value calculated using CBS-QB3 is higher by a factor of 1.72 at 1500 K. This follows from the barrier for this abstraction predicted by CBS-QB3, being 1.8 kcal/mol lower than the previous calculations, which is within their reported uncertainty of  $\pm 2$  kcal/mol for the M06-2X barrier heights. Additionally, Violi reported a barrier of 80 kcal/mol for migration of a hydrogen atom on the bay site of benzo[c]phenanthrene, resulting in the formation of a carbene site (Violi, 2005b). This is not too dissimilar to the migration barrier of 72.2 kcal/mol for A2R5 in this work, given that the

## 7 CHAPTER 7

---

results from [Violi \(2005b\)](#) were computed using energies at B3LYP/6-31G(d,p) compared to CBS-QB3.

Additionally, the barrier heights presented in Figure 4 were also computed using another higher level composite method, G4MP2, and a hybrid density functional known for improving the energetics of PAH systems, M06-2X ([Hou and You, 2017](#)). The comparison of barrier heights predicted by these three methods is displayed in Table 7.2.

**Table 7.2:** Comparison of barrier heights predicted by CBS-QB3, G4MP2, and M06-2X methods. The units are kcal/mol.

| Reaction                   | CBS-QB3 | G4MP2 | M06-2X |
|----------------------------|---------|-------|--------|
| R5+H→R5+H <sub>2</sub>     | 17.7    | 19.1  | 20.5   |
| R5+H <sub>2</sub> →R5+H    | 6.6     | 10.3  | 6.8    |
| R5+H→R5H                   | 1.4     | 2.2   | 1.7    |
| R5H→R5+H                   | 44.4    | 45.0  | 48.0   |
| R5→R5M                     | 72.2    | 71.6  | 73.9   |
| R5M→R5                     | 7.4     | 6.8   | 8.1    |
| R5H+H→R5M+H <sub>2</sub>   | 13.2    | 11.8  | 14.5   |
| R5M+H <sub>2</sub> →R5H+H  | 9.8     | 8.9   | 6.4    |
| R5H+H→R5+H <sub>2</sub>    | 10.9    | 9.0   | 11.9   |
| R5+H <sub>2</sub> →R5H+H   | 72.3    | 70.8  | 69.6   |
| R52H+H→R5H+H <sub>2</sub>  | 5.8     | 6.4   | 7.5    |
| R5H+H <sub>2</sub> →R52H+H | 26.3    | 26.2  | 23.1   |

The values above suggest a mean deviation of 1.2 kcal/mol between the barriers predicted by CBS-QB3 and G4MP2, suggesting good agreement. Previous bench-marking between CBS-QB3 and G2 energies suggested a difference in 1.1 kcal/mol ([Montgomery Jr et al., 2000](#)), so this is not entirely unexpected. There is a larger mean deviation of 2.3 kcal/mol between the barriers predicted by CBS-QB3 and M06-2X. This is significant, but not unreasonable. Given the uncertainty in M06-2X and CBS-QB3 methods are expected to be  $\pm 1-2$  kcal/mol, the difference in barrier heights is still at the point where the two methods are suggesting very similar behaviour.

For the barrierless recombination reactions, Mebel and coworkers computed the reaction energy of the H radical–naphthyl recombination as -111.0 kcal/mol



using G3(MP2,CC) (Mebel and Kislov, 2009). This reaction is similar to the H radical–A2R5- recombination, as is the energy of -115.5 kcal/mol predicted here. The reaction energy of A2R5M and H is also similar at -107.8 kcal/mol. The A2R5H recombination reaction energy is quite different at -84.0 kcal/mol, but the H radical attacks a carbon that already has a hydrogen, which is not true for the other reactions, so this difference is expected. Harding *et al.* computed the rate of the H radical–naphthyl recombination reaction using interaction energies determined by CASPT2/cc-pVDZ and VRC-TST for the rates (Harding *et al.*, 2005). In general, the rate constants calculated by Harding *et al.* (2005) for the H radical–naphthyl recombination are one to two orders of magnitude higher than the recombinations here. The calculations here are less accurate, as the interaction energies are determined by DFT and not a multi-reference method. On the other hand, it was noted that for hydrogen abstraction reactions, the reaction on A2R5 is several orders of magnitude lower than for naphthyl (Hou and You, 2017), so this difference may be due to the reactant molecule. Additionally, the rate of the H radical–A2R5- recombination was also computed using a complete-active-space SCF (CASSCF) calculation derived potential energy surface. The active space chosen consisted of two electrons and two orbitals, centered on the carbon-hydrogen bond in question in A2R5, essentially amounting to a CASSCF(2e,2o)/6-311G(d,p) calculation. A natural orbital calculation with mixing of the HOMO and LUMO orbitals in A2R5 was performed to provide the guess orbitals for the CASSCF calculation. The computed rate constant using this potential energy could then be compared, which is seen in Figure 7.6.

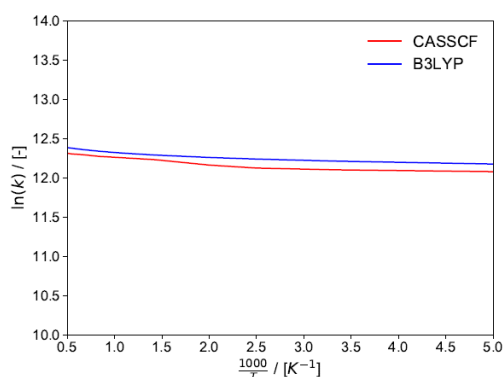


**Figure 7.6:** Comparison between rate constant computed for the A2R5- + H radical recombination reaction using B3LYP and CASSCF(2e,2o).

The comparison suggests that B3LYP overestimates the rate constant for the radical recombination by 6-11% when compared CASSCF and high and low temperatures respectively, due to B3LYP predicting a more attractive potential. Previous work on barrierless oxidation of PAH radicals by oxygen radicals also compared rate constants computed using B3LYP to those using the perturbation-corrected CASSCF, or CASPT2 (Frenklach et al., 2018). The authors found B3LYP overestimated the rate constant by about 8%, which agrees with the results here. This suggests that whilst B3LYP does overestimate the rate constant compared to multi-configuration and multi-reference methods, it is not by a very large amount, suggesting that the B3LYP method is a reasonable choice for providing potential energy surfaces for a first estimate of these rate constants. Nevertheless, further refinement of the rates of the barrierless reactions is necessary, as these will be the largest source of uncertainty in the kinetic mechanism.

### 7.3.3 Concentration profiles in flames

Figure 7.7 provides the kinetic simulations in a 0-D, homogeneous gas-phase reactor at 1 atmosphere of pressure using the 18 reactions that involve the five-membered ring detailed in Table 7.1.

The chosen reactant PAH is acecoronene, a coronene with a rim-based five-membered ring, or A7R5, representative of a slightly larger PAH. Since

### 7.3 Results and discussion

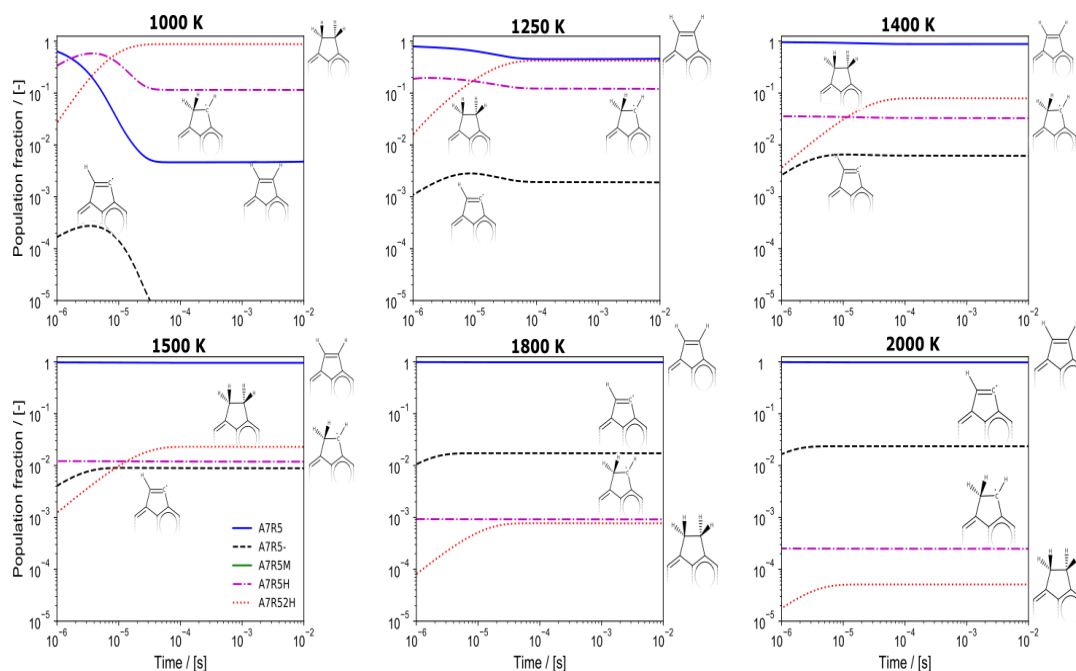


**Figure 7.7:** 0-dimensional homogeneous gas-phase reactor simulations of reactions involving acoronene (A7R5) at atmospheric pressure and typical flame compositions. The degree of saturation of the five-membered ring is shown in the figure.

reactions of carbons in the six-membered ring are not considered (as the five-membered ring is of primary interest), the choice of reactant PAH is largely unimportant. The rates computed for A2R5 are also likely very similar for larger PAHs, which has been observed for hydrogen abstraction by H radicals on PAHs (Hou and You, 2017). Computations performed of the rate constants for hydrogen abstraction, migration, and addition for A7R5 suggest this is indeed the case, as seen in figure 7.1. The kinetic simulations were conducted for six temperatures, including a lower temperature threshold for soot formation of  $>1000$  K, temperatures of 1250 and 1400 K where soot nucleation is found in flames (Glassman, 1989), a typical flame temperature of 1500 K, and temperatures representative of maximum values seen in flames of 1800 and 2000 K.

Figure 7.7 shows clear trends in the degree of saturation of the carbons on the five-membered ring. At 1000 K, the saturated products are preferred, with the fully saturated species being the dominant product at a population fraction (mole

fraction divided by total PAH mole fraction) close to one. In other words, most of the reactant PAH transforms to a fully saturated five-membered ring product. However, the localised  $\pi$ -radical is the second most favored product with population fraction close to 0.1. The reactant PAH is depleted, but then starts to reform at around 1 ms when the reverse reactions start to occur. At 1250 and 1400 K, it can be observed that the major product is the reactant with an unsaturated rim-based pentagonal ring, followed by the fully saturated five-membered ring and the localised  $\pi$ -radical. Comparing these results with the HR-AFM structures, a consistent frequency of rim-based pentagonal sites with a ratio of 27:12:4 for the unsaturated, saturated and partially saturated rim-based pentagonal rings is observed (Commodo et al., 2019). The population fraction of the saturated product is lower at these temperatures, but is still of the order of 1 to 0.1 for the fully saturated five-membered ring and 0.1 to 0.01 for the localised  $\pi$ -radical. This is a significant population fraction and is considerably higher than the  $\sigma$ -radicals, suggesting that if chemical cross-linking reactions leading to larger PAHs and/or soot are to occur at these temperatures, such reactions should also consider localised  $\pi$ -radicals as potential reactants. At 1500 K, the population fraction of the localised  $\pi$ -radical is stable at 0.01, with the population fraction of  $\sigma$ -radicals being very similar and the population fraction of the fully saturated product being only slightly higher. This suggests that even at 1500 K, the localised  $\pi$ -radicals could be as important as  $\sigma$ -radicals, even though the concentration is much lower than just the species with peripheral five-membered rings. At the higher temperatures of 1800 and 2000 K, the unsaturated states are favored, with the reactant and  $\sigma$ -radicals being the dominant species as consistent with the trend. However, it can be seen that the population fraction of  $\sigma$ -radicals at these temperatures is lower than what was observed for the  $\pi$ -radicals at lower temperatures.

A sensitivity analysis was performed on the population fractions of the main species (A7R5, A7R5-, A7R5M, A7R5H, and A7R52H) to the 18 reactions in the mechanism developed. This is done in order to test the robustness of the kinetic simulations. The normalized sensitivity coefficients were computed using the definition:

$$S_{ki} = \frac{x_i}{y_k} \frac{\partial y_k}{\partial x_i}, \quad (7.9)$$

where  $S_{ki}$  is the sensitivity of response  $y_k$  to a change in variable  $x_i$ . These sensitivity coefficients were computed at three temperatures: 1400, 1500, and 1800 K, representing the temperatures of most interest to flames and soot formation, and at a time of 1 ms, by which the population fractions of species and the sensitivity coefficients are at steady state.

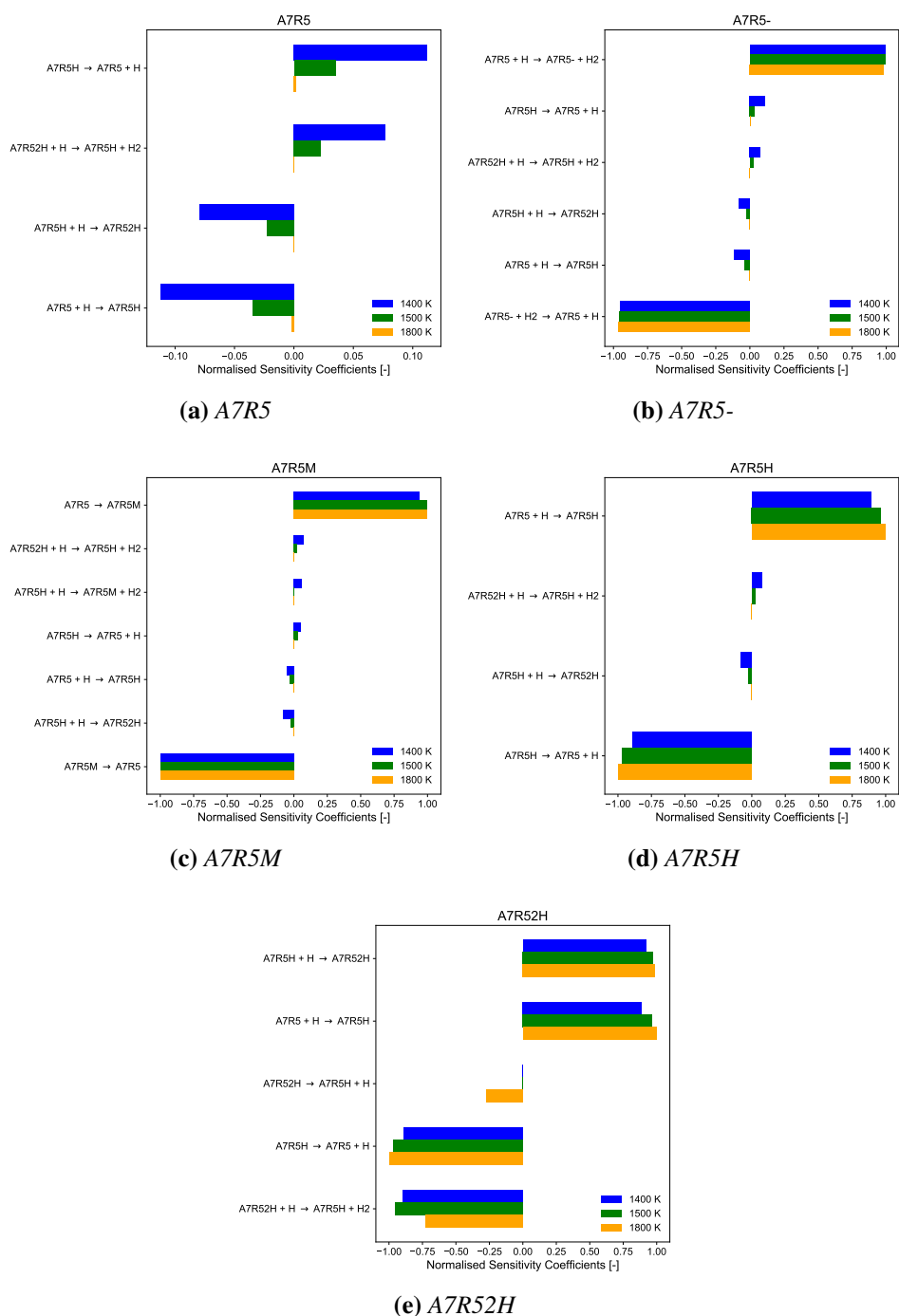


**Figure 7.8:** Normalised sensitivity coefficients for the main PAHs to the rate constants in the kinetic mechanism. Data is shown for three temperatures, 1400, 1500, and 1800 K. Only non-zero sensitivity coefficients are displayed.

Figure 7.8 shows that the PAHs are generally sensitive to only a few key reactions, with the sensitivity coefficients being of opposite signs for corresponding forward and backward reactions. For all species other than A7R5, the sensitivity coefficients are similar for the three temperatures and tend to be either close to 0 or 1. A7R5 has sensitivity coefficients that are between 0 and 0.1, most likely due to it being in such excess population fractions compared to the other PAHs. Figure 7.8a shows that A7R5 is most sensitive to the reaction with atomic hydrogen to produce A7R5H. This reaction has the lowest barrier of the reactions involving A7R5. Reactions that generate A7R5H from A7R52H also impact the fraction of A7R5 as a result. For A7R5-, figure 7.8b shows that the key reaction is the hydrogen abstraction from A7R5, which is expected as this is the only reaction producing A7R5. Similarly, the key reaction for A7R5M is the hydrogen migration occurring on A7R5 as seen in Figure 7.8c. A7R5H is entirely dependent on the hydrogenation of A7R5, with Figure 7.8d showing the opposite behavior of that for A7R5. Finally, for forming A7R52H, the key reactions are the barrierless hydrogen addition to A7R5H, and well as the preceding hydrogen addition to form A7R5H from A7R5. Overall, the reaction with the most importance is seen to be the hydrogenation of A7R5 to form A7R5H.

Additionally, as the sensitivity analysis suggests the importance of hydrogen radicals, simulations using initial H mole fractions of  $10^{-4}$  and 0.01 were also conducted to see the impact on the presented results. The results for two of the main temperatures, 1400 K and 1500 K are presented in Figure 7.9.

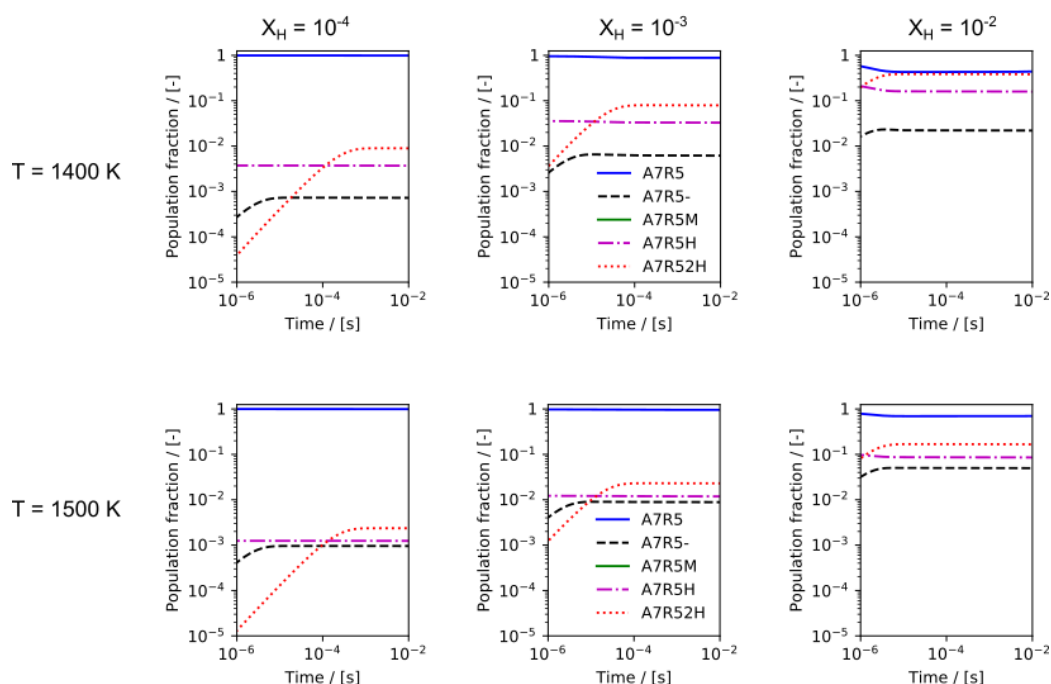


**Figure 7.9:** Kinetic simulations of a 0D homogeneous reactor with varying initial mole fractions of atomic hydrogen at temperatures of 1400 K and 1500 K.

The results in Figure 7.9 suggest that the mole fraction of atomic hydrogen does impact the fraction of reactant A7R5 that is converted to the  $\sigma$  radical A7R5-, localised  $\pi$ -radical A7R5H, and fully hydrogenated A7R52H as is expected from the sensitivity analysis. However, the relative amount of the three products is consistent regardless of initial atomic hydrogen concentration. The other main influence of the initial atomic hydrogen mole fraction is the speed at which the products form, which is also expected. These two analyses suggest that the localised  $\pi$ -radicals are important, but this is provided sufficient H-atom concentration is present.

Finally, a kinetic Monte Carlo scheme was developed to see if multiple localised  $\pi$ -radicals could be present on a single PAH with multiple rim-based pentagons (Figure 7.10). The lowest temperature (1000 K) was used to study the localised  $\pi$ -radicals as the kinetic simulations suggest that they are present in higher concentrations. In both cases, the population fraction of PAHs with one



localised  $\pi$ -radical reaches a maximum of  $\sim 0.5$  at around  $10^{-6}$  s. These PAHs subsequently react to form those with multiple localised  $\pi$ -radicals. In the two-site case, the two  $\pi$ -radical PAHs reach a significant population fraction of 0.35, whilst in the three-site case, the two and three  $\pi$ -radical PAHs of 0.4 and 0.2 respectively. At this point, a majority of PAHs have multiple localised  $\pi$ -radical sites. From here, the fully saturated product becomes dominant but in both cases a significant fraction of PAHs with single site localised  $\pi$ -radical remains. At very long timescales, the fully saturated product starts to reform the localised  $\pi$ -radical due to reversibility.

Comparing these results with the frequency of aromatic species imaged with HR-AFM ([Commodo et al., 2019](#)) just prior to soot nucleation, from a total of 49 molecules with  $>4$  rings; 28 contained at least one rim-based pentagonal ring, 12 contained two rim-based pentagonal rings and none of the imaged species contain three rim-based pentagonal rings. At least two reactive sites would be required to allow for a continuous mass accumulation into soot nanoparticles given a mechanism only involving ARLH. It should be mentioned that it was also found that the localised  $\pi$ -radical is able to form strong  $\pi$ -stacked complexes with the partially embedded rim-based pentagonal ([Martin et al., 2019b](#)). However, computing the concentrations of this site is outside the current scope of this work, as it requires detailed chemistry of PAH growth. The relative importance of  $\pi$ -radical versus  $\sigma$ -radical was also not explored due to the challenge of including van der Waals and possible curved PAH flexoelectric driven interactions for  $\pi$ -radicals in ARLH, which could significantly enhance the efficiency of reactions during collisions with flexoelectric species, which has been one of the challenges in  $\sigma$ -driven mechanisms ([Mao et al., 2018](#)). Given these considerations it appears, from these preliminary results, that  $\pi$ -radicals on rim-based pentagonal rings have sufficient concentrations and reactivity to be relevant to PAH and soot precursor chemistry.

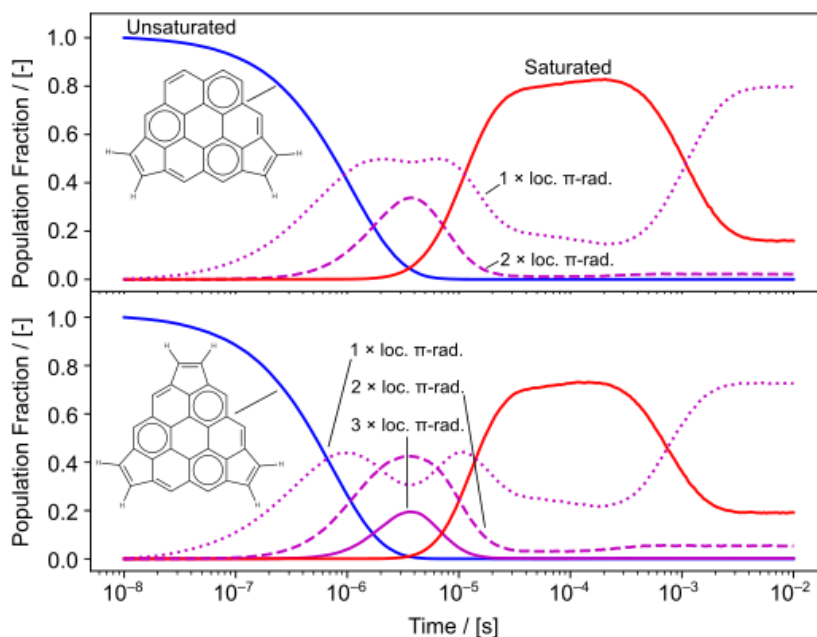


**Figure 7.10:** Kinetic Monte Carlo simulation for the time evolution of rim-based pentagonal rings for two (top) and three (bottom) site species at atmospheric pressure and typical flame compositions at 1000 K. These results are the average of five runs.

## 7.4 Conclusions

localisation of  $\pi$ -radicals was found to be governed by aromaticity rules developed from a Clar analysis. The partially saturated rim-based pentagonal ring was found to concentrate significant spin density on the pentagonal ring and be unchanged by extension of the aromatic ring, as opposed to  $\pi$ -radicals formed within the six-membered ring networks which delocalize. A reaction mechanism was developed, allowing the concentration of possible localised  $\pi$ -radicals to be computed within flame conditions with significant concentrations found in soot-forming temperatures provided sufficient H-radical concentrations are present. Finally, kinetic Monte Carlo simulations showed that multiple reactive sites can be formed on a single PAH, suggesting a chemical polymerization could be possible. Further computational and experimental work is required to verify this.



## Chapter 8

# Kinetics and equilibria of cross-linking reactions between different reactive edges on PAHs

*The thermodynamics and kinetics of cross-linking reactions between PAHs of various reactive edge types have been computed using density functional theory. The forward rate constants confirmed that reactions involving aryl  $\sigma$ -radicals are faster than others, but rate constants for reactions between aryl  $\sigma$ -radicals and localised  $\pi$ -radicals can be as large or even larger than for two aryl  $\sigma$ -radicals. However, rates for all reactions between small PAHs are likely too slow to explain the rapid formation of soot. Computed equilibrium constants showed that reactions involving  $\sigma$  and  $\pi$ -radical PAHs are the most favorable at flame temperatures. Equilibrium constants for larger PAHs showed that the ability to form bonded-and-stacked structures results in substantially enhanced equilibrium constants for the reaction of two large localised  $\pi$ -radicals compared to for other edge types. This suggests that combined physical and chemical interactions between larger  $\pi$ -radical PAHs could be important in flame environments.*

## Collaborative Contributions

The work presented in this chapter has been submitted for publication in *Journal of Physical Chemistry A* and includes collaboration with Jacob Martin. The electronic structure calculations, rate calculations, and equilibrium calculations were performed by the author. The analysis of results and preparation of figures was done by the author, with feedback from Jacob Martin. The manuscript was written by the author, with Jacob Martin helping in editing the manuscript.

## 8.1 Introduction

Several different types of PAHs with different reactive edges are known to exist and have been imaged in recent experimental works, such as those using high resolution atomic force microscopy (HR-AFM) (Schulz et al., 2019; Commodo et al., 2019) and tunable photoionisation time of flight mass spectrometry (PI-TOF MS) (Johansson et al., 2018).

The first, and perhaps most well-known of these are aryl-type  $\sigma$ -radicals, which are generated by abstraction of a hydrogen atom from the rim of a PAH (Hou and You, 2017; Howard, 1991).  $\sigma$ -radicals are known to play a central role in PAH growth in the well known hydrogen-abstraction-acetylene-addition (HACA) mechanism (Frenklach and Wang, 1991; Parker et al., 2014; Liu and Green, 2019). Additionally, rim-based pentagonal rings provide a double bond edge with significant reactivity (Violi et al., 2002; Frenklach and Mebel, 2020), as do curved PAHs, which have been seen to have enhanced oxidation and HACA growth rates (Raj et al., 2013; Raj, 2019). Even flat, PAHs like phenanthrene and pyrene are known to have low-aromaticity edges more prone to radical attacks (Clar et al., 1967). Bridge forming reactions between  $\sigma$ -radicals and five-member ring PAHs have been studied by Violi et al. (2002), who proposed the aromatic aliphatically linked hydrocarbon (AALH) mechanism. This has been expanded on more recently by Frenklach and Mebel (2020). Reactions between  $\sigma$ -radicals and delocalised  $\pi$  radicals have also been proposed by Johansson et al. (2018), who suggested the clustering of hydrocarbons by radical chain reactions (CHRCR) mechanism, which involves hydrogen loss from the intermediate to regenerate the

aromatic  $\pi$ -radical. However, recent studies have questioned whether the collision efficiency of  $\sigma$ -radicals with other species are rapid enough to provide significant nucleation fluxes, without some additional effects playing a role [Mao et al. \(2018\)](#); [Frenklach \(2019\)](#).

The second is the localised  $\pi$ -radicals, first suggested for soot formation by Wang [Wang \(2011\)](#). This includes diradicaloids such as acenes, which are known to have unique localisation properties and possess near diradical nature ([Stuyver et al., 2019](#)). This enables them to form multi-bridge structures ([Wang, 2011](#); [Koley et al., 2012](#); [Zhang et al., 2014](#)). A recent study by the authors [Martin et al. \(2019b\)](#), used electronic structure theory with reactivity indices to map the reactivity and bond energies of cross-links between PAHs of different edge types. Localisation of  $\pi$ -radicals was also demonstrated in partially saturated rim-based pentagonal rings, methylene groups, and five-member rings in PAHs. These species had been previously explored computationally by [Wang \(2011\)](#) and [Whitesides et al. \(2009\)](#) who both noted their stability and role in thermal rearrangements. It was found that these reactive sites are able to form stable complexes that are  $\pi$ -stacked *and* covalently bonded. These complexes were termed aromatic rim-linked hydrocarbons (ARLH). It was also shown in the previous chapter that these localised  $\pi$ -radicals can be present in substantial concentrations at flame conditions. Multiple localised  $\pi$ -radical sites on a single PAH was also shown to be possible, which means a chemical polymerisation of these PAHs could be feasible as well.

**The purpose of this chapter** is to build on the reactivity and bond energy analysis conducted previously in ([Martin et al., 2019b](#)), by estimating the rate constants and equilibrium constants for cross-linking reactions between PAHs of different types. The consideration of diradicaloid species such as acenes is added and extended from this previous work as well. Density functional theory is employed in conjunction with canonical transition state theory (TST) and variational theory (VTST) to provide an initial estimate for the rate constants and equilibrium constants of these cross-linking reactions to analyse which are likely to be relevant at flame temperatures. The equilibrium constants are also computed for larger PAHs that can form ARLH complexes to get an idea of the enhancement provided

by combined physical and chemical modes of complex formation.

## 8.2 Methodology

This work focuses on computing the kinetics and equilibria of reactions between PAH monomers containing different edge types. These monomers are shown in Figure 8.1.

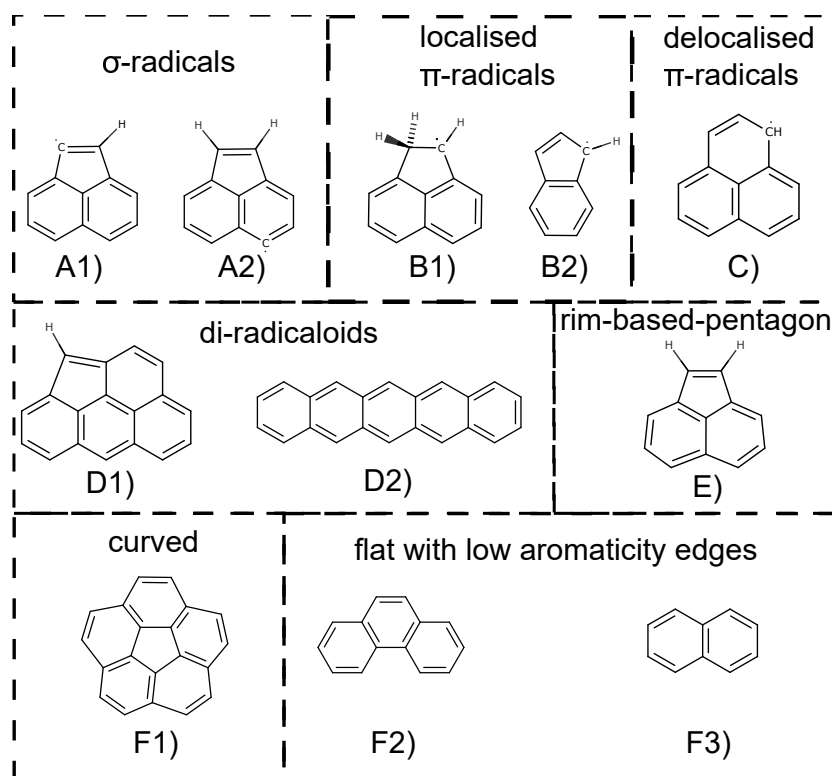


**Figure 8.1:** PAH monomers studied in this work classified by the reactive edge type they contain.

The monomers include  $\sigma$ -radical PAHs, with A1 having the radical site on the five-member ring, and A2 having the radical site on a six-member ring. Localised  $\pi$ -radicals, include partially saturated rim-based pentagons, such as B1, and those with an odd number of electrons in the  $\pi$ -network like B2. These localised  $\pi$ -radicals have their spin density concentrated on a particular site. Delocalised  $\pi$ -radicals like C also have an odd number of  $\pi$ -electrons, but in contrast the electron density de-localizes across the network, meaning the

reactivity is also spread across the rim. diradicaloids include partially-embedded cyclopentaphenathrene-type molecules, such as D1, and linear acenes, such as pentacene (D2), and have very low singlet-triplet electronic gaps, which hence impacts their reactive characteristics (Stuyver et al., 2019). Monomer E is acenaphthylene, and contains a rim-based pentagonal ring, which is known to be reactive due to the low-aromaticity five-member free edge, as well as stable and present in flames (Howard, 1991). Similarly, F1 is a curved PAH, which are known to have unique properties such as substantial permanent dipole moments due to flexoelectric effects (Martin et al., 2017c, 2018) and enhanced reactivities (Raj, 2019). Finally, phenanthrene and naphthalene, denoted F2 and F3, are well-known flat PAHs with lower aromaticity edges compared to maximally condensed benzenoid PAHs.

Geometries and frequencies in this work are derived using hybrid density functional theory (DFT) electronic structure calculations are performed at the B3LYP/6-311G(d,p) level of theory for all PAH reactants, intermediates, transition states and products. Transition states were located by means of a potential energy surface scan along the bond coordinate at the same level of theory before being optimised. Located transition states were confirmed by checking that only one imaginary frequency was present and that this vibrational mode corresponds to the reaction in question. To improve the estimate of energies of the species, single-point energy calculations were performed at the M06-2X/cc-pVTZ level of theory. This level of theory has been previously shown to describe energies and bond enthalpies for reactions between PAHs of different edge types (Martin et al., 2019b), and the M06-2X functional was developed specifically to treat organic radicals, with bond enthalpies and organic barrier heights expected to be accurate to within 2 kcal/mol (Zhao and Truhlar, 2008; Hou and You, 2017). Dispersion was included using the empirical GD3 method with M06-2X, denoted as M06-2X-D3, which is seen to estimate physical interactions to within 6 kcal/mol of high level SAPT(DFT) calculations at a fraction of the computational cost. Gaussian 16 (Frisch et al., 2016) was used to perform all quantum chemical calculations.

Rate constants for the formation of cross-links between the PAH monomers of



various edge types were computed using the DFT-derived molecular properties. In the case where a tight-transition state was identified, the rate was computed by canonical transition state theory:

$$k = \frac{k_B T}{h} \frac{q^\ddagger}{\prod_i^{n_{\text{reactants}}} q_i} \exp\left(\frac{-\Delta E_0}{RT}\right), \quad (8.1)$$

where  $k$  is the rate constant,  $k_B$  is the Boltzmann constant,  $T$  is temperature,  $h$  is Planck's constant,  $q$  is the total partition function, and  $\Delta E_0$  is the classical barrier height. A tunneling correction for the case of an asymmetric Eckart potential was also applied. The tight transition state rate constants were computed using Arkane as implemented in Reaction Mechanism Generator (RMG) (Gao et al., 2016).

If no transition state could be located from a potential energy surface scan, the reactions were treated as barrierless, and the rate constants were computed using angular-momentum resolved variational transition state theory as implemented in the ktools package within Multiwell (Barker et al., 2017a). Trial transition states were taken from points along the potential energy surface scan, with bond separation lengths between 1.8 Å and 3.2 Å. These trial transition states had their geometries and frequencies determined at the B3LYP/6-311G(d,p) level of theory and also had their energies further refined at the M06-2X-D3/cc-PVTZ level of theory, consistent with other species and tight transition states computed in this work. The potential energy surfaces used for the VTST calculations are shown in Figure 8.2.

## 8 CHAPTER 8

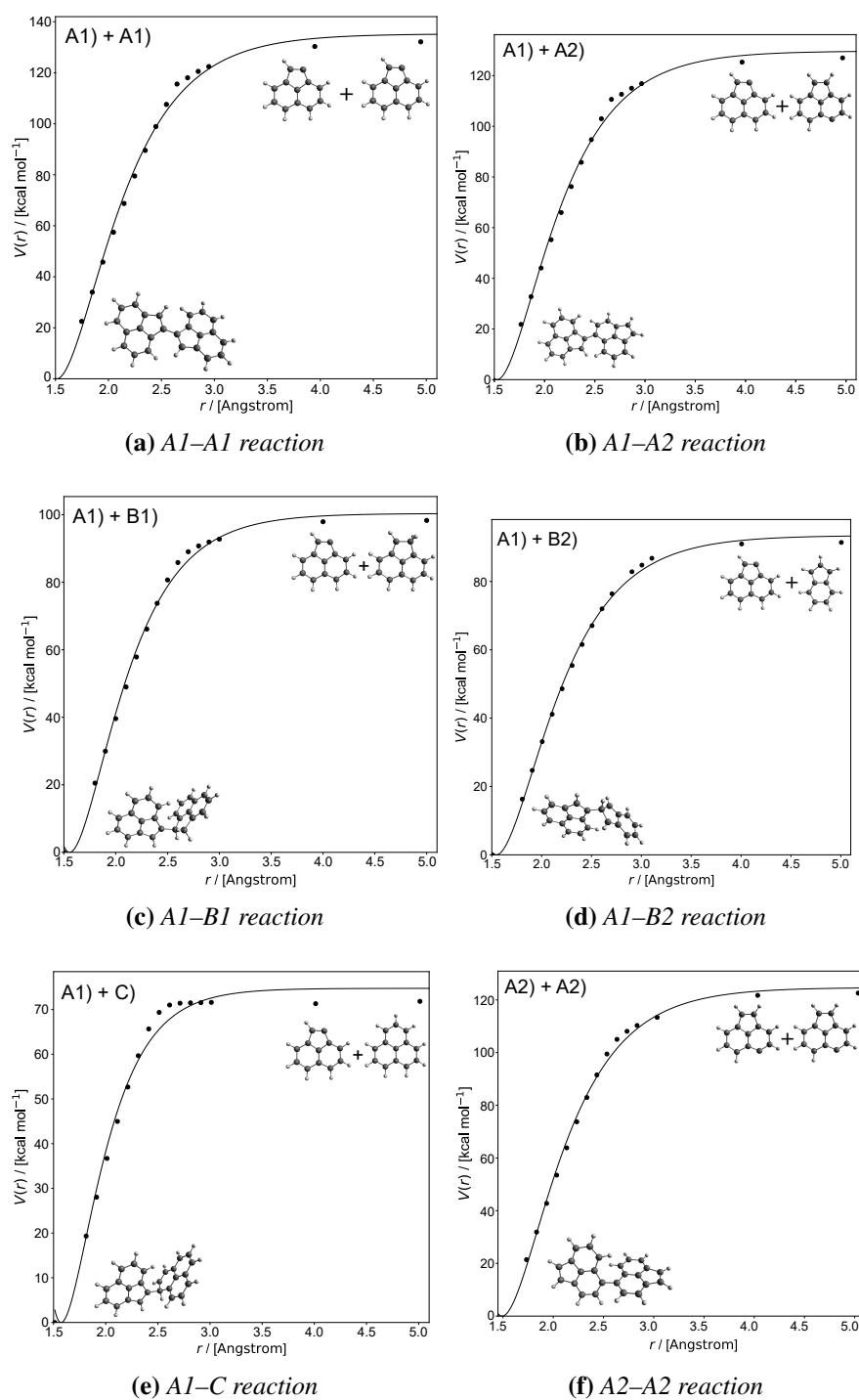


**Figure 8.2:** Potential energy surfaces for barrierless cross-linking reactions studied in this work. The energies are computed at the BS-UM06-2X/cc-PVTZ level of theory, and are fitted to a Morse potential.

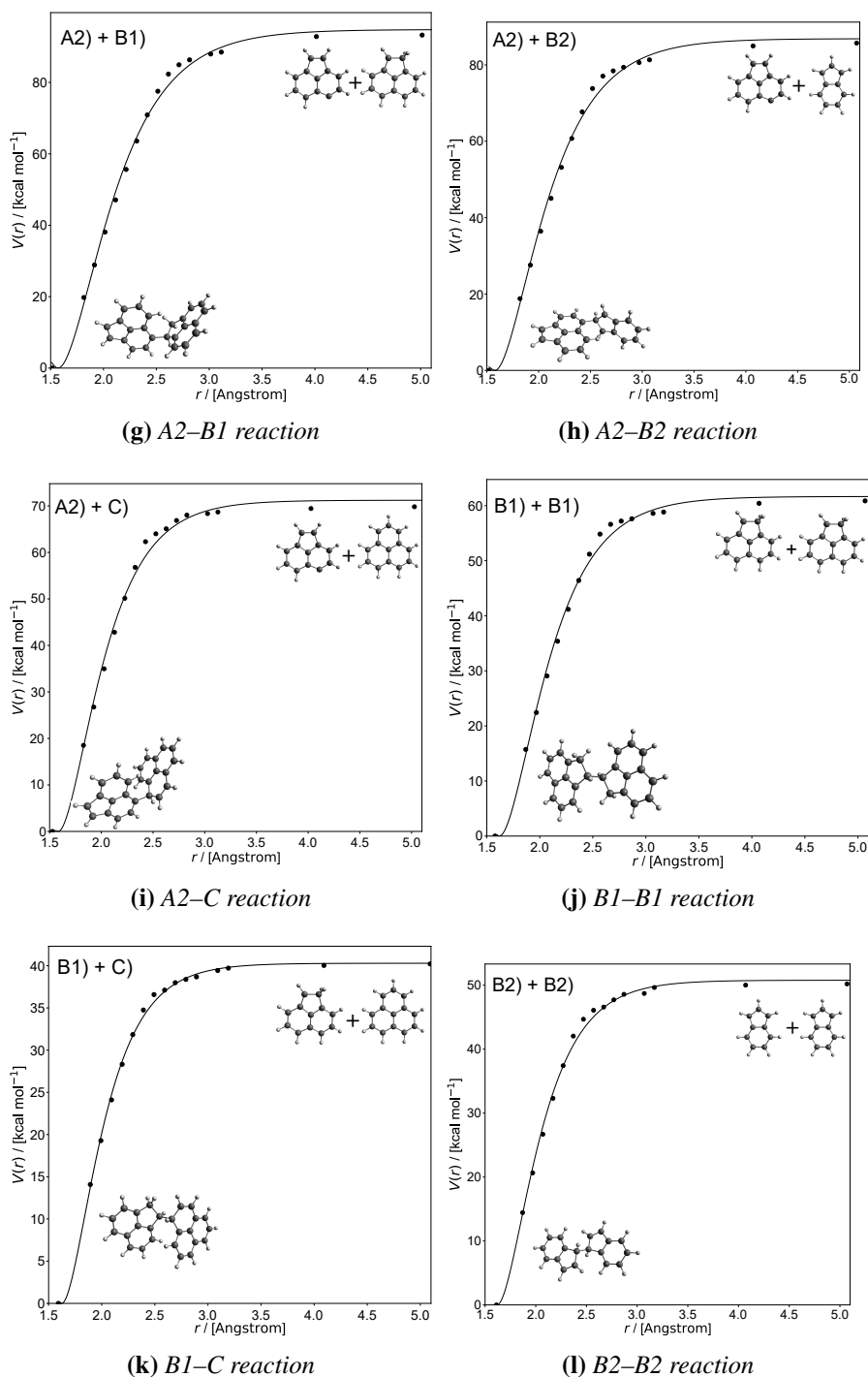


**Figure 8.2:** (Continued.) Potential energy surfaces for barrierless cross-linking reactions studied in this work. The energies are computed at the BS-UM06-2X/cc-PVTZ level of theory, and are fitted to a Morse potential.

The numerical parameters for the energy and angular momentum density of states integration were taken from [Barker et al. \(2017a\)](#). Namely, this involves an energy grain of  $10 \text{ cm}^{-1}$  and maximum energy of  $85000 \text{ cm}^{-1}$ , as well as an angular momentum grain of  $1 \text{ cm}^{-1}$  and maximum angular momentum of  $1000 \text{ cm}^{-1}$ .

It is worth mentioning that radical-radical reactions can require multireference methods to be modelled accurately. In this case, the PAHs studied here are large enough such that multi-reference methods would be very computationally demanding, and as such the broken symmetry approach with the unrestricted M06-2X (BS-UM06-2X) functional was chosen. Whilst this does not accurately describe the multi-configurational nature of a bond dissociation process, the broken symmetry approach and utilization of the unrestricted functional has been shown to give the correct dissociation limit, which is crucial for describing the potential energy surfaces ([Thompson and Hratchian, 2014](#)). The M06-2X functional gives good predictions of the energetics for bond dissociation, particularly among DFT methods, and should suffice for qualitative estimates of rate constants ([Zhao and Truhlar, 2008](#)).

As a test of the method, the rate constant for the recombination of phenyl radicals to produce biphenyl was computed using the methodology described above. This rate constant has been predicted theoretically by [Tranter et al. \(2010\)](#), who employed the multireference CASPT2(2e,2o) method as well as the cc-pVDZ basis set to model the interaction energy, along with variable reaction coordinate transition state theory (VRC-TST). A very recent high temperature shock tube study by [Jin et al. \(2020\)](#) also estimated the rate constant for phenyl radical recombination. These are used for comparison in [Figure 8.3](#).

[Figure 8.3](#) suggests reasonable agreement between the rate constant for phenyl radical recombination computed using the methodology of this work and the predictions of [Tranter et al. \(2010\)](#) and [Jin et al. \(2020\)](#) in the range of 1000–2000 K. The negative temperature dependence and order of magnitude predicted are captured by the use of BS-UM06-2X/cc-pVTZ and VTST, although the decrease in rate constant is steeper in comparison. This could be due to the less accurate interaction energies computed here when compared to the multireference methods employed by [Tranter et al. \(2010\)](#), as well as differences in the prediction

of the enthalpy of reaction for the recombination. This is predicted to be -119.1 kcal/mol by BS-UM06-2X/cc-pVTZ compared to -117.9 predicted by CASPT2(2e,2o)/cc-pVDZ. Nevertheless, the methodology here should suffice for initial estimates of the rate constants of radical-radical PAH reactions.

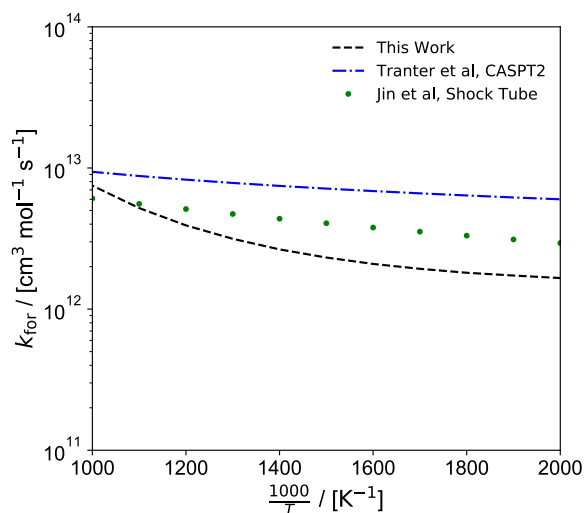


**Figure 8.3:** Comparison of the rate constant of phenyl radical recombination estimated using BS-UM06-2X/cc-pVTZ and VTST to those estimated by *Tranter et al. (2010)* and *Jin et al. (2020)*.

Additionally, several of the cross-linking reactions also possessed barriers below 2 kcal/mol, which is near the expected given the uncertainty in barrier height predictions with M06-2X. This means that these cross-linking reactions could actually have submerged barriers. However, as a tight transition state was found and confirmed, canonical transition state theory was still deemed appropriate to use to derive initial estimates of rate constants for these processes, but further refinement is likely necessary.

## 8.3 Results and Discussion

### 8.3.1 Bond energies and classification of cross-links


Figure 8.4 presents an updated version of the matrix of bond energies presented in *Martin et al. (2019b)*. The matrix has been updated to include an acene-type

## 8 CHAPTER 8

PAH, namely pentacene, which is known to possess diradical character (Minami et al., 2013). Indenyl has also been reclassified to a localised- $\pi$  radical, due to its spin mainly being concentrated on a single rim atom on the five-member ring. It was also found that for the  $\sigma$ -radicals and indenyl, the central pentagonal carbon atom is more reactive than the site given by the Clar analysis, which is corrected from the previous study by Martin et al. (2019b). Additionally, the type of cross-link has been classified and named by the type of radical or edge type that initiates the bond-forming reaction. For example, the reactions initiated by the  $\sigma$ -radicals A1 and A2 result in aromatic aryl-linked hydrocarbons (AALH), and reactions initiated by the localised- $\pi$  radical are termed aromatic rim-linked hydrocarbons (ARLH), in reference to the bonding at the rim as well as stacking that is only possible for localised  $\pi$ -radicals. Reactions between delocalised  $\pi$ -radicals and the diradicaloids result in multi-centre bonds, or pancake bonds, due to several different possible orientation centres, and are denoted as aromatic multicentre-linked hydrocarbons (AMLH). Finally, diradicaloids bonding along their zig-zag edges are given the acronym AZLH, but these reactions are observed to be symmetry forbidden in practice and so did not have rates computed due to

|  | aryl $\sigma$ -radical |        | localised $\pi$ -radical |       | delocal. $\pi$ -radical | diradicaloid |       | rim-based pentagon | cPAH  |       |       | low aromaticity | Classes |
|--|------------------------|--------|--------------------------|-------|-------------------------|--------------|-------|--------------------|-------|-------|-------|-----------------|---------|
|  | A1)                    | A2)    | B1)                      | B2)   | C)                      | D1)          | D2)   | E)                 | F1)   | F2)   | F3)   | Structures      |         |
| aromatic aryl-linked hydrocarbons (AALH)   | -130.4                 | -125.3 | -97.3                    | -91.0 | -73.6                   | -63.7        | -78.2 | -53.5              | -41.3 | -38.3 | -36.2 | A1)             |         |
|  |                        | -120.8 | -92.6                    | -86.8 | -69.0                   | -57.6        | -73.3 | -49.8              | -38.4 | -33.7 | -33.8 | A2)             |         |
| aromatic rim-linked hydrocarbons (ARLH)    |                        |        | -61.9                    | -34.0 | -39.9                   | -32.2        | -43.8 | -24.5              |       |       |       | B1)             |         |
|  |                        |        |                          | -50.9 | -33.4                   | -28.6        | -14.8 |                    |       |       |       | B2)             |         |
| aromatic multicentre-linked hydroc. (AMLH) |                        |        |                          |       | -17.0                   | -12.1        | -23.6 |                    |       |       |       | C)              |         |
| aromatic zigzag-linked hydrocarbons (AZLH) |                        |        |                          |       |                         | -29.6        |       |                    |       |       |       | D1)             |         |
|  |                        |        |                          |       |                         |              | -16.5 |                    |       |       |       | D2)             |         |

bond energy (kcal/mol)

-190  -40

**Figure 8.4:** Bond energies of cross-linking between PAHs of different edge types computed at the M06-2X-D3/cc-pVTZ level of theory.

their low bond energies.

In general, the bond energies decrease in strength from the aryl  $\sigma$ -radical type edges seen in A down to the low aromaticity edge types seen in F. Consequently, AALH species are much more likely to form bonds stable at flame temperatures, followed by ARLH and AMLH. Of note is the diradicaloid D2. This partially-embedded pentagon edge type generally forms stronger than expected bonds with the aryls as well as the localised and delocalised  $\pi$ -radical structures B1 and C, when compared to other  $\pi$ -radical and diradicaloids B2, C, and D1.

### 8.3.2 Barrier Heights

In subsequent discussions, the reactions can be separated into reactions with and without barriers. The barrierless reactions include the reactions of the aryl  $\sigma$ -radicals with any other PAH with a radical edge-type, that is A1 and A2 reacting with any PAH with edge type A, B, or C, reactions of localised  $\pi$ -radical B1 with itself and delocalised  $\pi$ -radical C, as well as the reaction between indenyl(B2) and itself. As is expected, the barrierless reactions are generally those between radicals of different types that result in high bond energies. All other cross-linking reactions were seen to have barriers, in that a transition state for the reaction was located. These barriers are provided in Table 8.1:

It is known that barrier heights for a family of reactions tend to have a relationship between the barrier height and the enthalpy of reaction. Figure 8.5 presents a plot of the barrier heights of the various cross-linking reactions against their bond enthalpy as a Brønsted-Evans-Polanyi (BEP) type plot for the reactions with barriers.

Three regions can be identified. Firstly, for weaker bonds with an enthalpy less than 40 kcal/mol and barriers greater than approximately 2 kcal/mol, an approximate BEP relationship can be seen, where the relationship between the classical barrier height and bond enthalpy is roughly linear. Cross-linking reactions occurring in this regime include reactions involving the delocalised  $\pi$ -radical C with other edge types, reactions of localised  $\pi$ -radical edge type B with all non-diradicaloid edge types, namely B, C and E, and reactions of the aryl

## 8 CHAPTER 8

---

**Table 8.1:** *Predicted barrier heights for formation of cross-links between PAHs at the M06-2X-D3/cc-pVTZ level of theory.*

| Reaction        | Barrier Height / kcal mol <sup>-1</sup> |
|-----------------|---|
| A1 + D1 → A1D1  | 1.29                                    |
| A1 + D2 → A1D2  | 1.12                                    |
| A1 + E → A1E    | 0.55                                    |
| A1 + F1 → A1F1  | 0.76                                    |
| A1 + F2 → A1F2  | 1.63                                    |
| A1 + F3 → A1F3  | 2.77                                    |
| A2 + D1 → A2D1  | 1.22                                    |
| A2 + D2 → A2D2  | 0.45                                    |
| A2 + E → A2E    | 1.27                                    |
| A2 + F1 → A2F1  | 1.63                                    |
| A2 + F2 → A2F2  | 2.61                                    |
| A2 + F3 → A2F3  | 3.20                                    |
| B1 + B2 → B1B2  | 4.11                                    |
| B1 + D1 → B1D1  | 1.67                                    |
| B1 + D1 → B1D1b | 1.44                                    |
| B1 + D2 → B1D2  | 2.10                                    |
| B1 + E → B1E    | 5.35                                    |
| B2 + C → B2C    | 2.51                                    |
| B2 + D1 → B2D1  | 1.26                                    |
| B2 + D2 → B2D2  | 15.37                                   |
| C + C → CC      | 9.88                                    |
| C + D1 → CD1    | 4.03                                    |
| C + D2 → CD2    | 8.51                                    |

radical edge types A with the low aromaticity edges of standard planar PAHs F2 and F3. The delocalised  $\pi$ -radical C is generally seen to have high barriers for its cross-linking reactions. This is most likely due to its aromatic stabilization, which also results in delocalised electron density and lower reactivity, hence the higher barriers. Other high barrier-low bond enthalpy reactions include the reactions between B2 and D2, as well as B1 and E. Both of these reactions involve a cross-link forming between two carbon atoms in five-member rings, with the two carbons forming the bond also being bonded to a hydrogen as well. This would suggest that bonds between five-member rings are likely less favorable unless there is sufficient radical character among the reacting PAHs.



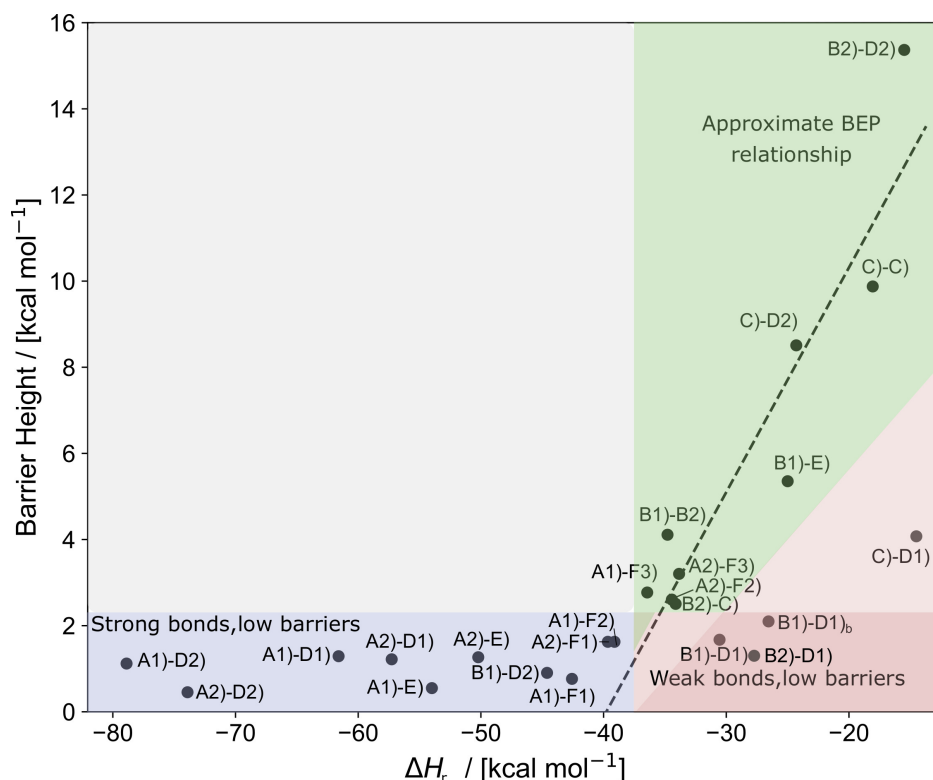


**Figure 8.5:** Full BEP plot of the barrier heights against bond enthalpy for the various cross-linking reactions.

The next region seen on the plot also shows cross-linking reactions that have low bond enthalpies, but whose classical threshold energies for the reaction are much lower than is expected if a BEP relationship is followed. The reactions in this regime all involve the diradicaloid pentacene or D1 reacting with the various  $\pi$ -radicals of edge type B and C. This would suggest that although the bonds formed are weak, it is quite facile to do so. Diradicaloids are known to have near radical character, and acenes like D1 are known to have increasing degrees of diradical character with increasing size from Clar analyses (Szczepanik et al., 2018). This can result in increasing reactivity around the central ring of such acenes. In the case of D2, the strongest cross-links with B1, B2, and C all formed on the central ring, in line with the Clar analyses of the diradical Stuyver et al. (2019). This would suggest that the diradicaloid nature of the acenes contributes to their barriers being much lower than what would be expected solely from the

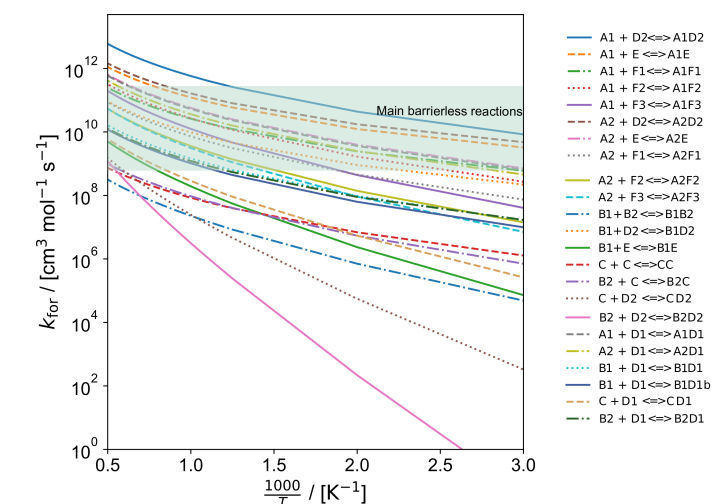
bond enthalpies.

The third and final region is for cross-links with bond enthalpies greater than 40 kcal/mol and classical barriers lower than 2 kcal/mol. As mentioned previously, the uncertainty in M06-2X is around the 2 kcal/mol as well, and so the predicted barriers in this region must be viewed with caution. The cross-links present in this region are the majority of those involving the aryl radical edge type A, which is not surprising given their high bond enthalpies. Reactions between edge type A and the curved PAH edge type F1 can be seen to have lower expected barriers in contrast to the low aromaticity flat edge type of PAHs F2 and F3. In addition, most cross-linking reactions involving A1 have lower predicted barriers than those involving A2, suggesting that the aryl  $\sigma$ -radical on a rim five-member ring may be more reactive than on a six-member ring. These predictions are in agreement with previous studies that suggest curved PAHs and five-member rings possess higher reactivity (Whitesides et al., 2009; Raj, 2019) than counterpart flat PAHs and six-member rings. Notably, the only cross-link not involving a PAH with edge type A is the one between B1 and D2. As noted above, D2 forms stronger cross-links than expected, and this is reflected in the low barriers for the cross-linking reaction. This once again suggests that diradicaloids containing five-member rings are substantially more reactive than other types of closed-shell PAHs.

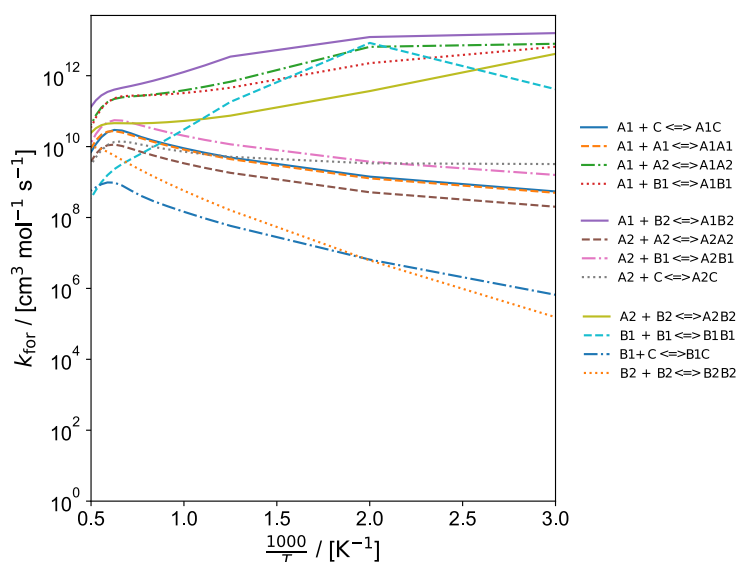
### 8.3.3 Rate Constants

Figure 8.6 presents the Arrhenius plots for the forward rate constants for forming cross-links between PAHs with different reactive edge types.

The forward rate constants for the reactions with barriers are all concave in nature, which is the expected behaviour for most rate constants, with the phenomenological activation energies increasing with temperature. Looking at the rate constants, at the higher temperature range of interest to flames (1500–2000 K), the rate constants span four orders of magnitude, from approximately  $10^8 \text{ cm}^3\text{mol}^{-1}\text{s}^{-1}$  for the reactions with the highest threshold energies, to  $10^{12} \text{ cm}^3\text{mol}^{-1}\text{s}^{-1}$  for the cross-linking reactions in the strong bond-low barrier regime in the BEP plot. Of note are the rate constants for



(a) Cross-link reactions with Barriers



(b) Cross-link reactions without Barriers

**Figure 8.6:** Arrhenius plots for the forward rate constants of forming a cross-linking between PAHs with different reactive edge types.

the reactions of A1 and A2 with the diradicaloid D2 as well as the reaction between A1 and rim-based pentagon E. These reactions have very low barriers and yet are estimated to be of the same order of magnitude as the barrierless combination reactions across the temperature range of 300–2000 K. These rate constants are of the order of the abstraction and acetylene addition steps in

## 8 CHAPTER 8

---

the well known hydrogen-abstraction-acetylene-addition (HACA) PAH growth mechanism ([Frenklach et al., 2019](#)).

In the case of the barrierless reactions, at the temperature range of 1500–2000 K, the rate constants are in a similar range, from approximately  $10^8 \text{ cm}^3\text{mol}^{-1}\text{s}^{-1}$  for the reactions with the lowest bond energies between localised  $\pi$ -radical B and delocalised  $\pi$ -radical C, to slightly below  $10^{12} \text{ cm}^3\text{mol}^{-1}\text{s}^{-1}$  for the higher bond energies between reactive edge types A and B. It can also be seen that the barrierless reactions between two indenyls or B2 and between B1 and C1, are lower in magnitude and more temperature dependent. In contrast, the reactions between A1 and A2, A1 and B1, A1 and B2, and A2 and B2 are higher in magnitude. The other reactions involving the aryl  $\sigma$ -radicals are also weakly temperature dependent, which is commonly observed for barrierless reactions ([Harding et al., 2005](#)).

The rate constants for all of the barrierless reactions do show regions of negative temperature dependence. This negative temperature dependence tends to manifest either at higher temperatures of around 1600–1700 K for the reactions which are below  $10^{11} \text{ cm}^3\text{mol}^{-1}\text{s}^{-1}$  in magnitude. Similar behaviours were observed for the rate constants computed using VRC-TST and CASPT2 interaction energies for combination channels involving phenyl and propargyl radicals ([Morozov and Mebel, 2020](#)). In the case of the reaction between two B1 monomers, A1 and B2, A2 and B2, A1 and B1, and A1 and A2, the negative temperature dependence is observed for the bulk of the temperature range. Persistent negative temperature dependence is usually attributed to high-energy collisional effects limiting the flux through the dividing surface, and has also been observed for recombination reactions between phenyl and allyl radicals ([Morozov and Mebel, 2019, 2020](#)).

Additionally, Figure 8.6b also shows that the radical-combination rate constants involving species A1 are larger than for the counterpart reactions involving species A2. This again suggests that the reactivity of the aryl  $\sigma$ -radical is higher for a radical site on a rim five-member ring than a six-member ring. However, it is worth noting that the largest rate constant for the aryl-aryl reactions is that between A1 and A2, which is one of the fastest reactions in the temperature range and is much faster than two A1 monomers or two A2 monomers reaction. This

highlights the potential significance of reactions between radical sites on five and six-member ring species.

The Arrhenius plot also highlights the potential importance of localised  $\pi$  radical species. This is exemplified in the fact that the rate constants for the reactions between A1 and the localised  $\pi$ -radicals B1 and B2 are some of the largest, with the reaction between A1 and B2 being even faster than the reaction between A1 and A2. The next predicted fastest reactions in the flame temperature range of 1500–2000 K are all again reactions between a  $\sigma$ -radical and a localised  $\pi$ -radicals, namely the reactions between A1 and B1, A2 and B2, and A2 and B1. This suggests that reactions between  $\sigma$ -radicals and localised  $\pi$ -radicals are possible and may indeed be important. Finally, the rate constant between two B1 monomers, that is the localised  $\pi$ -radical can also be observed to have a substantially large rate constant at lower temperatures, where it is noticeably much faster than any other re-combination reaction between two identical PAHs. The B1-B1 reaction is competitive with reactions between A1 and B2, A1 and A2, and A1 and B1 until 800 K, and could be important in this range. At 1000 K, the combination of two B1 monomers appears to be competitive with reactions between A2 and localised  $\pi$ -radicals. It was previously seen that at these lower temperatures, the localised  $\pi$ -radicals on a rim five-member ring are expected to be in higher concentrations than the  $\sigma$ -radical A1, and so the B1-B1 reaction may play a role. Even at the lower flame temperature ranges of 1400-1500 K, the rate constant is competitive with the combination reactions of A2 with A2, A1 and C, and B2 as well as the reaction between two B2 molecules. At temperatures above this, this reaction is substantially slower. This ability of the partially saturated rim five-member rings to react suggest that the formation of PAHs with bridge bonds between pentagons, or penta-linked PAHs, is important at lower temperatures, but is substantially less important at higher temperatures.

In the case of the reactions with barriers, the forward and reverse rate constants have been fitted to the modified Arrhenius expression:

$$k = AT^n \exp\left(\frac{-E_a}{RT}\right) \quad (8.2)$$

## 8 CHAPTER 8

---

In the case of barrierless reactions, the forward rate constants required a sum of two modified Arrhenius expressions to achieve a suitable fitting, which are given the subscripts 1 and 2. The reverse cross-link breaking reactions in this case could be suitably fitted to a single modified Arrhenius expression. The rate constants for these reactions are presented in Table 8.2.

**Table 8.2:** Arrhenius fittings for the rate constants for the cross-linking between PAHs possessing different reactive edge types. Rates are computed at the M06-2X/cc-pVTZ//B3LYP/6-311G(d,p) level of theory. The units are cm, kcal, mol, K, and s.

| Reaction            | $A_1$                 | $n_1$ | $E_{A,1}$ | $A_2$ | $n_2$ | $E_{A,2}$ |
|---------------------|-----------------------|-------|-----------|-------|-------|-----------|
| <i>With Barrier</i> |                       |       |           |       |       |           |
| A1 + D1 → A1D1      | 49.46                 | 3.09  | 1.08      |       |       |           |
| A1D1 → A1 + D1      | $1.62 \times 10^{13}$ | 0.56  | 61.59     |       |       |           |
| A1 + D2 → A1D2      | 860.41                | 3.01  | 0.98      |       |       |           |
| A1D2 → A1 + D2      | $2.80 \times 10^{14}$ | 0.56  | 78.54     |       |       |           |
| A1 + E → A1E        | 86.62                 | 3.07  | 0.32      |       |       |           |
| A1E → A1 + E        | $8.06 \times 10^{13}$ | 0.43  | 53.63     |       |       |           |
| A1 + F1 → A1F1      | 19.87                 | 3.07  | 0.47      |       |       |           |
| A1F1 → A1 + F1      | $2.15 \times 10^{13}$ | 0.40  | 42.37     |       |       |           |
| A1 + F2 → A1F2      | 25.43                 | 3.10  | 1.26      |       |       |           |
| A1F2 → A1 + F2      | $1.95 \times 10^{13}$ | 0.46  | 39.67     |       |       |           |
| A1 + F3 → A1F3      | 17.35                 | 3.12  | 2.35      |       |       |           |
| A1F3 → A1 + F3      | $1.63 \times 10^{13}$ | 0.43  | 38.27     |       |       |           |

Continued on next page.

### 8.3 Results and Discussion

*Continued from previous page.*

| Reaction        | $A_1$                 | $n_1$ | $E_{A,1}$ | $A_2$ | $n_2$ | $E_{A,2}$ |
|-----------------|-----------------------|-------|-----------|-------|-------|-----------|
| A2 + D1 → A2D1  | 20.06                 | 3.16  | 0.97      |       |       |           |
| A2D1 → A2 + D1  | $1.51 \times 10^{12}$ | 0.64  | 57.04     |       |       |           |
| A2 + D2 → A2D2  | 135.21                | 3.04  | 0.26      |       |       |           |
| A2D2 → A2 + D2  | $7.93 \times 10^{13}$ | 0.60  | 72.76     |       |       |           |
| A2 + E → A2E    | 52.50                 | 3.09  | 1.05      |       |       |           |
| A2E → A2 + E    | $8.66 \times 10^{13}$ | 0.46  | 50.34     |       |       |           |
| A2 + F1 → A2F1  | 5.42                  | 3.13  | 1.21      |       |       |           |
| A2F1 → A2 + F1  | $9.78 \times 10^{12}$ | 0.45  | 40.21     |       |       |           |
| A2 + F2 → A2F2  | 4.82                  | 3.12  | 2.17      |       |       |           |
| A2F2 → A2 + F2  | $5.30 \times 10^{12}$ | 0.48  | 35.86     |       |       |           |
| A2 + F3 → A2F3  | 4.80                  | 3.13  | 2.69      |       |       |           |
| A2F3 → A2 + F3  | $8.81 \times 10^{12}$ | 0.44  | 35.98     |       |       |           |
| B1 + B2 → B1B2  | 2.43                  | 2.57  | 3.36      |       |       |           |
| B1B2 → B1 + B2  | $1.80 \times 10^{11}$ | 0.59  | 35.01     |       |       |           |
| B1 + D1 → B1D1  | 1.90                  | 3.05  | 1.20      |       |       |           |
| B1D1 → B1 + D1  | $3.46 \times 10^{11}$ | 0.85  | 29.42     |       |       |           |
| B1 + D1 → B1D1b | 1.44                  | 3.05  | 1.35      |       |       |           |
| B1D1b → B1 + D1 | $2.54 \times 10^{11}$ | 0.78  | 26.14     |       |       |           |
| B1 + D2 → B1D2  | 8.85                  | 3.05  | 0.50      |       |       |           |
| B1D2 → B1 + D2  | $9.49 \times 10^{11}$ | 0.90  | 29.42     |       |       |           |
| B1 + E → B1E    | 1.78                  | 3.02  | 4.62      |       |       |           |
| B1E → B1 + E    | $4.37 \times 10^{11}$ | 0.68  | 27.94     |       |       |           |
| B2 + C → B2C    | 2.64                  | 2.66  | 2.01      |       |       |           |
| B2C → B2 + C    | $2.77 \times 10^{11}$ | 0.70  | 32.96     |       |       |           |
| B2 + D1 → B2D1  | 1.50                  | 3.04  | 0.99      |       |       |           |
| B2D1 → B2 + D1  | $5.44 \times 10^{11}$ | 0.68  | 27.62     |       |       |           |
| B2 + D2 → B2D2  | 0.34                  | 3.37  | 14.39     |       |       |           |
| B2D2 → B2 + D2  | $1.78 \times 10^{11}$ | 0.87  | 28.79     |       |       |           |

Continued on next page.

## 8 CHAPTER 8

*Continued from previous page.*

| Reaction                   | $A_1$                  | $n_1$  | $E_{A,1}$ | $A_2$                 | $n_2$  | $E_{A,2}$ |
|----------------------------|------------------------|--------|-----------|-----------------------|--------|-----------|
| $C + C \rightarrow CC$     | 2.02                   | 2.64   | 5.62      |                       |        |           |
| $CC \rightarrow C + C$     | $5.61 \times 10^{11}$  | 0.54   | 16.53     |                       |        |           |
| $C + D1 \rightarrow CD1$   | 1.17                   | 3.06   | 3.67      |                       |        |           |
| $CD1 \rightarrow C + D1$   | $7.69 \times 10^{11}$  | 0.58   | 15.43     |                       |        |           |
| $C + D2 \rightarrow CD2$   | 0.62                   | 3.10   | 7.84      |                       |        |           |
| $CD2 \rightarrow C + D2$   | $2.60 \times 10^{11}$  | 0.71   | 30.65     |                       |        |           |
| <i>Barrierless</i>         |                        |        |           |                       |        |           |
| $A1 + A1 \rightarrow A1A1$ | $2.33 \times 10^1$     | 2.83   | -0.24     | $6.26 \times 10^4$    | 2.65   | 26.26     |
| $A1A1 \rightarrow A1 + A1$ | $1.85 \times 10^{21}$  | -1.76  | 134.98    |                       |        |           |
| $A1 + A2 \rightarrow A1A2$ | $2.71 \times 10^{14}$  | -1.05  | -1.76     | 20.31                 | 4.00   | 31.69     |
| $A1A2 \rightarrow A1 + A2$ | $1.44 \times 10^{31}$  | -4.65  | 126.98    |                       |        |           |
| $A1 + B1 \rightarrow A1B1$ | $1.81 \times 10^{10}$  | 0.21   | -3.09     | $2.09 \times 10^{61}$ | -12.55 | 79.16     |
| $A1B1 \rightarrow A1 + B1$ | $7.34 \times 10^{26}$  | -3.51  | 97.80     |                       |        |           |
| $A1 + B2 \rightarrow A1B2$ | $7.15 \times 10^{24}$  | -4.03  | 2.01      | $1.61 \times 10^{21}$ | -3.59  | -0.85     |
| $A1B2 \rightarrow A1 + B2$ | $1.82 \times 10^{33}$  | -5.31  | 92.95     |                       |        |           |
| $A1 + C \rightarrow A1C$   | $4.25 \times 10^4$     | 2.33   | 1.71      | $3.09 \times 10^4$    | 2.38   | 1.88      |
| $A1C \rightarrow A1 + C$   | $2.25 \times 10^{20}$  | -1.64  | 76.77     |                       |        |           |
| $A2 + A2 \rightarrow A2A2$ | 7.91                   | 2.86   | -0.26     | $2.14 \times 10^{21}$ | -1.92  | 42.84     |
| $A2A2 \rightarrow A2 + A2$ | $6.71 \times 10^{20}$  | -1.74  | 124.90    |                       |        |           |
| $A2 + B1 \rightarrow A2B1$ | $1.01 \times 10^3$     | 2.45   | -0.07     | $2.11 \times 10^{21}$ | -2.19  | 37.14     |
| $A2B1 \rightarrow A2 + B1$ | $5.03 \times 10^{23}$  | -2.40  | 97.39     |                       |        |           |
| $A2 + B2 \rightarrow A2B2$ | 16.47                  | 2.68   | -7.17     | $2.08 \times 10^{21}$ | -2.70  | 17.30     |
| $A2B2 \rightarrow A2 + B2$ | $8.60 \times 10^{16}$  | -0.76  | 81.22     |                       |        |           |
| $A2 + C \rightarrow A2C$   | 932.05                 | 2.20   | -1.53     | $2.14 \times 10^{21}$ | -2.18  | 34.72     |
| $A2C \rightarrow A2 + C$   | $5.40 \times 10^{23}$  | -2.77  | 72.12     |                       |        |           |
| $B1 + B1 \rightarrow B1B1$ | $5.50 \times 10^{23}$  | -4.14  | -0.98     | $1.34 \times 10^{23}$ | -3.97  | -1.23     |
| $B1B1 \rightarrow B1 + B1$ | $1.29 \times 10^{-53}$ | -11.91 | 72.32     |                       |        |           |
| $B1 + C \rightarrow B1C$   | $2.16 \times 10^{-1}$  | 3.12   | 2.07      | $2.37 \times 10^{36}$ | -6.32  | 56.99     |
| $B1C \rightarrow B1 + C$   | $4.50 \times 10^{17}$  | -1.05  | 46.57     |                       |        |           |

Continued on next page.



*Continued from previous page.*

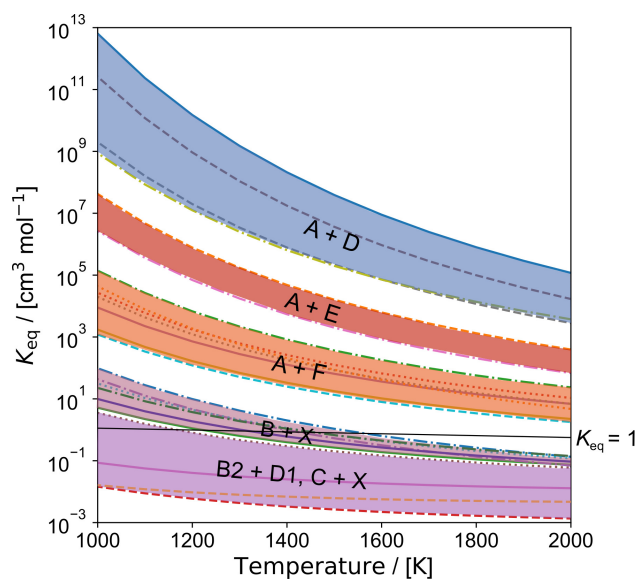
| Reaction                   | $A_1$                 | $n_1$ | $E_{A,1}$ | $A_2$                 | $n_2$ | $E_{A,2}$ |
|----------------------------|-----------------------|-------|-----------|-----------------------|-------|-----------|
| $B2 + B2 \rightarrow B2B2$ | $1.46 \times 10^2$    | 2.62  | 5.95      | $2.42 \times 10^{36}$ | -5.54 | 76.25     |
| $B2B2 \rightarrow B2 + B2$ | $4.01 \times 10^{14}$ | 0.27  | 58.35     |                       |       |           |

### 8.3.4 Equilibrium Constants

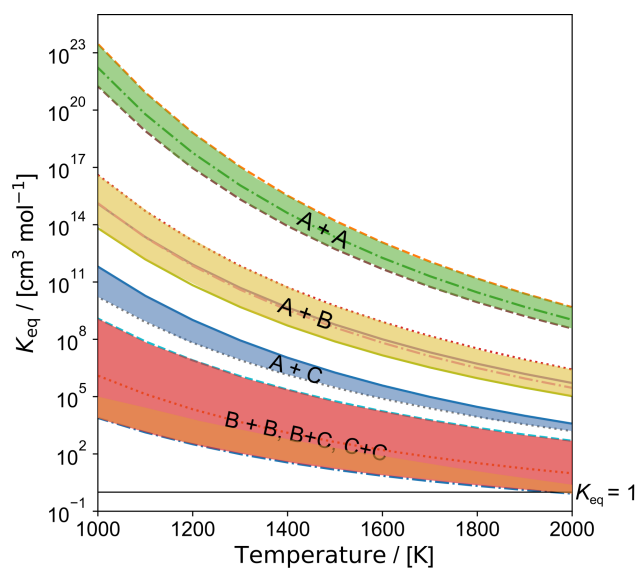
Whilst the forward rate constants for several of the reactions between different edge types were seen to be of the order of  $10^{11}$  and  $10^{12}$   $\text{cm}^3\text{mol}^{-1}\text{s}^{-1}$  at flame temperatures, it is known that reversibility is particularly important in soot nucleation (Eaves et al., 2015; Veshkini et al., 2016). Previous works on physical dimerization between small PAHs such as pyrene have similarly fast forward rate constants, but is known to be highly reversible at flame temperatures and thus unfavorable (Wang, 2011; Totton et al., 2012). To get an idea of reversibility and favorability at flame temperatures of these cross-linking reactions, the equilibrium constant can be computed. This is presented in Figure 8.7.

Figure 8.7 shows that the equilibrium constants do group by the reactive edge types involved, which is represented by the shaded bands in the plot. The magnitude of the equilibrium constants also mostly reflect the bond energies of the cross-link, which is expected as this is the enthalpic contribution to the equilibrium constant. The largest equilibrium constants are seen for the reactions containing the aryl  $\sigma$ -radical edge type A, followed by reactions between these radicals and the localised  $\pi$ -radicals B as a consequence. Most of the cross-linking reactions here have equilibrium constants well above 1 at flame temperatures, and thus have low reversibility as a result. The exceptions to this are the reactions involving edge types B and C with edge types C, D, and E that also have a barrier to reaction. These are seen to be quite reversible at flame temperatures. Several, but not all, of these reactions do have correspondingly low bond energies.

However, there are clear entropic contributions to the equilibrium constant as well, which is reflected in the fact that the reactions between A1 or A2 and B2 have equilibrium constants that are one to several orders of magnitude greater



(a) Cross-link reactions with Barriers



(b) Cross-link reactions without Barriers

**Figure 8.7:** Equilibrium constants for forming a cross-link between PAHs with different reactive edge types.

than those between edge types A and D, despite the fact that the bond energy for B2 with A1 and A2 is noticeably lower than that for D2 with A1 and A2. The equilibrium constant for two B2 PAHs forming a cross-link is also greater than those for reactions between edge types A and E. Additionally, the equilibrium

constant for two B1 monomers reacting is also slightly larger than those between edge types A and D, again despite the lower bond energies. Likewise, the reaction between the  $\pi$ -radicals B1 and C has an equilibrium constant substantially higher than those between B1 and D1 or D2, as well as between B2 and B1 and B2 and C, even though the bond energies are rather similar. The equilibrium constant for the reaction between two C molecules is also comparable to those between edge types A and F, despite the C–C bond energy being substantially weaker, again suggesting the importance of the entropic contributions, as well as highlighting the favorable nature of reactions involving  $\pi$ -radicals that are not necessarily reflected in simply the bond energies.

### 8.3.5 Enhancement due to Bonding and Stacking

The equilibrium constants show that cross-linking between certain reactive edge types on PAHs form very stable bonds which are much less likely to be reversible. However, a previous study on bridge-forming reaction kinetics between acepyrene (edge type E) and pyrenyl (edge type A), found that even with a forward rate constant of the order of  $10^{12} \text{ cm}^3\text{mol}^{-1}\text{s}^{-1}$ , the process was insufficient to generate the required nucleation flux for soot formation (Frenklach and Mebel, 2020). Another previous work of dimerization of two pyrene  $\sigma$ -radicals (edge type A) using reactive molecular dynamics, showed collision efficiencies of 0.01 significantly lower than the 0.1–1.0 values required in models Mao et al. (2018). Given reactions with type-A edges possess the highest rates this suggests insufficient rates are found for all reactions explored for small PAH soot formation.

It was previously suggested that such an enhancement could arise from the fact that larger localised- $\pi$  radical species are able to both bond and stack in rim-bonds. Namely, they can condense through physical interactions and subsequently chemically cross-link, which is something that aryl  $\sigma$ -radicals are unable to achieve (Martin et al., 2019b). (Martin et al., 2019b) initially demonstrated the additive stabilisation effect of intermolecular interactions on top of the covalent bonding for a variety of rim-linked PAHs (Martin et al., 2019b).

To further explore the potential enhancement effect of bonding and stacking,

## 8 CHAPTER 8

the equilibrium constant was calculated for larger PAHs containing the different reactive edge types that can bond and stack (B,C,D and E). These larger PAHs were all chosen to have similar molecular weight, roughly in the range of 420-430 Da, compared to 150-160 Da for monomers B,C, and E. It is worth noting that the M06-2X-D3 does overestimate the physical interactions by roughly 6 kcal/mol compared to SAPT(DFT) results, suggesting again that the comparison between sites is the focus of this section (Martin et al., 2019b). This is seen in Figure 8.8.

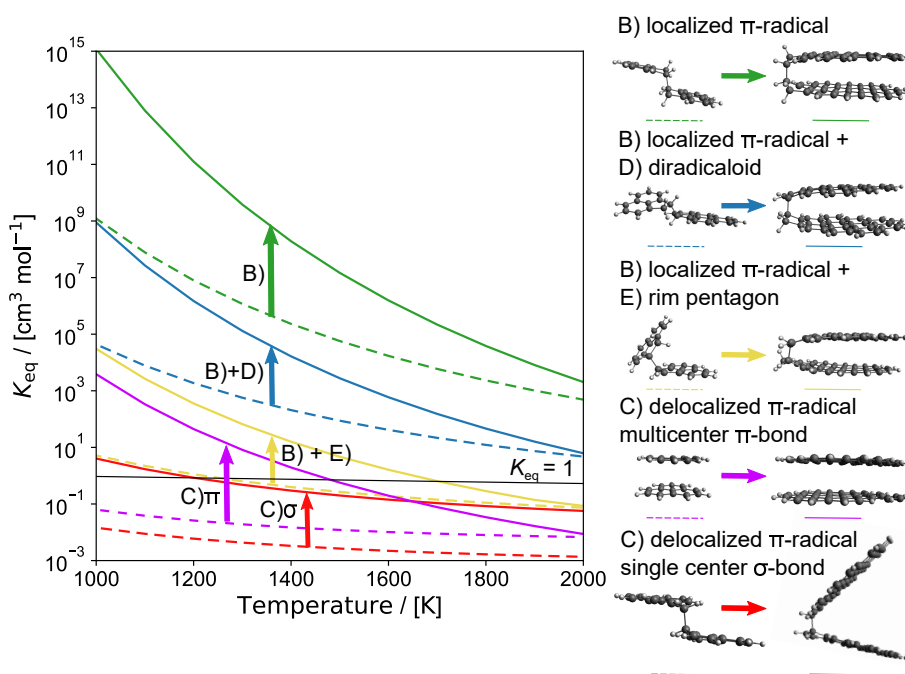


**Figure 8.8:** Equilibrium constants for cross-linking reactions between larger PAH reactions that can result in bonded and stacked structures. The dashed lines represent the equilibrium constant for smaller PAHs with the same reactive edge types, and the arrows represent the enhancement effect.

Figure 8.8 shows that there are substantial increases in the equilibrium constant for the larger PAHs compared with the smaller PAHs discussed so far. It is clear that the degree of enhancement is dependent on the type of reactive edges and the type of bond and stacking configuration. The enhancement in equilibrium constant is largest for a rim-linked structure between two localised  $\pi$ -radicals of edge type

B, followed by edge type B and D, and finally edge type B and E. The dispersion enhancements for B and D and B and E are only slightly less than for a stacked, multi-centre  $\pi$ -bond between two larger delocalised  $\pi$ -radicals of edge type C. Overall, the increase in equilibrium constant is one to two orders of magnitude larger for a rim-bonded structure of two localised  $\pi$ -radicals edge types compared to the increases for other edge types.

It is worth noting that whilst the delocalised  $\pi$ -radical C can also form a  $\sigma$ -bond (otherwise known as a  $\sigma$ -dimerisation), the resulting structure does not stack, and the contribution of dispersion interactions is significantly lower than for reactions involving a localised  $\pi$ -radical (justifying our new naming as rim-linked). As a consequence, this reaction has the smallest enhancement effect, but this enhancement effect is more consistent across the 1000–2000 K range. Nevertheless, dimerisation of a larger delocalised  $\pi$ -radical like C is most likely still unfavorable at temperatures above 1500 K. In contrast, even though the enhancement wanes at higher temperatures, the bond and stack effect does mean that at this same temperature of 1500 K, the reaction between larger PAHs of edge type B and E is still favorable, which was not the case for smaller PAHs with these edge types. The effect is still most promising for reactions between two localised  $\pi$ -radical PAHs, which was also seen to have rate constants rivaling reactions between aryl  $\sigma$ -radicals in edge type A.

The estimation here is also likely to be a lower bound, as the effect of first forming a physically bound PAH dimer followed by a subsequent rim-bond formation on the thermodynamics and kinetics has not been considered and could be enhanced further by internal rotors as recently suggested by Frenklach and Mebel [Frenklach and Mebel \(2020\)](#). They argued that rotationally excited collisions could enhance the stability and frequency of such bridge forming reactions, resulting in a substantial increase in the nucleation flux. A possible way in which such an enhancement could occur is due to physical interactions between PAHs before internal rotation and subsequent rim-bond formation. However, determining how much these effects will enhance collision efficiencies and reaction rates between the PAHs would likely require molecular dynamics and is the topic of further work.

Another enhancement could occur from having multiple localised  $\pi$ -radical sites on a single PAH containing multiple rim pentagonal rings. We have previously shown that an appreciable fraction of such PAHs can form diradicals in the flame as hydrogen is added and abstracted from these sites ?. More sites per molecules would allow for more opportunities to bond after physical condensation. This could also allow for a chain reaction to proceed.

All in all, the preliminary results here do suggest that the combined chemical and physical aggregation between localised  $\pi$ -radical PAHs is quite favorable at flame temperatures, and whether or not this provide a route to forming larger clusters of PAHs and ultimately soot warrants further investigation.

### 8.4 Conclusions

In this work, the thermodynamics and kinetics of cross-linking reaction between PAHs possessing different reactive edge types has been studied by means of density functional theory calculations. Computations of the bond energies and barrier heights generally affirmed that cross-linking reactions that resulted in the formation of strong bonds generally had low barriers. This was primarily the case for reactions involving PAHs with edge type A, or aryl-type  $\sigma$ -radicals. One noticeable exception was for reactions between localised- $\pi$  radicals, or edge type B, and acene diradicaloids, or edge type D1. These reactions were seen to have very low barriers, despite forming weak bonds. Additionally, reactions involving two PAH radicals were broadly barrierless, namely reactions between two PAHs of types A (aryl  $\sigma$ -radicals), B (localised- $\pi$  radicals), and C (delocalised- $\pi$  radicals).

The computation of the forward rate constants confirmed that reactions involving edge type A are faster than others. It was noted that generally having the  $\sigma$ -radical on the five-member ring resulted in faster kinetics than when the  $\sigma$ -radical was on the six-member ring. At flame temperatures of 1400–2000 K, the forward rate constants were generally of the order of  $10^8 \text{ cm}^3 \text{ mol}^{-1} \text{ s}^{-1}$  to  $10^{12} \text{ cm}^3 \text{ mol}^{-1} \text{ s}^{-1}$ . Notably, the rate constants between PAHs with edge type A and edge type D and edge type A and edge type B were seen to be as large or even larger than for

that between two of edge type A. It was also seen that the rate constant for the reaction between A1 and A2 was substantially faster than between A1 and A1 or A2 and A2. The reaction between two localised  $\pi$ -radicals on rim five-member rings was seen to be notably faster at temperatures below 1000 K, but then declines and is one of the slowest reactions at 2000 K. Reactions involving combinations of edge types B, C, D, and E were generally seen to be slower in comparison. Generally, all computed rate constants are unlikely to be high enough to result in substantial enough fluxes for processes such as soot formation on their own, including suggestions involving cross-links on five-member rings (D'Anna et al., 2001) and delocalised  $\pi$ -radicals PAHs (Johansson et al., 2018).

Analysis of the equilibrium constants showed most of these cross-linking reactions have substantial equilibrium constants and stability at flame temperatures, provided they involved one PAH of edge type A, or two PAHs with radical edge types A, B, or C. The localised  $\pi$ -radicals were seen to have large equilibrium constants for reactions with edge types A, B, and C, and were seen to be more reactive than all edge types aside from type A. It was also noted that despite having large forward rate constants in some cases, reactions of PAHs with diradicaloid edge type D were seen to have lower equilibrium constants than those involving edge types A, B, and C, highlighting their relative reversibility.

Computations of the equilibrium constants for larger PAHs that are able to bond and stack in rim-bonds showed that there is a substantial enhancement in the equilibrium constant that is dependent on the PAH edge types. It was observed that a larger enhancement was present for reactions between two localised- $\pi$  radicals PAHs of edge type B than for other edge types that could bond and stack, which highlights the difference in dispersion interactions between different edge types. This suggests that these dispersion effects could potentially promote reactions of larger localised  $\pi$ -radicals. These effects could be further enhanced by considering the role of dynamics such as internal rotors and multiple localised  $\pi$ -radical sites on the same aromatic species. Further work is necessary to study the dynamics of reactions and combined physical and chemical interactions involving these localised  $\pi$ -radicals to determine if such reactions are able to provide the nucleation flux required to explain soot formation.





# Chapter 9

## Conclusions

### 9.1 Conclusions of the thesis

To conclude, the main investigations and findings of each chapter of the thesis are summarised.

The HSE06 functional was used to compute the optical band gap (OBG) of a variety of polyaromatic hydrocarbons (PAHs), with this method checked against UV/visible spectroscopy measurements. The observed inverse power-law correlation of the OBG with number of rings was in agreement with previous reports. In case of homogeneous cross-linked PAHs, it was shown that orbital localization effects cause an asymptotic decrease in the OBG with increasing number of monomers. This effect was especially pronounced for larger PAH monomers. For cross-linking between two different PAHs, the OBG was shown to reflect the OBG of the largest monomer PAH and not the average of the monomers. The effect of PAH curvature was also studied by computing the OBG of peri-condensed curved PAHs with varying number of pentagons. These calculations showed that curved PAHs are expected to have larger OBGs than flat PAHs, but the effect wanes for larger structures. The effect of radical character on the OBG of PAHs was also studied.  $\sigma$ -radical PAHs were seen to have the same OBG as their equivalent closed-shell structure. On the other hand,  $\pi$ -radical PAHs were seen to have significantly lower optical band gaps than flat peri-condensed

## Conclusions

---

species of the same size, meaning that smaller  $\pi$ -radicals may also be important PAHs to consider.

It was demonstrated that curved PAHs containing 15 or more rings, with 2 pentagonal rings, are unable to invert at flame temperatures and are persistently polar at flame temperatures. The transition from invertible to rigid at 1500 K was found to be at a size range between 11 and 15 rings.  $\Pi$ -radicals and chemi-ions were not found to influence the inversion barrier substantially. *Ab initio* MD simulations suggested curved PAHs will still have substantial dipole moments even in flame conditions. Dynamics between a chemi-ion and curved PAH showed that the chemi-ion mainly interacted with the pentagonal atoms on the curved PAH due to the flexoelectric effect as well as the rim due to charge concentration. These results indicate that the polarity of curved PAH is substantial even at flame conditions and may be important to consider in soot formation.

The kinetics of forming a seven member ring adjacent to a five member ring in PAHs has been studied by means of *ab initio* density functional theory calculations and kinetic simulations of 0D reactors at standard flame concentrations and a variety of temperatures. The computed potential energy surfaces for the two HACA growths show that the formation of a seven member ring in a closed shell PAH (PAH A) and a resonance-stabilized-radical PAH (PAH B) follows the same general trends, with the loss of hydrogen being the most energetically difficult step. The computed potential energy surfaces for the four bay closure routes for PAH C and PAH D were seen to be generally similar as well, with atomic hydrogen and H<sub>2</sub> losses seen to be the most energetically difficult steps. For both routes and PAHs, there was not significant dependence on the initial carbon attacked by the hydrogen radical. The exception is the direct cyclisation route, with PAH C able to undergo H<sub>2</sub> loss directly after cyclisation, but PAH D requiring several migrations to cyclise.

The kinetic simulations in 0D homogeneous reactors for PAH A showed both HACA pathways contributed to the product formation, whereas for PAH B, addition to the five-member ring was crucial to form the seven-member ring containing product. For the bay closures, the hydrogen abstraction facilitated bay closure was seen to be the main contributor to seven-member ring formation at

1000, 1500, and 2000 K. At 2500 K, the carbene route becomes the dominant contributor, suggesting this pathway could be important at very high temperatures. In general, the HACA growth and bay closure processes did occur to some extent at all temperatures, suggesting seven-member ring formation in PAHs already containing five-member rings could be important to consider in flames.

The localization of  $\pi$ -radicals was analysed by means of Clar and spin density analyses. The partially saturated rim-based pentagonal ring was found to concentrate significant spin density on the pentagonal ring, resulting in a localised  $\pi$ -radical. In contrast,  $\pi$ -radicals formed within the six-member ring networks, delocalize and have their spin-density spread across the aromatic network. A reaction mechanism was developed, allowing the concentration of possible localised  $\pi$ -radicals to be computed at flame conditions. Significant concentrations of localised  $\pi$ -radicals are present in soot-forming temperatures, provided sufficient H-radical concentrations are also present in the flames. Finally, kinetic Monte Carlo simulations showed that multiple localised  $\pi$ -radical reactive sites can be formed on a single PAH. These PAHs with multiple reactive sites could potentially chemically polymerize, suggesting a new potential route to inception of soot particles.

The thermodynamics and kinetics of cross-linking reaction between PAHs possessing different reactive edge types was studied using density functional theory calculations. Computations of the bond energies and barrier heights showed that reactions involving PAHs with edge type A, or aryl-type  $\sigma$ -radicals, resulted in strong bonds and low barriers. Reactions involving two PAH radicals were generally barrierless, namely reactions between two PAHs with edge types A (aryl  $\sigma$ -radicals), B (localised  $\pi$ -radicals), and C (delocalised  $\pi$ -radicals). The computation of the forward rate constants confirmed that reactions involving edge type A are faster than others. It was noted that generally having the  $\sigma$ -radical on the five-member ring resulted in faster kinetics than when the  $\sigma$ -radical was on the six-member ring. However, the rate constants for reactions between PAHs with  $\sigma$ -radicals and diradicaloids,  $\sigma$ -radicals and localised  $\pi$ -radicals, were seen to be as large or even larger than for that between two aryls. The reaction between two localised  $\pi$ -radicals with partially protonated rim five-member rings was seen to

## Conclusions

---

be important as lower temperatures. The computed rate constants for cross-linking are unlikely to be high enough to result in substantial soot nucleation flux.

Analysis of the equilibrium constants showed most of these cross-linking reactions have substantial equilibrium constants at flame temperatures, provided they involved one PAH of edge type A, or two PAHs with radical edge types A, B, or C. The localised  $\pi$ -radicals were seen to have large equilibrium constants for reactions with edge types A, B, and C, and were seen to be more reactive than all edge types aside from type A. Computations of the equilibrium constants for larger PAHs showed a substantial enhancement in the equilibrium constant due to bonding and stacking effects that is dependent on the PAH edge types. It was observed that a larger enhancement was present for reactions between two localised  $\pi$ -radicals PAHs than for other edge types that could bond and stack. This suggests that these bond-and-stack effects could potentially promote reactions of larger localised  $\pi$ -radicals. This links to the finding that larger PAHs could actually form multi-radicals with multiple localised  $\pi$ -radical sites, meaning chains of rim-linked-structures are a possibility.

## 9.2 Suggestions for further work

The work in this dissertation has identified and studied the properties and formation of PAHs of interest to soot formation, notably of curved PAHs and localised  $\pi$ -radical PAHs. However, there are a great many questions that remain unanswered with regards to soot formation. Three suggestions for future research avenues that builds upon this work and the work of others have been detailed in the following sections.

### 9.2.1 Cross-link reaction pathways for PAHs

Cross-linking and stacking between PAHs between reactive edge types has been identified as a potentially important process that could be relevant to soot nucleation, as it was seen that there are PAHs that can form these bonded-and-stacked structures. However, so far, only the kinetics of the initial cross-link formation have been computed, and this was limited to smaller PAHs.

Deriving rate constants for larger PAHs that can bond and stack would be useful to see if the predicted enhancement in equilibrium translates to faster kinetics and stabilization of a physically and chemically bound complex.

Additionally, there are many pathways related to cross-linking beyond the formation of the initial cross-link that still need to be considered. Some of these include important routes by which a cross-link could break, such as through hydrogen or radical fragmentation. Additionally, several condensation and bay-closure processes are possible once a cross-link has been formed between PAHs. In a sense, these are competitive to continuous chemical polymerization of PAHs, as such reactions will result in a re-arrangement of the PAH. However, such cross-link condensation routes could also be important for the formation and growth of the larger PAHs that are typically considered for soot nucleation.

### 9.2.2 Molecular dynamics studies on combined physical and chemical clustering between PAHs

Translating the reactions between PAHs into a mechanism for combined physical and chemical nucleation of PAHs is also necessary to fully understand whether these reactions between different reactive edge types on PAHs can produce sufficient nucleation flux, and to derive an appropriate rate of nucleation. Molecular dynamics studies on the physical and chemical clustering of curved and localised  $\pi$ -radical PAHs would shed some insight on the rates and mechanisms of nucleation of nascent soot particles, as similar studies have done for homogeneous nucleation (Totton et al., 2012) and  $\sigma$ -radicals (Mao et al., 2017).

Such molecular dynamics studies would need to parametrize a reactive force field to describe the bonding and energetics of PAHs with these different reactive edge types, for which the DFT results in this thesis could provide useful data to fit the force field to. Studies on the collision efficiency of species of interest, such as the localised  $\pi$ -radicals, and studies of properties such as cluster size, clustering free energy, and clustering propensity are all necessary to truly test whether reactive cross-linking between PAHs is dynamically favorable. Colleagues are already

## Conclusions

---

performing such studies both for the clustering of larger curved PAHs with ions as well as for studying the clustering of localised  $\pi$  radicals.

### 9.2.3 Implementation of process rates into kinetic Monte Carlo simulations

Additionally, consideration of whether curved PAHs, PAHs with seven member rings, and localised  $\pi$ -radical PAHs could form under flame conditions has been limited to kinetic simulations in 0D homogenous gas-phase reactors. Whilst such studies are useful to consider relative pathways and importance, they are certainly not fully representative of flame conditions, where transport effects and the presence of several other species will have a significant impact. Also, the interaction of these gas-phase PAHs with the soot particle phase has not been considered, and the impact of such PAH processes on the nanostructure of soot particles in flames is an important question.

An approach that does this that is utilized by colleagues is to run a flame simulation to get the key temperature and gas phase species profiles, and then post process the results with a kinetic Monte Carlo simulation to describe the growth and formation of larger PAHs, the dynamics of soot formation, and the coupling between the two. This gives a much clearer picture of how (and if) the reactions and formation of PAHs studied in this work occur in flames.

Work by colleagues has already integrated the seven-member ring formation into a kinetic Monte Carlo scheme to look at their formation at realistic flame conditions, confirming that they do indeed form. Expanding this to include reactions involving localised  $\pi$ -radicals would be useful to get an idea of the expected concentration of larger localised  $\pi$ -radical PAHs in comparison to standard peri-condensed species that are typically modelled. Implementation of cross-linking reactions in a kinetic Monte Carlo framework is also an avenue for future work. This would help elucidate how such cross-linking reactions impact the growth of PAHs and interact with other well known mechanisms such as HACA. Studying cross-linking reactions between PAHs in soot particles could

## 9.2 Suggestions for further work

---

also help lead to a more detailed understanding carbonisation and maturation of soot particles, as has been hypothesised previously ([Kholghy et al., 2016](#)).

These future studies could all help improve the understanding of how the PAH chemistry and properties studied in this work impact and occur in flames. The hope is that being able to describe and capture these phenomena will work towards finally untangling the long-standing mystery behind soot formation, and guide the design of processes that either allow for its mitigation, or tuning of its properties for the appropriate application.

# Nomenclature

## Acronyms

$\mu$ TST Microcanonical Transition State Theory

0D 0-Dimensional

AALH Aromatic-Aliphatically-Linked-Hydrocarbon

ADMP Atom Density Matrix Propagation

AFM Atomic Force Microscopy

AIMD *Ab Initio* Molecular Dynamics

AMLH Aromatic Multicentre-Linked Hydrocarbons

ARLH Aromatic Rim-Linked Hydrocarbons

AZLH Aromatic Zig-zag Linked Hydrocarbons

BEP Brønsted-Evans-Polanyi

BOMD Born-Oppenheimer Molecular Dynamics

CAS Complete Active Space

CASPT2 Complete Active Space with Second Order Perturbation Theory

CASSCF Complete Active Space Self Consistent Field



- CBS Complete Basis Set extrapolation
- CC[SD(T)] Coupled Cluster. S includes single excitations, D doubles. A letter in parenthesis indicates the effect is estimated with perturbation theory
- CHRCR Clustering of Hydrocarbons by Radical Chain Reactions
- CI[SD(T)] Configuration Interaction. S includes single excitations, D doubles, and T triples. A letter in parenthesis indicates the effect is estimated with perturbation theory.
- cPAH curved PAH
- CSF Configuration State Function
- CTST Canonical Transition State Theory
- CVTST Canonical Variational Transition State Theory
- DFT Density Functional Theory
- FTIR Fourier Transform Infrared Spectroscopy
- G<sub>n</sub>* Gaussian Composite. *n* indicates its particular version
- GGA Generalized Gradient Approximation
- GTO Gaussian Type Orbital
- HAB Height Above Burner
- HACA Hydrogen-Abstraction-Carbon-Addition
- HF Hartree-Fock
- HIM Helium Ion Microscopy
- HOMO Highest Occupied Molecular Orbital
- HR-AFM High Resolution Atomic Force Microscopy
- HRTEM High Resolution Transmission Electron Microscopy

## NOMENCLATURE

---

|          |   |
|----------|---|
| KMC      | Kinetic Monte Carlo   |
| LDA      | Local Density Approximation                                 |
| LIF      | Laser Induced Fluorescence                                  |
| LII      | Laser Induced Incandescence                                 |
| LUMO     | Lowest Unoccupied Molecular Orbital                         |
| MCSCF    | Multi Configuration Self Consistent Field                   |
| ME       | Master Equation   |
| MP $n$   | Möller Plesset Perturbation Theory of the $n$ th order      |
| MRCI     | Multireference Configuration Interaction                    |
| Nd:YAG   | Neodymium-doped Yttrium Aluminium Garnet                    |
| NMR      | Nuclear Magnetic Resonance                                  |
| OBG      | Optical Band Gap  |
| P.E      | Percentage Error  |
| PAH      | PolyAromatic Hydrocarbons                                   |
| PES      | Potential Energy Surface                                    |
| QCI      | Quadratic Configuration Interaction                         |
| RAS-CI   | Restricted Active Space Configuration Interaction           |
| REMPI-MS | Resonance-Enhanced MultiPhoton Ionisation Mass Spectrometry |
| RMG      | Reaction Mechanism Generator                                |
| ROHF     | Restricted Open-Shell Hartree-Fock                          |
| RRHO     | Rigid Rotor Harmonic Oscillator                             |
| RRKM     | Rice–Ramsperger–Kassel–Markus theory                        |

|         |  |
|---------|--|
| RSR     | Resonance-Stabilised-Radical                             |
| SCF     | Self Consistent Field                                    |
| SEM     | Scanning Electron Microscopy                             |
| STO     | Slater Type Orbital                                      |
| TD-DFT  | Time-Dependent Density Functional Theory                 |
| TEM     | Transmission Electron Microscopy                         |
| TOF-MS  | Time-Of-Flight Mass Spectrometry                         |
| TS      | Transition State   |
| TST     | Transition State Theory                                  |
| UHF     | Unrestricted Hartree-Fock                                |
| UV      | UltraViolet  |
| VPT2    | Vibrational Perturbation Theory, 2nd order.              |
| VRC-TST | Variable Reaction Coordinate Transition State Theory     |
| VTST    | Variational Transition State Theory                      |
| VUV-AMS | Vacuum UltraViolet Aerosol Mass Spectrometry             |
| $W_n$   | Weizmann Composite. $n$ indicates its particular version |
| ZPE     | Zero Point Energy  |

### **Roman Uppercase Symbols**

$\Delta H_r^0$  Reaction enthalpy at 0 K

$\Delta H_r^{298}$  Reaction enthalpy at 298 K

$\hat{F}_i$  Fock operator for  $i$ th electron

## NOMENCLATURE

---

|                         |   |
|-------------------------|---|
| $\hat{H}$               | Hamiltonian operator in the Schrödinger equation                                |
| $\hat{H}^0$             | Unperturbed Hamiltonian operator  |
| $\hat{H}'$              | Perturbed Hamiltonian operator  |
| $\hat{H}_e$             | Hamiltonian operator in the electronic Schrödinger equation                     |
| $\hat{J}_{ij}$          | Coulomb operator representing interactions between $i$ th and $j$ th electrons  |
| $\hat{K}_{qi}$          | Exchange operator representing interactions between $i$ th and $q$ th electrons |
| $\hat{T}$               | Kinetic energy operator in the Schrödinger equation                             |
| $\hat{T}_e$             | Kinetic energy operator of the electrons  |
| $\hat{T}_n$             | Kinetic energy operator of the nuclei   |
| $\hat{V}$               | Potential energy operator in the Schrödinger equation                           |
| $\hat{V}_i^{\text{HF}}$ | Potential energy operator of $i$ th electron in Hartree-Fock method             |
| $\hat{V}_e$             | Potential energy operator of the electrons                                      |
| $\hat{V}_n$             | Potential energy operator of the nuclei   |
| $\hat{V}_{e-e}$         | Potential energy operator of the electrons-electrons repulsions                 |
| $\hat{V}_{n-e}$         | Potential energy operator of the nuclei-electrons attractions                   |
| $\vec{R}_k$             | Position of the $k$ th nucleus  |
| $A$                     | Helmholtz Free Energy (Chapter 3)   |
| $A$                     | Pre-exponential Factor (Chapters 5-8)   |
| $E[\rho(\vec{r})]$      | Total energy functional in DFT  |
| $E_A$                   | Activation Energy   |
| $E_i$                   | Energy of target system in perturbation theory                                  |
| $E_i^{(0)}$             | Energy of reference system in perturbation theory                               |

## NOMENCLATURE

---

|                         |   |
|-------------------------|---|
| $E_i^{(j)}$             | $j$ th term in Taylor expansion of the energy   |
| $E_T$                   | Energy of trial wavefunction  |
| $E_{xc}[\rho(\vec{r})]$ | Exchange energy functional in DFT   |
| $G$                     | Gibbs Free energy   |
| $G_m$                   | Molar Gibbs Free energy   |
| $G_r$                   | Gibbs Free energy of reaction   |
| $G_u$                   | Generation term of species $u$ in a chemical mechanism  |
| $H$                     | Enthalpy  |
| $I_k$                   | $k$ th moment of inertia, $k \in (x, y, z)$   |
| $J$                     | Total angular momentum quantum number   |
| $J[\rho(\vec{r})]$      | Potential energy functional for non-interacting system in DFT   |
| $K$                     | Equilibrium constant  |
| $L_u$                   | Loss term of species $u$ in a chemical mechanism  |
| $M$                     | Number of rings in aromatic species (Chapter 4)   |
| $M_k$                   | Atomic mass of the $k$ th nucleus   |
| $M_w$                   | Molecular Weight  |
| $N$                     | Number of particles or electrons  |
| $N^\ddagger(E, J)$      | Number of states at energy less than or equal to $E$ and angular momentum quantum number equal to $J$ |
| $N_A$                   | Avogadro constant   |
| $P$                     | Pressure  |
| $P(E)$                  | Probability distribution of energies  |

## NOMENCLATURE

---

|                      |  |
|----------------------|--|
| $Q$                  | System partition function  |
| $R$                  | Gas constant   |
| $S$                  | Entropy  |
| $S_{ki}$             | Normalised sensitivity coefficient of $k$ th parameter on model variable $i$ |
| $T$                  | Temperature  |
| $T[\rho(\vec{r})]$   | Kinetic energy functional for interacting system in DFT                      |
| $T_k$                | $k$ th term in coupled cluster expansion                                     |
| $T_s[\rho(\vec{r})]$ | Kinetic energy functional for non-interacting system in DFT                  |
| $U$                  | Internal Energy  |
| $V$                  | Volume   |
| $V(x)$               | Potential function for tunneling   |
| $V[\rho(\vec{r})]$   | Potential energy functional for interacting system in DFT                    |
| $V_0$                | Potential barrier to rotation for an internal rotor                          |
| $W$                  | Threshold Energy in Eckart tunneling corrections                             |
| $X$                  | Mole Fraction  |
| $Y$                  | Mass Fraction  |
| $Z_k$                | Atomic charge of the $k$ th nucleus  |
| $C_p$                | Heat capacity at constant pressure   |
| $C_v$                | Heat capacity at constant volume   |
| $D_e$                | Bond dissociation energy   |
| $E$                  | Energy   |
| $E_0$                | Threshold Energy   |

|                 |   |
|-----------------|---|
| $E_e$           | Energy eigenvalues of electronic Schrödinger Equation     |
| $\hat{V}_{n-n}$ | Potential energy operator of the nuclei-nuclei repulsions |
| $\mathbf{R}$    | Nuclear position vector (Chapter 5)                       |

**Roman Lowercase Symbols**

|                  |  |
|------------------|--|
| $\hat{h}_i$      | One-electron Hamiltonian operator  |
| $\hbar$          | Planck's Constant divided by $2\pi$  |
| $\vec{r}$        | Position vector of electrons   |
| $\vec{x}$        | Position vector of electrons in DFT  |
| $n$              | Temperature exponent in modified Arrhenius Expression                                  |
| $a$              | Fitting coefficient for inverse power law (Chapter 4)                                  |
| $a$              | Length of box in translational partition function (Chapter 3)                          |
| $b$              | Fitting coefficient for inverse power law (Chapter 4)                                  |
| $c$              | Fitting coefficient for inverse power law (Chapter 4)                                  |
| $c_G$            | Complex coefficient of the plane wave  |
| $c_u$            | Concentration of species $u$ in a chemical mechanism                                   |
| $c_W$            | Wigner tunnelling correction factor  |
| $c_{ij}$         | $j$ th expansion coefficient in the basis function for $i$ th atomic/molecular orbital |
| $d$              | Fitting coefficient for inverse power law (Chapter 4)                                  |
| $dk_a$           | Rate constant coefficient for activation   |
| $f_{\text{vib}}$ | Anharmonic correction factor to partition function                                     |

## NOMENCLATURE

---

|              |  |
|--------------|--|
| $g_i$        | Degeneracy of the $i$ th molecular energy level            |
| $h$          | Planck's Constant  |
| $k$          | Rate constant coefficient                                  |
| $k_0$        | Low pressure limited rate constant coefficient             |
| $k_\infty$   | High pressure limited rate constant coefficient            |
| $k_B$        | Boltzmann constant   |
| $k_{uni}$    | Unimolecular rate constant coefficient                     |
| $l$          | Angular momentum quantum number                            |
| $m$          | Mass of particle   |
| $n$          | Quantum numbers (Chapter 3)                                |
| $p$          | Plane wave basis function                                  |
| $q$          | Total molecular partition function                         |
| $q^\ddagger$ | Total molecular partition function of the transition state |
| $q^E$        | Electronic molecular partition function                    |
| $q^R$        | Rotational molecular partition function                    |
| $q^T$        | Translational molecular partition function                 |
| $q^V$        | Vibrational molecular partition function                   |
| $q_R$        | Total molecular partition function of reactants            |
| $r$          | Distance coordinate  |
| $r_{eq}$     | Equilibrium distance between fragments                     |
| $s$          | Position of the trial dividing surface                     |
| $t$          | Time variable  |



|              |  |
|--------------|--|
| $x_i$        | Variable in sensitivity analysis             |
| $y_i$        | Response to variable in sensitivity analysis |
| $z_i$        | Rate of progress of reaction $i$             |
| $\mathbf{r}$ | Electron positions (Chapter 7)               |

**Greek Uppercase Symbols**

|                  |   |
|------------------|---|
| $\Psi$           | Wavefunction  |
| $\Psi^*$         | Complex conjugate of the wavefunction                   |
| $\Psi_i$         | Wavefunction of target system in perturbation theory    |
| $\Psi_i^{(0)}$   | Wavefunction of reference system in perturbation theory |
| $\Psi_i^{(j)}$   | $j$ th term in Taylor expansion of the wavefunction     |
| $\Theta_{rot,i}$ | $i$ th rotational constant, $i \in (x, y, z)$           |

**Greek Lowercase Symbols**

|                 |  |
|-----------------|--|
| $\alpha$        | Constants in Eckart tunneling function             |
| $\beta$         | Morse function parameter                           |
| $\chi$          | Basis set function                                 |
| $\varepsilon$   | Total energy of the $i$ th molecular level         |
| $\varepsilon^E$ | Electronic energy of the $i$ th molecular level    |
| $\varepsilon^R$ | Rotational energy of the $i$ th molecular level    |
| $\varepsilon^T$ | Translational energy of the $i$ th molecular level |

## NOMENCLATURE

---

|                    |  |
|--------------------|--|
| $\varepsilon^V$    | Vibrational energy of the $i$ th molecular level                                 |
| $\gamma_{ui}''$    | Reverse stoichiometric coefficient of species $u$ in reaction $i$                |
| $\gamma_{ui}'$     | Forward stoichiometric coefficient of species $u$ in reaction $i$                |
| $\kappa$           | Tunneling coefficient  |
| $\kappa_E$         | Eckart Tunneling coefficient   |
| $\kappa_W$         | Wigner Tunneling coefficient   |
| $\lambda$          | Perturbation expansion parameter   |
| $\mu$              | Reduced mass   |
| $\nu^\ddagger$     | vibrational frequency of transition state  |
| $\nu_i$            | $i$ th vibrational frequency   |
| $\omega$           | Collisional frequency  |
| $\phi$             | Atomic or molecular orbital functions  |
| $\pi$ -            | In reference to a $\pi$ -radical   |
| $\psi$             | Spinorbital functions  |
| $\rho(\mathbf{r})$ | Electronic spin density  |
| $\rho(\vec{r})$    | Electron density in DFT  |
| $\rho(E, J)$       | Density of states at energy $E$ and angular momentum quantum number equal to $J$ |
| $\sigma$           | Rotational symmetry number   |
| $\sigma$ -         | In reference to a $\sigma$ -radical  |
| $\tau$             | Characteristic time for inversion  |
| $\varepsilon$      | Expectation value of the Hamiltonian in variational method                       |

## NOMENCLATURE

---

|          |  |
|----------|--|
| $\xi$    | Parameter in Eckart tunneling                      |
| $\zeta$  | Number of basis functions per orbital in basis set |
| $\alpha$ | Electronic spin direction alpha                    |
| $\beta$  | Electronic spin direction beta                     |



# Bibliography

- Abdourazak, A. H., Sygula, A., Rabideau, P. W. (1993). "locking" the bowl-shaped geometry of corannulene: cyclopentacorannulene. *Journal of the American Chemical Society* **115** (7), 3010–3011. doi:[10.1021/ja00060a073](https://doi.org/10.1021/ja00060a073).
- Abid, A. D., Heinz, N., Tolmachoff, E. D., Phares, D. J., Campbell, C. S., Wang, H. (2008). On evolution of particle size distribution functions of incipient soot in premixed ethylene–oxygen–argon flames. *Combustion and Flame* **154** (4), 775–788. doi:[10.1016/j.combustflame.2008.06.009](https://doi.org/10.1016/j.combustflame.2008.06.009).
- Abid, A. D., Tolmachoff, E. D., Phares, D. J., Wang, H., Liu, Y., Laskin, A. (2009). Size distribution and morphology of nascent soot in premixed ethylene flames with and without benzene doping. *Proceedings of the Combustion Institute* **32** (1), 681–688. doi:[10.1016/j.proci.2008.07.023](https://doi.org/10.1016/j.proci.2008.07.023).
- Adkins, E., Giaccai, J., Miller, J. (2017). Computed electronic structure of polynuclear aromatic hydrocarbon agglomerates. *P. Combust. Inst.* **36** (1), 957–964. doi:<https://doi.org/10.1016/j.proci.2016.06.186>.
- Adkins, E., Miller, J. (2015). Extinction measurements for optical band gap determination of soot in a series of nitrogen-diluted ethylene/air non-premixed flames. *Physical Chemistry Chemical Physics* **17** (4), 2686–2695. doi:[10.1039/C4CP04452E](https://doi.org/10.1039/C4CP04452E).
- Adkins, E., Miller, J. (2017). Towards a taxonomy of topology for polynuclear aromatic hydrocarbons: linking electronic and molecular structure. *Phys. Chem. Chem. Phys.* **19**, 28458–28469. doi:[10.1039/C7CP06048C](https://doi.org/10.1039/C7CP06048C).
- Akbar Ali, M., Barker, J. R. (2015). Comparison of three isoelectronic multiple-well reaction systems: OH + CH<sub>2</sub>O, OH + CH<sub>2</sub>CH<sub>2</sub>, and OH + CH<sub>2</sub>NH. *J. Phys. Chem. A.* **119** (28), 7578–7592. doi:[10.1021/acs.jpca.5b00910](https://doi.org/10.1021/acs.jpca.5b00910).

## BIBLIOGRAPHY

---

- A.L. Lafleur, J.B. Howard, J.A. Marr, T. Yapesh (1993). Proposed fullerene precursor corannulene identified in flames both in the presence and absence of fullerene production. *J. Phys. Chem. C* **97** (51), 13539–13543. doi:[10.1021/j100153a020](https://doi.org/10.1021/j100153a020).
- Andreu, R., Garín, J., Orduna, J. (2001). Electronic absorption spectra of closed and open-shell tetrathiafulvalenes: the first time-dependent density-functional study. *Tetrahedron* **57** (37), 7883 – 7892. doi:[https://doi.org/10.1016/S0040-4020\(01\)00766-9](https://doi.org/10.1016/S0040-4020(01)00766-9).
- Atkins, P. W., Friedman, R. S. (1997). *Molecular Quantum Mechanics*. Oxford University Press.
- Atkins, P. W., Friedman, R. S. (2011). *Molecular quantum mechanics*. Oxford university press.
- Bachmann, M., Wiese, W., Homann, K.-H. (1996). PAH and aromers: Precursors of fullerenes and soot. *Symposium (International) on Combustion* **26** (2), 2259 – 2267. doi:[https://doi.org/10.1016/S0082-0784\(96\)80053-1](https://doi.org/10.1016/S0082-0784(96)80053-1).
- Bao, J. L., Truhlar, D. G. (2017). Variational transition state theory: theoretical framework and recent developments. *Chemical Society Reviews* **46** (24), 7548–7596. doi:[10.1039/C7CS00602K](https://doi.org/10.1039/C7CS00602K).
- Barker, J., Nguyen, T., Stanton, J., Aieta, C., Ceotto, M., Gabas, F., Kumar, T., Li, C., Lohr, L., Maranzana, A., et al. (2017a). Multiwell-2017 software suite. *Ann Arbor, Michigan*
- Barker, J., Nguyen, T., Stanton, J., Aieta, C., Ceotto, M., Gabas, F., Kumar, T. J., Li, C., Lohr, L., Maranzana, A., Ortiz, N., Preses, J., Simmie, J., Sonk, J., Stimac, P. (2017b). Multiwell-2017 software suite; j.r. barker, university of michigan, ann arbor, michigan, usa, 2017. URL <http://clasp-research.engin.umich.edu/multiwell/>.
- Barker, J. R. (2001). Multiple-Well, multiple-path unimolecular reaction systems. I. MultiWell computer program suite. *International Journal of Chemical Kinetics* **33** (4), 232–245. doi:[10.1002/kin.1017](https://doi.org/10.1002/kin.1017).
- Barker, J. R. (2009). Energy transfer in master equation simulations: A new approach. *International Journal of Chemical Kinetics* **41** (12), 748–763. doi:[10.1002/kin.20447](https://doi.org/10.1002/kin.20447).

## BIBLIOGRAPHY

---

- Baroncelli, M., Mao, Q., Galle, S., Hansen, N., Pitsch, H. (2020). Role of ring-enlargement reactions in the formation of aromatic hydrocarbons. *Physical Chemistry Chemical Physics* **22** (8), 4699–4714. doi:[10.1039/C9CP05854K](https://doi.org/10.1039/C9CP05854K).
- Barone, A., d'Alessio, A., d'Anna, A. (2003). Morphological characterization of the early process of soot formation by atomic force microscopy. *Combustion and Flame* **132** (1-2), 181–187. doi:[10.1016/S0010-2180\(02\)00434-0](https://doi.org/10.1016/S0010-2180(02)00434-0).
- Barone, V., Hod, O., Peralta, J. E., Scuseria, G. E. (2011). Accurate prediction of the electronic properties of low-dimensional graphene derivatives using a screened hybrid density functional. *Accounts of chemical research* **44** (4), 269–279. doi:[10.1021/ar100137c](https://doi.org/10.1021/ar100137c).
- Baum, T., Löffler, S., Löffler, P., Weilmünster, P., Homann, K.-H. (jul 1992). Fullerene ions and their relation to PAH and soot in low-pressure hydrocarbon flames. *Berichte der Bunsengesellschaft für physikalische Chemie* **96** (7), 841–857. doi:[10.1002/bbpc.19920960702](https://doi.org/10.1002/bbpc.19920960702).
- Becke, A. D. (1993). Density-functional thermochemistry. III. The role of exact exchange. *Journal of Chemical Physics* **98** (7), 5648–5651. doi:[10.1063/1.464913](https://doi.org/10.1063/1.464913).
- Bell, R. (1959). The tunnel effect correction for parabolic potential barriers. *Transactions of the Faraday Society* **55**, 1–4. doi:[10.1039/TF9595500001](https://doi.org/10.1039/TF9595500001).
- Bhadwal, A. S., Tripathi, R. M., Gupta, R. K., Kumar, N., Singh, R. P., Shrivastav, A. (2014). Biogenic synthesis and photocatalytic activity of cds nanoparticles. *RSC Adv.* **4**, 9484–9490. doi:[10.1039/C3RA46221H](https://doi.org/10.1039/C3RA46221H).
- Biedermann, P. U., Pogodin, S., Agranat, I. (1999). Inversion barrier of corannulene. a benchmark for bowl-to-bowl inversions in fullerene fragments. *The Journal of Organic Chemistry* **64** (10), 3655–3662. doi:[10.1021/jo9900174](https://doi.org/10.1021/jo9900174).
- Bockhorn, H. (1994). *Soot formation in combustion: mechanisms and models*, vol. 59. Springer Science & Business Media.

## BIBLIOGRAPHY

---

- Bond, T. C., Doherty, S. J., Fahey, D. W., Forster, P. M., Bernsten, T., Deangelo, B. J., Flanner, M. G., Ghan, S., Kärcher, B., Koch, D., Kinne, S., Kondo, Y., Quinn, P. K., Sarofim, M. C., Schultz, M. G., Schulz, M., Venkataraman, C., Zhang, H., Zhang, S., Bellouin, N., Guttikunda, S. K., Hopke, P. K., Jacobson, M. Z., Kaiser, J. W., Klimont, Z., Lohmann, U., Schwarz, J. P., Shindell, D., Storelvmo, T., Warren, S. G., Zender, C. S. (2013). Bounding the role of black carbon in the climate system: A scientific assessment. *Journal of Geophysical Research Atmospheres* **118** (11), 5380–5552. doi:[10.1002/jgrd.50171](https://doi.org/10.1002/jgrd.50171).
- Botero, M., Adkins, E., Gonzalez-Calera, S., Miller, J., Kraft, M. (2016a). PAH structure analysis of soot in a non-premixed flame using high-resolution transmission electron microscopy and optical band gap analysis. *Combustion and Flame* **164**, 250–258. doi:[10.1016/j.combustflame.2015.11.022](https://doi.org/10.1016/j.combustflame.2015.11.022).
- Botero, M. L., Adkins, E. M., González-Calera, S., Miller, H., Kraft, M. (2016b). PAH structure analysis of soot in a non-premixed flame using high-resolution transmission electron microscopy and optical band gap analysis. *Combustion and Flame* **164**, 250–258. doi:[10.1016/j.combustflame.2015.11.022](https://doi.org/10.1016/j.combustflame.2015.11.022).
- Botero, M. L., Sheng, Y., Akroyd, J., Martin, J., Dreyer, J. A., Yang, W., Kraft, M. (2018). Internal structure of soot particles in a diffusion flame. *Carbon* **141**, 635–642. doi:[10.1016/j.carbon.2018.09.063](https://doi.org/10.1016/j.carbon.2018.09.063).
- Bowal, K., Martin, J. W., Misquitta, A. J., Kraft, M. (2019). Ion-induced soot nucleation using a new potential for curved aromatics. *Combustion Science and Technology* **191** (5-6), 747–765. doi:[10.1080/00102202.2019.1565496](https://doi.org/10.1080/00102202.2019.1565496).
- Bross, D. H., Jasper, A. W., Ruscic, B., Wagner, A. F. (2019). Toward accurate high temperature anharmonic partition functions. *Proceedings of the Combustion Institute* **37** (1), 315–322. doi:[10.1016/j.proci.2018.05.028](https://doi.org/10.1016/j.proci.2018.05.028).
- Burke, K. (2012). Perspective on density functional theory. *The Journal of chemical physics* **136** (15), 150901. doi:[10.1063/1.4704546](https://doi.org/10.1063/1.4704546).
- Caglar, Y., Ilican, S., Caglar, M. (Aug 2007). Single-oscillator model and determination of optical constants of spray pyrolyzed amorphous SnO<sub>2</sub> thin films. *Eur. Phys. J. B.* **58** (3), 251–256. doi:[10.1140/epjb/e2007-00227-y](https://doi.org/10.1140/epjb/e2007-00227-y).



## BIBLIOGRAPHY

---

- Cain, J., Laskin, A., Kholghy, M. R., Thomson, M. J., Wang, H. (2014). Molecular characterization of organic content of soot along the centerline of a coflow diffusion flame. *Physical Chemistry Chemical Physics* **16** (47), 25862–25875. doi:[10.1039/c4cp03330b](https://doi.org/10.1039/c4cp03330b).
- Cain, J. P., Gassman, P. L., Wang, H., Laskin, A. (2010). Micro-FTIR study of soot chemical composition—evidence of aliphatic hydrocarbons on nascent soot surfaces. *Physical Chemistry Chemical Physics* **12** (20), 5206–5218. doi:[10.1039/b924344e](https://doi.org/10.1039/b924344e).
- Calcote, H. F., Olson, D. B., Keil, D. G. (1988). Are ions important in soot formation? *Energy & Fuels* **2** (4), 494–504. doi:[10.1021/ef00010a016](https://doi.org/10.1021/ef00010a016).
- Canneaux, S., Bohr, F., Henon, E. (2014). Kisthelp: A program to predict thermodynamic properties and rate constants from quantum chemistry results. *Journal of computational chemistry* **35** (1), 82–93. doi:[10.1002/jcc.23470](https://doi.org/10.1002/jcc.23470).
- Carbone, F., Canagaratna, M. R., Lambe, A. T., Jayne, J. T., Worsnop, D. R., Gomez, A. (2019). Exploratory analysis of a sooting premixed flame via on-line high resolution (APi-TOF) mass spectrometry. *Proceedings of the Combustion Institute* **37** (1), 919–926. doi:[10.1016/j.proci.2018.08.020](https://doi.org/10.1016/j.proci.2018.08.020).
- Celani, P., Werner, H.-J. (2003). Analytical energy gradients for internally contracted second-order multireference perturbation theory. *Journal of Chemical Physics* **119** (10), 5044–5057. doi:[10.1063/1.1597672](https://doi.org/10.1063/1.1597672).
- Chen, D., Totton, T. S., Akroyd, J. W., Mosbach, S., Kraft, M. (2014a). Size-dependent melting of polycyclic aromatic hydrocarbon nano-clusters: A molecular dynamics study. *Carbon* **67** (Supplement C), 79 – 91. doi:<https://doi.org/10.1016/j.carbon.2013.09.058>.
- Chen, D., Wang, H. (2017). Cation- $\pi$  interactions between flame chemi-ions and aromatic compounds. *Energy & Fuels* **31** (3), 2345–2352. doi:[10.1021/acs.energyfuels.6b02354](https://doi.org/10.1021/acs.energyfuels.6b02354).
- Chen, H., Dobbins, R. (2000). Crystallogenesis of particles formed in hydrocarbon combustion. *Combust. Sci. Technol.* **159** (1), 109–128. doi:[10.1080/00102200008935779](https://doi.org/10.1080/00102200008935779).

## BIBLIOGRAPHY

---

- Chen, M.-K., Hsin, H.-J., Wu, T.-C., Kang, B.-Y., Lee, Y.-W., Kuo, M.-Y., Wu, Y.-T. (jan 2014b). Highly Curved Bowl-Shaped Fragments of Fullerenes: Synthesis, Structural Analysis, and Physical Properties. *Chemistry - A European Journal* **20** (2), 598–608. doi:[10.1002/chem.201303357](https://doi.org/10.1002/chem.201303357).
- Chickos, J. S., Webb, P., Nichols, G., Kiyobayashi, T., Cheng, P.-C., Scott, L. (aug 2002). The enthalpy of vaporization and sublimation of corannulene, coronene, and perylene at T= 298.15 K. *The Journal of Chemical Thermodynamics* **34** (8), 1195–1206. doi:[10.1006/jcht.2002.0977](https://doi.org/10.1006/jcht.2002.0977).
- Chu, T.-C., Buras, Z. J., Oßwald, P., Liu, M., Goldman, M. J., Green, W. H. (2019). Modeling of aromatics formation in fuel-rich methane oxy-combustion with an automatically generated pressure-dependent mechanism. *Physical Chemistry Chemical Physics* **21** (2), 813–832. doi:[10.1039/C8CP06097E](https://doi.org/10.1039/C8CP06097E).
- Clar, E., McAndrew, B., Zander, M. (1967). The establishment of double bond character in methyl derivatives of phenanthrene, pyrene, chrysene and coronene by NMR. *Tetrahedron* **23** (2), 985–993. doi:[10.1016/0040-4020\(67\)85046-4](https://doi.org/10.1016/0040-4020(67)85046-4).
- Clark, S. J., Robertson, J. (Aug 2010). Screened exchange density functional applied to solids. *Phys. Rev. B* **82**, 085–208. doi:[10.1103/PhysRevB.82.085208](https://doi.org/10.1103/PhysRevB.82.085208).
- Cole, J., Bittner, J., Longwell, J., Howard, J. (1984). Formation mechanisms of aromatic compounds in aliphatic flames. *Combustion and Flame* **56** (1), 51–70. doi:[10.1016/0010-2180\(84\)90005-1](https://doi.org/10.1016/0010-2180(84)90005-1).
- Commodo, M., Kaiser, K., De Falco, G., Minutolo, P., Schulz, F., D’Anna, A., Gross, L. (2019). On the early stages of soot formation: Molecular structure elucidation by high-resolution atomic force microscopy. *Combustion and Flame* **205**, 154–164. doi:[10.1016/j.combustflame.2019.03.042](https://doi.org/10.1016/j.combustflame.2019.03.042).
- Costa, J. C., Taveira, R. J., Lima, C. F., Mendes, A., Santos, L. M. (2016). Optical band gaps of organic semiconductor materials. *Opt. Mater.* **58** (Supplement C), 51 – 60. doi:<https://doi.org/10.1016/j.optmat.2016.03.041>.
- Cramer, C. J. (2013). *Essentials of computational chemistry: theories and models*. John Wiley & Sons.
- Curtiss, L. A., Raghavachari, K., Redfern, P. C., Rassolov, V., Pople, J. A. (1998). Gaussian-3 (G3) theory for molecules containing first and second-row atoms. *Journal of Chemical Physics* **109** (18), 7764–7776. doi:[10.1063/1.477422](https://doi.org/10.1063/1.477422).

## BIBLIOGRAPHY

---

- Curtiss, L. A., Raghavachari, K., Trucks, G. W., Pople, J. A. (1991). Gaussian-2 theory for molecular energies of first- and second-row compounds. *Journal of Chemical Physics* **94**, 7221–7230. doi:[10.1063/1.460205](https://doi.org/10.1063/1.460205).
- Curtiss, L. A., Redfern, P. C., Raghavachari, K. (2007). Gaussian-4 theory using reduced order perturbation theory. *Journal of Chemical Physics* **127** (12), 124105–1–124105–8. doi:[10.1063/1.2770701](https://doi.org/10.1063/1.2770701).
- D'Alessio, A., D'Anna, A., Gambi, G., Minutolo, P. (1996). The optical band gap model in the interpretation of the UV-visible absorption spectra of rich premixed flames. *Symposium (International) on Combustion* **26** (1), 951–957. doi:[10.1016/S0082-0784\(96\)80307-9](https://doi.org/10.1016/S0082-0784(96)80307-9).
- D'Anna, A., Sirignano, M., Commodo, M., Pagliara, R., Minutolo, P. (2008). An experimental and modelling study of particulate formation in premixed flames burning methane. *Combustion science and technology* **180** (5), 950–958. doi:[10.1080/00102200801894448](https://doi.org/10.1080/00102200801894448).
- D'Anna, A., Violi, A. (1998). A kinetic model for the formation of aromatic hydrocarbons in premixed laminar flames. In *Symposium (International) on Combustion*, vol. 27, pp. 425–433. Elsevier. doi:[10.1016/S0082-0784\(98\)80431-1](https://doi.org/10.1016/S0082-0784(98)80431-1).
- D'Anna, A., Violi, A., D'Alessio, A., Sarofim, A. F. (2001). A reaction pathway for nanoparticle formation in rich premixed flames. *Combustion and Flame* **127** (1), 1995–2003. doi:[10.1016/S0010-2180\(01\)00303-0](https://doi.org/10.1016/S0010-2180(01)00303-0).
- Das, A., Muller, T., Plasser, F., Lischka, H. (2016). Polyradical character of triangular non-kekulé structures, zethrenes, p-quinodimethane-linked bisphenalenyl, and the clar goblet in comparison: an extended multireference study. *The Journal of Physical Chemistry A* **120** (9), 1625–1636. doi:[10.1021/acs.jpca.5b12393](https://doi.org/10.1021/acs.jpca.5b12393).
- Das, R., Chattaraj, P. K. (2014). Gas storage potential of ExBox4+ and its Li-decorated derivative. *Physical Chemistry Chemical Physics* **16** (40), 21964–21979. doi:[10.1039/c4cp02199a](https://doi.org/10.1039/c4cp02199a).
- Denis, P. A. (2015). Pristine graphene-based catalysis: Significant reduction of the inversion barriers of adsorbed and confined corannulene, sumanene, and dibenzo[a,g]corannulene. *Journal of Physical Chemistry A* **119** (22), 5770–5777. doi:[10.1021/acs.jpca.5b02181](https://doi.org/10.1021/acs.jpca.5b02181).

## BIBLIOGRAPHY

---

- Denkler, K. (2004). Sir Percivall Pott, Sir James Paget, and soot cancer of the hand. *The Lancet* **364** (9434), 582. doi:[10.1016/S0140-6736\(04\)16848-7](https://doi.org/10.1016/S0140-6736(04)16848-7).
- Desgroux, P., Mercier, X., Thomson, K. A. (2013). Study of the formation of soot and its precursors in flames using optical diagnostics. *Proceedings of the Combustion Institute* **34** (1), 1713–1738. doi:[10.1016/j.proci.2012.09.004](https://doi.org/10.1016/j.proci.2012.09.004).
- Di Stasio, S., Legarrec, J. L., Mitchell, J. B. (2011). Synchrotron radiation studies of additives in combustion, II: Soot agglomerate microstructure change by alkali and alkaline-earth metal addition to a partially premixed flame. *Energy and Fuels* **25** (3), 916–925. doi:[10.1021/ef1012209](https://doi.org/10.1021/ef1012209).
- Dobbins, R., Fletcher, R., Lu, W. (1995). Laser microprobe analysis of soot precursor particles and carbonaceous soot. *Combustion and Flame* **100** (1-2), 301–309. doi:[10.1016/0010-2180\(94\)00047-V](https://doi.org/10.1016/0010-2180(94)00047-V).
- Dobbins, R. A., Fletcher, R. A., Chang, H.-C. (1998). The evolution of soot precursor particles in a diffusion flame. *Combustion and Flame* **115** (3), 285–298. doi:[10.1016/S0010-2180\(98\)00010-8](https://doi.org/10.1016/S0010-2180(98)00010-8).
- Dobrowolski, M. A., Ciesielski, A., Cyrański, M. K. (2011). On the aromatic stabilization of corannulene and coronene. *Physical Chemistry Chemical Physics* **13** (46), 20557. doi:[10.1039/c1cp21994d](https://doi.org/10.1039/c1cp21994d).
- Dunning, T. H. (1989). Gaussian basis sets for use in correlated molecular calculations. I. The atoms boron through neon and hydrogen. *Journal of Chemical Physics* **90** (2), 1007–1023. doi:[10.1063/1.456153](https://doi.org/10.1063/1.456153).
- Eaves, N., Dworkin, S., Thomson, M. (2015). The importance of reversibility in modeling soot nucleation and condensation processes. *Proceedings of the Combustion Institute* **35** (2), 1787–1794. doi:[10.1016/j.proci.2014.05.036](https://doi.org/10.1016/j.proci.2014.05.036).
- Eggen, B., Heggie, M., Jungnickel, G., Latham, C., Jones, R., Briddon, P. (1996). Autocatalysis during fullerene growth. *Science* **272** (5258), 87–90. doi:[10.1126/science.272.5258.87](https://doi.org/10.1126/science.272.5258.87).
- Elvati, P., Violi, A. (2013). Thermodynamics of poly-aromatic hydrocarbon clustering and the effects of substituted aliphatic chains. *P. Combust. Inst.* **34** (1), 1837 – 1843. doi:<https://doi.org/10.1016/j.proci.2012.07.030>.
- Evans, M., Polanyi, M. G. (1935). The activated complex in chemical reactions. *Transactions of the Faraday Society* **31**, 875–894. doi:[10.1039/TF9353100875](https://doi.org/10.1039/TF9353100875).

- Ewels, C., Heggie, M., Briddon, P. (2002). Adatoms and nanoengineering of carbon. *Chemical Physics Letters* **351** (3-4), 178–182. doi:[10.1016/S0009-2614\(01\)01371-9](https://doi.org/10.1016/S0009-2614(01)01371-9).
- Eyring, H. (1935). The activated complex in chemical reactions. *Journal of Chemical Physics* **3**, 107–115. doi:[10.1063/1.1749604](https://doi.org/10.1063/1.1749604).
- Ezawa, M. (Dec 2007). Metallic graphene nanodisks: Electronic and magnetic properties. *Phys. Rev. B* **76**, 245415. doi:[10.1103/PhysRevB.76.245415](https://doi.org/10.1103/PhysRevB.76.245415).
- Faccinotto, A., Desgroux, P., Ziskind, M., Therssen, E., Focsa, C. (2011). High-sensitivity detection of polycyclic aromatic hydrocarbons adsorbed onto soot particles using laser desorption/laser ionization/time-of-flight mass spectrometry: An approach to studying the soot inception process in low-pressure flames. *Combustion and Flame* **158** (2), 227–239. doi:[10.1016/j.combustflame.2010.08.012](https://doi.org/10.1016/j.combustflame.2010.08.012).
- Fascella, S., Cavallotti, C., Rota, R., Carrà, S. (2005). The peculiar kinetics of the reaction between acetylene and the cyclopentadienyl radical. *The Journal of Physical Chemistry A* **109** (33), 7546–7557. doi:[10.1021/jp051508x](https://doi.org/10.1021/jp051508x).
- Fernandez-Alos, V., Watson, J. K., vander Wal, R., Mathews, J. P. (2011). Soot and char molecular representations generated directly from HRTEM lattice fringe images using Fringe3D. *Combustion and Flame* **158** (9), 1807 – 1813. doi:[10.1016/j.combustflame.2011.01.003](https://doi.org/10.1016/j.combustflame.2011.01.003).
- Fernández-Rossier, J., Palacios, J. J. (2007). Magnetism in graphene nanoislands. *Physical Review Letters* **99** (17), 177204. doi:[10.1103/PhysRevLett.99.177204](https://doi.org/10.1103/PhysRevLett.99.177204).
- Ferrari, A., Robertson, J. (2000). Interpretation of Raman spectra of disordered and amorphous carbon. *Phys. Rev. B* **61** (20), 14095–14107. doi:[10.1103/PhysRevB.61.14095](https://doi.org/10.1103/PhysRevB.61.14095).
- Fialkov, A. (1997). Investigations on ions in flames. *Progress in Energy and Combustion Science* **23**, 399–528. doi:[10.1016/S0360-1285\(97\)00016-6](https://doi.org/10.1016/S0360-1285(97)00016-6).
- Fiore, A. M., Naik, V., Leibensperger, E. M. (2015). Air quality and climate connections. *Journal of the Air & Waste Management Association* **65** (6), 645–685. doi:[10.1080/10962247.2015.1040526](https://doi.org/10.1080/10962247.2015.1040526).
- Foresman, J. B., Frish, A. E. (1996). *Exploring chemistry with electronic structure methods*. Gaussian; 2nd edition.

## BIBLIOGRAPHY

---

- Forse, A. C., Griffin, J. M., Presser, V., Gogotsi, Y., Grey, C. P. (2014). Ring current effects: factors affecting the NMR chemical shift of molecules adsorbed on porous carbons. *The Journal of Physical Chemistry C* **118** (14), 7508–7514. doi:[10.1021/jp502387x](https://doi.org/10.1021/jp502387x).
- Forse, A. C., Merlet, C., Allan, P. K., Humphreys, E. K., Griffin, J. M., Aslan, M., Zeiger, M., Presser, V., Gogotsi, Y., Grey, C. P. (2015). New insights into the structure of nanoporous carbons from NMR, Raman, and pair distribution function analysis. *Chemistry of Materials* **27** (19), 6848–6857. doi:[10.1021/acs.chemmater.5b03216](https://doi.org/10.1021/acs.chemmater.5b03216).
- Frenklach, M. (2002a). Reaction mechanism of soot formation in flames. *Phys. Chem. Chem. Phys.* **4**, 2028–2037. doi:[10.1039/B110045A](https://doi.org/10.1039/B110045A).
- Frenklach, M. (2002b). Reaction mechanism of soot formation in flames. *Physical Chemistry Chemical Physics* **4** (11), 2028–2037. doi:[10.1039/b110045a](https://doi.org/10.1039/b110045a).
- Frenklach, M. (2019). New form for reduced modeling of soot oxidation: Accounting for multi-site kinetics and surface reactivity. *Combustion and Flame* **201**, 148 – 159. doi:<https://doi.org/10.1016/j.combustflame.2018.12.023>.
- Frenklach, M., Ebert, L. B. (1988). Comment on the proposed role of spheroidal carbon clusters in soot formation. *The Journal of Physical Chemistry* **92** (2), 561–563. doi:[10.1021/j100313a061](https://doi.org/10.1021/j100313a061).
- Frenklach, M., Liu, Z., Singh, R. I., Galimova, G. R., Azyazov, V. N., Mebel, A. M. (2018). Detailed, sterically-resolved modeling of soot oxidation: Role of O atoms, interplay with particle nanostructure, and emergence of inner particle burning. *Combustion and Flame* **188**, 284–306. doi:[10.1016/j.combustflame.2017.10.012](https://doi.org/10.1016/j.combustflame.2017.10.012).
- Frenklach, M., Mebel, A. M. (2020). On the mechanism of soot nucleation. *Physical Chemistry Chemical Physics* **22** (9), 5314–5331. doi:[10.1039/D0CP00116C](https://doi.org/10.1039/D0CP00116C).
- Frenklach, M., Ramachandra, M., Matula, R. (1985). Soot formation in shock-tube oxidation of hydrocarbons. *Symposium (International) on Combustion* **20** (1), 871 – 878, twentieth Symposium (International) on Combustion. doi:[https://doi.org/10.1016/S0082-0784\(85\)80576-2](https://doi.org/10.1016/S0082-0784(85)80576-2).

## BIBLIOGRAPHY

---

- Frenklach, M., Singh, R. I., Mebel, A. M. (2019). On the low-temperature limit of HACA. *Proceedings of the Combustion Institute* **37** (1), 969–976. doi:[10.1016/j.proci.2018.05.068](https://doi.org/10.1016/j.proci.2018.05.068).
- Frenklach, M., Wang, H. (1991). Detailed modeling of soot particle nucleation and growth. *Symposium (International) on Combustion* **23** (1), 1559–1566. doi:[10.1016/S0082-0784\(06\)80426-1](https://doi.org/10.1016/S0082-0784(06)80426-1).
- Frisch, M., Trucks, G., Schlegel, H., Scuseria, G., Robb, M., Cheeseman, J., Montgomery, J., Vreven, T., Kudin, K., Burant, J., Millam, J., Iyengar, S., Tomasi, J., Barone, V. (2004). Gaussian 03, Revision C.02. Gaussian, Inc., Wallingford, CT, 2004.
- Frisch, M., Trucks, G., Schlegel, H., Scuseria, G., Robb, M., Cheeseman, J., Scalmani, G., Barone, V., Mennucci, B., Petersson, G., Nakatsuji, H. (2009). Gaussian 09 revision d.1. Gaussian Inc. Wallingford CT 2009.
- Frisch, M., Trucks, G., Schlegel, H., Scuseria, G., Robb, M., Cheeseman, J., Scalmani, G., Barone, V., Petersson, G., Nakatsuji, H., et al. (2016). Gaussian 16. *Revision A 3*, gaussian Inc. Wallingford CT 2016.
- Gao, C. W., Allen, J. W., Green, W. H., West, R. H. (2016). Reaction Mechanism Generator: Automatic construction of chemical kinetic mechanisms. *Computer Physics Communications* **203**, 212–225. doi:[doi:10.1016/j.cpc.2016.02.013](https://doi.org/10.1016/j.cpc.2016.02.013).
- Garza, A. J., Scuseria, G. E. (2016). Predicting band gaps with hybrid density functionals. *The Journal of Physical Chemistry Letters* **7** (20), 4165–4170. doi:[10.1021/acs.jpcllett.6b01807](https://doi.org/10.1021/acs.jpcllett.6b01807).
- Georgievskii, Y., Klippenstein, S. J. (2003). Transition state theory for multichannel addition reactions: Multifaceted dividing surfaces. *Journal of Physical Chemistry A* **107** (46), 9776–9781. doi:[10.1021/jp034564b](https://doi.org/10.1021/jp034564b).
- Gerhardt, P., Löffler, S., Homann, K. (1987). Polyhedral carbon ions in hydrocarbon flames. *Chemical Physics Letters* **137** (4), 306 – 310. doi:[https://doi.org/10.1016/0009-2614\(87\)80889-8](https://doi.org/10.1016/0009-2614(87)80889-8).
- Gilbert, R. G., Smith, S. C. (1990). *Theory of Unimolecular and Recombination Reactions*. Blackwell Scientific Publications.



## BIBLIOGRAPHY

---

- Gillen, R., Robertson, J. (2010). The screened-exchange approximation as alternative method for dft calculations on graphene structures. *physica status solidi (b)* **247** (11-12), 2945–2948. doi:[10.1002/pssb.201000136](https://doi.org/10.1002/pssb.201000136).
- Glassman, I. (1989). Soot formation in combustion processes. *Symposium (International) on Combustion* **22** (1), 295–311. doi:[10.1016/S0082-0784\(89\)80036-0](https://doi.org/10.1016/S0082-0784(89)80036-0).
- Goodwin, D. G., Moffat, H. K., Speth, R. L. (2009). Cantera: An object-oriented software toolkit for chemical kinetics, thermodynamics, and transport processes. *Caltech, Pasadena, CA*
- Grimme, S. (nov 2006). Semiempirical GGA-type density functional constructed with a long-range dispersion correction. *Journal of Computational Chemistry* **27** (15), 1787–1799. doi:[10.1002/jcc.20495](https://doi.org/10.1002/jcc.20495).
- Grimme, S. (2011). Density functional theory with london dispersion corrections. *Wiley Interdisciplinary Reviews: Computational Molecular Science* **1** (2), 211–228.
- Hamprecht, F. A., Cohen, A. J., Tozer, D. J., Handy, N. C. (1998). Development and assessment of new exchange-correlation functionals. *Journal of Chemical Physics* **109** (15), 6264–6271. doi:[10.1063/1.477267](https://doi.org/10.1063/1.477267).
- Hansen, N., Cool, T. A., Westmoreland, P. R., Kohse-Höinghaus, K. (2009). Recent contributions of flame-sampling molecular-beam mass spectrometry to a fundamental understanding of combustion chemistry. *Progress in Energy and Combustion Science* **35** (2), 168–191. doi:[10.1016/j.pecs.2008.10.001](https://doi.org/10.1016/j.pecs.2008.10.001).
- Hansen, N., Kasper, T., Klippenstein, S. J., Westmoreland, P. R., Law, M. E., Taatjes, C. A., Kohse-Höinghaus, K., Wang, J., Cool, T. A. (2007). Initial steps of aromatic ring formation in a laminar premixed fuel-rich cyclopentene flame. *The Journal of Physical Chemistry A* **111** (19), 4081–4092. doi:[10.1021/jp0683317](https://doi.org/10.1021/jp0683317).
- Hansen, N., Kasper, T., Yang, B., Cool, T. A., Li, W., Westmoreland, P. R., Oßwald, P., Kohse-Höinghaus, K. (2011). Fuel-structure dependence of benzene formation processes in premixed flames fueled by c6h12 isomers. *Proceedings of the Combustion Institute* **33** (1), 585–592. doi:[10.1016/j.proci.2010.05.056](https://doi.org/10.1016/j.proci.2010.05.056).



- Hansen, N., Li, W., Law, M. E., Kasper, T., Westmoreland, P. R., Yang, B., Cool, T. A., Lucassen, A. (2010). The importance of fuel dissociation and propargyl+ allyl association for the formation of benzene in a fuel-rich 1-hexene flame. *Physical Chemistry Chemical Physics* **12** (38), 12112–12122. doi:[10.1039/C0CP00241K](https://doi.org/10.1039/C0CP00241K).
- Happold, J., Grotheer, H., Aigner, M. (2007a). Distinction of gaseous soot precursor molecules and soot precursor particles through photoionization mass spectrometry. *Rapid Communications in Mass Spectrometry* **21** (7), 1247–1254. doi:[10.1002/rcm.2955](https://doi.org/10.1002/rcm.2955).
- Happold, J., Grotheer, H. H., Aigner, M. (2007b). Soot precursors consisting of stacked pericondensed PAHs. In Bockhorn, H., D'Anna, A., Sarofim, A. F., Wang, H. (Eds.), *Combustion Generated Fine Carbonaceous Particles*, pp. 275–285. Karlsruhe University Press.
- Harding, L. B., Georgievskii, Y., Klippenstein, S. J. (2005). Predictive theory for hydrogen atom- hydrocarbon radical association kinetics. *The Journal of Physical Chemistry A* **109** (21), 4646–4656. doi:[10.1021/jp0508608](https://doi.org/10.1021/jp0508608).
- Hayhurst, A. N., Jones, H. R. N. (1987). Ions and soot in flames. *Journal of the Chemical Society, Faraday Transactions 2* **83** (1), 1. doi:[10.1039/f29878300001](https://doi.org/10.1039/f29878300001).
- Head-Gordon, M., Pople, J. A. (1988). MP2 energy evaluation by direct methods. *Chemical Physics Letters* **153** (6), 503–506. doi:[10.1016/0009-2614\(88\)85250-3](https://doi.org/10.1016/0009-2614(88)85250-3).
- Heidenreich, R. D., Hess, W. M., Ban, L. L. (1968). A test object and criteria for high resolution electron microscopy. *Journal of Applied Crystallography* **1** (1), 1–19. doi:[10.1107/S0021889868004930](https://doi.org/10.1107/S0021889868004930).
- Herbinet, O., Rodriguez, A., Husson, B., Battin-Leclerc, F., Wang, Z., Cheng, Z., Qi, F. (2016). Study of the formation of the first aromatic rings in the pyrolysis of cyclopentene. *The Journal of Physical Chemistry A* **120** (5), 668–682. doi:[10.1021/acs.jpca.5b09203](https://doi.org/10.1021/acs.jpca.5b09203).
- Herdman, J. D., Connelly, B. C., Smooke, M. D., Long, M. B., Miller, J. H. (2011). A comparison of raman signatures and laser-induced incandescence with direct numerical simulation of soot growth in non-premixed ethylene/air flames. *Carbon* **49** (15), 5298–5311. doi:[10.1016/j.carbon.2011.07.050](https://doi.org/10.1016/j.carbon.2011.07.050).

## BIBLIOGRAPHY

---

- Hessler, J., Seifert, S., Winans, R. (2002). Spatially resolved small-angle x-ray scattering studies of soot inception and growth. *Proceedings of the Combustion Institute* **29** (2), 2743 – 2748. doi:[10.1016/S1540-7489\(02\)80334-0](https://doi.org/10.1016/S1540-7489(02)80334-0).
- Heyd, J., Peralta, J. E., Scuseria, G. E., Martin, R. L. (2005). Energy band gaps and lattice parameters evaluated with the heyd-scuseria-ernzerhof screened hybrid functional. *J. Chem. Phys.* **123** (17), 174101. doi:[10.1063/1.2085170](https://doi.org/10.1063/1.2085170).
- Hohenberg, P., Kohn, W. (1964). Inhomogeneous electron gas. *Physical Reviews* **136**, B864–B871. doi:[10.1103/PhysRev.136.B864](https://doi.org/10.1103/PhysRev.136.B864).
- Homann, K. (1985). Formation of large molecules, particulates and ions in premixed hydrocarbon flames; progress and unresolved questions. In *Symposium (International) on Combustion*, vol. 20, pp. 857–870. Elsevier. doi:[10.1016/S0082-0784\(85\)80575-0](https://doi.org/10.1016/S0082-0784(85)80575-0).
- Homann, K. H. (1998). Fullerenes and soot formation - New pathways to large particles in flames. *Angewandte Chemie, International Edition in English* **37** (18), 2435–2451. doi:[10.1002/\(SICI\)1521-3773\(19981002\)37:18<2434::AID-ANIE2434>3.0.CO;2-L](https://doi.org/10.1002/(SICI)1521-3773(19981002)37:18<2434::AID-ANIE2434>3.0.CO;2-L).
- Hou, D., You, X. (2017). Reaction kinetics of hydrogen abstraction from polycyclic aromatic hydrocarbons by H atoms. *Physical Chemistry Chemical Physics* **19** (45), 30772–30780. doi:[10.1039/C7CP04964A](https://doi.org/10.1039/C7CP04964A).
- Howard, J. B. (1991). Carbon addition and oxidation reactions in heterogeneous combustion and soot formation. *Symposium (International) on Combustion* **23** (1), 1107 – 1127, twenty-Third Symposium (International) on Combustion. doi:[https://doi.org/10.1016/S0082-0784\(06\)80371-1](https://doi.org/10.1016/S0082-0784(06)80371-1).
- Iyengar, S. S., Schlegel, H. B., Millam, J. M., Voth, G. A., Scuseria, G. E., Frisch, M. J. (2001). Ab initio molecular dynamics: Propagating the density matrix with Gaussian orbitals. II. Generalizations based on mass-weighting, idempotency, energy conservation and choice of initial conditions. *Journal of Chemical Physics* **115** (22), 10291–10302. doi:[10.1063/1.1416876](https://doi.org/10.1063/1.1416876).
- Jacobson, R. S., Korte, A. R., Vertes, A., Miller, J. H. (2020). The molecular composition of soot. *Angewandte Chemie* **132** (11), 4514–4520. doi:[10.1002/ange.201914115](https://doi.org/10.1002/ange.201914115).

## BIBLIOGRAPHY

---

- Jäger, C., Huisken, F., Mutschke, H., Jansa, I. L., Henning, T. (May 2009). Formation of Polycyclic Aromatic Hydrocarbons and Carbonaceous Solids in Gas-Phase Condensation Experiments. *Astrophys. J.* **696**, 706–712. doi:[10.1088/0004-637X/696/1/706](https://doi.org/10.1088/0004-637X/696/1/706).
- Janowski, T., Pulay, P., Sasith Karunarathna, A. A., Sygula, A., Saebø, S. (2011). Convex-concave stacking of curved conjugated networks: Benchmark calculations on the corannulene dimer. *Chemical Physics Letters* **512** (4-6), 155–160. doi:[10.1016/j.cplett.2011.07.030](https://doi.org/10.1016/j.cplett.2011.07.030).
- Jin, H., Giri, B. R., Liu, D., Farooq, A. (2020). A high temperature shock tube study of phenyl recombination reaction using laser absorption spectroscopy. *Proceedings of the Combustion Institute* doi:[10.1016/j.proci.2020.06.164](https://doi.org/10.1016/j.proci.2020.06.164).
- Johansson, K., Head-Gordon, M., Schrader, P., Wilson, K., Michelsen, H. (2018). Resonance-stabilized hydrocarbon-radical chain reactions may explain soot inception and growth. *Science* **361** (6406), 997–1000. doi:[10.1126/science.aat3417](https://doi.org/10.1126/science.aat3417).
- Johansson, K. O., Dillstrom, T., Elvati, P., Campbell, M. F., Schrader, P. E., Popolan-Vaida, D. M., Richards-Henderson, N. K., Wilson, K. R., Violi, A., Michelsen, H. A. (2017). Radical–radical reactions, pyrene nucleation, and incipient soot formation in combustion. *Proceedings of the Combustion Institute* **36** (1), 799–806. doi:[10.1016/j.proci.2016.07.130](https://doi.org/10.1016/j.proci.2016.07.130).
- Juríček, M., Strutt, N. L., Barnes, J. C., Butterfield, A. M., Dale, E. J., Baldrige, K. K., Stoddart, J. F., Siegel, J. S. (2014). Induced-fit catalysis of corannulene bowl-to-bowl inversion. *Nature Chemistry* **6** (3), 222–228. doi:[10.1038/nchem.1842](https://doi.org/10.1038/nchem.1842).
- Karton, A. (2014). Inversion and rotation processes involving non-planar aromatic compounds catalyzed by extended polycyclic aromatic hydrocarbons. *Chemical Physics Letters* **614**, 156–161. doi:[10.1016/j.cplett.2014.09.032](https://doi.org/10.1016/j.cplett.2014.09.032).
- Kassel, L. S. (1928). Studies in homogeneous gas reactions. ii. introduction of quantum theory. *Journal of Physical Chemistry* **32** (7), 1065–1079. doi:[10.1021/j150289a011](https://doi.org/10.1021/j150289a011).

## BIBLIOGRAPHY

---

- Keller, A., Kovacs, R., Homann, K.-H. (2000). Large molecules, ions, radicals and small soot particles in fuel-rich hydrocarbon flames. Part IV. Large polycyclic aromatic hydrocarbons and their radicals in a fuel-rich benzene–oxygen flame. *Physical Chemistry Chemical Physics* **2** (8), 1667–1675. doi:[10.1039/A908190I](https://doi.org/10.1039/A908190I).
- Kholghy, M. R., Veshkini, A., Thomson, M. J. (2016). The core-shell internal nanostructure of soot - A criterion to model soot maturity. *Carbon* **100** (January), 508–536. doi:[10.1016/j.carbon.2016.01.022](https://doi.org/10.1016/j.carbon.2016.01.022).
- Kislov, V., Islamova, N., Kolker, A., Lin, S., Mebel, A. (2005). Hydrogen abstraction acetylene addition and Diels - Alder mechanisms of PAH formation: A detailed study using first principles calculations. *Journal of Chemical Theory and Computation* **1** (5), 908–924. doi:[10.1021/ct0500491](https://doi.org/10.1021/ct0500491).
- Kislov, V., Sadovnikov, A., Mebel, A. (2013). Formation mechanism of polycyclic aromatic hydrocarbons beyond the second aromatic ring. *The Journal of Physical Chemistry A* **117** (23), 4794–4816. doi:[10.1021/jp402481y](https://doi.org/10.1021/jp402481y).
- Klippenstein, S. J. (1991). A bond length reaction coordinate for unimolecular reactions. II. Microcanonical and canonical implementations with application to the dissociation of NCNO. *Journal of Chemical Physics* **94** (10), 6469–6482. doi:[10.1063/1.460276](https://doi.org/10.1063/1.460276).
- Klippenstein, S. J., Georgievskii, Y., Harding, L. B. (2006). Predictive theory for the combination kinetics of two alkyl radicals. *Journal of Physical Chemistry Chemical Physics* **8**, 1133–1147. doi:[10.1039/B515914H](https://doi.org/10.1039/B515914H).
- Kohn, W., Sham, L. J. (1965). Self-consistent equations including exchange and correlation effects. *Physical review* **140** (4A), A1133. doi:[10.1103/PhysRev.140.A1133](https://doi.org/10.1103/PhysRev.140.A1133).
- Koley, D., Arunan, E., Ramakrishnan, S. (2012). Computational investigations on covalent dimerization/oligomerization of polyacenes: Is it relevant to soot formation? *Journal of Computational Chemistry* **33** (21), 1762–1772. doi:[10.1002/jcc.23014](https://doi.org/10.1002/jcc.23014).
- Krueger, R. A., Blanquart, G. (2019). Predicting aromatic exciplex fluorescence emission energies. *Physical Chemistry Chemical Physics* **21** (20), 10325–10335. doi:[10.1039/C9CP02027F](https://doi.org/10.1039/C9CP02027F).

## BIBLIOGRAPHY

---

- Lafleur, A. L., Howard, J. B., Marr, J. A., Yadav, T. (1993). Proposed fullerene precursor corannulene identified in flames both in the presence and absence of fullerene production. *The Journal of Physical Chemistry* **97** (51), 13539–13543. doi:[10.1021/j100153a020](https://doi.org/10.1021/j100153a020).
- Laidler, K. J., King, M. C. (1983). Development of transition-state theory. *The Journal of physical chemistry* **87** (15), 2657–2664. doi:[10.1021/j100238a002](https://doi.org/10.1021/j100238a002).
- Lawton, J., Weinberg, F. (1969). *Electrical aspects of combustion*. Clarendon P.
- Lehre, T., Jungfleisch, B., Suntz, R., Bockhorn, H. (2003). Size distributions of nanoscaled particles and gas temperatures from time-resolved laser-induced-incandescence measurements. *Applied Optics* **42** (12), 2021–2030. doi:[10.1364/AO.42.002021](https://doi.org/10.1364/AO.42.002021).
- Leon, G., Eaves, N., Akroyd, J., Mosbach, S., Kraft, M. (2019). A new methodology to calculate process rates in a kinetic monte carlo model of pah growth. *Combustion and Flame* **209**, 133–143. doi:[10.1016/j.combustflame.2019.07.032](https://doi.org/10.1016/j.combustflame.2019.07.032).
- Lewars, E. (2003). Computational chemistry. *Introduction to the theory and applications of molecular and quantum mechanics*
- Li, X., Moore, D. T., Iyengar, S. S. (may 2008). Insights from first principles molecular dynamics studies toward infrared multiple-photon and single-photon action spectroscopy: Case study of the proton-bound dimethyl ether dimer. *The Journal of Chemical Physics* **128** (18), 184308. doi:[10.1063/1.2903446](https://doi.org/10.1063/1.2903446).
- Li, Y., Zhang, L., Tian, Z., Yuan, T., Wang, J., Yang, B., Qi, F. (2009). Experimental study of a fuel-rich premixed toluene flame at low pressure. *Energy & Fuels* **23** (3), 1473–1485. doi:[10.1021/ef800902t](https://doi.org/10.1021/ef800902t).
- Lin, H., Liu, P., He, Z., Zhang, Y., Guan, B., Huang, Z. (2016). Formation of the first aromatic ring through the self-recombination of but-1-ene-3-yne with h-assistance in combustion. *International Journal of Hydrogen Energy* **41** (31), 13736–13746. doi:[10.1016/j.ijhydene.2016.06.123](https://doi.org/10.1016/j.ijhydene.2016.06.123).
- Liu, M., Green, W. H. (2019). Capturing aromaticity in automatic mechanism generation software. *Proc. Combust. Inst.* **37** (1), 575–581. doi:[10.1016/j.proci.2018.06.006](https://doi.org/10.1016/j.proci.2018.06.006).

## BIBLIOGRAPHY

---

- Liu, P., He, Z., Hou, G.-L., Guan, B., Lin, H., Huang, Z. (2015). The diagnostics of laser-induced fluorescence (LIF) spectra of PAHs in flame with TD-DFT: special focus on five-membered ring. *The Journal of Physical Chemistry A* **119** (52), 13009–13017. doi:[10.1021/acs.jpca.5b10114](https://doi.org/10.1021/acs.jpca.5b10114).
- Liu, P., Li, Z., Bennett, A., Lin, H., Sarathy, S. M., Roberts, W. L. (2019). The site effect on PAHs formation in HACA-based mass growth process. *Combustion and Flame* **199**, 54 – 68. doi:<https://doi.org/10.1016/j.combustflame.2018.10.010>.
- Long, A. E., Merchant, S. S., Vandeputte, A. G., Carstensen, H.-H., Vervust, A. J., Marin, G. B., Van Geem, K. M., Green, W. H. (2018). Pressure dependent kinetic analysis of pathways to naphthalene from cyclopentadienyl recombination. *Combustion and Flame* **187**, 247–256. doi:[10.1016/j.combustflame.2017.09.008](https://doi.org/10.1016/j.combustflame.2017.09.008).
- Lowe, J. S., Lai, J. Y., Elvati, P., Violi, A. (2015). Towards a predictive model for polycyclic aromatic hydrocarbon dimerization propensity. *P. Combust. Inst.* **35** (2), 1827 – 1832. doi:<https://doi.org/10.1016/j.proci.2014.06.142>.
- Lu, T., Chen, F. (2012). Multiwfn: A multifunctional wavefunction analyzer. *J. Comput. Chem.* **33** (5), 580–592. doi:[10.1002/jcc.22885](https://doi.org/10.1002/jcc.22885).
- Ma, J., Alfè, D., Michaelides, A., Wang, E. (2009). Stone-Wales defects in graphene and other planar sp<sup>2</sup>-bonded materials. *Physical Review B* **80** (3), 033407. doi:[10.1103/PhysRevB.80.033407](https://doi.org/10.1103/PhysRevB.80.033407).
- Mao, Q., Hou, D., Luo, K. H., You, X. (2018). Dimerization of polycyclic aromatic hydrocarbon molecules and radicals under flame conditions. *J. Phys. Chem A*. **122** (44), 8701–8708. doi:[10.1021/acs.jpca.8b07102](https://doi.org/10.1021/acs.jpca.8b07102).
- Mao, Q., Luo, K. H. (2019). Trace metal assisted polycyclic aromatic hydrocarbons fragmentation, growth and soot nucleation. *Proceedings of the Combustion Institute* **37** (1), 1023–1030. doi:[10.1016/j.proci.2018.06.106](https://doi.org/10.1016/j.proci.2018.06.106).
- Mao, Q., van Duin, A. C., Luo, K. (2017). Formation of incipient soot particles from polycyclic aromatic hydrocarbons: A ReaxFF molecular dynamics study. *Carbon* **121**, 380 – 388. doi:<https://doi.org/10.1016/j.carbon.2017.06.009>.
- Marcus, R. A. (1952). Unimolecular dissociations and free radical recombination reactions. *Journal of Chemical Physics* **20** (3), 359–364. doi:[10.1063/1.1700424](https://doi.org/10.1063/1.1700424).

## BIBLIOGRAPHY

---

- Márquez, I. R., Castro-Fernández, S., Millán, A., Campaña, A. G. (2018). Synthesis of distorted nanographenes containing seven- and eight-membered carbocycles. *Chemical Communications* **54** (50), 6705–6718. doi:[10.1039/C8CC02325E](https://doi.org/10.1039/C8CC02325E).
- Martin, J., McIntosh, G., Arul, R., Oosterbeek, R., Kraft, M., Söhnel, T. (dec 2017a). Giant fullerene formation through thermal treatment of fullerene soot. *Carbon* **125**, 132–138. doi:[10.1016/j.carbon.2017.09.045](https://doi.org/10.1016/j.carbon.2017.09.045).
- Martin, J., Slavchov, R., Yapp, E., Akroyd, J., Mosbach, S., Kraft, M. (2017b). The polarization of polycyclic aromatic hydrocarbons curved by pentagon incorporation: The role of the flexoelectric dipole. *J. Phys. Chem. C*. **0** (ja) doi:[10.1021/acs.jpcc.7b09044](https://doi.org/10.1021/acs.jpcc.7b09044).
- Martin, J. W. (2019). Martin, jacob w and bowal, kimberly and menon, angiras and slavchov, radomir i and akroyd, jethro and mosbach, sebastian and kraft, markus. *Proceedings of the Combustion Institute* **37** (1), 1117 – 1123. doi:<https://doi.org/10.1016/j.proci.2018.05.046>.
- Martin, J. W., Botero, M., Slavchov, R. I., Bowal, K., Akroyd, J., Mosbach, S., Kraft, M. (2018). Flexoelectricity and the formation of carbon nanoparticles in flames. *The Journal of Physical Chemistry C* **122** (38), 22210–22215. doi:[10.1021/acs.jpcc.8b08264](https://doi.org/10.1021/acs.jpcc.8b08264).
- Martin, J. W., de Tomas, C., Suarez-Martinez, I., Kraft, M., Marks, N. A. (2019a). Topology of disordered 3D graphene networks. *Physical Review Letters* **123** (11), 116105. doi:[10.1103/PhysRevLett.123.116105](https://doi.org/10.1103/PhysRevLett.123.116105).
- Martin, J. W., Hou, D., Menon, A., Pascazio, L., Akroyd, J., You, X., Kraft, M. (2019b). Reactivity of polycyclic aromatic hydrocarbon soot precursors: Implications of localized  $\pi$ -radicals on rim-based pentagonal rings. *The Journal of Physical Chemistry C* **123** (43), 26673–26682. doi:[10.1021/acs.jpcc.9b07558](https://doi.org/10.1021/acs.jpcc.9b07558).
- Martin, J. W., McIntosh, G. J., Arul, R., Oosterbeek, R. N., Kraft, M., Söhnel, T. (2017c). Giant fullerene formation through thermal treatment of fullerene soot. *Carbon* **125**, 132–138. doi:[10.1016/j.carbon.2017.09.045](https://doi.org/10.1016/j.carbon.2017.09.045).



## BIBLIOGRAPHY

---

- Martin, J. W., Slavchov, R. I., Yapp, E. K. Y., Akroyd, J., Mosbach, S., Kraft, M. (2017d). The polarization of polycyclic aromatic hydrocarbons curved by pentagon incorporation: the role of the flexoelectric dipole. *The Journal of Physical Chemistry C* **121** (48), 27154–27163. doi:[10.1021/acs.jpcc.7b09044](https://doi.org/10.1021/acs.jpcc.7b09044).
- Matito, E., Duran, M., Sola, M. (2005). The aromatic fluctuation index (flu): A new aromaticity index based on electron delocalization. *J. Chem. Phys.* **122** (1), 014109. doi:[10.1063/1.1824895](https://doi.org/10.1063/1.1824895).
- Mayo, P. J., Weinberg, F. J. (1970). On the size, charge and number-rate of formation of carbon particles in flames subjected to electric fields. *Proceedings of the Royal Society A: Mathematical, Physical and Engineering Sciences* **319** (1538), 351–371. doi:[10.1098/rspa.1970.0183](https://doi.org/10.1098/rspa.1970.0183).
- McKinnon, J., Howard, J. (1990). Application of soot formation model: effects of chlorine. *Combustion science and technology* **74** (1-6), 175–197. doi:[10.1080/00102209008951687](https://doi.org/10.1080/00102209008951687).
- McQuarrie, D. A., Simon, J. D. (1999). *Molecular thermodynamics*.
- Mebel, A., Kislov, V. (2009). Can the  $C_5H_5^+C_5H_5 \longrightarrow C_{10}H_{10} \longrightarrow C_{10}H_9^+H/C_{10}H_8^+H_2$  reaction produce naphthalene? an ab initio/rrkm study. *J. Phys. Chem. A* **113** (36), 9825–9833. doi:[10.1021/jp905931j](https://doi.org/10.1021/jp905931j).
- Mebel, A. M., Kaiser, R. I. (2015). Formation of resonantly stabilised free radicals via the reactions of atomic carbon, dicarbon, and tricarbon with unsaturated hydrocarbons: theory and crossed molecular beams experiments. *International Reviews in Physical Chemistry* **34** (4), 461–514. doi:[10.1080/0144235X.2015.1075280](https://doi.org/10.1080/0144235X.2015.1075280).
- Mebel, A. M., Landera, A., Kaiser, R. I. (2017). Formation mechanisms of naphthalene and indene: From the interstellar medium to combustion flames. *The Journal of Physical Chemistry A* **121** (5), 901–926. doi:[10.1021/acs.jpca.6b09735](https://doi.org/10.1021/acs.jpca.6b09735).
- Michelsen, H., Liu, F., Kock, B. F., Bladh, H., Boïarciuc, A., Charwath, M., Dreier, T., Hadeif, R., Hofmann, M., Reimann, J., et al. (2007). Modeling laser-induced incandescence of soot: a summary and comparison of LII models. *Applied physics B* **87** (3), 503–521. doi:[10.1007/s00340-007-2619-5](https://doi.org/10.1007/s00340-007-2619-5).



## BIBLIOGRAPHY

---

- Miller, J. A., Klippenstein, S. J. (2000). Theoretical considerations in the  $\text{NH}_2 + \text{NO}$  reaction. *Journal of Physical Chemistry A* **104** (10), 2061–2069. doi:[10.1021/jp992836y](https://doi.org/10.1021/jp992836y).
- Miller, J. A., Klippenstein, S. J. (2006). Master equation methods in gas phase chemical kinetics. *Journal of Chemical Physics* **110** (36), 10528–10544. doi:[10.1021/jp062693x](https://doi.org/10.1021/jp062693x).
- Miller, J. A., Klippenstein, S. J., Robertson, S. H. (2000). A theoretical analysis of the reaction between vinyl and acetylene: Quantum chemistry and solution of the master equation. *Journal of Physical Chemistry A* **104** (32), 7525–7536. doi:[10.1021/jp000687+](https://doi.org/10.1021/jp000687+).
- Miller, J. H. (2005). Aromatic excimers: evidence for polynuclear aromatic hydrocarbon condensation in flames. *Proceedings of the Combustion Institute* **30** (1), 1381–1388. doi:[10.1016/j.proci.2004.08.192](https://doi.org/10.1016/j.proci.2004.08.192).
- Minami, T., Ito, S., Nakano, M. (2013). Fundamental of diradical-character-based molecular design for singlet fission. *The Journal of Physical Chemistry Letters* **4** (13), 2133–2137. doi:[10.1021/jz400931b](https://doi.org/10.1021/jz400931b).
- Mitchell, J., Di Stasio, S., LeGarrec, J.-L., Florescu-Mitchell, A. I., Narayanan, T., Sztucki, M. (2009). Small angle X-ray scattering study of flame soot nanoparticle aggregation and restructuring. *Journal of Applied Physics* **105** (12), 124904. doi:[10.1063/1.3147902](https://doi.org/10.1063/1.3147902).
- Møller, C., Plesset, M. S. (1934). Note on an approximation treatment for many-electron systems. *Physical Review Letters* **46**, 618–622. doi:[10.1103/PhysRev.46.618](https://doi.org/10.1103/PhysRev.46.618).
- Montgomery, J. A., Ochterski, J. W., Petersson, G. A. (1999). A complete basis set model chemistry. vi. use of density functional geometries and frequencies. *Journal of Chemical Physics* **110** (6), 2822–2827. doi:[10.1063/1.477924](https://doi.org/10.1063/1.477924).
- Montgomery Jr, J. A., Frisch, M. J., Ochterski, J. W., Petersson, G. A. (2000). A complete basis set model chemistry. VII. Use of the minimum population localization method. *The Journal of Chemical Physics* **112** (15), 6532–6542. doi:[10.1063/1.481224](https://doi.org/10.1063/1.481224).

## BIBLIOGRAPHY

---

- Morozov, A. N., Mebel, A. M. (2019). Theoretical study of the reaction mechanism and kinetics of the phenyl+ allyl and related benzyl+ vinyl associations. *The Journal of Physical Chemistry A* **123** (9), 1720–1729. doi:[10.1021/acs.jpca.9b00345](https://doi.org/10.1021/acs.jpca.9b00345).
- Morozov, A. N., Mebel, A. M. (2020). Theoretical study of the reaction mechanism and kinetics of the phenyl+ propargyl association. *Physical Chemistry Chemical Physics* **22** (13), 6868–6880. doi:[10.1039/D0CP00306A](https://doi.org/10.1039/D0CP00306A).
- Mughal, E. U., Kuck, D. (2012). Merging tribenzotriquinacene with hexa-peri-hexabenzocoronene: a cycloheptatriene unit generated by Scholl reaction. *Chemical Communications* **48** (71), 8880–8882. doi:[10.1039/C2CC34245F](https://doi.org/10.1039/C2CC34245F).
- Neves, A. R., Fernandes, P. A., Ramos, M. J. (2011). The accuracy of density functional theory in the description of cation- $\pi$  and  $\pi$ -hydrogen bond interactions. *Journal of Chemical Theory and Computation* **7** (7), 2059–2067. doi:[10.1021/ct2001667](https://doi.org/10.1021/ct2001667).
- Nielsen, H. H. (1951). The vibration-rotation energies of molecules. *Reviews of Modern Physics* **23** (2), 90. doi:[10.1103/RevModPhys.23.90](https://doi.org/10.1103/RevModPhys.23.90).
- Niranjan, R., Thakur, A. K. (2017). The toxicological mechanisms of environmental soot (black carbon) and carbon black: focus on oxidative stress and inflammatory pathways. *Frontiers in Immunology* **8**, 763. doi:[10.3389/fimmu.2017.00763](https://doi.org/10.3389/fimmu.2017.00763).
- Novakov, T., Rosen, H. (2013). The black carbon story: early history and new perspectives. *Ambio* **42** (7), 840–851. doi:[10.1007/s13280-013-0392-8](https://doi.org/10.1007/s13280-013-0392-8).
- Observatory, L., Bohrweg, N., Leiden, N.-C. A. (2018). Formation of Covalently Bonded Polycyclic Aromatic Hydrocarbons in the Interstellar Medium. *The Astrophysical Journal* **866** (2), 113. doi:[10.3847/1538-4357/aae38f](https://doi.org/10.3847/1538-4357/aae38f).
- Öktem, B., Tolocka, M. P., Zhao, B., Wang, H., Johnston, M. V. (sep 2005). Chemical species associated with the early stage of soot growth in a laminar premixed ethylene–oxygen–argon flame. *Combustion and Flame* **142** (4), 364–373. doi:[10.1016/j.combustflame.2005.03.016](https://doi.org/10.1016/j.combustflame.2005.03.016).

## BIBLIOGRAPHY

---

- Park, D. G., Choi, B. C., Cha, M. S., Chung, S. H. (2014). Soot reduction under DC electric fields in counterflow non-premixed laminar ethylene flames. *Combustion Science and Technology* **186** (4-5), 644–656. doi:[10.1080/00102202.2014.883794](https://doi.org/10.1080/00102202.2014.883794).
- Parker, D. S. N., Kaiser, R. I., Troy, T. P., Ahmed, M. (2014). Hydrogen abstraction/acetylene addition revealed. *Angewandte Chemie - International Edition* **53** (30), 7740–7744. doi:[10.1002/anie.201404537](https://doi.org/10.1002/anie.201404537).
- Peña, G. D. G., Raj, A., Stephen, S., Anjana, T., Hammid, Y. A. S., Brito, J. L., Al Shoaibi, A. (2017). Physicochemical properties of soot generated from toluene diffusion flames: Effects of fuel flow rate. *Combustion and Flame* **178**, 286–296. doi:[10.1016/j.combustflame.2017.01.009](https://doi.org/10.1016/j.combustflame.2017.01.009).
- Pilar, F. L. (March 2001). *Elementary Quantum Chemistry*. Courier Dover Publications.
- Pitzer, K. S., Gwinn, W. D. (1942). Energy levels and thermodynamic functions for molecules with internal rotation I. rigid frame with attached tops. *Journal of Chemical Physics* **10**, 428–440. doi:[10.1063/1.1723744](https://doi.org/10.1063/1.1723744).
- Place, E. R., Weinberg, F. J. (jan 1966). Electrical control of flame carbon. *Proceedings of the Royal Society A: Mathematical, Physical and Engineering Sciences* **289** (1417), 192–205. doi:[10.1098/rspa.1966.0006](https://doi.org/10.1098/rspa.1966.0006).
- Plumley, J. A., Dannenberg, J. J. (2011). A comparison of the behavior of functional/basis set combinations for hydrogen-bonding in the water dimer with emphasis on basis set superposition error. *J. Comp. Chem.* doi:[10.1002/jcc.21729](https://doi.org/10.1002/jcc.21729).
- Pople, J. A., Head-Gordon, M., Fox, D. J., Raghavachari, K., Curtiss, L. A. (1989). Gaussian-1 theory: A general procedure for prediction of molecular energies. *Journal of Chemical Physics* **90**, 5622–5629. doi:[10.1063/1.456415](https://doi.org/10.1063/1.456415).
- Pople, J. A., Head-Gordon, M., Raghavachari, K. (1987). Quadratic configuration interaction. a general technique for determining electron correlation energies. *The Journal of chemical physics* **87** (10), 5968–5975. doi:[10.1063/1.453520](https://doi.org/10.1063/1.453520).
- Quay, B., Lee, T.-W., Ni, T., Santoro, R. (1994). Spatially resolved measurements of soot volume fraction using laser-induced incandescence. *Combustion and Flame* **97** (3-4), 384–392. doi:[10.1016/0010-2180\(94\)90029-9](https://doi.org/10.1016/0010-2180(94)90029-9).

## BIBLIOGRAPHY

---

- Raj, A. (2019). Structural effects on the growth of large polycyclic aromatic hydrocarbons by C<sub>2</sub>H<sub>2</sub>. *Combustion and Flame* **204**, 331–340. doi:[10.1016/j.combustflame.2019.03.027](https://doi.org/10.1016/j.combustflame.2019.03.027).
- Raj, A., Celnik, M., Shirley, R., Sander, M., Patterson, R., West, R., Kraft, M. (2009). A statistical approach to develop a detailed soot growth model using pah characteristics. *Combustion and Flame* **156** (4), 896–913. doi:[10.1016/j.combustflame.2009.01.005](https://doi.org/10.1016/j.combustflame.2009.01.005).
- Raj, A., Yang, S. Y., Cha, D., Tayouo, R., Chung, S. H. (2013). Structural effects on the oxidation of soot particles by O<sub>2</sub>: Experimental and theoretical study. *Combustion and Flame* **160** (9), 1812–1826. doi:[10.1016/j.combustflame.2013.03.010](https://doi.org/10.1016/j.combustflame.2013.03.010).
- Ricca, A., Bauschlicher Jr, C. W., Allamandola, L. J. (2011). The infrared spectroscopy of polycyclic aromatic hydrocarbons with five- and seven-membered fused ring defects. *The Astrophysical Journal* **729** (2), 94. doi:[10.1088/0004-637X/729/2/94](https://doi.org/10.1088/0004-637X/729/2/94).
- Rice, O. K., Ramsperger, H. C. (1927). Theories of unimolecular gas reactions at low pressures. *Journal of the American Chemical Society* **49** (7), 1617–1629. doi:[10.1021/ja01406a001](https://doi.org/10.1021/ja01406a001).
- Richter, H., Howard, J. (2000). Formation of polycyclic aromatic hydrocarbons and their growth to soot—a review of chemical reaction pathways. *Progress in Energy and Combustion Science* **26** (4), 565 – 608. doi:[https://doi.org/10.1016/S0360-1285\(00\)00009-5](https://doi.org/10.1016/S0360-1285(00)00009-5).
- Richter, H., Labrocca, A. J., Grieco, W. J., Taghizadeh, K., Lafleur, A. L., Howard, J. B. (1997). Generation of higher fullerenes in flames. *Journal of Physical Chemistry B* **101** (9), 1556–1560. doi:[10.1021/jp962928c](https://doi.org/10.1021/jp962928c).
- Robertson, J., O'Reilly, E. (1987). Electronic and atomic structure of amorphous carbon. *Phys. Rev. B* **35** (6), 2946–2957. doi:[10.1103/PhysRevB.35.2946](https://doi.org/10.1103/PhysRevB.35.2946).
- Ruiz-Morales, Y. (2002). HOMO-LUMO gap as an index of molecular size and structure for polycyclic aromatic hydrocarbons (pahs) and asphaltenes: A theoretical study. I. *J. Phys. Chem. A* **106** (46), 11283–11308. doi:[10.1021/jp021152e](https://doi.org/10.1021/jp021152e).

- Rynefors, K. (1982). UNIMOL: A program for Monte Carlo simulation of RRKM unimolecular decomposition in molecular beam experiments. *Comp. Phys. Commun.* **27** (2), 201–212. doi:[10.1016/0010-4655\(82\)90074-1](https://doi.org/10.1016/0010-4655(82)90074-1).
- Sabbah, H., Biennier, L., Klippenstein, S. J., Sims, I. R., Rowe, B. R. (2010). Exploring the role of paha in the formation of soot: Pyrene dimerization. *The Journal of Physical Chemistry Letters* **1** (19), 2962–2967. doi:[10.1021/jz101033t](https://doi.org/10.1021/jz101033t).
- Saha, B., Irle, S., Morokuma, K. (2010). Formation mechanism of polycyclic aromatic hydrocarbons in benzene combustion: Quantum chemical molecular dynamics simulations. *The Journal of Chemical Physics* **132** (22), 224303. doi:[10.1063/1.3447895](https://doi.org/10.1063/1.3447895).
- Saito, M., Arai, T., Arai, M. (1999). Control of soot emitted from acetylene diffusion flames by applying an electric field. *Combustion and Flame* **119** (3), 356–366. doi:[10.1016/S0010-2180\(99\)00065-6](https://doi.org/10.1016/S0010-2180(99)00065-6).
- Salzner, U., Aydin, A. (2011). Improved prediction of properties of  $\pi$ -conjugated oligomers with range-separated hybrid density functionals. *J. Chem. Theory Comput.* **7** (8), 2568–2583. doi:[10.1021/ct2003447](https://doi.org/10.1021/ct2003447).
- Sandoval-Salinas, M. E., Carreras, A., Casanova, D. (2019). Triangular graphene nanofragments: open-shell character and doping. *Physical Chemistry Chemical Physics* doi:[10.1039/C9CP00641A](https://doi.org/10.1039/C9CP00641A).
- Schenk, M., Lieb, S., Vieker, H., Beyer, A., Götzhäuser, A., Wang, H., Kohse-Höinghaus, K. (2013). Imaging nanocarbon materials: Soot particles in flames are not structurally homogeneous. *ChemPhysChem* **14** (14), 3248–3254. doi:[10.1002/cphc.201300581](https://doi.org/10.1002/cphc.201300581).
- Schlegel, H. B., Iyengar, S. S., Li, X., Millam, J. M., Voth, G. A., Scuseria, G. E., Frisch, M. J. (nov 2002). Ab initio molecular dynamics: Propagating the density matrix with Gaussian orbitals. III. Comparison with Born – Oppenheimer dynamics. *The Journal of Chemical Physics* **117** (19), 8694–8704. doi:[10.1063/1.1514582](https://doi.org/10.1063/1.1514582).
- Schlegel, H. B., Millam, J. M., Iyengar, S. S., Voth, G. A., Daniels, A. D., Scuseria, G. E., Frisch, M. J. (jun 2001). Ab initio molecular dynamics: Propagating the density matrix with Gaussian orbitals. *The Journal of Chemical Physics* **114** (22), 9758–9763. doi:[10.1063/1.1372182](https://doi.org/10.1063/1.1372182).

## BIBLIOGRAPHY

---

- Schuetz, C. A., Frenklach, M. (2002). Nucleation of soot: Molecular dynamics simulations of pyrene dimerization. *Proceedings of the Combustion Institute* **29** (2), 2307–2314. doi:[10.1016/S1540-7489\(02\)80281-4](https://doi.org/10.1016/S1540-7489(02)80281-4).
- Schulz, F., Commodo, M., Kaiser, K., Falco, G. D., Minutolo, P., Meyer, G., D'Anna, A., Gross, L. (2019). Insights into incipient soot formation by atomic force microscopy. *Proceedings of the Combustion Institute* **37** (1), 885 – 892. doi:<https://doi.org/10.1016/j.proci.2018.06.100>.
- Schwerdtfeger, P., Wirz, L. N., Avery, J. (2015). The topology of fullerenes. *Wiley Interdisciplinary Reviews: Computational Molecular Science* **5** (1), 96–145. doi:[10.1002/wcms.1207](https://doi.org/10.1002/wcms.1207).
- Scott, L. T. (1996). Fragments of fullerenes: novel syntheses, structures and reactions. *Pure and applied chemistry* **68** (2), 291–300. doi:[10.1351/pac199668020291](https://doi.org/10.1351/pac199668020291).
- Scott, L. T., Hashemi, M. M., Bratcher, M. S. (1992). Corannulene bowl-to-bowl inversion is rapid at room temperature. *Journal of the American Chemical Society* **114** (5), 1920–1921. doi:[10.1021/ja00031a079](https://doi.org/10.1021/ja00031a079).
- Seiders, T. J., Baldrige, K. K., Grube, G. H., Siegel, J. S. (2001). Structure/energy correlation of bowl depth and inversion barrier in corannulene derivatives: Combined experimental and quantum mechanical analysis. *Journal of the American Chemical Society* **123** (4), 517–525. doi:[10.1021/ja0019981](https://doi.org/10.1021/ja0019981).
- Senosiain, J. P., Miller, J. A. (2007). The Reaction of n- and i-C<sub>4</sub>H<sub>5</sub> Radicals with Acetylene. *The Journal of Physical Chemistry A* **111** (19), 3740–3747. doi:[10.1021/jp0675126](https://doi.org/10.1021/jp0675126).
- Shamasundar, K. R., Knizia, G., Werner, H.-J. (2011). A new internally contracted multi-reference configuration interaction method. *Journal of Chemical Physics* **135** (5), 054101–1–054101–17. doi:[10.1063/1.3609809](https://doi.org/10.1063/1.3609809).
- Sherrill, C. D., Schaefer, H. F. (1995). The configuration interaction method: Advances in highly correlated approaches. In Löwdin, P.-O., Sabin, J. R., Zerner, M. C., Brändas, E. (Eds.), *Advances in Quantum Chemistry*, vol. 34, ch. 3, pp. 143–269. Elsevier, US.

## BIBLIOGRAPHY

---

- Shi, B., Nachtigallova, D., Aquino, A. J. A., Machado, F. B. C., Lischka, H. (2019). High-level theoretical benchmark investigations of the uv-vis absorption spectra of paradigmatic polycyclic aromatic hydrocarbons as models for graphene quantum dots. *The Journal of Chemical Physics* **150** (12), 124302. doi:[10.1063/1.5086760](https://doi.org/10.1063/1.5086760).
- Siegmann, K., Hepp, H., Sattler, K. (1995). Reactive dimerization: A new PAH growth mechanism in flames. *Combustion Science and Technology* **109** (1-6), 165–181. doi:[10.1080/00102209508951900](https://doi.org/10.1080/00102209508951900).
- Simonsson, J., Olofsson, N. E., Bladh, H., Sanati, M., Bengtsson, P. E. (2017). Influence of potassium and iron chloride on the early stages of soot formation studied using imaging LII/ELS and TEM techniques. *Proceedings of the Combustion Institute* **36** (1), 853–860. doi:[10.1016/j.proci.2016.07.003](https://doi.org/10.1016/j.proci.2016.07.003).
- Singh, R., Frenklach, M. (2016). A mechanistic study of the influence of graphene curvature on the rate of high-temperature oxidation by molecular oxygen. *Carbon* **101**, 203 – 212. doi:<https://doi.org/10.1016/j.carbon.2016.01.090>.
- Sinha, S., Raj, A. (2016). Polycyclic aromatic hydrocarbon (pah) formation from benzyl radicals: a reaction kinetics study. *Phys. Chem. Chem. Phys.* **18**, 8120–8131. doi:[10.1039/C5CP06465A](https://doi.org/10.1039/C5CP06465A).
- Sirignano, M., Bartos, D., Conturso, M., Dunn, M., D'Anna, A., Masri, A. R. (2017). Detection of nanostructures and soot in laminar premixed flames. *Combustion and Flame* **176**, 299–308. doi:[10.1016/j.combustflame.2016.10.009](https://doi.org/10.1016/j.combustflame.2016.10.009).
- Skeen, S. A., Michelsen, H. A., Wilson, K. R., Popolan, D. M., Violi, A., Hansen, N. (2013). Near-threshold photoionization mass spectra of combustion-generated high-molecular-weight soot precursors. *Journal of Aerosol Science* **58**, 86–102. doi:[10.1016/j.jaerosci.2012.12.008](https://doi.org/10.1016/j.jaerosci.2012.12.008).
- Slater, J. C. (1951). A simplification of the Hartree-Fock Method. *Physical Reviews* **81**, 385–390. doi:[10.1103/PhysRev.81.385](https://doi.org/10.1103/PhysRev.81.385).
- Slater, J. C. (1953). A generalized self-consistent field method. *Physical Reviews* **91**, 528–530. doi:[10.1103/PhysRev.91.528](https://doi.org/10.1103/PhysRev.91.528).



## BIBLIOGRAPHY

---

- Small, D., Zaitsev, V., Jung, Y., Rosokha, S. V., Head-Gordon, M., Kochi, J. K. (2004). Intermolecular  $\pi$ -to- $\pi$  bonding between stacked aromatic dyads. experimental and theoretical binding energies and near-ir optical transitions for phenalenyl radical/radical versus radical/cation dimerizations. *Journal of the American Chemical Society* **126** (42), 13850–13858. doi:[10.1021/ja046770i](https://doi.org/10.1021/ja046770i).
- Solà, M. (2013). Forty years of Clar's aromatic  $\pi$ -sextet rule. *Front. Chem.* **1**, 22. doi:[10.3389/fchem.2013.00022](https://doi.org/10.3389/fchem.2013.00022).
- Stein, S. E., Fahr, A. (1985). High-Temperature Stabilities of Hydrocarbons. *Journal of Physical Chemistry* **89**, 3714–3725. doi:[10.1021/j100263a027](https://doi.org/10.1021/j100263a027).
- Stuyver, T., Chen, B., Zeng, T., Geerlings, P., De Proft, F., Hoffmann, R. (2019). Do diradicals behave like radicals? *Chemical reviews* **119** (21), 11291–11351. doi:[10.1021/acs.chemrev.9b00260](https://doi.org/10.1021/acs.chemrev.9b00260).
- Sun, C. H., Lu, G. Q., Cheng, H. M. (2006). Nonplanar distortions and strain energies of polycyclic aromatic hydrocarbons. *Journal of Physical Chemistry B* **110** (10), 4563–4568. doi:[10.1021/jp054603e](https://doi.org/10.1021/jp054603e).
- Szabo, A., Ostlund, N. S. (2012). *Modern quantum chemistry: introduction to advanced electronic structure theory*. Courier Corporation.
- Szczepanik, D. W., Solà, M., Krygowski, T. M., Szatyłowicz, H., Andrzejak, M., Pawelek, B., Dominikowska, J., Kukułka, M., Dyduch, K. (2018). Aromaticity of acenes: the model of migrating  $\pi$ -circuits. *Physical Chemistry Chemical Physics* **20** (19), 13430–13436. doi:[10.1039/C8CP01108G](https://doi.org/10.1039/C8CP01108G).
- Tauc, J., Grigorovici, R., Vancu, A. (1966). Optical Properties and Electronic Structure of Amorphous Germanium. *Phys. Status Solidi (B)* **15** (2), 627–637. doi:[10.1002/pssb.19660150224](https://doi.org/10.1002/pssb.19660150224).
- Temelso, B., Sherrill, C. D., Merkle, R. C., Freitas, R. A. (2006). High-level ab initio studies of hydrogen abstraction from prototype hydrocarbon systems. *The Journal of Physical Chemistry A* **110** (38), 11160–11173. doi:[10.1021/jp061821e](https://doi.org/10.1021/jp061821e).
- Thompson, L. M., Hratchian, H. P. (2014). Spin projection with double hybrid density functional theory. *The Journal of Chemical Physics* **141** (3), 034108.
- Tielens, A. G. (2008). Interstellar polycyclic aromatic hydrocarbon molecules. *Annu. Rev. Astron. Astrophys.* **46**, 289–337.



## BIBLIOGRAPHY

---

- Tomasi, J., Mennucci, B., Cammi, R. (2005). Quantum mechanical continuum solvation models. *Chemical reviews* **105** (8), 2999–3094. doi:[10.1021/cr9904009](https://doi.org/10.1021/cr9904009).
- Totton, T., Misquitta, A., Kraft, M. (2012). A quantitative study of the clustering of polycyclic aromatic hydrocarbons at high temperatures. *Physical Chemistry Chemical Physics* **14** (12), 4081. doi:[10.1039/c2cp23008a](https://doi.org/10.1039/c2cp23008a).
- Tranter, R. S., Klippenstein, S. J., Harding, L. B., Giri, B. R., Yang, X., Kiefer, J. H. (2010). Experimental and theoretical investigation of the self-reaction of phenyl radicals. *The Journal of Physical Chemistry A* **114** (32), 8240–8261. doi:[10.1021/jp1031064](https://doi.org/10.1021/jp1031064).
- Truhlar, D. G., Garrett, B. C., Klippenstein, S. J. (1996). Current status of transition-state theory. *Journal of Physical Chemistry* **100**, 12771–12800. doi:[10.1021/jp953748q](https://doi.org/10.1021/jp953748q).
- Truhlar, D. G., Kuppermann, A. (1971). Exact tunneling calculations. *Journal of the American Chemical Society* **93** (8), 1840–1851. doi:[10.1021/ja00737a002](https://doi.org/10.1021/ja00737a002).
- Unterreiner, B. V., Sierka, M., Ahlrichs, R. (2004). Reaction pathways for growth of polycyclic aromatic hydrocarbons under combustion conditions, a DFT study. *Physical Chemistry Chemical Physics* **6** (18), 4377–4384. doi:[10.1039/B407279K](https://doi.org/10.1039/B407279K).
- Vander, R. L., Strzelec, A., Toops, T. J., Daw, C. S., Genzale, C. L. (2013). Forensics of soot : C5-related nanostructure as a diagnostic of in-cylinder chemistry. *Fuel* **113**, 522–526. doi:[10.1016/j.fuel.2013.05.104](https://doi.org/10.1016/j.fuel.2013.05.104).
- Vander Wal, R., Weiland, K. (1994). Laser-induced incandescence: development and characterization towards a measurement of soot-volume fraction. *Applied Physics B* **59** (4), 445–452. doi:[10.1007/BF01081067](https://doi.org/10.1007/BF01081067).
- Vander Wal, R. L., Ticich, T. M., Stephens, A. B. (1999). Can soot primary particle size be determined using laser-induced incandescence? *Combustion and flame* **116** (1-2), 291–296. doi:[10.1007/s00340-019-7219-7](https://doi.org/10.1007/s00340-019-7219-7).
- Vander Wal, R. L., Tomasek, A. J. (2003). Soot oxidation: dependence upon initial nanostructure. *Combustion and flame* **134** (1-2), 1–9. doi:[10.1016/S0010-2180\(03\)00084-1](https://doi.org/10.1016/S0010-2180(03)00084-1).

## BIBLIOGRAPHY

---

- Vander Wal, R. L., Tomasek, A. J. (2004). Soot nanostructure: dependence upon synthesis conditions. *Combustion and Flame* **136** (1-2), 129–140. doi:[10.1016/j.combustflame.2003.09.008](https://doi.org/10.1016/j.combustflame.2003.09.008).
- Veshkini, A., Eaves, N. A., Dworkin, S. B., Thomson, M. J. (2016). Application of pah-condensation reversibility in modeling soot growth in laminar premixed and nonpremixed flames. *Combustion and Flame* **167**, 335–352. doi:[10.1016/j.combustflame.2016.02.024](https://doi.org/10.1016/j.combustflame.2016.02.024).
- Violi, A. (2005a). Cyclodehydrogenation reactions to cyclopentafused polycyclic aromatic hydrocarbons. *Journal of Physical Chemistry A* **109** (34), 7781–7787. doi:[10.1021/jp052384r](https://doi.org/10.1021/jp052384r).
- Violi, A. (2005b). Cyclodehydrogenation reactions to cyclopentafused polycyclic aromatic hydrocarbons. *The Journal of Physical Chemistry A* **109** (34), 7781–7787. doi:[10.1021/jp052384r](https://doi.org/10.1021/jp052384r).
- Violi, A., Kubota, A., Truong, T., Pitz, W., Westbrook, C., Sarofim, A. (2002). A fully integrated kinetic monte carlo/molecular dynamics approach for the simulation of soot precursor growth. *Proceedings of the Combustion Institute* **29** (2), 2343–2349. doi:[10.1016/S1540-7489\(02\)80285-1](https://doi.org/10.1016/S1540-7489(02)80285-1).
- Violi, A., Sarofim, A. F., Voth, G. A. (2004). Kinetic Monte Carlo–molecular dynamics approach to model soot inception. *Combustion Science and Technology* **176** (5-6), 991–1005. doi:[10.1080/00102200490428594](https://doi.org/10.1080/00102200490428594).
- Wang, C., Huddle, T., Huang, C. H., Zhu, W., Vander Wal, R. L., Lester, E. H., Mathews, J. P. (2017). Improved quantification of curvature in high-resolution transmission electron microscopy lattice fringe micrographs of soots. *Carbon* **117**, 174–181. doi:[10.1016/j.carbon.2017.02.059](https://doi.org/10.1016/j.carbon.2017.02.059).
- Wang, H. (2011). Formation of nascent soot and other condensed-phase materials in flames. *Proceedings of the Combustion Institute* **33** (1), 41–67. doi:[10.1016/j.proci.2010.09.009](https://doi.org/10.1016/j.proci.2010.09.009).
- Wang, H., Frenklach, M. (1994). Transport properties of polycyclic aromatic hydrocarbons for flame modeling. *Combustion and flame* **96** (1-2), 163–170.
- Wang, H., Frenklach, M. (1997). A detailed kinetic modeling study of aromatics formation in laminar premixed acetylene and ethylene flames. *Combust. Flame* **110** (1), 173 – 221. doi:[10.1016/S0010-2180\(97\)00068-0](https://doi.org/10.1016/S0010-2180(97)00068-0).

## BIBLIOGRAPHY

---

- Wang, H., Zhao, B., Wyslouzil, B., Streletzky, K. (2002). Small-angle neutron scattering of soot formed in laminar premixed ethylene flames. *Proceedings of the Combustion Institute* **29** (2), 2749–2757. doi:[10.1016/S1540-7489\(02\)80335-2](https://doi.org/10.1016/S1540-7489(02)80335-2).
- Warnatz, J., Dibble, R. (2006). *Combustion: Physical and chemical fundamentals, modeling and simulation, experiments, and pollutant formation*. Springer.
- Weber, R., Wilson, A. K. (2015). Do composite methods achieve their target accuracy? *Computational and Theoretical Chemistry* **1072**, 58–62. doi:[10.1016/j.comptc.2015.08.015](https://doi.org/10.1016/j.comptc.2015.08.015).
- Whitesides, R., Domin, D., Salomón-Ferrer, R., Lester, W. A., Frenklach, M. (2009). Embedded-ring migration on graphene zigzag edge. *Proceedings of the Combustion Institute* **32 I** (1), 577–583. doi:[10.1016/j.proci.2008.06.096](https://doi.org/10.1016/j.proci.2008.06.096).
- Whitesides, R., Frenklach, M. (2010). Detailed kinetic monte carlo simulations of graphene-edge growth. *The Journal of Physical Chemistry A* **114** (2), 689–703. doi:[10.1021/jp906541a](https://doi.org/10.1021/jp906541a).
- Wigner, E. (Jun 1932). On the quantum correction for thermodynamic equilibrium. *Physical Review* **40**, 749–759. doi:[10.1103/PhysRev.40.749](https://doi.org/10.1103/PhysRev.40.749).
- Wong, D., Whitesides, R., Schuetz, C., Frenklach, M. (2009). Molecular dynamics simulations of PAH dimerization. In *Combustion Generated Fine Carbonaceous Particles*, pp. 247–257. KIT Scientific Publishing Karlsruhe.
- Wu, T.-C., Chen, M.-K., Lee, Y.-W., Kuo, M.-Y., Wu, Y.-T. (jan 2013). Bowl-Shaped Fragments of C 70 or Higher Fullerenes: Synthesis, Structural Analysis, and Inversion Dynamics. *Angewandte Chemie International Edition* **52** (4), 1289–1293. doi:[10.1002/anie.201208200](https://doi.org/10.1002/anie.201208200).
- Wu, X. Z., Yao, Y. R., Chen, M. M., Tian, H. R., Xiao, J., Xu, Y. Y., Lin, M. S., Abella, L., Tian, C. B., Gao, C.-L., Zhang, Q., Xie, S. Y., Huang, R. B., Zheng, L. S. (2016). Formation of curvature subunit of carbon in combustion. *Journal of the American Chemical Society* **138** (30), 9629–9633. doi:[10.1021/jacs.6b04898](https://doi.org/10.1021/jacs.6b04898).
- Xue, X., Scott, L. T. (2007). Thermal cyclodehydrogenations to form 6-membered rings: Cyclizations of [5]helicenes. *Organic Letters* **9** (20), 3937–3940. doi:[10.1021/ol7015516](https://doi.org/10.1021/ol7015516).

## BIBLIOGRAPHY

---

- Yang, B., Li, Y., Wei, L., Huang, C., Wang, J., Tian, Z., Yang, R., Sheng, L., Zhang, Y., Qi, F. (2007). An experimental study of the premixed benzene/oxygen/argon flame with tunable synchrotron photoionization. *Proceedings of the Combustion Institute* **31** (1), 555–563. doi:[10.1016/j.proci.2006.07.171](https://doi.org/10.1016/j.proci.2006.07.171).
- Yapp, E. K., Patterson, R. I., Akroyd, J., Mosbach, S., Adkins, E. M., Miller, J. H., Kraft, M. (2016). Numerical simulation and parametric sensitivity study of optical band gap in a laminar co-flow ethylene diffusion flame. *Combust. Flame* **167**, 320 – 334. doi:<https://doi.org/10.1016/j.combustflame.2016.01.033>.
- Yapp, E. K., Wells, C. G., Akroyd, J., Mosbach, S., Xu, R., Kraft, M. (2017a). Modelling PAH curvature in laminar premixed flames using a detailed population balance model. *Combustion and Flame* **176**, 172–180. doi:[10.1016/j.combustflame.2016.10.004](https://doi.org/10.1016/j.combustflame.2016.10.004).
- Yapp, E. K., Wells, C. G., Akroyd, J., Mosbach, S., Xu, R., Kraft, M. (2017b). Modelling PAH curvature in laminar premixed flames using a detailed population balance model. *Combustion and Flame* **176**, 172–180. doi:[10.1016/j.combustflame.2016.10.004](https://doi.org/10.1016/j.combustflame.2016.10.004).
- Yapp, E. K. Y., Kraft, M. (2013). *Modelling Soot Formation: Model of Particle Formation*, pp. 389–407. Springer London, London.
- Yeh, C.-N., Chai, J.-D. (2016). Role of Kekulé and non-Kekulé structures in the radical character of alternant polycyclic aromatic hydrocarbons: a TAO-DFT study. *Scientific reports* **6**, 30562. doi:[10.1038/srep30562](https://doi.org/10.1038/srep30562).
- You, X., Whitesides, R., Zubarev, D., Lester Jr, W. A., Frenklach, M. (2011). Bay-capping reactions: Kinetics and influence on graphene-edge growth. *Proceedings of the Combustion Institute* **33** (1), 685–692. doi:[10.1016/j.proci.2010.05.110](https://doi.org/10.1016/j.proci.2010.05.110).
- Zabula, A. V., Filatov, A. S., Spisak, S. N., Rogachev, A. Y., Petrukhina, M. A. (2011). A main group metal sandwich: Five lithium cations jammed between two corannulene tetraanion decks. *Science* **333** (6045), 1008–1011. doi:[10.1126/science.1208686](https://doi.org/10.1126/science.1208686).
- Zdetsis, A., Economou, E. (2016). Interrelation of aromaticity and conductivity of graphene dots/antidots and related nanostructures. *J. Phys. Chem. C* **120** (51), 29463–29475. doi:[10.1021/acs.jpcc.6b09532](https://doi.org/10.1021/acs.jpcc.6b09532).

## BIBLIOGRAPHY

---

- Zhang, F., Wang, R., Wang, Y., Zhang, X., Liu, B. (2019). Targeted and selective HOMO energy control by fine regulation of molecular planarity and its effect on the interfacial charge transfer process in dye-sensitized solar cells. *Phys. Chem. Chem. Phys.* doi:[10.1039/C9CP00091G](https://doi.org/10.1039/C9CP00091G).
- Zhang, H.-B., You, X., Wang, H., Law, C. K. (2014). Dimerization of polycyclic aromatic hydrocarbons in soot nucleation. *The Journal of Physical Chemistry A* **118** (8), 1287–1292. doi:[10.1021/jp411806q](https://doi.org/10.1021/jp411806q).
- Zhang, W., Shao, C., Sarathy, S. M. (2020). Analyzing the solid soot particulates formed in a fuel-rich flame by solvent-free matrix-assisted laser desorption/ionization fourier transform ion cyclotron resonance mass spectrometry. *Rapid Communications in Mass Spectrometry* **34** (4), e8596. doi:[10.1002/rcm.8596](https://doi.org/10.1002/rcm.8596).
- Zhao, B., Uchikawa, K., Wang, H. (2007). A comparative study of nanoparticles in premixed flames by scanning mobility particle sizer, small angle neutron scattering, and transmission electron microscopy. *Proceedings of the Combustion Institute* **31 I**, 851–860. doi:[10.1016/j.proci.2006.08.064](https://doi.org/10.1016/j.proci.2006.08.064).
- Zhao, L., Kaiser, R. I., Xu, B., Ablikim, U., Ahmed, M., Evseev, M. M., Bashkirov, E. K., Azyazov, V. N., Mebel, A. M. (2018). Low-temperature formation of polycyclic aromatic hydrocarbons in titan's atmosphere. *Nature Astronomy* **2** (12), 973. doi:[10.1038/s41550-018-0585-y](https://doi.org/10.1038/s41550-018-0585-y).
- Zhao, L., Prendergast, M., Kaiser, R. I., Xu, B., Ablikim, U., Lu, W., Ahmed, M., Oleinikov, A. D., Azyazov, V. N., Howlader, A. H., et al. (2019). How to add a five-membered ring to polycyclic aromatic hydrocarbons (PAHs)—molecular mass growth of the 2-naphthyl radical (C<sub>10</sub>H<sub>7</sub>) to benzindenes (C<sub>13</sub>H<sub>10</sub>) as a case study. *Physical Chemistry Chemical Physics* **21** (30), 16737–16750. doi:[10.1039/C9CP02930C](https://doi.org/10.1039/C9CP02930C).
- Zhao, Y., Truhlar, D. G. (2008). The M06 suite of density functionals for main group thermochemistry, thermochemical kinetics, noncovalent interactions, excited states, and transition elements: two new functionals and systematic testing of four M06-class functionals and 12 other functionals. *Theoretical Chemistry Accounts* **120** (1-3), 215–241. doi:[10.1007/s00214-007-0310-x](https://doi.org/10.1007/s00214-007-0310-x).
- Ziegler, T. (1991). Approximate density functional theory as a practical tool in molecular energetics and dynamics. *Chemical Reviews* **91**, 651–667. doi:[10.1021/cr00005a001](https://doi.org/10.1021/cr00005a001).



# Appendix A

## Additional data for Chapter 4

The structures of the 19 molecules whose OBG was measured experimentally by UV-Visible spectroscopy are displayed in Fig. [A.1](#). P of these PAHs and the supplier are detailed in Table [A.1](#) below. The measured and calculated optical band gaps are also provided in Table [A.2](#). The calculated optical band gaps for naphthalene, biphenyl, and fluorene using a variety of hybrid functions are provided in Table [A.3](#).

## Additional data for Chapter 4

---

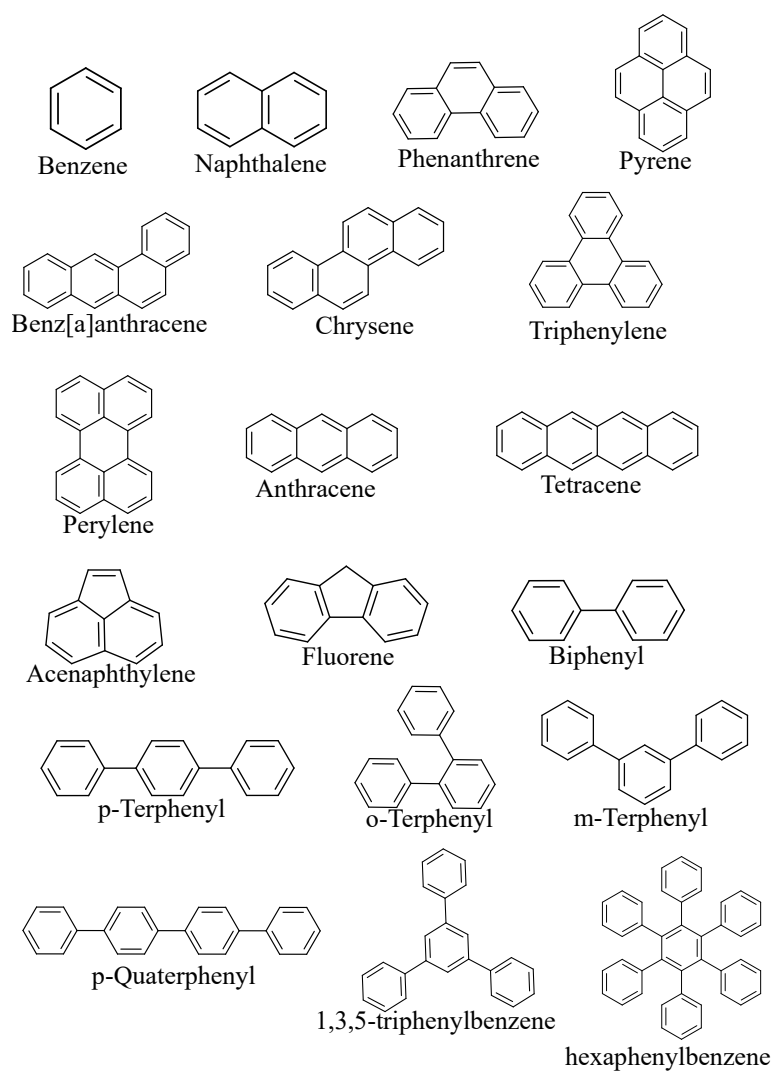


**Figure A.1:** Structures of the 19 molecules studied both experimentally and computationally in the main paper.



*Table A.1: List of PAHs studied experimentally in this work and their properties.*

| Species                | Number of Rings | $\frac{C}{H}$ ratio | Category             | Supplier      |
|------------------------|-----------------|---------------------|----------------------|---------------|
| Benzene                | 1               | 1.0                 | N/A                  | TCI           |
| Naphthalene            | 2               | 1.25                | Peri-Condensed/Acene | Sigma Aldrich |
| Phenanthrene           | 3               | 1.4                 | Peri-Condensed       | Sigma Aldrich |
| Pyrene                 | 4               | 1.6                 | Peri-Condensed       | Sigma Aldrich |
| Benz[a]anthracene      | 4               | 1.5                 | Peri-Condensed       | TCI           |
| Chrysene               | 4               | 1.5                 | Peri-Condensed       | TCI           |
| Triphenylene           | 4               | 1.5                 | Peri-Condensed       | Sigma Aldrich |
| Perylene               | 5               | 1.67                | Peri-Condensed       | TCI           |
| Anthracene             | 3               | 1.4                 | Acene                | Acros         |
| Tetracene              | 4               | 1.5                 | Acene                | Acros         |
| Acenaphthylene         | 3(1 pentagonal) | 1.5                 | Pentagonal           | Sigma Aldrich |
| Fluorene               | 3(1 pentagonal) | 1.3                 | Pentagonal           | Sigma Aldrich |
| Biphenyl               | 2               | 1.2                 | Cross-linked         | TCI           |
| p-Terphenyl            | 3               | 1.29                | Cross-linked         | TCI           |
| m-Terphenyl            | 3               | 1.29                | Cross-linked         | TCI           |
| o-Terphenyl            | 3               | 1.29                | Cross-linked         | TCI           |
| p-Quaterphenyl         | 4               | 1.33                | Cross-linked         | TCI           |
| 1,3,5-Triphenylbenzene | 4               | 1.33                | Cross-linked         | Sigma Aldrich |
| Hexaphenylbenzene      | 6               | 1.4                 | Cross-linked         | Sigma Aldrich |

## Additional data for Chapter 4

**Table A.2:** *Experimental and DFT Band Gaps, HOMO energies, and LUMO energies in electron volts.*

| Species                | $E_{g,Exp}$ | $E_{g,DFT}$ | $E_{LUMO}$ | $E_{HOMO}$ |
|------------------------|-------------|-------------|------------|------------|
| Benzene                | 5.79        | 6.28        | -0.64      | -6.92      |
| Naphthalene            | 4.22        | 4.31        | -1.57      | -5.88      |
| Phenanthrene           | 4.16        | 4.02        | -1.74      | -5.76      |
| Pyrene                 | 3.64        | 3.42        | -2.07      | -5.49      |
| Benz[a]anthracene      | 3.34        | 3.34        | -2.08      | -5.43      |
| Chrysene               | 3.80        | 3.84        | -1.79      | -5.63      |
| Triphenylene           | 4.10        | 4.43        | -1.50      | -5.93      |
| Perylene               | 2.79        | 2.89        | -2.53      | -5.41      |
| Anthracene             | 3.27        | 3.23        | -2.11      | -5.34      |
| Tetracene              | 2.63        | 2.33        | -2.68      | -5.01      |
| Acenaphthylene         | 3.59        | 3.68        | -2.38      | -6.06      |
| Fluorene               | 4.06        | 4.33        | -1.36      | -5.68      |
| Biphenyl               | 4.44        | 4.94        | -1.20      | -6.14      |
| p-Terphenyl            | 4.00        | 4.32        | -1.65      | -5.97      |
| m-Terphenyl            | 4.43        | 4.69        | -1.46      | -6.15      |
| o-Terphenyl            | 4.21        | 4.68        | -1.33      | -6.01      |
| p-Quaterphenyl         | 3.79        | 4.01        | -1.81      | -5.83      |
| 1,3,5-Triphenylbenzene | 4.35        | 4.55        | -1.50      | -6.05      |
| Hexaphenylbenzene      | 4.14        | 4.45        | -1.58      | -6.02      |

**Table A.3:** *HOMO-LUMO gaps of naphthalene, biphenyl, and Fluorene as computed by various different hybrid functionals, given in electron volts.*

| Functional      | $E_{H-L,Naphthalene}$ | $E_{H-L,Biphenyl}$ | $E_{H-L,Fluorene}$ |
|-----------------|-----------------------|--------------------|--------------------|
| HSE06           | 4.31                  | 4.94               | 4.33               |
| B3LYP           | 4.85                  | 5.46               | 5.05               |
| CAM-B3LYP       | 7.39                  | 7.92               | 7.56               |
| B971            | 4.94                  | 5.44               | 5.13               |
| PBE0            | 5.22                  | 5.73               | 5.41               |
| $\omega$ -B97xD | 8.55                  | 9.09               | 8.72               |
| M06             | 5.26                  | 5.76               | 5.44               |
| B972            | 4.83                  | 5.43               | 5.04               |

---

## Determining Optical Band Gaps from UV/Visible Spectroscopy

We determine the optical band gap from UV/Visible spectroscopy using the absorption edge method as detailed in other works [Caglar et al. \(2007\)](#); [Bhadwal et al. \(2014\)](#); [Costa et al. \(2016\)](#). The peak of the low absorption band is located and then extrapolation is performed to locate the absorption edge, the point at which the absorption starts to occur, by finding the intersection between the baseline and the slope determined from the low absorption band maximum. This wavelength is then converted to the optical band gap using the standard formula:

$$E_g = \frac{1240}{\lambda_{a.e.}} \quad (\text{A.1})$$

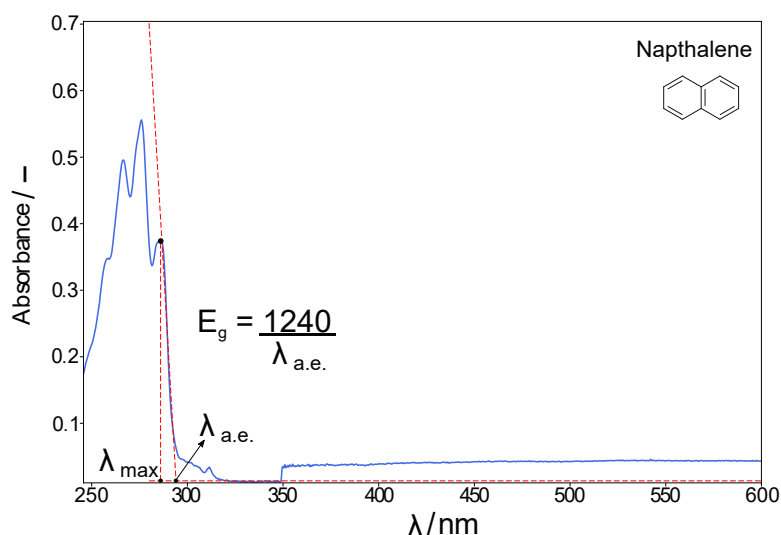


**Figure A.2:** Example plot of absorbance against wavelength spectra for naphthalene zoomed in on the low energy absorption band. The method for determining the wavelength at the absorption edge is illustrated, along with the method of extrapolation.

The baseline value changes at 350 nm due to the change in light source from Visible to UV. The baseline value is taken as the baseline just before the absorption starts to occur. There is some noise present in the baseline prior to the start of the absorption, so an average is taken for the baseline value before absorption occurs.